MICRO-SCALE COMPLEX FLOWS ENABLES ROBUST DNA REPLICATION, ENHANCED TRANSPORT AND TUNABLE FLUID-PARTICLE INTERACTIONS

A Dissertation

by

AASHISH PRIYE

Submitted to the Office of Graduate and Professional Studies of
Texas A&M University
in partial fulfillment of the requirements for the degree of

DOCTOR OF PHILOSOPHY

Chair of Committee,	Victor M. Ugaz
Committee Members,	William H. Marlow
	Yassin Hassan
	Tahir Cagin
Head of Department,	Nazmul Karim

May 2015

Major Subject: Chemical Engineering

ABSTRACT

The ability of convective flows in micro-scale confinement to direct chemical processes along accelerated kinetic pathways has been recognized for some time. However, practical applications have been slow to emerge because optimal results are often counterintuitively achieved in flows that appear to possess undesirably high disorder. Here we investigate the nature of these thermal instability driven Rayleigh-Bénard convective flows by altering the Rayleigh number and geometry of the cylindrical enclosure and thus identifying the chaotic flow regime. We then assess the ability of these flows to replicate DNA through polymerase chain reaction (PCR) across a broad ensemble of geometric states. The resulting parametric map reveals an unexpectedly wide chaotic regime where reaction rates remain constant over 2 orders of magnitude of the Rayleigh number, enabling robust convective PCR.

With the new optimal design rules, we engineer a rugged, ultra-portable (300 g), inexpensive (<$20) bioanalysis platform for rapid nucleic acid-based diagnostics. The isothermal convective isothermal PCR format enables low power operation (5 V USB source). Time-resolved fluorescence detection and quantification is achieved using a smart-phone camera and integrated image analysis app. These advancements make it possible to provide gold standard nucleic acid-based diagnostics to remote field sites using consumer class quad-copter drones.

The surprising interplay between reactions and micro-scale convective flows led us to consider adaptations beyond PCR. Specifically, we demonstrate that such flows,

naturally established over a broad range of hydrothermally relevant pore sizes, function as highly efficient conveyors to continually shuttle molecular precursors from the bulk fluid to targeted locations on the solid boundaries, enabling greatly accelerated chemical synthesis. Insights from this study has the potential to provide a breakthrough in our understanding of the fundamental biochemical processes underlying the origin of life.

The phenomenon of particle resuspension plays a vital role in numerous fields and thus an accurate description and formulation of van der Waals (vdW) interactions between the particle and substrate is of utmost importance. An approach based on Lifshitz continuum theory has been developed to calculate the principal many body interactions between arbitrary geometries at all separation distances to a high degree of accuracy. The new formulation can now provide realistic interactions for various particle-substrate systems which can then be coupled with computational fluid dynamics (CFD) models to improve the predictive capabilities of particle resuspension dynamics.

Finally, We analyze trajectories of micro sized particles subject to all relevant hydrodynamic forces and torques by coupling discrete element modeling with CFD. The results provide us with important design rules to construct membraneless microfluidic filtration channels where pressure driven transverse flows and curvature induced dean flows can be simultaneously harnessed to assist size based particle separation with high throughput.

DEDICATION

To my grandmother for always believing in me.

Big whorls have little whorls
which feed on their velocity
and little whorls have lesser whorls
and so on to viscosity…
- Lewis Richardson

ACKNOWLEDGEMENTS

First of all I would like to acknowledge the department of chemical engineering for providing me with the opportunity to pursue my doctoral studies at Texas A&M University. Needless to say, I express my utmost gratitude to Prof. Ugaz for not only providing me with the support and guidance throughout my PhD but also for being a very patient and influential mentor to me. Through those countless one-on-one meetings and email correspondences, your capacity to generate original ideas and out of the box thinking has really helped me identify the key aspects of being a good scientist, researcher and educator. I also truly value all the unique opportunities you presented to me, specially the freedom to try out new things (like developing phone apps) or the chance to design and conduct experiments aimed to enhance student learning experience in the classroom. I am also grateful to Prof. Marlow for guiding me through the intricacies of van der Waals (vdW) interactions, a subject which was new to me but has greatly intrigued my interest in the field of electromagnetism in condensed matter. I will remember the long discussions we had on the scope and application of vdW forces and the field in general. Thanks to Prof. Hassan and Prof. Cagin for providing valuable insights that have strengthened my dissertation over the course of study.

There are others who deserve a sincere recognition for significantly progressing my research along the way. Thanks to Dr. Nimisha Srivastava for providing valuable guidance during my internship at NVS technologies and Dr. Season Wong for the valuable suggestions regarding convective PCR. Thanks to Jeff for accommodating my odd request of running large number of simulations on the cluster for longer than allotted time, Randy for training me on various instruments in the machine shop and Adrian for training me on the equipments in the aggie fabrication lab. Thanks to Kyle Palmer (REU student) for assistance in the PCR kinetic model formulation and the entire undergraduate Aggie-Challenge program team (Yuanpeng Bi, Miguel Carpio, Jamison Chang, Danielle Cope, Jacob Harris, James Johnson, Alexandra Keller, Richard Lim, Stanley Lu, Alex Millard, Mauricio Coen, Adriano Pangelinan, Neal Patel, Luke Smith) for notably advancing the convective PCR project. I feel privileged to have taken courses from Prof. Chen (Advanced computational fluid dynamics) and Prof. Girimaji (excellent introduction to turbulence modeling) along with numerous online courses from other universities which has allowed me to conveniently employ intricate concepts in my research.

I am pleased to have worked with wonderful and intellectual lab-mates, namely Radha, Wendy, Serdar, Tony, Nan, Clemente, Fanxu, Duanduan, Ravi and Choi. I will not only remember the spectrum of ideas that were exchanged between us but will also cherish the random chat sessions we had both in and out of the lab. Thanks for bailing me out on the numerous occasions I was locked out of the office with my keys inside.

I honestly think that my life outside the lab would not have been easy without the few amazing friends I had over the years. I really appreciate the company of my room-mates who not only were very considerable but also quite accommodating towards my kitchen/microwave experiments. Thanks Rohit for teaching me how to drive here, Bhanesh for accompanying me on those long distance runs, Nishant for fascinating me with the phenomenal world of mathematics and Shreya for those melodious karaoke nights. I would also like to pay my sincere gratitude to my dear friend and colleague Dr. Tulsyan with whom I share the long and fruitful journey of getting admitted into and completing a PhD program. Thanks for constantly pushing me to do more and raising the bar for me. A special thanks to Loveleena for the wonderful moments we shared.

Finally I would not be here without the unconditional love, support and liberal upbringing of my family. Thank you father (Jai) for embedding in me the ability to enjoy my work and ask the right questions, mother (Anjana) for instilling in me the capacity to laugh and appreciate life even when circumstances are tough and my sister (Aashima) for inspiring me to read. I would also like to thank my uncle who encouraged me to pursue a doctoral program in the first place.

TABLE OF CONTENTS

Page

LIST OF FIGURES

LIST OF TABLES

Page

CHAPTER I

INTRODUCTION TO RAYLEIGH-BÉNARD CONVECTION AT MICROSCALE

Introduction

Convection is the collective motion of fluid due to its molecular motion (diffusion via Brownian motion) and large scale motion of bulk fluid volume (advection). Convective flows can be forced where the motion of fluid is driven by an external momentum source such as a fan. More interestingly, convection can be thermally driven where the motion of the fluid is caused by buoyancy forces that result from temperature gradient induced local density variations. This is called free or natural convection and it is a very important and common occurrence responsible for numerous physical phenomenon such as regulation of earth’s surface temperature, motion of the rocky mantle, cloud formation, crystal growth etc.

Even though the concept of convection is quite old, the first quantitative experiments were performed by Henri-Bénard only around a century ago (1900) where he studied the stability of thin layer of fluid (wax) which was heated from below and open to the atmosphere on the top. His observations led to the depiction and quantification of periodic hexagonal cell pattern formation on the top layer of the fluid known as Bénard cells. It was later (1916) that Rayleigh provided a formal analysis of Bénard cells via hydrodynamic stability theory[1] on a Boussinesq fluid[2]. Since then, Rayleigh Bénard convective flows has been studied quite frequently and had many applications.

Convective flow polymerase chain reaction (PCR)

Recently, it was shown that Rayleigh Bénard convective flows within micro-scaled cylindrical enclosures (mini lava lamps) can be harnessed to actuate biochemical reactions which replicate DNA via polymerase chain reaction (PCR)[3]. PCR is a very important tool in molecular biology which enables a sequence of DNA to be replicated across several orders of magnitude, generating billions of copies from a single molecule by cycling the PCR reagents through the prescribed temperatures. The PCR mixture is first heated to ~ 95 ºC where the double stranded DNA molecule unwinds to two single stranded DNA molecules (Denaturation). The temperature is then lowered ~60 ºC where target specific primers (oligomers) bracket the region of amplification (annealing). Finally the temperature is increased to ~ 72 ºC where the polymerase enzyme extends the two single strands into two double stranded DNA molecules (extension). Thus in every subsequent cycle, the number of the target DNA molecules doubles, yielding a billion copies in just 30 cycles. These heating and cooling steps are typically done in instruments called thermo-cyclers (Figure 1 a) which are programmed to repeatedly change the temperature of heavy metallic blocks containing the PCR mixture. These are often bulky and slow taking more than an hour to complete the PCR thermal cycling. With recent advances in microfluidics, there have been constant efforts geared towards developing PCR systems that are faster and more efficient. In Rayleigh Bénard Convective PCR, the aqueous reaction mixture is confined in small (~millimeter sized) cylindrical enclosures whose bottom surface is maintained at higher temperature (~95 ºC) than the top (~55 ºC). The resulting circulatory convective flow drives the PCR mixture from the hot bottom region where denaturation takes place to the top cooler region where annealing takes place, followed by the middle region where extension takes place, thus completing a PCR thermal cycle pseudo-isothermally (Figure 1 b).

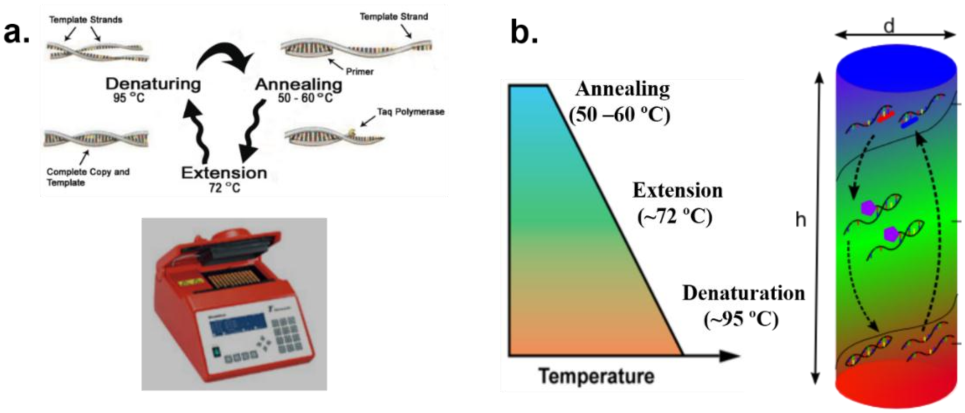

Figure 1: Pseudo-isothermal PCR in a simple Rayleigh Bénard convection cell as opposed to traditional thermo-cycling format. (a) Metallic blocks are programmed to heat and cool the PCR mixture repeatedly in thermo-cyclers. (b) PCR in a Rayleigh Bénard convection cell of diameter *d* and height *h*. The three steps of steps are sequentially executed as the PCR mixture is shuffled through the hot (bottom) and cold (top) regions of the cylindrical reactor repeatedly

Even though the design and implementation of the convective PCR seems simple, the underlying physics and emerging thermal instability driven convective flow fields are quite complicated. Key insights about the stability modes of Rayleigh Bénard convective flows can be gained by performing linear stability analysis on the governing hydrodynamic equations (Navier-Stokes equations) coupled with the energy equations with Boussinesq approximation. Non dimensionalizing these equations with appropriate scaling constants, forces out natural dimensionless parameters which ultimately governs the stability of the base flow state (no convective flow) and its transition to more intricate stable flow states upon perturbing the base state.

$$\begin{aligned}
&\nabla^* \cdot v^* = 0 \\
&\frac{\partial v^*}{\partial t^*} + v^* \cdot \nabla^* v^* = -\frac{1}{\mathrm{Re}} \nabla^* P^* + \frac{\mathrm{Ra}}{\mathrm{Pr}} \theta \hat{e}_z + \frac{1}{\mathrm{Re}} \nabla^{*2} v^* \\
&\frac{\partial \theta}{\partial t^*} + v^* \cdot \nabla^* \theta = \frac{1}{\mathrm{Re.Pr}} \nabla^{*2} \theta
\end{aligned} \qquad [1.1]$$

Where *v**, *p**, *θ*, *t**, *Re, Ra,* and *Pr*; represents the dimensionless velocity, pressure, temperature, time, Reynolds number, Rayleigh number, and Prandtl number respectively. Reynolds number measures the relative magnitudes of inertial and viscous effects in the fluid. The two important dimensionless numbers for the Rayleigh Bénard flows are the Rayleigh and Prandtl numbers. Rayleigh number (*Ra*) expresses the ratio of the destabilizing buoyancy term (driving force for convection) to the stabilizing thermal and viscous diffusion term and can be cast as

$$Ra = \frac{\beta g \Delta T h^3}{\nu \alpha} \qquad [1.2]$$

Where *g, h,* ΔT, *β, ν* and *α* represents the acceleration due to gravity (9.8 m^2/s), height of the fluid layer, temperature difference across *h,* thermal expansion coefficient, dynamic viscosity and thermal diffusivity of the fluid respectively. Prandtl number ($Pr = \nu / \alpha$) on the other hand is the ratio of the viscous to thermal diffusion in the fluid and is only a property of the fluid. Therefore in convective PCR system the *Pr* is practically fixed and is determined by the fluid properties of the aqueous PCR reagent mixture which is essentially water (Appendix B). In the original stability analysis of equations[1.1], the fluid layer was assumed to be infinitely wide with no bounding vertical walls. This simplified boundary condition enabled the equations to be recast into normal modes (Helmholtz's equations) resulting in an eigenvalue problem which could then be solved to yield stability characteristics of the flow as a function of *Ra* (Appendix A). Critical values of *Ra* can be determined by analyzing the growth/decay of the normal modes subject to small perturbations to the stable base flow state. These solutions are also useful in examining the structure of the flow in systems with similar boundary conditions (such as both top and bottom free surfaces). The critical Rayleigh number (Ra_c) obtained from linear stability analysis for free (top) – free (bottom), free (top) - rigid (bottom) and rigid (top) - rigid (bottom) boundaries are 657.5, 1101 and 1708 respectively. However for more realistic scenarios and the convective PCR based application the side wall effect can no longer be neglected (instead of an infinitely wide fluid layer). This is only possible by solving equations [1.1] numerically for the prescribed boundary conditions.

Spectrum of convective flow states

We used computational fluid dynamics (CFD) to investigate the various flow regimes and its implication on convective PCR (Appendix C). Cylindrical reactors were used to perform convective PCR experiments as it was fairly easy to manufacture (see chapter II). This yielded only two geometric parameters (height (*h*), diameter (*d*)) to determine shape and size of the reactor. It was found that the final stable flow state in these micro-scaled reactors uniquely depends on the Rayleigh number (*Ra*) of the system and cylinder aspect ratio (*h*/*d*) of the reactor. Thus tuning these two parameters (*Ra* and *h*/*d*) independently allowed us to access a spectrum of convective flow states within the system.

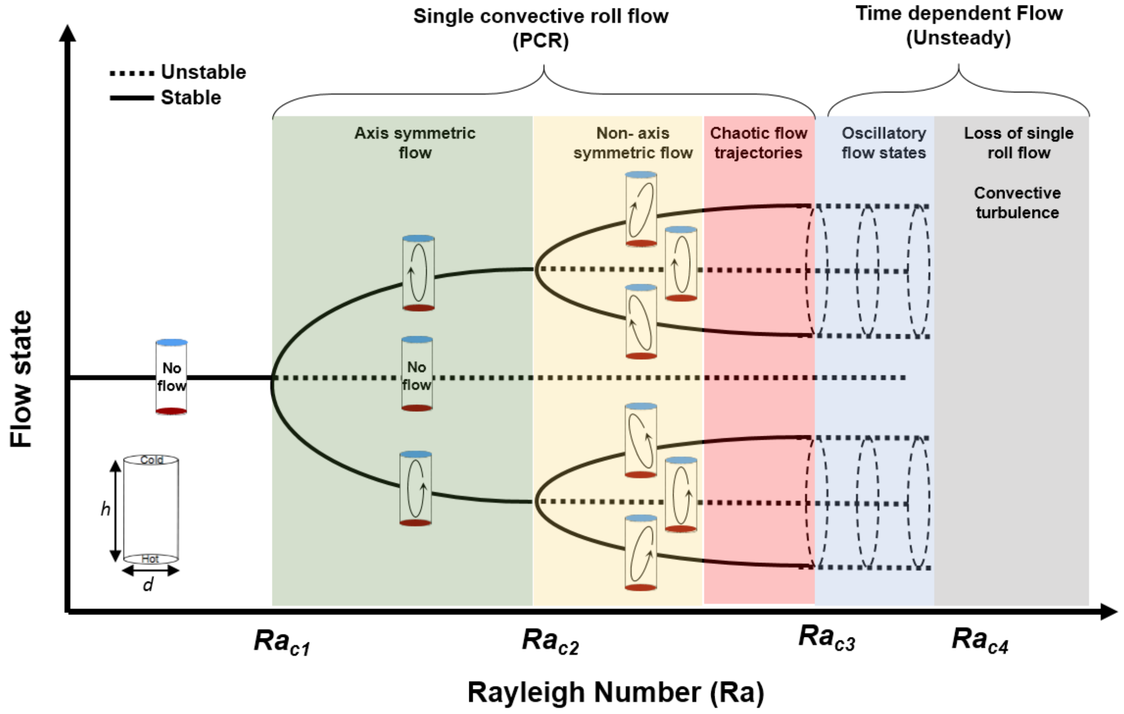

Figure 2: Bifurcation diagram of convective flow in micro-scaled reactors. For a given aspect ratio, the base flow state of no convective flow transitions to single rolled convective flow as the Rayleigh number is increased above the critical *Ra* (Ra_{c1}). Ra_{c2}, Ra_{c3} and Ra_{c4} represent the transition Rayleigh numbers for the emergence of non-axis symmetric, oscillatory and unsteady convective flows respectively.

For example, for a given cylinder aspect ratio, at low *Ra* the buoyancy force is not strong enough to drive the flow. As *Ra* is increased above the critical Rayleigh number (Ra_c), the base state of no flow becomes unstable and a slight perturbation initiates a single rolled axis symmetric flow which may be clockwise or counter clockwise depending on the initial disturbance. Upon further increasing *Ra*, the axis symmetric flow itself becomes unstable, and the flow stabilizes to non-axis symmetric flow (Figure 2). The flow at this stage exhibits chaotic fluid trajectories where the fluid elements no longer follow periodic closed paths. Upon further increasing the *Ra* the flow oscillates between the possible non-axis symmetric flow state before it finally loses its single roll flow structure to enter the regime of unsteady flows and convective turbulence.

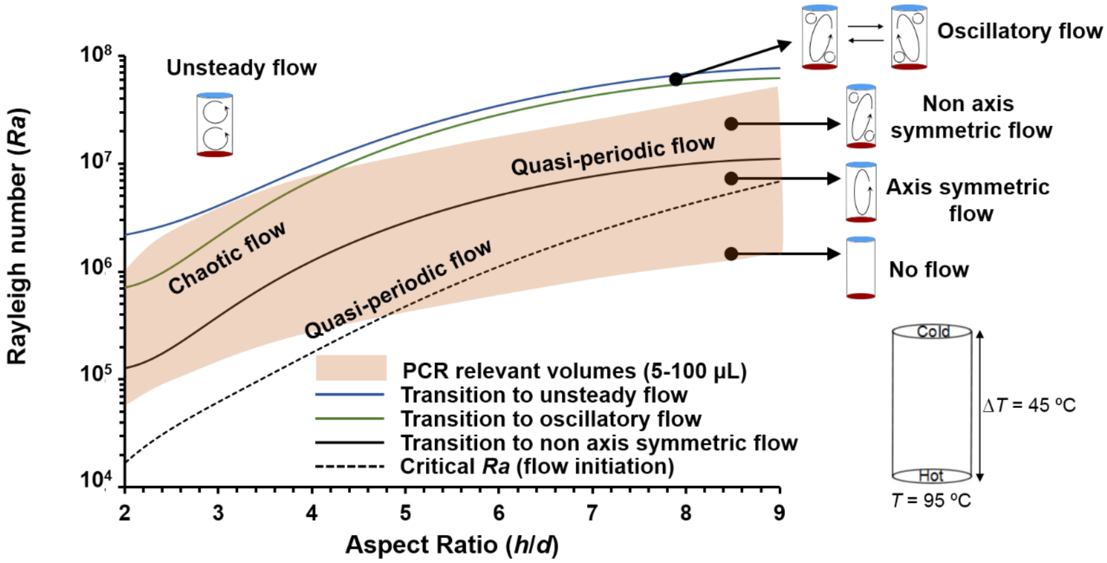

Figure 3: Ra - h/d parametric flow map reveals a spectrum of accessible convective flow states. The shaded region in the map represents cylinders with volumes relevant for PCR. Within this region, different combinations of size ($Ra \propto h^3$) and shape (h/d) of the cylinder yields flows containing fluid elements with periodic, quasi-periodic and chaotic trajectories.

It should be noted that apart from the availability of single rolled convective flow structure, convective PCR also requires that the temperature distribution be fixed within the cylindrical reactor. This requirement “roughly” fixes the temperature of the top and bottom surface (ΔT) along with fluid properties. Thus, the Rayleigh number of the system, for most parts depends heavily on the cylinder height ($Ra \propto h^3$). Based on the above analysis a $Ra - h/d$ parametric map can be constructed exhibiting a spectrum of flow states and the transition boundaries separating them [4] (Figure 3).The geometry has to lie above the critical *Ra* line corresponding to the onset of flow and below the transition line corresponding to the onset of unsteady convective flow, such that the emergent flow is relevant for convective PCR. At the onset of convective flow the fluid elements follow closed periodic orbits within the reactor. As *Ra* is increased the convective flow becomes more disordered to the extent where fluid elements follow chaotic flow trajectories. This chaotic nature of the flow increases as the flow enters the unsteady regime. One can also change the aspect ratio of the cylinder at a given *Ra* to alter the flow paths. For a given *Ra*, the convective flows in wider geometries (smaller aspect ratio) generate flows which are more disordered when compared to taller geometries (higher aspect ratio). This can be attributed to a much stronger transverse flow (flow in the horizontal plane) component in the wider geometry (Figure 4). One would expect that the closed periodic flows in taller geometry where fluid elements experience quasi-periodic thermal profile might be better for convective PCR (as the fluid elements experience periodic thermal cycling profile similar to conventional thermo-cyclers) but our experiments and computational models surprisingly reveals a more counterintuitive result in which the reactions are actually executed more efficiently in wider geometries with chaotic flow trajectories (where fluid elements experience chaotic thermal cycling profile) (Chapter II). Therefore it is of interest to analyze the chaotic nature of the emerging fluid trajectories in Rayleigh-Bénard convective flows.

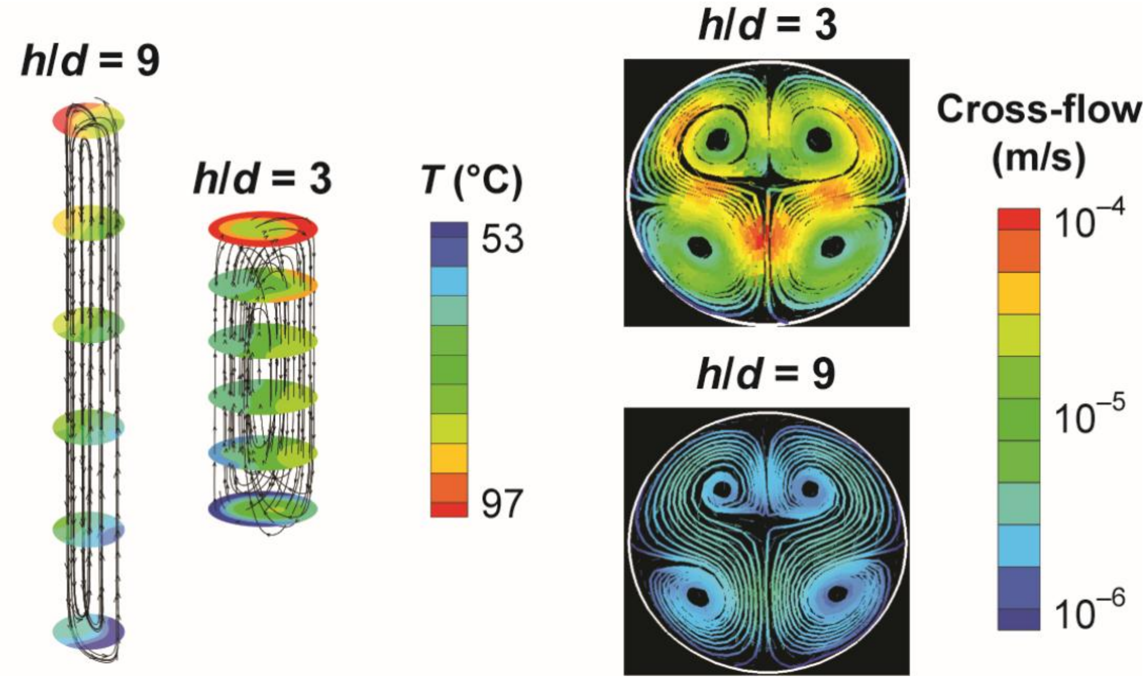

Figure 4: Strong transverse flow component gives rise to more disordered flow trajectories in small aspect ratio cylinders. The secondary transverse flow i.e. the flow component in the plane perpendicular to the primary convective flow, is much stronger in the lower aspect ratio geometry yielding more disordered flow trajectories when compared to a higher aspect ratio geometry.

Chaotic flows

Although complex dynamical systems had been studied quite rigorously (Henri Poincaré, Hadamard), the first comprehensive study of chaotic systems was done by Lorentz where he found that a certain system of linear differential equations (Lorentz equations) displayed extreme sensitivity to some initial conditions for a set of parametric values. Lorentz equations are actually a truncated form for Rayleigh Bénard hydrodynamics equations (eq. [1.1]) in two dimensions which has now become an archetypical model to study various chaotic systems (pattern forming systems, self-organization and nonlinear dynamical systems). Such chaotic systems exhibit unique characteristic traits such as extreme sensitivity to initial conditions, deterministic unpredictability, emergence of strange attractors and fractal patterns among others.

Chaos can also arise in fluid "flow" resulting in stretching, folding and distribution of fluid elements. Even if the velocity field is very well ordered and deterministic, the trajectories of fluid elements or tracers in the flow may be chaotic in the sense that nearby trajectories will separate exponentially in time. Chaotic flows are quite frequently encountered, playing crucial roles in a variety of physical phenomena such as fluid mixing[5, 6], accelerated biochemistry[7] and enhanced molecular transport. Study of chaotic mixing is important as it helps quantify the mixing efficiency and it also provides a visual analogue for chaos in area preserving maps.

For efficient PCR, the convective flow must be single rolled and time independent. Even though the dynamical system representing the convective flow is at steady state, it is of interest to analyze another dynamical system consisting of the individual fluid elements in the flow. The phase space of this dynamical system is then the physical space in which the flow occurs.

$$\begin{aligned}\frac{dx}{dt} &= u(x,y,z,t)\\ \frac{dy}{dt} &= v(x,y,z,t)\\ \frac{dz}{dt} &= w(x,y,z,t)\end{aligned} \qquad [1.3]$$

Where *x*, *y*, *z* and *t* represent the position and time coordinates of a fluid element and *u*, *v* and *w* represents the components of the velocity vector field which are obtained by numerically solving the Navier stokes and thermal equations simultaneously (eq. [1.1]). Equations [1.3] forms a non-integrable Hamiltonian system with three degrees of freedom, thus displaying features of Hamiltonian chaos[8]. The methods developed to study chaos in phase space variables can now be readily applied to study the dynamics of fluid elements in real space. Chaotic behavior is characterized by divergence of nearby trajectories in phase space. There are various methods to quantify chaos in such time series dynamical variable systems such as Lyapunov exponents, correlation dimension, Kolmogorov-Sinia (K-S) entropy, fractal dimensions, probability density of stretching and Poincare sections[7-9]. Here we quantify the chaotic strength of Rayleigh-Bénard convective flows both visually via Poincaré maps and quantitatively via Lyapunov exponents[10].

Poincaré maps

It is possible to study the extent of "mixing" or exchange among flow trajectories by using Poincaré maps. A Poincaré section for a three dimensional trajectory is defined as the collection of points obtained when this trajectory pierces a chosen plane. Poincaré maps can be derived using the velocity field of the trajectory. It can be readily understood that if a trajectory exhibits a periodic closed path, then the Poincaré section will show distinct islands corresponding to the three dimensional trajectory; however, if the trajectory exhibits no periodicity, then the Poincaré sections will contain a disordered collection of points, which is an indication of chaos.

We have obtained Poincaré maps by finding the location of the point where a given streamtrace pierces the mid-plane of the cylinder along its height. The characteristics of the flow trajectories for the reactor geometries used to perform PCR at aspect ratio 3 and 9 respectively were visualized using Poincaré maps, shown in (Figure 5 a, c). This analysis shows that for the cylinder with aspect ratio 9, the fluid elements follow tightly closed paths whose loci generate distinct Kolmogorov-Arnold-Moser (KAM) curves. Consequently, reagents are exposed to a thermal profile characterized by quasi-periodic oscillation between upper and lower extremes, as seen when temperature versus time is plotted following a fluid element. A much different flow field emerges at $h/d = 3$ ($Ra = 1.45 \text{ x } 10^6$)(Figure 5 a, c), appearing disordered in the sense that fluid elements follow complex 3D trajectories that do not produce well-defined KAM boundaries in the Poincaré map but instead yield a broadly distributed pattern consistent with the emergence of chaos. These effects disrupt the thermal profile's periodicity and increase the reagent's exposure to intermediate temperatures. Thus, Poincaré maps can be used to qualitatively visualize the extent of mixing present in a flow.

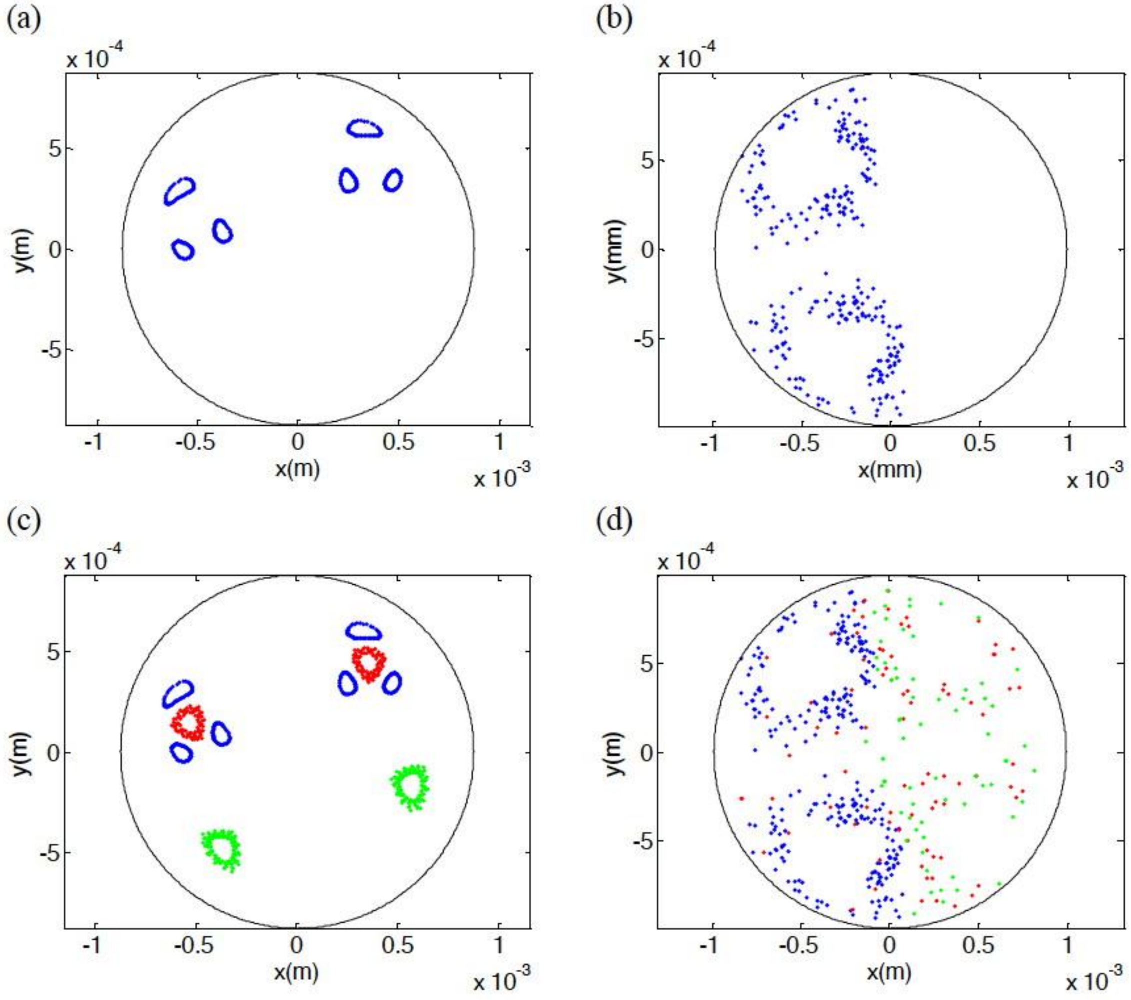

Figure 5: Poincaré section provides a Stroboscopic map of circulating fluid trajectories. (a, b) Poincaré maps for a single fluid element trajectory for cylinders with aspect ratio 9 and 3 respectively. (c, d) Poincaré maps for a collection of fluid trajectories for cylinders with aspect ratio 9 and 3 respectively.

Lyapunov exponents

Lyapunov exponent (*LE*) measures the average exponential rate of divergence of nearby trajectories and is regarded as one of the most important measures to quantify mixing and deformation in fluid flows. Since *LE* depends on the spatial coordinates of the initial fluid element, the analysis results in a spectrum of Lyapunov exponents. The largest *LE* is positive for chaotic flows with its magnitude proportional to the chaotic strength of the flow. About 300 densely packed lagrangian fluid elements originating from the mid horizontal plane of the cylinder were tracked for 5 minutes (Figure 6 a). Each fluid element was paired with its nearest neighbor and the coordinates of the paired system was integrated in time (eq. [1.3]) to yield a time series representation of their separation distance. The finite time Lyapunov exponent was then calculated using eq. [1.4] with the separation distance being normalized after each time step.

$$LE = \frac{1}{n\Delta t} \sum_{n=1}^{n=T/\Delta t} ln\left[\frac{d\left(\left(n+1\right)\Delta t\right)}{d\left(n\Delta t\right)}\right] \qquad [1.4]$$

Where *LE* is the Lyapunov exponent, Δt is the time step, *T* is the total time the fluid elements are tracked and *d* is the separation distance between the pair of fluid elements. Initial separation distance and the time step (Δt) were independently varied to determine their optimum values for all further simulations. Repeating the procedure for all the fluid elements originating from the mid horizontal plane yielded a spectrum of *LE* (Figure 6 b) with the smallest and largest *LE* values corresponding to slowest and the largest rates of divergence of fluid element pair respectively (Figure 6 c, d).

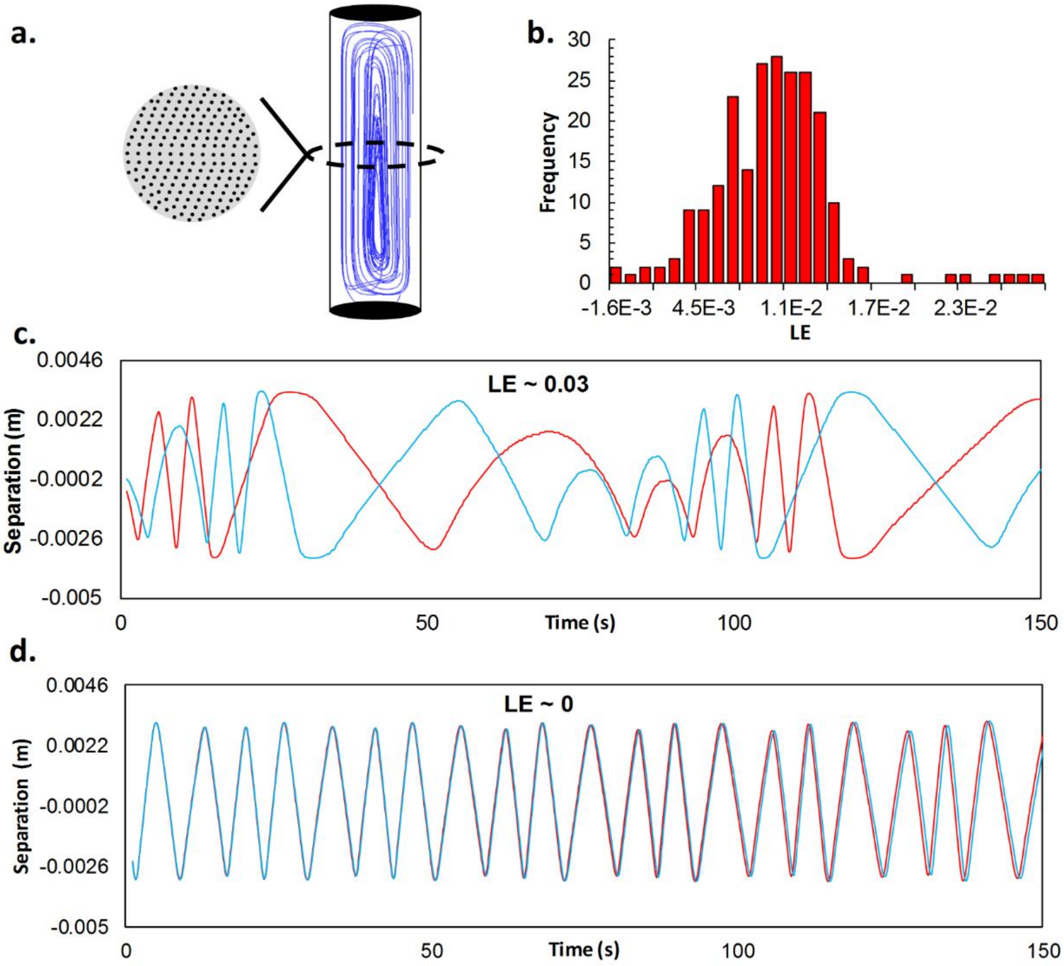

Figure 6: Lyapunov exponents quantifies the disorder in Rayleigh Bernard convective flows. (a) Fluid element trajectories originating from mid horizontal plane. (b) Spectrum of Lyapunov exponents resembles a Gaussian distribution. Time series separation data between initially close trajectory pairs yielding (c) maximum and (d) minimum Lyapunov exponents. (Cylinder volume = 10 µL, *h*/*d* = 5)

The largest *LE* from the spectrum can then be used to quantify chaotic strength of the convective flow fields in cylinders of different shapes and sizes (Figure 7 a). Smaller aspect ratio cylinders (*h*/*d*<5) display a larger value of maximum *LE* for all cylinder sizes. A larger chaotic component in these cylinders facilitates efficient exchange of reagents between flow trajectories enabling robust PCR. As the aspect ratio is further increased, the maximum *LE* decreases generating more ordered flow trajectories in these cylinders. In the convective format, the rate of global PCR amplification can be quantified by doubling time of the reaction i.e. the time taken for the DNA molecules to double in number. Thus, smaller doubling times corresponds to faster convective PCR reactions [11] (Chapter II). The decrease of the Max *LE* with cylinder aspect ratio is reflected in the increase in the doubling time verifying the role chaotic advection in enhancing convective PCR (Figure 7 b).

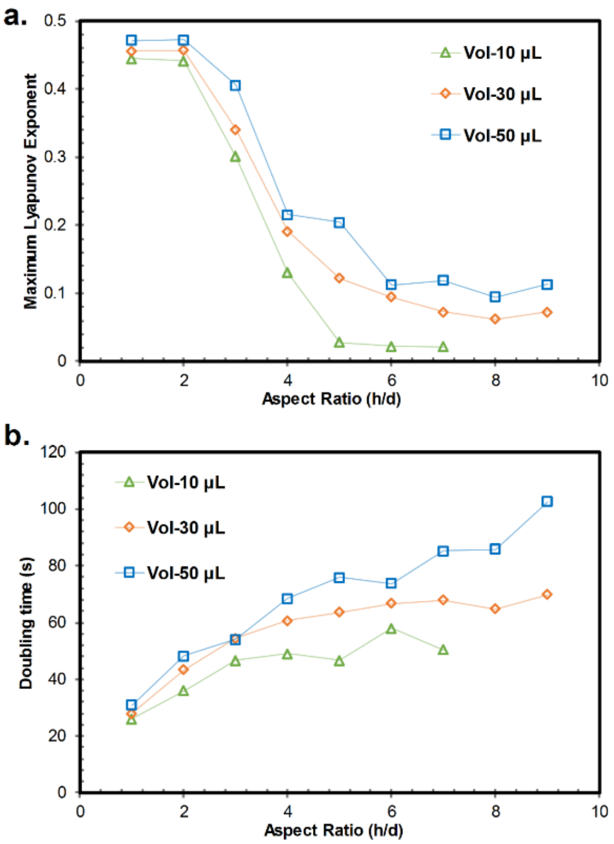

Figure 7: Maximum Lyapunov exponents. The maximum LE decreases for convective flow in cylinders with higher aspect ratio. The decrease in the chaotic strength of the flow is accompanied by an increased doubling time of convective PCR.

Conclusion

These results prove that the chaotic flow acts in a way to enhance thermally actuated biochemical reactions by collectively exposing a large fraction of the reaction volume to favorable conditions resulting in smaller reaction times in the cylinder with smaller aspect ratio. In contrast, the cylinder with higher aspect ratio exhibits a quasi-periodic behavior, which results in reagents getting stuck in unfavorable temperature zones, leading to larger reaction times. By modeling the flow and reactions simultaneously using an unsteady solver, it is possible to observe the dynamics of the PCR reaction – the initial lag time, the exponential rise in DNA concentration, and finally, a saturation state when the primers have been depleted (Chapter II).

CHAPTER II

MAPPING CHAOTIC FLOW STATES FOR ROBUST CONVECTIVE PCR*

Introduction

Thermal convection has emerged as a promising approach to enable rapid DNA replication the polymerase chain reaction (PCR) [12-15]. One of the most straightforward implementations of this concept involves harnessing Rayleigh Bénard convection, owing to the inherent simplicity of housing the aqueous reagent mixture in a microliter-scale enclosure (typically cylindrical in shape) heated from below (Figure 8). As discussed in Chapter I, The interplay between the destabilizing buoyancy force and restoring action of thermal and viscous diffusion in this configuration is expressed in terms of the dimensionless Rayleigh number ($Ra = [g\beta(T_2 - T_1)h^3]/v\alpha$; where β is the fluid's thermal expansion coefficient, g is gravitational acceleration,T_1 and T_2 are the temperatures of the top (cold) and bottom (hot) surfaces respectively, h is the height of the cylindrical reactor, α is the thermal diffusivity, and v is the kinematic viscosity). This quantity, coupled with the geometric parameter h/d, completely specifies the available flow states[14]. The convective arrangement confers an operational advantage because thermo-cycling is actuated pseudo-isothermally by maintaining a gradient between opposing fixed-temperature surfaces, in contrast to conventional designs where the entire bulk volume must be repeatedly heated and cooled. But this outward simplicity is deceiving because

---

*Reprinted with permission from "Microscale Chaotic Advection Enables Robust Convective DNA Replication", A. Priye, Y. A. Hassan and V. Ugaz, 2013, *Analytical Chemistry*, 10536-10541, Copyright 2013 by American Chemical Society.

the internal flow fields generated under PCR conditions are not the closed 2D circulatory trajectories conventionally assumed. Instead, the fluid motion displays an unexpectedly rich complexity owing to the onset of chaotic advection in a regime of transition to convective turbulence even though the flow is inertially laminar (characteristic Reynolds numbers ~ 30 – 40). A subset of flow states in this regime are capable of significantly accelerating the reaction, yielding extremely rapid DNA replication rates and a counterintuitive finding that optimal reaction performance occurs under conditions where some of the most disordered flows are generated [14]. In this chapter, we seek to elucidate the role of chaotic advection and precisely quantify its interplay with the underlying PCR biochemistry throughout the entire 3D reactor volume. These new insights lead to discovery of an incredibly robust operating zone wherein DNA replication rates remain constant over two orders of magnitude of *Ra*, encompassing virtually all possible combinations of temperature and reactor volume associated with realistic PCR conditions.

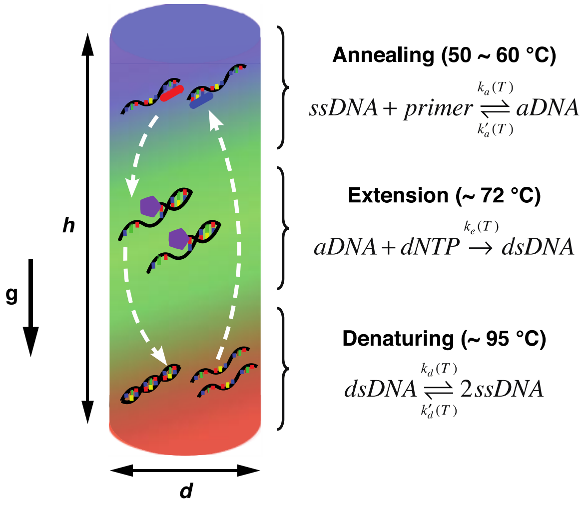

Figure 8: DNA replication via the PCR in a Rayleigh Bénard convection cell. Thermal-cycling is executed in a cylindrical reactor geometry of height *h* and diameter *d* by imposing a temperature gradient between the top and bottom surfaces. A 3-reaction model is depicted whereby a DNA replication cycle occurs as reagents are sequentially transported through temperature zones associated with annealing (top), extension (middle), and denaturing (bottom) processes.

Residence time analysis

DNA replication occurs when reagents are sequentially transported through temperature zones associated with each stage of the reaction (e.g., denaturation, annealing, and extension), and occupy each zone for a sufficient residence time. To analyze the residence times of the reagents in convective flow, the CFD model was used to generate the lagrangian temperature versus time history (Figure 9) experienced by an ensemble of over 300 randomly selected passive tracer trajectories during 5 min of convective PCR in cylindrical reactors of varying aspect ratio (*h/d*; here *d* was held constant at 1.5 mm).

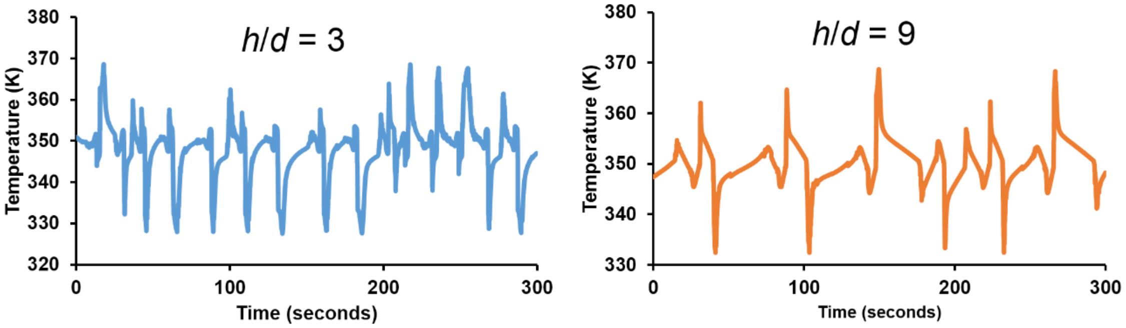

Figure 9: Thermal cycling profile of a fluid element in a tall and wide reactor. Fluid elements in the wider geometry (*h*/*d* = 3) experiences a more chaotic temperature variation when compared to fluid element in the taller geometry (*h*/*d* = 9).

Our simulations reveal that reagents occupy the extension zone—the rate limiting step in PCR—for a longer time in tall narrow reactors where the flow is laminar (e.g., *h/d* = 9), whereas a higher frequency of entry is observed in wider geometries where chaotic advection predominates (e.g., *h/d* = 3) (Figure 10 b). Between these extremes, ensemble averages of the residence time and frequency of entry decrease and increase, respectively, with increasing aspect ratio. Residence times in the annealing and denaturing zones are relatively independent of aspect ratio (Figure 10 a,c), but the frequency of entry in both zones is higher in chaotic flows. These trends are also mirrored in geometric dependence of the averaged quantities.

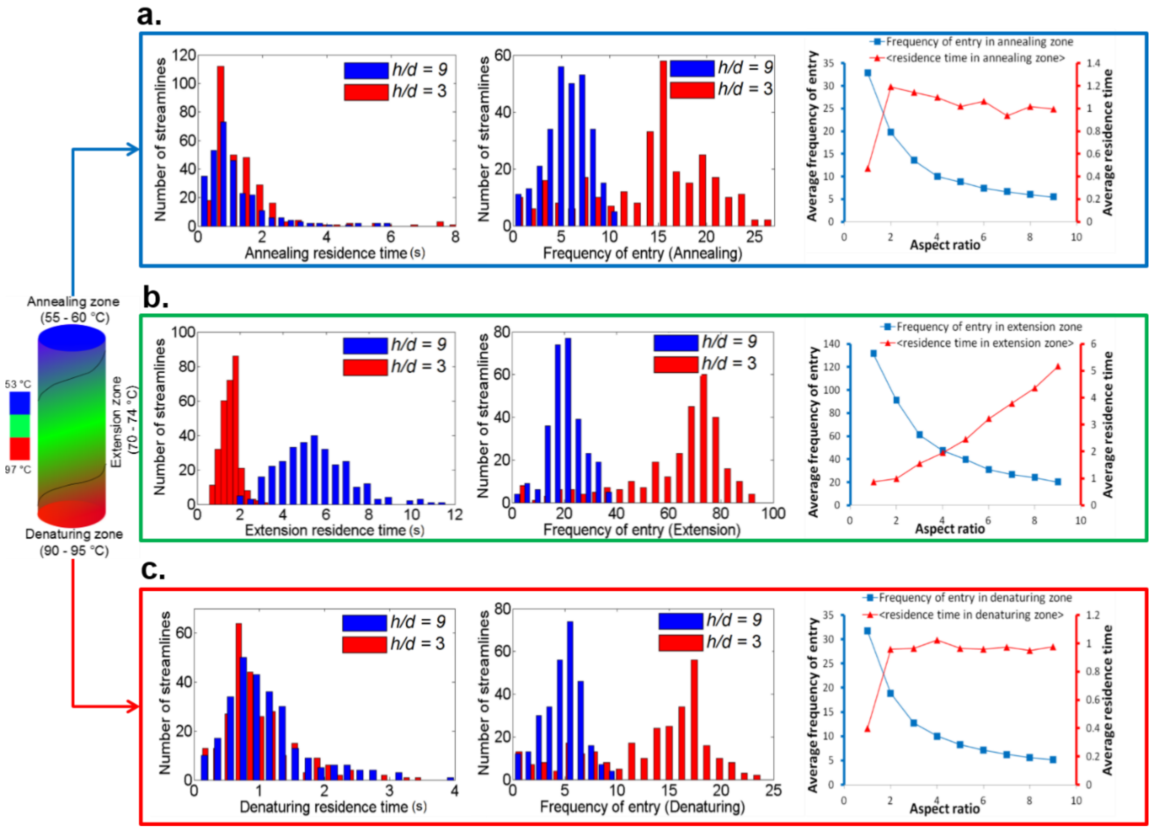

Figure 10: Residence time analysis of fluid elements in a wide and tall reactor. (b) Periodic flows (*h/d* = 9) generate longer residence times in the extension temperature zone (left) whereas chaotic flows (*h/d* = 3) produce a higher frequency of entry (middle), with a gradual transition between extremes at intermediate geometries (right). Both flows yield similar residence times in the (a) annealing and (c) denaturing temperature zones, but the frequency of entry is greater in chaotic flows and the relative trends are maintained across the majority of the geometric parameter space.

A key parameter is the number of complete replication cycles occurring over the course of each Lagrangian trajectory (i.e., representing sequential transport through annealing, extension, and denaturing zones). A much broader distribution (up to 15 complete cycles) is obtained at *h/d* = 3, whereas no more than 5 complete cycles occur at *h/d* = 9 (Figure 11). These observations can be attributed to the convective flow field's increasingly chaotic characteristics at low aspect ratios, in contrast to the quasi-periodic motion evident in taller geometries [16]. Thus chaotic phenomena are fundamentally important because they drive two competing factors that govern PCR efficiency: (1) high aspect ratio (laminar, quasi-periodic) geometries are favorable because they deliver longer residence times in the extension zone, but (2) low aspect ratios (chaotic flow) are also favorable because they provide a higher frequency of entry and greater capacity to actuate complete replication cycles.

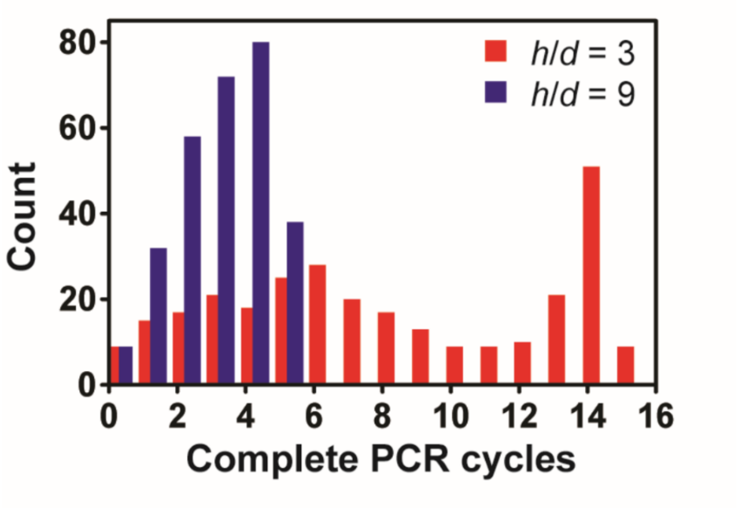

Figure 11: Wider reactors are capable of executing more complete replication cycles than taller ones. Complete PCR cycles defined as trajectories sequentially traversing annealing, extension, and denaturing temperature zones, reveal that more complete cycles are executed under chaotic flow conditions.

Coupling reaction kinetics with convective flow

We next incorporated reaction kinetics into the flow model to better understand the interplay between the intricate convective flow fields and DNA amplification rate. PCR kinetics in general is quite complicated with multiple reactions occurring simultaneously in each step. However, one can neglect dynamics at molecular scale and model the system from a mass action based kinetic framework to capture the amplification of DNA to a good approximation. The analysis presented here is based on a simplified 3-reaction framework[17, 18] involving denaturation of the double stranded DNA template (dsDNA) into two single stranded constituents (ssDNA) at ~ 95 °C, annealing of target specific oligomers (primers) to each ssDNA strand at ~ 50 – 60 °C to generate annealed complexes (aDNA), and enzyme catalyzed incorporation nucleotide species at ~ 72 °C to synthesize the complementary strand yielding a completed dsDNA copy. We also introduced further complexity by incorporating reversibility into the denaturing and annealing steps (5-reaction model), and by considering side reactions associated with primer-dimer formation (7-reaction model). Although a complete description of PCR kinetics involves a complex network of multiple simultaneous processes (e.g., incomplete extension, polymerase deactivation, etc.), we focused our analysis on these simplified cases where rate constant data are readily obtainable[19].

Mass action kinetics

The time evolution of individual species concentrations was simultaneously evaluated via equation [2.1], where rates of production and consumption of individual species (r_i) are expressed by equations [2.2] based on elementary mass action kinetics. The rate constants for individual reactions (Table 1) were multiplied by temperature mapping functions (Figure 12) to restrict individual reactions within their respective zones in the reactor.

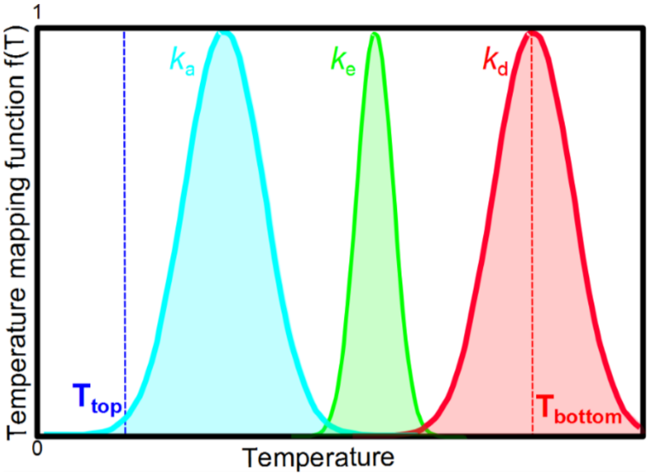

Figure 12: Gaussian temperature mapping functions. The rate constants for PCR relevant reactions are multiplied by Gaussian mapping functions to constrain the reactions within respective temperature range within the reactor.

$$\frac{\partial C_i}{\partial t} + u \bullet \nabla C_i = D_i \nabla^2 C_i + r_i \qquad [2.1]$$

$$\begin{aligned}
r_{dsDNA} &= k_e f_e(T) C_{aDNA} C_{dNTP} + 0.5 k_d^{'} f_a(T) C_{ssDNA}^2 - k_d f_d(T) C_{dsDNA} \\
r_{ssDNA} &= 2k_d f_d(T) C_{dsDNA} - k_d^{'} f_a(T) C_{ssDNA}^2 + k_a^{'} f_d(T) C_{aDNA} - k_a f_a(T) C_{ssDNA} C_{primer} \\
r_{aDNA} &= k_a f_a(T) C_{ssDNA} C_{primer} - k_a^{'} f_d(T) C_{aDNA} - k_e f_e(T) C_{aDNA} C_{dNTP} \\
r_{primer} &= k_a^{'} f_d(T) C_{aDNA} - k_a f_a(T) C_{ssDNA} C_{primer} + 0.5 k_{pd}^{'} f_d(T) C_{dimer} - k_{pd} f_a(T) C_{primer}^2 \\
r_{dimer} &= 0.5 k_{pd}^{'} f_d(T) C_{dimer} - k_{pd} f_a(T) C_{primer}^2 \\
r_{dNTP} &= -k_e f_e(T) C_{aDNA} C_{dNTP}
\end{aligned} \qquad [2.2]$$

Here C_i denotes the concentration of each individual species, k_i represents the rate constant associated with each reaction, and v and D_i denote fluid velocity and species diffusivity respectively. Gaussian mapping functions $f_i(T)$ were applied to localize each process within its respective temperature zone[18]. Chemical reactions were formulated as part of a reaction-diffusion balance that was simultaneously solved with the transient convective flow profile to obtain the time resolved evolution of individual species concentrations[14].

$$f_i(T) = e^{-\frac{\left(\frac{T-T_i}{T_{bottom}-T_{top}}\right)}{2\sigma_i^2}} \qquad [2.3]$$

Table 1: Simulated PCR kinetic models.

Step	Reaction	T (°C)	Rate constant
3-reaction model			
Denaturing	dsDNA → 2(ssDNA)	92 – 97	$k_d = 10\ \mathrm{s}^{-1}$
Annealing	ssDNA + primer → aDNA	55 – 60	$k_a = 5 \text{ x } 10^5\ \mathrm{M}^{-1}\ \mathrm{s}^{-1}$
Extension	aDNA + dNTP → dsDNA	70 – 74	$k_e = 10^6\ \mathrm{M}^{-1}\ \mathrm{s}^{-1}$
5-reaction model			
Renaturing	2(ssDNA) → dsDNA	55 – 60	$k'_d = 10^6\ \mathrm{M}^{-1}\ \mathrm{s}^{-1}$
Reverse annealing	aDNA → ssDNA + primer	92 – 97	$k'_a = 100\ \mathrm{s}^{-1}$
7-reaction model			
Primer dimer complex	2(primer) → dimer	55 – 60	$k_{pd} = 5 \text{ x } 10^3\ \mathrm{M}^{-1}\ \mathrm{s}^{-1}$
Dimer dissociation	dimer → 2(primer)	92 – 97	$k'_{pd} = 10^4\ \mathrm{s}^{-1}$

The mean (T_i) and standard deviation (σ_i) parameters of the Gaussian distributions applied to each reaction in our model are summarized below in Table 2.

Table 2: Gaussian properties of the distribution.

Step	Reaction	T (°C)	Gaussian mapping function $f_i(T)$	
3-reaction model			Mean T_i (°C)	Std. σ_i
Denaturing	dsDNA → 2(ssDNA)	92 – 97	94	0.05
Annealing	ssDNA + primer → aDNA	55 – 60	58	0.05
Extension	aDNA + dNTP → dsDNA	70 – 74	72	0.025
5-reaction model				
Renaturing	2(ssDNA) → dsDNA	55 – 60	58	0.05
Reverse annealing	aDNA → ssDNA + primer	92 – 97	94	0.05
7-reaction model				
Primer dimer complex	2(primer) → dimer	55 – 60	58	0.05
Dimer dissociation	dimer → 2(primer)	92 – 97	94	0.05

Initial concentrations of target DNA, primers, and dNTPs (Table 3) were estimated from experimental values (based on a 10 μL reagent volume) as follows.

Table 3: Initial concentration of species.

Species	Molecular weight (gm/mol)	Initial mass (kg)	Initial number of molecules (copies)
dsDNA	194,700	2.14968×10^{-19}	665
Primers	8,250	5.40073×10^{-11}	3.94286×10^{12}
dNTPs	89,100	1.94427×10^{-7}	1.31429×10^{15}

Diffusivity of DNA

In addition to the convective flow field, reagents are also transported by molecular diffusion. The diffusivity of DNA in free solution depends on its length and topology[20], and is characterized by parameters such as the contour length (length of uncoiled molecule), persistence length (p, measure of backbone rigidity), and radius of gyration (R_g, measure of coil size). The radius of gyration can be estimated from the Kratky-Porod equation[21], enabling diffusion to be captured by the Zimm model[22] (eq [2.4]) where k_B is Boltzman's constant, and T and μ are the temperature and the viscosity of the fluid. Even though there are more accurate models to compute the molecular diffusivity of DNA molecules[23], we have used the simplified Zimm model in our calculations due to its ease of implementation. This relationship expresses the length dependent diffusivity of each species, yielding results in agreement with experimentally measured values[24]. More recently, accurate DNA diffusivity data has been compiled [25].

$$D = \frac{k_B T}{6\pi\eta R} = \frac{k_B T}{4\pi\eta R_g}, \quad \text{where} \quad R_g = \sqrt{\frac{p l_c}{3}\left[1 - 3\left(\frac{p}{l_c}\right) + 6\left(\frac{p}{l_c}\right)^2 - 6\left(\frac{p}{l_c}\right)^3\left(1 - e^{\frac{-l_c}{p}}\right)\right]} \qquad [2.4]$$

In our model, the persistence and contour lengths were assigned values of $p = 50$ nm and $l_c = 85$ nm (0.34 nm x number of base pairs) respectively for a 250 bp dsDNA molecule[26].

Doubling time of convective PCR

Replication of a 250 bp dsDNA target was modeled, with the upper and lower surfaces of the cylindrical reactors held constant at 97 and 53 °C, respectively. Initial concentrations of individual species were selected based on conditions used in our previous experiments (Table 3). This model successfully captures the characteristic lag, exponential, and plateau phases of the PCR. In the early stages of PCR, there are only few ssDNA molecules resulting in a slower annealing rate than the denaturation rate which in turn leads to an initial depletion in the dsDNA concentration (lag phase). When sufficient amount of ssDNA molecules accumulates, the annealing rate increases leading to an exponential increase in the dsDNA concentration (exponential phase). The exponential growth is inhibited when the annealing rate decreases again due to depletion of available primers in the solution (plateau phase) (Figure 13).

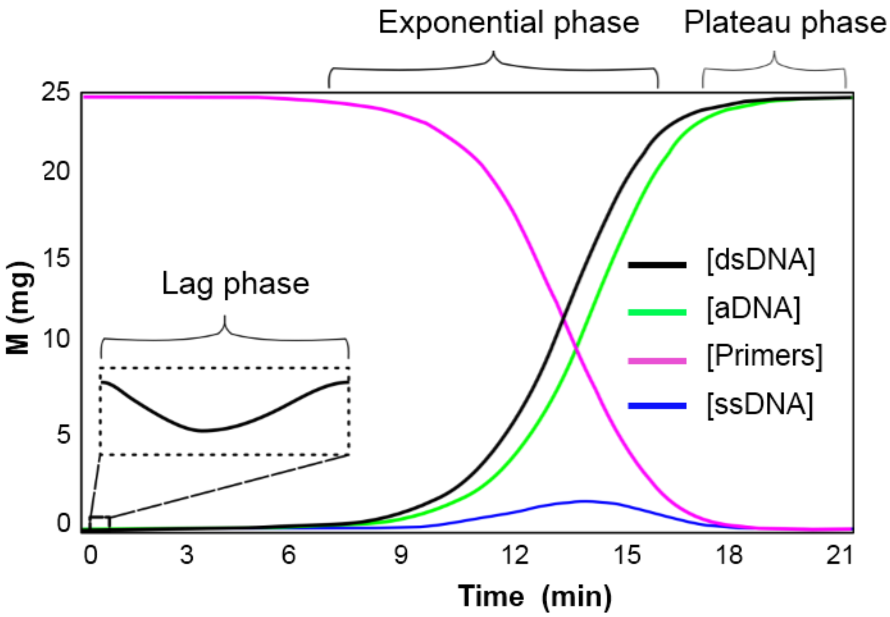

Figure 13: Coupled flow and reaction kinetics of convective PCR reproduces a real time q-PCR like curve. The time evolution of each species involved in a 3-reaction PCR model (Table 1) under chaotic flow conditions (*h/d* = 3) captures the characteristic lag, exponential, and plateau phases of DNA replication, resulting in a 10^9 fold increase in target yield over the initial template loading in less than 20 min.

In conventional PCR the concept of a cycling time can be precisely defined because the reaction is executed uniformly throughout the bulk. Since this quantity is not straightforward to determine in the convective format due to the multiplicity of thermal trajectories present, we instead express the replication rate in terms of a characteristic doubling time. Comparing the effects of kinetic model complexity reveals that doubling times remain essentially unchanged in all geometries with aspect ratio greater than 2 (Figure 13 a). The slightly increased doubling time at very low aspect ratios when the 5 and 7 reaction models are applied likely reflects the reduced residence times available in these geometries (particularly in the extension zone) that would favor side reactions competing for ssDNA and thereby reduce the rate of target replication. The effect of DNA molecular diffusivity on the doubling time can be studied by introducing a dimensionless number called the Péclet number (*Pe*) which quantifies the strength of convective transport with respect to diffusive transport of DNA molecules ($Pe = Ud/D$, U is the average convective velocity and D is the diffusivity of DNA molecules). Our simulations reveal that the change in the target DNA diffusivity does not appreciably impact the doubling time. A sudden increase in the doubling time occurs at $Pe \sim O$ (1) corresponding to unrealistic DNA diffusivity where the overall reaction rate decreases due to diffusion effects (Figure 13 b). We next evaluated the effect of initial concentrations of template DNA, primers, and nucleotides (Figure 13 c, d, and e) which were normalized with their experimentally determined initial concentrations. Increasing the amount of template DNA does not alter the doubling time, whereas kinetics are significantly slowed at normalized concentrations below 10^{-4} (i.e., the single copy limit). Replication is also sensitive to the initial primer concentration, with a decrease in doubling time of 1 – 2 orders of magnitude (to less than 20 s) as the normalized concentration is increased. Likewise, the initial quantity of nucleotides in the reagent mixture does not significantly affect replication except at very low concentrations. Collectively, new insights make it possible to rationally select optimal reagent formulations to maximize the DNA replication rate.

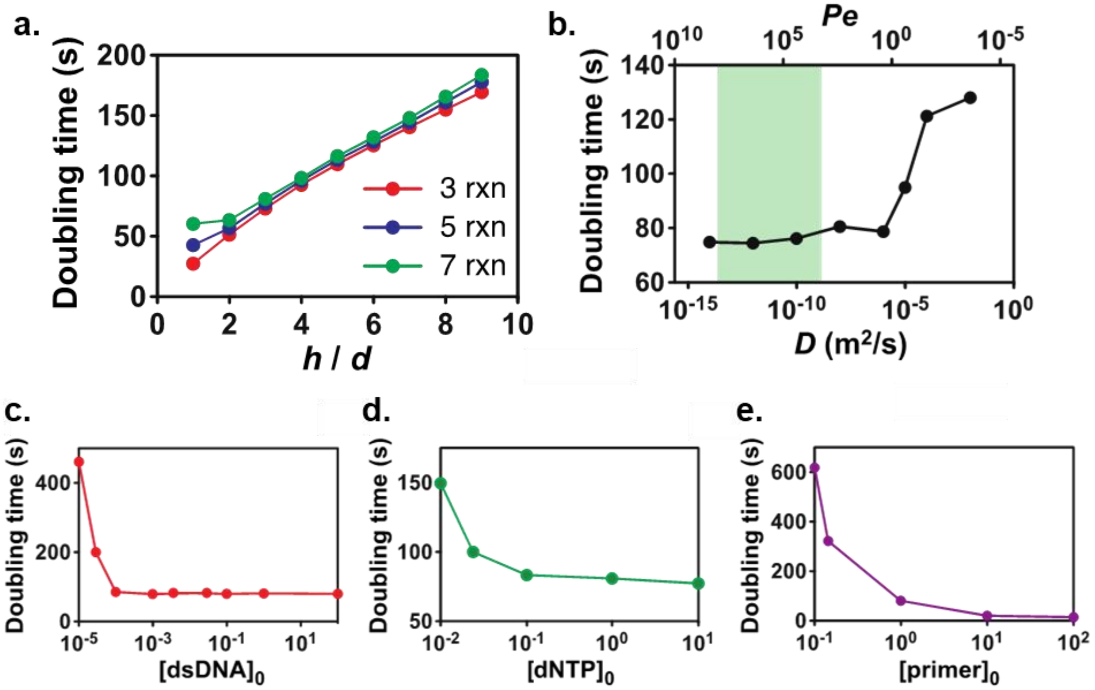

Figure 14: Sensitivity of doubling time on reaction model parameters. (a) Increasing the complexity of the reaction model by addition of side reactions (Table 1) does not appreciably impact the replication rate. (b) The variation of doubling time with Péclet number (*Ud*/*D*) reveals a relatively constant replication rate over the full range of realistic parameter values (shaded region). Replication rates are also computed as a function of initial concentrations (normalized with respect to their experimentally determined initial values) of (c) template DNA, (d) dNTPs, and (e) primers to establish optimal ranges for the convective format. All simulations were performed in the chaotic flow regime (h/d = 3).

Convective PCR experiments

Cylindrical reactors were constructed from 0.5 inch dia. polycarbonate rod stock (Amazon Supply) by cutting them to lengths and machining holes to produce reactors with an aspect ratio of h/d= 3 at heights of h = 4.5, 6, and 7.5 mm. PCR experiments were performed to replicate a 237 base pair target from a λ-phage DNA template. A typical 100 μL reaction mixture contained 10 μL of 10x buffer solution, 4 μL of 25 mM $MgCl_2$, 10 µL of dNTPs (2 mM each), 67.8 µL of DI water, 3 µL of each forward and reverse primer, 2 µL of template DNA and 0.8 µL of KOD polymerase (2.5 units/ µL). The enzyme, buffer (buffer #1), MgCl2, and dNTPs were supplied with the KOD DNA Polymerase Kit (cat. no. 71085-3; Novagen). Reactors were first rinsed with a 10 mg/mL aqueous solution of bovine serum albumin (cat. no. A2153; Sigma-Aldrich) followed by Rain-X Anti-Fog (SOPUS Products), and dried. We found that these rinsing steps helped minimize adsorption at the sidewalls that may otherwise inhibit the reaction while also enhancing surface wettability so that reagents could be loaded without trapping air pockets inside the reactor. The lower surface of the polycarbonate reactor was sealed using three layers of aluminum tape (cat. no. PCR-AS-200; Axygen, Inc.), after which reagents were pipetted inside and the top surface sealed with another layer of tape. The reactors were then sandwiched between the preheated hot (95 °C) and cold (58 °C) plates of the convective device (Figure 15). After incubation for a desired time, the reactors were removed and the products were pipetted out of the wells for subsequent analysis by agarose gel electrophoresis (2 wt% gel (cat. no. 161-3107; Bio-Rad) with 1x TAE running buffer (cat. no. 141-0743; Bio-Rad)). Fluorescently stained DNA samples were prepared containing 2 µL 100x SYBR Green I solution (Invitrogen/Molecular Probes), 2 µL DNA sample, 2 µL 6x Orange Loading Dye (Fermentas), and 4 µL TAE buffer. Samples were run at 60 V for 1 h with a 100 bp DNA ladder sizing marker (cat. no. 170-8202; Bio-Rad). A step by step instruction of lyntech setup can be found in the appendix (Appendix D).

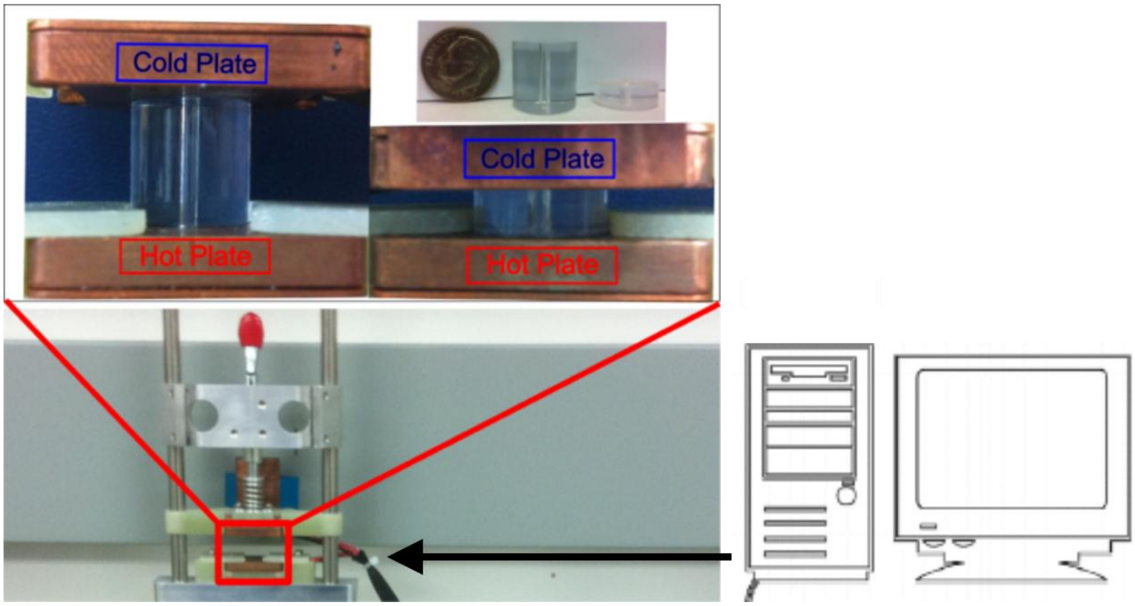

Figure 15: Isothermal metal plates conforms to an appropriate convective PCR setup. The polycarbonate cylindrical reactors are sandwiched between preheated hot and cold plates. The temperature of the plates is controlled and monitored via a computer interface.

Convective PCR global amplification map

Finally, we evaluated our reaction model across a wide range of *Ra* and *h*/*d* to establish a parametric mapping in terms of the generation rate, a quantity representing the number of target DNA doubling events per hour (i.e., the reciprocal of the doubling time). These results reveal that some of the most rapid generation rates are achieved in quasi-periodic laminar flow states immediately above the critical *R*a associated with the onset of flow in the vicinity of $3 \geq h/d \geq 6$ (Figure 16). These geometries have the smallest allowable height at a given aspect ratio, thereby enabling reagents to circulate quickly throughout the reactor. More significantly, a broad zone is evident within the central chaotic flow regime where generation rates remain essentially unchanged. Although replication is not quite as fast as in the vicinity of the critical *Ra*, reactions nevertheless proceed rapidly enough to execute the equivalent of a typical 30 cycle PCR in 10 – 20 minutes, consistent with our experiment results [14]. Remarkably, generation rates in the chaotic flow regime remain essentially constant over nearly two orders of magnitude of *Ra*, thereby encompassing virtually all possible combinations of temperature and reactor volume associated with realistic PCR conditions. We verified the robustness of PCR performed within the chaotic flow regime by amplifying a 237 bp fragment associated with λ-phage DNA in three different reactor geometries ($h/d = 3$, with $h = 4.5$, 6.0 and 7.5 mm). All reactions were allowed to run for 12 min. Successful amplification was achieved in all three geometries within this accelerated reaction time (Figure 16), consistent with the predicted generation rate in this regime. More broadly, our predictions are corroborated by results from previous studies involving PCR under Rayleigh Bénard convection summarized in Table 4 and indicated on the parametric map in Figure 16.

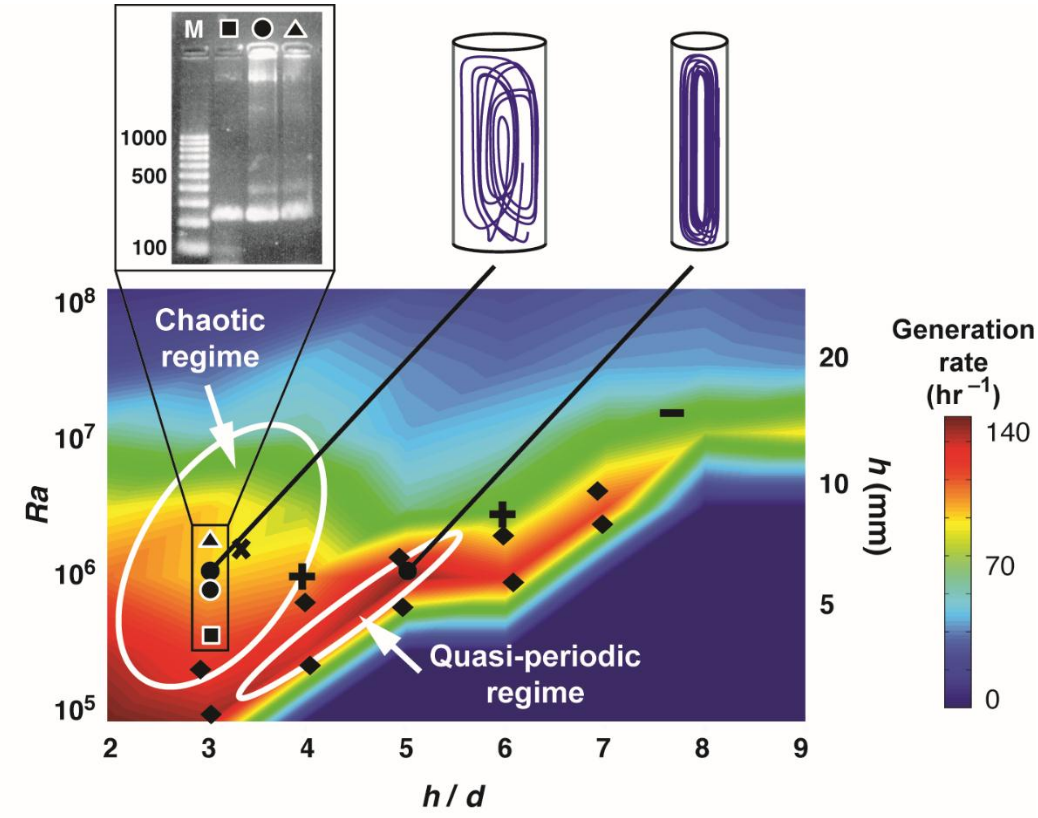

Figure 16: Microscale chaotic advection enables robust DNA replication. Replication timescales expressed in terms of a generation rate (i.e., number of doubling events per hour) are simulated over a wide range of parameters. The parametric map reveals a zone in the chaotic flow regime where accelerated DNA replication is stably achievable over a span of two orders of magnitude in *Ra*, suggesting that reactors designed within this zone are capable of delivering consistent replication performance under virtually any combination of temperature and reactor volume associated with the PCR. Data points represent experiment results reported in literature (see Table 4). Symbols in the gel electropherogram correspond to amplification of a 237 bp λ-phage DNA target in 12 min reported in this work using three different reactor geometries.

Table 4: Overview of experiments reported in literature involving convective PCR under Rayleigh-Bénard convection.

Reference	Replication Target	Reaction time (min)	Symbol in Figure 16
Priye, et al. [27]	λ-phage DNA (237 bp)	12	■, ●, ▲
Priye, et al. [15]	λ-phage DNA (237 bp)	10 – 20	✚
Muddu, el al. [14]	Human β-actin gene (295 bp)	10	✖
Yao, et al. [28]	Calf thymus DNA (407 bp)	8 – 17	□
Chou, et al. [29]	pHBV-48, HCV plasmid, HIV-1 vector pNL4-3 (122 to 222 bp)	10 – 30	–
Chang, et al. [30]	Yellow head virus (67 bp)	10 – 20	Off scale (h/d = 11.6)
Krishnan, et al. [13]	Influenza A Virus (191 bp), Human β-actin gene (295 bp)	15 – 30	Off scale (h/d >9)
Ugaz, et al. [31]	Influenza A Virus (191 bp), Human β-actin gene (474 bp)	15 – 30	Off scale (h/d >9)
Krishnan, et al. [12]	Human β-actin gene (295 bp)	90	Off scale (h/d = 10)

Comparison with 2D simulations

We also evaluated our coupled flow and reaction model in 2D rectangular geometries. We remark that the boundaries of these kinetic regimes are mis-predicted by simplified 2D models. Since secondary flows cannot exist in 2D, the corresponding residence times and frequencies of entry in each reaction zone (Figure 17) are very different than those obtained from a 3D model (Figure 10). Namely, fluid elements in 2D follow similar periodic trajectories at both *h/d* = 3 and 9, resulting in no sharp distinction between residence times or frequencies of entry into each reaction zone as compared with the 3D model.

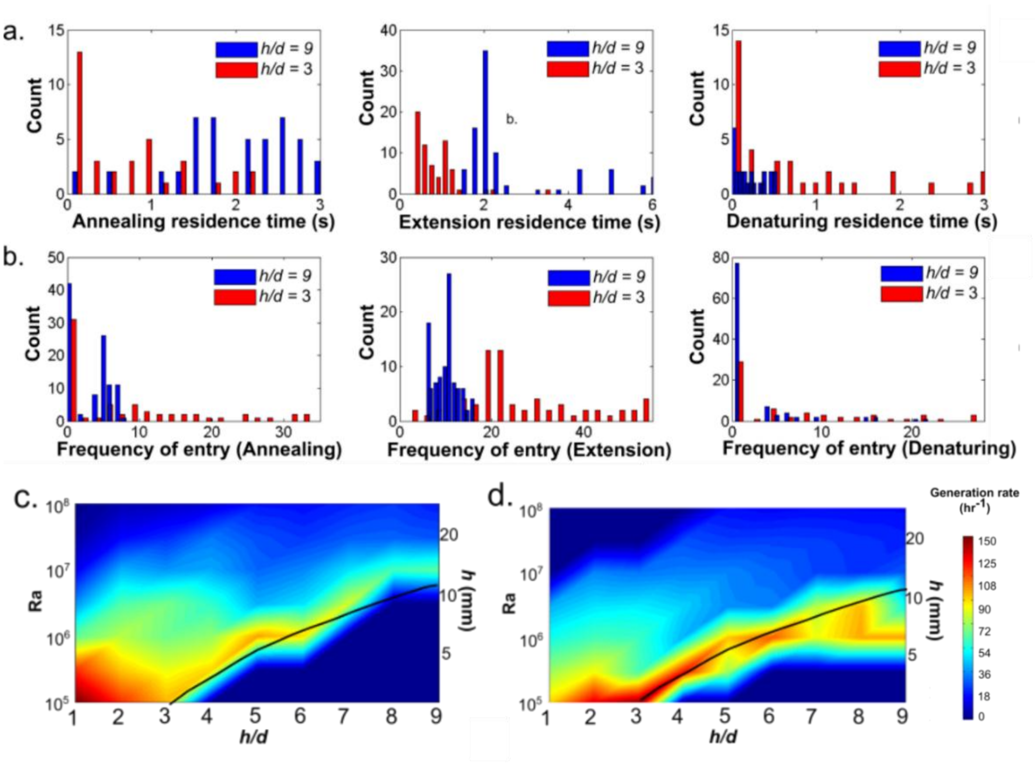

Figure 17: Convective flow under PCR conditions simulated using a 2D model. (a) Average residence times in each reaction zone display a much flatter distribution instead of the well-defined values obtained in the 3D model. (b) A peak frequency of entry near zero in the denaturing and annealing data suggests that the majority of fluid elements remain trapped within closed paths that do not extend to the bottom and the top of the reactor respectively. Consequently, generation rates (i.e., number of doubling events per hour) in the *Ra*-*h*/*d* parameter space simulated using (c) 3D and (d) 2D models are very different, with the 2D model unrealistically predicting DNA replication under conditions where the thermal driving force is insufficient to drive convective motion (i.e., below the solid line in each plot).

Surprisingly, the 2D model predicts that most fluid elements never enter the annealing and denaturing zones. Consequently, the corresponding parametric map of PCR generation rates constructed from a 2D analysis significantly mis-predicts the phenomena (Figure 17 c, d). Therefore the emerging chaotic effects are inherently three-dimensional, and cannot be fully captured by previously assumed simplified 2D view which may lead to unrealistic conclusions[17, 18].

Conclusion

Our results reveal an incredibly robust regime where rapid DNA replication is achievable independent of specific reactor geometries and temperatures, addressing limitations that have been previously viewed as a major drawback of the convective thermos-cycling format. Because the convective flow field is inherently dependent on the geometric and thermal conditions imposed, it has been generally accepted that the versatility of convective PCR is limited because reactor geometries would need to be specifically matched to the biochemical requirements of individual reactions.. Our kinetic mapping contradicts this view, suggesting instead that a properly designed standard reactor geometry within the chaotic flow regime can be universally functional (e.g., analogous to conventional PCR tubes).

CHAPTER III

SMARTPHONE ENABLED PORTABLE DNA DIAGNOSTICS

Introduction

The recent Ebola outbreak has exposed some of the key limitations facing current infectious disease management strategies, particularly when applied in remote underdeveloped areas. Existing approaches are highly resource intensive, relying on dispatching specially trained personnel to isolated locations where biological samples are collected and returned to dedicated laboratories for analysis. These inefficient channels become overwhelmed when field sites are not connected by a modern transportation infrastructure, introducing a considerable time lag between sample collection, diagnosis, and implementation of countermeasures. The resulting information flow is often extremely limited, delaying treatment of infected individuals and making it challenging for public health agencies to proactively formulate courses of action to effectively mitigate outbreaks. A need therefore exists for inexpensive and robust tools that can be broadly deployed to accelerate diagnosis, enable pinpoint delivery of therapeutics, and provide real-time data to better inform decision making.

Nucleic acid-based approaches like the polymerase chain reaction (PCR) are generally considered to be diagnostic gold standards in terms of both sensitivity and specificity. But PCR is largely ruled out as a viable candidate for deployment in resource-limited settings due to an unfavorable combination of (i) excessive electrical power requirements associated with repeated heating and cooling of reagents during thermo-cycling, and (ii) complexities involved with inexpensively implementing fluorescence-based detection of the reaction products. Here we show how convective thermo-cycling can be leveraged to overcome these limitations, laying the foundation for a new generation of simple ruggedized PCR-based diagnostic platforms. The same natural convection phenomena at play in ordinary lava lamps enable the PCR to be isothermally executed using a single heater maintained at the reaction's denaturing temperature. This inherently simple design dramatically reduces electrical power consumption and can be readily interfaced with a fluorescence detection system that exploits the versatility and connectivity ordinary smart-phones. These breakthroughs make it possible to construct ultra-portable, rapid, and quantitatively accurate DNA analysis systems for under $20 ($US)—a price point that makes widespread deployment truly feasible.

Since its first introduction a little over a decade ago, convective thermo-cycling has remained an intriguing avenue to enable rapid PCR. But a crucial roadblock to practical implementation of this approach has been the inherent interdependence between the internal flow field and the reactor geometry (expressed in terms of the height, h, and diameter, d, of a cylindrically shaped configuration, Chapter I). The spatial temperature gradient established between the top (cool) and bottom (hot) surfaces of the reactor not only actuates the denaturing, annealing, and extension steps necessary to perform the PCR, it also supplies the driving force to physically transport reagents between these reaction zones. It has previously been assumed that this interplay implies a need to custom design reactor geometries to match the individual thermal requirements of each PCR assay to be performed (e.g., when different primers with different annealing temperatures are employed), and that robustness is constrained by a need to maintain a specific orientation with respect to the gravitational driving force. We recently developed a 3D coupled flow-reaction model that challenges this assumption, revealing an unexpectedly broad design space dominated by chaotic advection where reaction rates are greatly accelerated and remain essentially unchanged over virtually the entire range of realistic PCR condition[27] (Chapter II). Any reactor geometry selected within this regime is therefore universally functional (i.e., analogous to standardized PCR tubes and plates), making it possible to execute a 30 cycle PCR in 10 – 20 min regardless of temperature setpoints and spatial orientation.

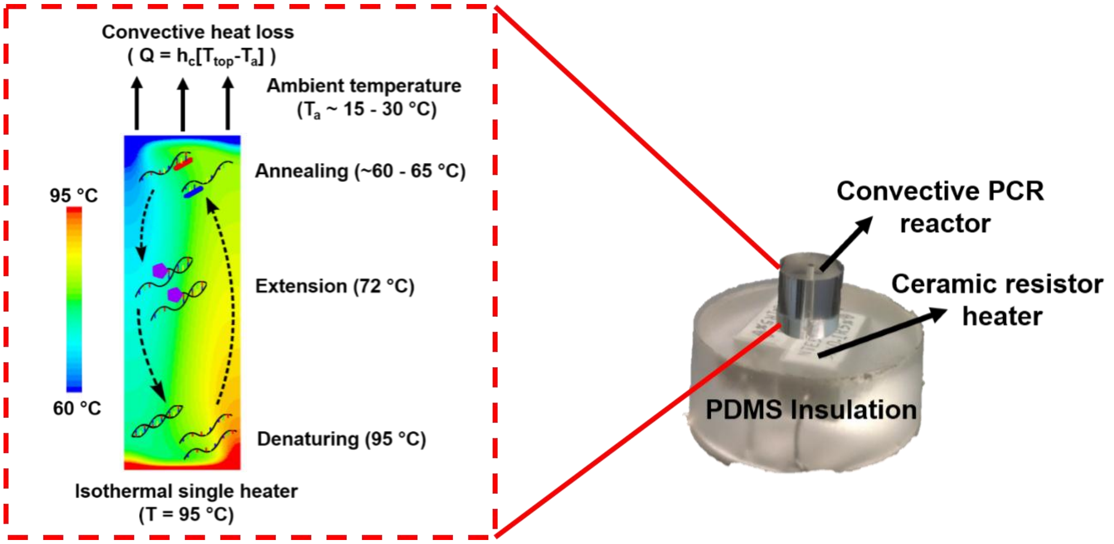

Figure 18: Single heater enabled convective PCR. Rayleigh Bernard convection enables PCR to be performed in a pseudo-isothermal manner with denaturing, annealing and extension reactions occurring at different temperature zones within the reactor. The top surface experiences heat loss (Q) to the surroundings (T_a) at a rate dependent on the convective heat transfer coefficient (h_c). The PCR reactor is mounted on a single ceramic heater encased in polydimethylsiloxane (PDMS) for insulation.

Single heater design

We wanted to leverage this new fundamental understanding to reduce the electrical power requirements associated with the repeated temperature changes needed to perform conventional thermocycling. Having found the optimum thermal and geometric parameters for the design and operation of convective PCR unit, we can now proceed to engineer a complete DNA analysis unit. Our previous two heater convective PCR setup [27, 32] was simplified by operating with only a bottom heater (Figure 18). We accomplished this by first selecting a cylindrically-shaped reactor geometry within the above mentioned chaotic advection design space, and then tuning its height *h* such that passive heat loss to the surrounding environment automatically imposes the desired annealing conditions at the top surface when the bottom is held at the denaturing temperature (Figure 18).

Thermal management is achieved by using off the shelf ceramic resistors which convert current to heat via joule heating. A temperature sensor monitors the temperature of the resistor and regulates the flow of current through a MOSFET based feedback loop programmed to maintain the temperature at 95 °C by means of an Arduino based microcontroller (Figure 19 a). A polydimethylsiloxane (PDMS) casing around the resistor ensures insulation and efficient heat transfer to the reactor bottom. In this way, the PCR is actuated isothermally by maintaining a single heater at a constant temperature, drastically reducing electrical consumption to a level that can be supplied by standard 5 V USB sources that power ordinary consumer mobile devices and solar battery packs. The resulting vertical temperature gradient within reactor induces convective flow enabling rapid PCR. The circuit also powers a blue LED light source for detection of PCR products in real time. Details of the circuit design and electronic parts for the single heater are provided in the following section.

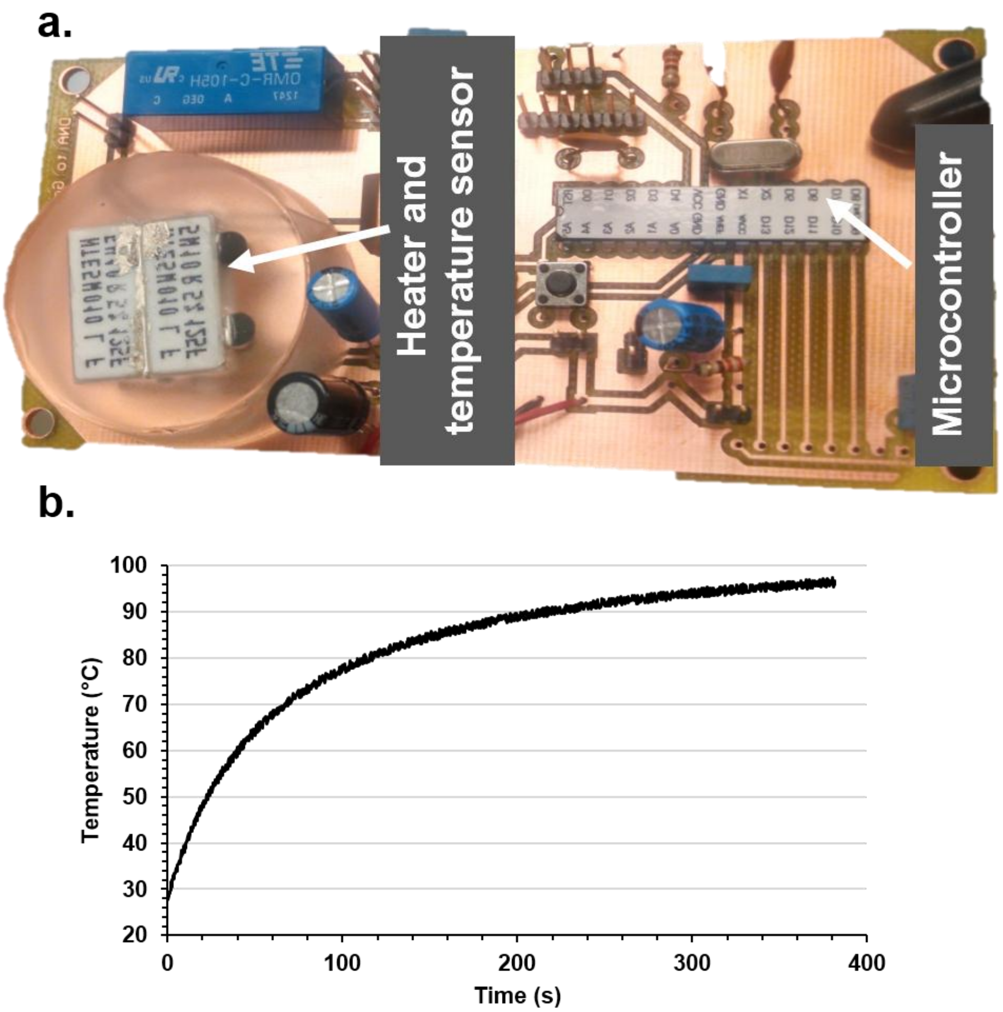

Figure 19: Circuit design for single heater. (a) Circuit board consisting of a ceramic heater and temperature sensor with a microcontroller programmed via Arduino interface. (b) The USB powered ceramic heater is able to reach the denaturing temperature (95 °C) in ~ 5 minutes.

Circuit design

The isothermal heater, LED and LCD screen were operated via a microcontroller taken from the Arduino UNO R3 (Atmega328 - assembled) along with few other electrical components to ensure safe and smooth functionality of the circuit. Two 10 ohms ceramic wire wound resistors (Mouser electronics) in parallel functioned as heaters by converting current to heat. The Polydimethylsiloxane (PDMS) casing around the heaters provided good insulation and allowed the heaters to reach the desired set point (95 °C) much faster (Figure 19 b). One of the digital pins (D3) in the microcontroller was assigned to provide the heater 5V input voltage through a MOSFET. A temperature probe (tmp35) sensed the temperature of the heater and the signal was sent to one of the analog pins in the microcontroller (A5). This analog reading was converted into temperature which was continuously monitored to operate the heaters isothermally. The 16 MHz quartz crystal resonator (Mouser electronics) with two 22pF capacitors (Mouser electronics) connected to the microcontroller generated a clock signal to control timing in the circuit. A low-dropout (LDO) regulator (TLV2217-33) with two capacitors (10 and 47 µF; Mouser electronics) and a 100 ohm resistor (Mouser electronics) provided a constant 3.3 V to a blue LED (5mW. Ebay). A LCD (Nokia 5110) was connected to 6 digital pins (D6, D9, D10, D11, D12, D13) in the microcontroller and was used to display and monitor real-time relevant circuit information such as the heater temperature and LED status. Capacitors were used in various locations to stabilize the voltage to within each device's specification.

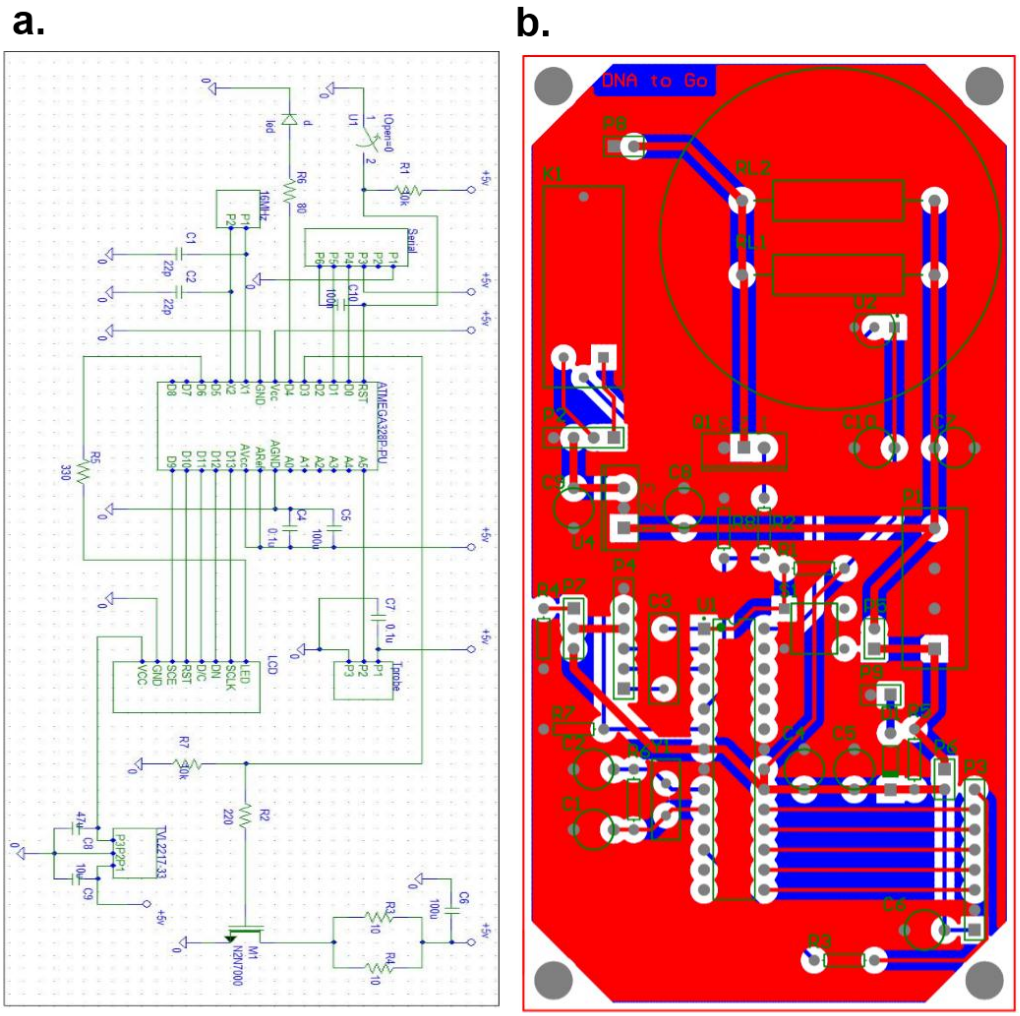

Figure 20: Printed circuit board design. (a) Circuit diagram highlighting all the electronic components and their connection to the microcontroller. (b) Printed circuit board layout.

The Arduino program (Appendix E) was written and compiled in Arduino 1.0.6 integrated development environment (IDE) and was loaded into the microcontroller through an FTDI chip (Sparkfun). The final circuit and all the components were soldered on a printed circuit board (Figure 20 b) which was then encapsulated in a plastic case designed and printed using FreeCAD and 3D printer (MakerGearM2) respectively (Figure 21). The device can be powered by any 1A 5V power source such as solar battery packs, portable phone chargers, hand crank powered charger etc. A detailed part list of the circuit is provided in Table 5.

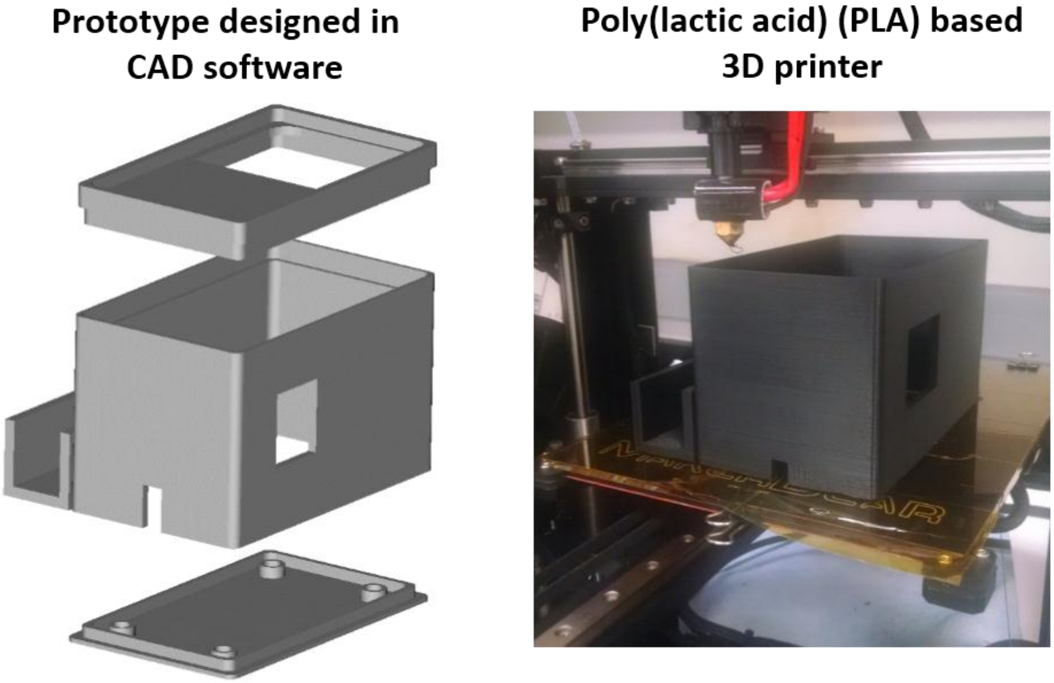
Prototype designed in CAD software

Poly(lactic acid) (PLA) based 3D printer

Figure 21: 3D printed case compactly packages all components together while simultaneously providing a dark room environment. The case for the device was made in three parts keeping all the relevant design parameters in mind in openSCAD. An extrusion based 3D printer (MakerGear M2) was then employed to print the components of the case. The three components would easily snap into place, yielding a compact enclosure for the convective PCR setup.

Table 5: Electronic circuit board part list.

Component	Part name	Purpose	Cost per unit ($)
Microcontroller	Atmega328	Embedded computer system to control and program input/output peripherals in an electronic circuit.	5.00
Ceramic resonator	16 Mhz ceramic resonator	Generates a clock signal for the microcontroller	0.20
Ceramic resistor	Wire wound 10 ohms ceramic resistors	Converts current to heat via joule heating	0.36
Temperature sensor	TMP35	Provides a voltage output that is linearly proportional to temperature (° C)	1.50
LED	5 mm round blue LED, 5 mW	Illuminates the reactor with blue light	0.02
LCD	Nokia 5110 LCD	Displays text on the LCD screen	5.00
MOSFET	IRF 520	Provides input voltage to the heaters	0.93
Low-dropout (LDO) regulator	TLV2217-33	Drops the voltage down and regulates it	0.36
Reset button	Push button switch	Resets the microcontroller	0.05
Capacitors	2 22 pF capacitor	For the ceramic resonator clock	0.05
Capacitor	100 nF capacitor	For reset programming switch	0.05
Capacitors	0.1 µF, 100 µF capacitor	To regulate power to microcontroller	0.05
Capacitors	10 µF, 47 µF capacitor	For low-dropout (LDO) regulator	0.05
Capacitor	0.1 µF capacitor	For LCD	0.05
Capacitor	100 µF capacitor	For ceramic heaters	0.05
Capacitor	0.1 µF capacitor	For temperature sensors	0.05
Resistor	330 ohms	For LCD back light	0.05
Resistor	100 ohms	For LED	0.05
Resistor	10 k ohm	Pull up resistor for reset switch	0.05
Total estimated cost			= 12.99

Smart-phone based detection

Successful nucleic acid amplification can be quantified either in real time via fluorescence detection or after PCR through gel electrophoresis requiring additional instrumentation and time. Full diagnostic utility requires the ability to perform quantitatively accurate product analysis, but fluorescence-based approaches are often challenging to implement in a portable format due to issues associated with size, cost, and ruggedness. Smart-phones have become an ubiquitous handheld device which not only are an essential part of telecommunication but also provides state of the art imaging, computations and data analysis. They are extremely user friendly, thus eliminating the need for any prior user training requirements. These features have enabled smart-phones to emerge as promising analysis tool for point of care systems [33-35]. We incorporated a smart-phone to image the top of the convective reactor with a SYBR-PCR based fluorescence detection. The reactor is illuminated with a blue LED light source (480 nm, 5 mW) coupled with an excitation band pass filter (480 nm) and the resulting fluorescence signal is filtered through emission band pass filter (520 nm) (Figure 22). This adaptation of smart-phones to flurophore based PCR detection required us create an image analysis application ("PCR to Go") which allows the user to analyze the PCR products either at end point mode, yielding a yes-no type detection or in real time mode providing a more quantitative analysis (Figure 23). The app can access the phone's optical hardware to fix the camera exposure time and focal length ensuring consistent lighting, a feature which is typically disabled for the inbuilt point and shoot camera type use. CMOS sensor array of the smart-phone camera then acquires images of the top of the convective PCR reactor which is enclosed in an opaque 3D printed case ensuring a dark room environment for consistent lighting (Figure 21). Imaging from the reactor top also ensures strongest fluorescent signal due to lower temperatures here.

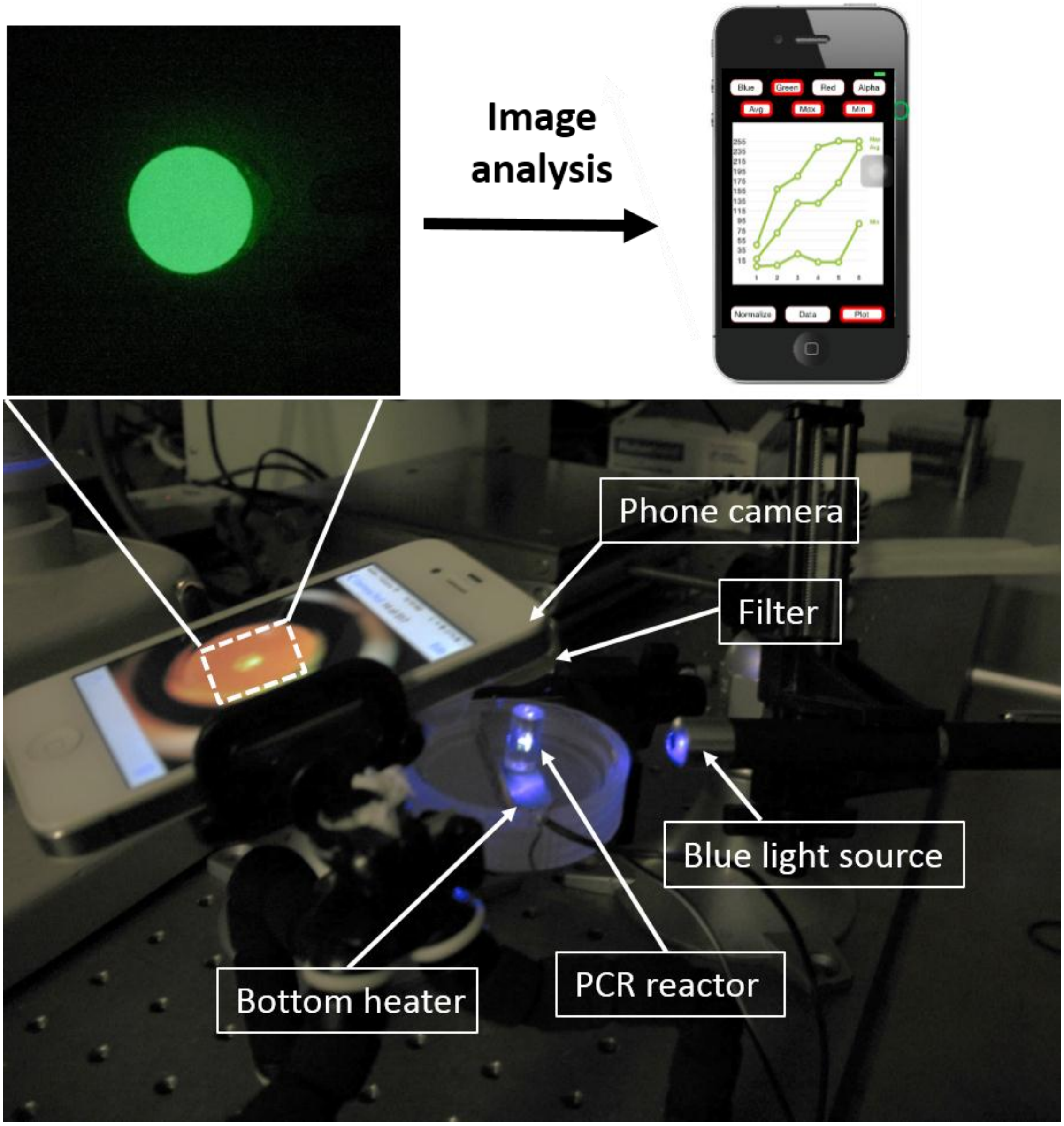

Figure 22: Real time fluorescent detection of convective PCR products via SYBR-PCR chemistry. A blue light source illuminates the convective PCR reactor and the images of the reactor top are taken with smart-phone camera which are subsequently analyzed with a built in image analysis app called PCRtoGo.

PCR to Go iPhone app

The "PCR to go" application was written and developed in Xcode 5.0 using objective C. The core graphics and AVFoundation frameworks were incorporated from Apple's iOS software development kit (SDK) to access and control advanced iPhone camera features such as control over the exposure time and focal length. This enabled images to be accessed via either the phones inbuilt library or the camera. A clip on magnifying lens (amazon supply) enabled a 10X optical zoom to the camera and the "PCR to go" app interface allowed an additional 6X digital zoom via SDK's core graphics affine transformation framework, allowing the user to work with a maximum of 60X zoom. The focus and exposure were locked before image acquisition session enabling constant lighting.

The app interface allows the user to automatically capture images at regular time intervals. User touch gestures were incorporated to select the desired area of interest for image analysis. The selected analysis area was converted into bitmap image data stored as a mutable date set containing 4 bits per pixel (one for each red, blue, green and alpha pixel values) corresponding to RGBA color space. The average, maximum and minimum RGBA pixel values for each image was calculated and could either be tabulated on screen or exported via email for further analysis. The average green pixel values was used for all fluorescence intensity analysis. These intensity values were transformed by the application of gamma correction to take into account the nonlinear fashion in which our eyes perceive luminescence.

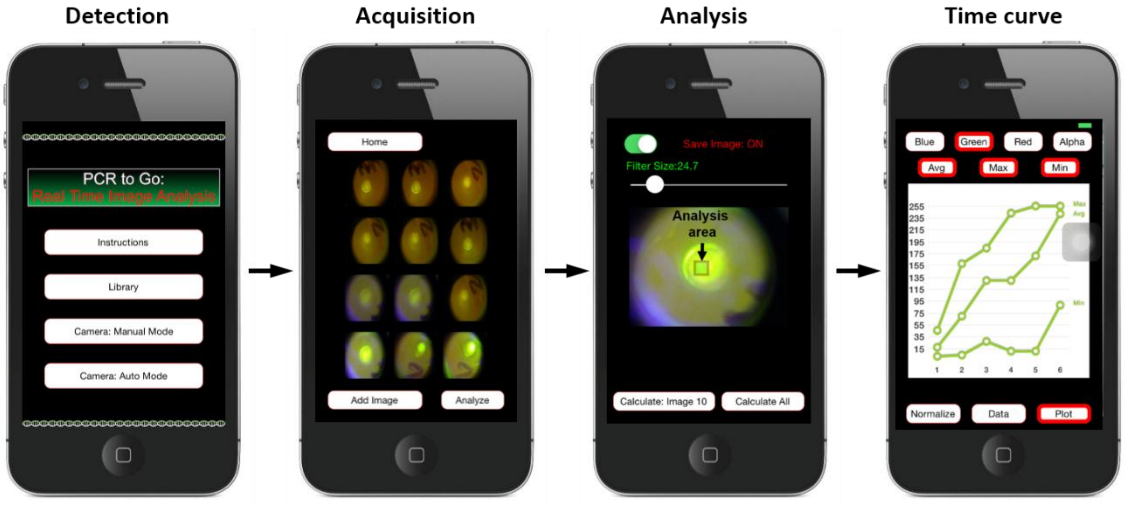

Figure 23: PCR to Go iPhone app. The images can either be chosen from the built in photo library or be captured through the phone camera during operation. Before the image acquisition session, the camera exposure time and focus are locked to ensure uniform lighting in all images. The user can then choose the size and position of the analysis area (filter) within the chosen/captured images. The app then generates red, blue, green and alpha channels for each of the selected images and displays the average, maximum and minimum pixel values corresponding to each channel within the analysis area. These value can either be tabulated or plotted for product quantification

$$I_{corrected} = \left(\frac{I_{original}}{255} \right)^{\gamma} \qquad [3.1]$$

where $I_{original}$ is the original pixel intensity taken from the phone camera and $I_{corrected}$ is the corresponding gamma corrected image. A value of 2.2 was assigned for γ in our calculations. The background intensity was then subtracted from all images by subtracting the intensity of the first image yielding a common intensity baseline for all real time PCR runs. The resulting quantitative PCR curve was fit into a typical sigmoidal curve equation given by eq. [3.2].

$$I = \frac{I_{\max}}{\left(1 + e^{-(t - t_{1/2})/k}\right)} + I_o \qquad [3.2]$$

where $I_{\max}$, I_o, $t_{1/2}$ and k represent maximum fluroscence, background fluorescence, time required for intensity to reach half of the maximum value and slope of the curve respectively. I and t are the image intensity and the corresponding time respectively. Critical threshold (C_t) values were then determined by the intersection of the sigmoid curve with the critical threshold line (threshold value = 20).

Lab on drone

All components are integrated within an enclosure incorporating an interchangeable smart-phone cradle that ensures proper alignment of the camera and optical components independent of the specific mobile device employed (Figure 24). The instrument is incredibly lightweight (Table 6), making pinpoint deployment into remote field locations feasible using ordinary consumer-class quad-copter drones. Unprecedented ruggedness is achievable, as evident by successful in-flight PCR performed across different target/template systems while being carried as a drone payload (Figure 25 e).

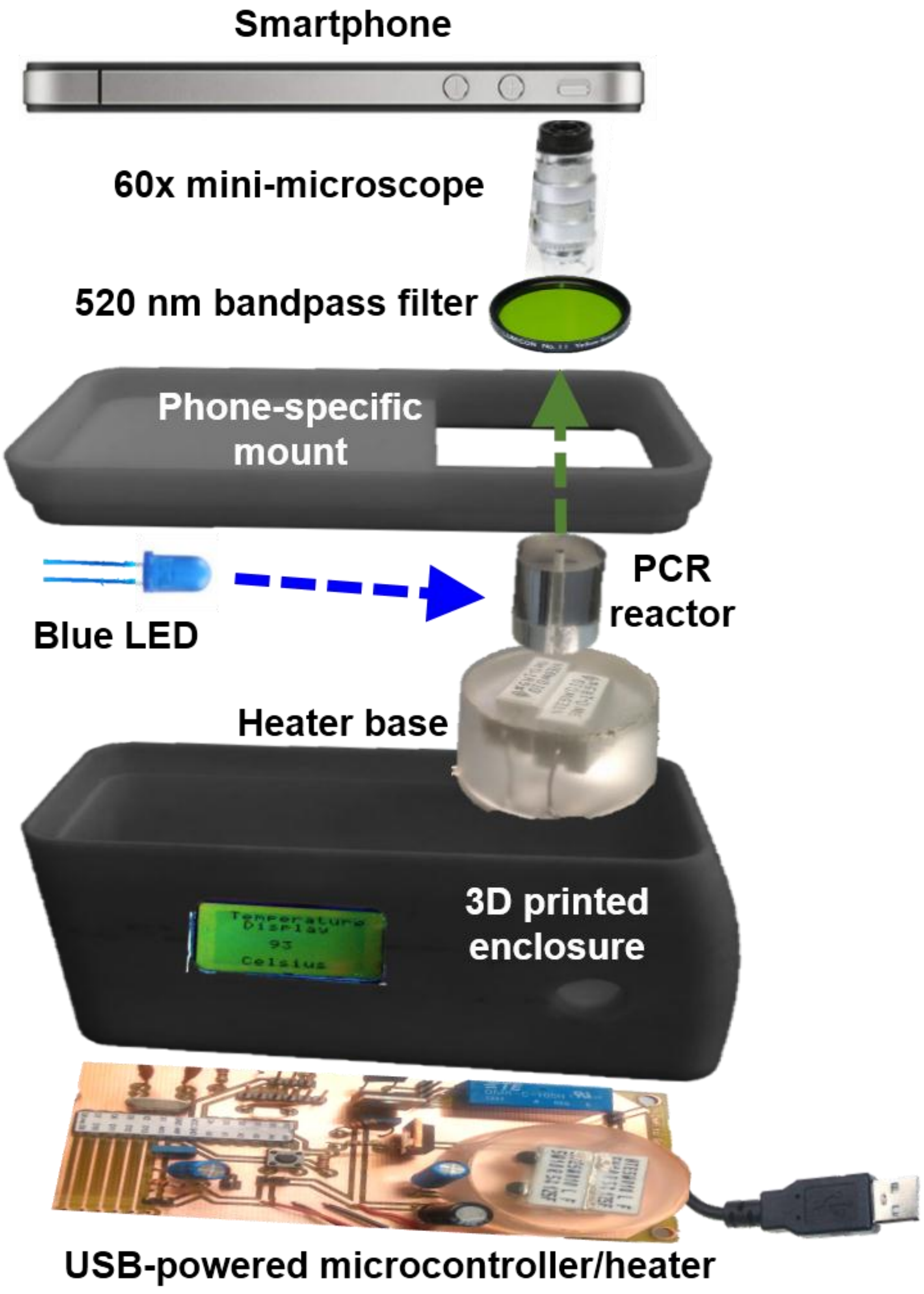

Figure 24: Complete assembled device consisting of all relevant components. All components are integrated and housed in an enclosure incorporating an interchangeable smart-phone cradle that ensures proper alignment of the camera and optical components regardless of the type of mobile device employed. The PCB powers both the isothermal heater and blue LED through a 5V USB source such as a phone charger or solar battery packs.

The 3D Robotics IRIS+ quad-copter was used for aerial flight convective PCR tests. It is capable of providing a full flight time of 15 - 22 minutes with a payload of about 400 grams (8 lbs). The heater base was preheated for 3 to 5 minutes and then the PCR reactor was secured on the heater base via clear adhesive tape (office tape). The device was tightly fastened to the drone via plastic disposable cuffs (commercial electric, 36 inch heavy duty ties). A 3200 mAh portable external battery charger (Vinsic Tulip, 5 V, 1 A) was used to power the convective PCR device while the drone was powered by an internal high capacity rechargeable flight battery which allowed us to fly the completely assembled convective PCR device and the attached iPhone 4 for about 17 minutes. The quad-copter's two axis gimbal stabilization enabled steady control and motion as it was maneuvered around using the remote controller. The post flight PCR sample was collected and analyzed further after the drone landed (Figure 25).

Table 6: Weight analysis of components of convective PCR device.

Component	Weight (grams)
Phone (Iphone 4s)	140
PLA Case	108
Battery pack	83
Printed circuit board and reactor	72
Optics	30
USB wire for power	10
Total	443

Figure 25: Lab on drone and in-field testing. (a) The convective PCR device with the circuit board, phone mount, iPhone, hand crank charger and IRIS+ quad copter. (b) Sample preparation and loading for in-field testing. (c) Ultra-portable design and implementation enables deployment of the convective PCR test unit via unmanned aerial drones to remote locations. (d) Post flight de-assembled device. (e) In flight PCR amplification of 1: 150 bp sequence of 16sRNA of Staphylococcus aureus (16 minutes) 2: 237 bp of lambda DNA (18 minutes). (f) Device in operation.

Detection limit and sensitivity of convective PCR

The sensitivity of the device was tested by amplifying a 237 bp target DNA sequence of lambda DNA incorporating SYBR dye chemistry with varying initial copy number. The smart-phone optics was able to detect a rise in fluorescence intensity with a copy number as low as 1000 copies/μL (Figure 26 a, b, c), a level sufficient for many diagnostic assays and particularly impressive considering the simplified instrument format. Furthermore, the convective PCR device itself is sensitive to an initial copy number as low as 100 copies/μL (Figure 26 d) as verified by gel electrophoresis.

Effect of tilting the PCR reactor

Ruggedization is also an essential consideration in the context of portable field operation. The drone we used GPS to position and maneuver and hence are very stable. However, movement along the horizontal plan requires them to tilt. Variations in the reactor's orientation with respect to the vertical direction therefore is an important consideration given the gravitational origin of the driving force for convective transport. Remarkably, coordinated experiments and simulations both reveal that reaction performance is not appreciably altered as the reactor's tilt angle is increased, even to extreme nearly horizontal levels approaching 82° (Figure 27). This invariance with spatial orientation is a reflection of the chaotic transport regime's inherent robustness where consistent results are predicted over orders of magnitude in the thermal driving force (Chapter II).

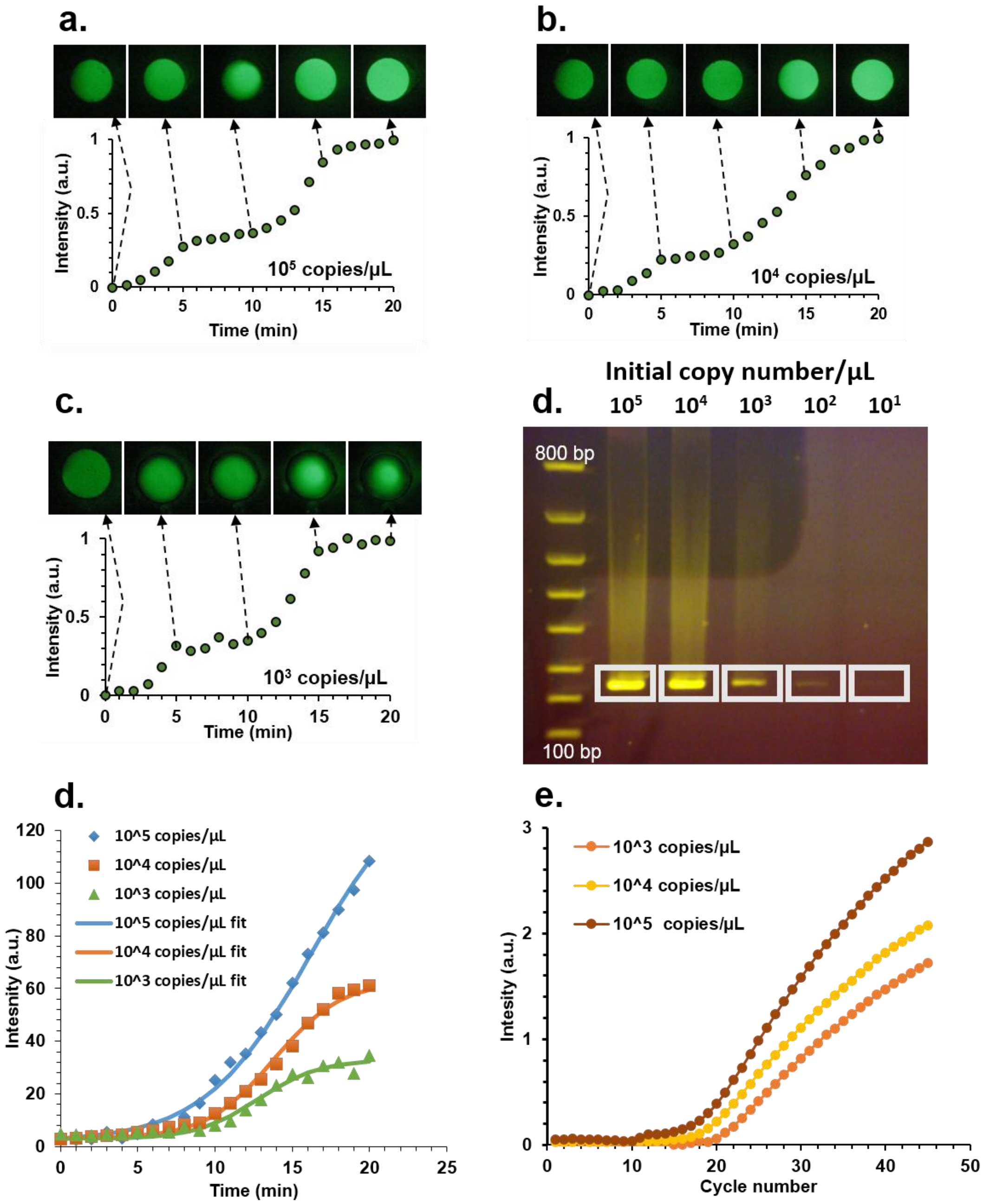

Figure 26: Smart-phone based PCR detection. (a, b, c) Real time quantification of a targeted 237 bp segment of lambda DNA for 10^5, 10^4 and 10^3 initial DNA copy numbers respectively. (d) Gel electropherograms revealed that the convective PCR is capable of amplifying the targeted sequence from an initial copy number as low as ~100 copies/uL. (e) Average real time quantification using PCRtoGo app with gamma correction and corresponding sigmoidal curve fit. (f) Real time PCR run on a benchtop qPCR machine (Roche).

Thermo-cycling becomes degraded beyond 82° due to the onset of secondary circulatory flow patterns within the cylindrical reactor volume. This inhibits PCR significantly as the reagents are now trapped in closed fluid trajectories which do not get to sample the correct temperatures as was verified by post PCR analysis also (Figure 27 c).

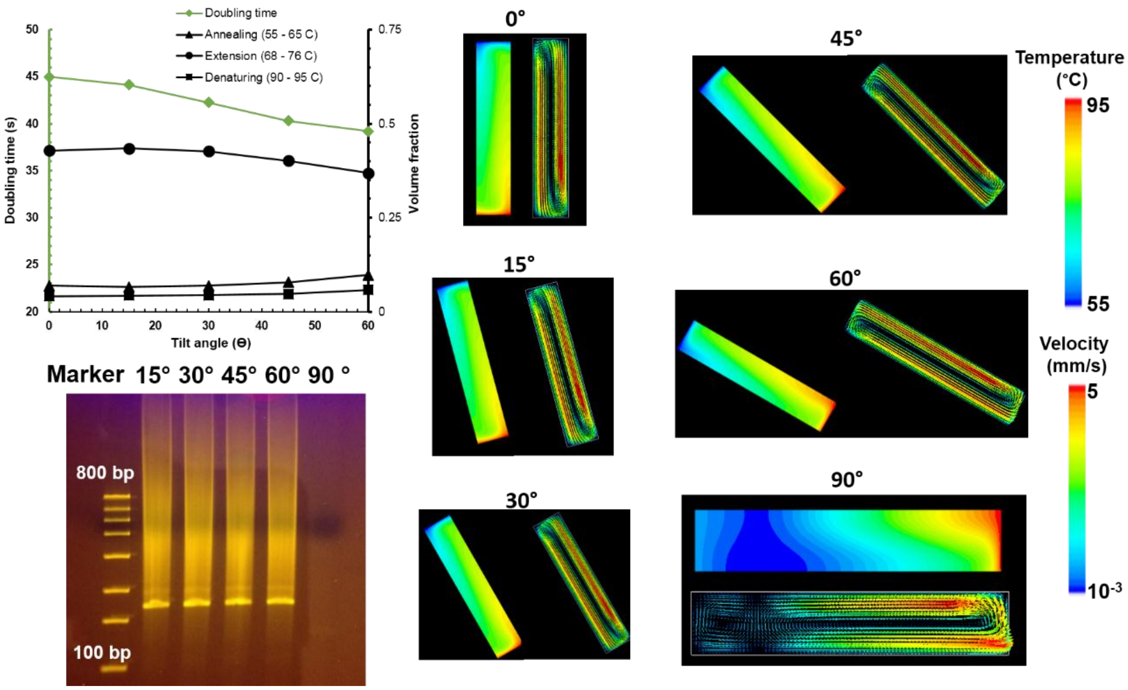

Figure 27: Effect of tilt angle on convective PCR. (a, b) Simulation results reveal the tilt angle of the reactor from the vertical axis does not alter the replication doubling time and volume of the respective reaction zones. (c) Gel electropherograms confirm correct amplification products are preserved at different tilt angles. (d) Changing the tilt angle of the convective PCR cell does not change the temperature and velocity fields appreciably for angles less than 82º.

Effect of ambient temperature

Since different environments would host different ambient temperatures, we quantified its effect of convective PCR efficiency by running the reaction in different environments. Ambient temperature conditions impact thermo-cycling performance by virtue of their influence on the thermal gradient established within the reactor. It was found that convective PCR is most efficient in cold environments (5 ºC) with the product yield decreasing as the ambient temperature increases (35 ºC). At even higher temperatures, the target is not amplified (Figure 28 a) as it becomes difficult to maintain the spatially distinct temperature zones required to actuate each stage of the reaction and these results are mirrored in the simulated doubling times (Figure 28 b). Further CFD analysis reveals that the drop in the PCR efficiency at higher ambient temperatures is due to the decrease in the volume of the extension reaction zone within the convective reactor (Figure 28 b).

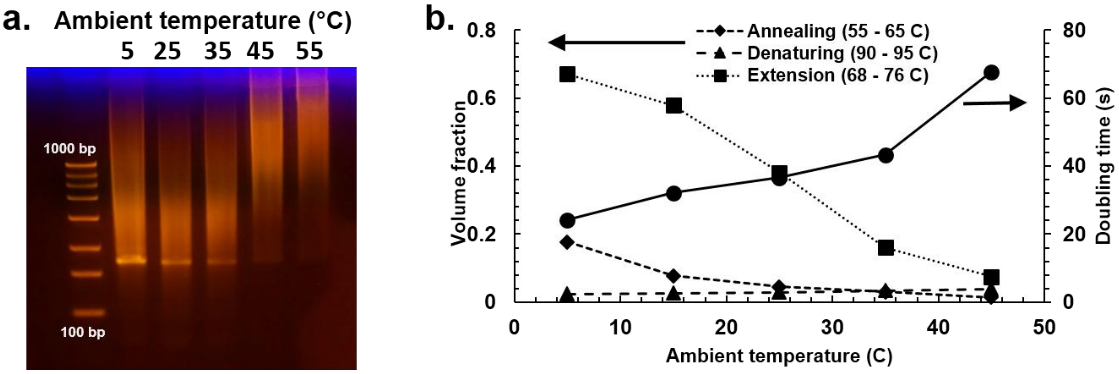

Figure 28: Effect of ambient temperature on convective PCR. (a) Gel electropherogram quantifying the effect of ambient temperature on convective PCR (b) Simulation model predicts the reaction takes longer time when the ambient temperature is increased due to the decrease in extension volume in the reactor.

Modified computational fluid dynamics model

Detailed formulation of the computational fluid dynamics and the PCR kinetic model has been discussed in Chapter I and II. For the single heater setup, the isothermal boundary condition at the reactor top was replaced with a convective heat loss term ($Q=h_c(T_{top} - T_{amb})$; h_c is the convective heat transfer coefficient (1000 $W/(m^2K)$); T_{top} is the top boundary temperature and T_{amb} is the ambient temperature). There was no appreciable change in the velocity and temperature fields when the adiabatic side walls were replaced with conductive acrylic walls. The new model was used to test the effect of ambient temperature (Figure 28) and tilt angle (Figure 27) of the efficiency of convective PCR.

Convective PCR experimental methods

Cylindrical reactors were constructed from 1 inch dia. polycarbonate rod stock (Amazon Supply) by cutting them to lengths and machining holes to produce reactors of desired height (10 mm) and diameter (2.5 mm). Smartphone enabled real time PCR experiments were performed to replicate a 237 base pair target from a λ-phage DNA template with SYBR green PCR master mix (Table 7). Sensitivity to initial copy number, ambient temperature and inclination angles of convective reactor was established by replicating a 237 base pair target from λ-phage DNA template with KOD polymerase enzyme (Table 8). Detection of Ebola (Table 9) and Staphylococcus aureus (Table 10Table 9) were performed with their respective PCR kits. Details of the individual PCR mix composition and protocol are listed below.

Table 7: Real time detection on the smartphone and benchtop qPCR machine.

Reagent	Volume (μL)	Source
SYBR master mix (2x)	50	SYBR Green PCR Master Mix, Applied Biosystems
Forward primer (10 μM)	10	CTGAGGCCGGGTTATTCTTG (Amplicon size: 237 bp fragment of λ DNA)
Reverse prime (10 μM)	10	CGACTGGCCAAGATTAGAGA (Amplicon size: 237 bp fragment of λ DNA)
Lambda DNA (1 μg/mL)	1	
PCR grade water	29	

Protocol: The hot start step (95 °C for 10 minutes) was performed in a regular thermocycler (Boimetra, Tpersonal) prior to the convective runs. All real time convective reactions were run for 20 minutes with the isothermal bottom heater maintained at 95 °C.

Table 8: Sensitivity to initial copy number, ambient temperature and inclination angles of convective reactor on the reaction.

Reagent	Volume (µL)	Source
Buffer solution #1 (10x)	10	KOD DNA Polymerase Kit (cat. no. 71085-3; Novagen)
$MgCl_2$ (25 mM)	4	KOD DNA Polymerase Kit (cat. no. 71085-3; Novagen)
dNTPs (2 mM each)	10	KOD DNA Polymerase Kit (cat. no. 71085-3; Novagen)
Forward primer (10 µM)	3	CTGAGGCCGGGTTATTCTTG (Amplicon size: 237 bp fragment of λ DNA)
Reverse primer (10 µM)	3	CGACTGGCCAAGATTAGAGA (Amplicon size: 237 bp fragment of λ DNA)
Lambda DNA (1 µg/mL (10^7 copies/µL) stock solution diluted down to achieve different initial copy numbers)	1	
KOD polymerase (2.5 units/mL)	0.8	KOD DNA Polymerase Kit (cat. no. 71085-3; Novagen)
PCR grade water	67.8	

Protocol: No hot start required. The convective reactions were run for 20 minutes with the isothermal bottom heater maintained at 95 °C.

Table 9: Detection of Ebola 2014 virus strain.

Reagent	Volume (μL)	Source
qRT-PCR master mix	50	oasig OneStep qRT-PCR mastermix; Cat. # : OneStep-oasig 150
Primer/probe mix	5	EBOV_2014 Primer/Probe mix, genesig Cat. # : Path-EBOV_2014-Standard
Positive control	10	genesig Cat. # : Path-EBOV_2014-Standard; 2 x 10^4 copies/ μL
RNAse/DNAse free water	35	(genesig Cat. # : Path-EBOV_2014-Standard

Protocol: One step amplification protocol was followed where the reagent mixture was held at 42 °C for 10 minutes for reverse transcription followed by 95 °C for 2 minutes for enzyme activation. These constant temperature hold steps were accomplished in a regular thermocycler (Boimetra, Tpersonal) followed by convective reaction for 25 minutes with the isothermal bottom heater maintained at 95 °C.

Table 10: Detection of Staphylococcus aureus DNA.

Reagent	Volume (µL)	Source
Master mix	50	Johns Hopkins University
Forward primer (10 µM)	5	5' – TGG AGC ATG TGG TTT AAT TCG A – 3' (amplicon size: 147 bp)
Reverse primer (10 µM)	5	5' – TGC GGG ACT TAA CCC AAC A – 3'(amplicon size: 147 bp)
Probe	5	6FAM 5' – CCT TTG ACA ACT CTA GAG ATA GAG CCT TCC C – 3'
Positive control (16S RNA)	1	Johns Hopkins University (Professor Charlotte Gaydos) 5 x 10^4 copies/µL
PCR grade water	30	
One step amplification protocol was followed where the reagent mixture was held at 42 °C for 10 minutes for reverse transcription followed by 95 °C for 2 minutes for enzyme activation. These constant temperature hold steps were accomplished in a regular thermocycler (Boimetra, Tpersonal) followed by convective reaction for 25 minutes.		

Prior to reagent loading, convective reactors were rinsed with a 10 mg/mL aqueous solution of bovine serum albumin (cat. no. A2153; Sigma-Aldrich) followed by Rain-X Anti-Fog (SOPUS Products) and dried to minimize sidewall adsorption and enhance surface wettability. After loading reagents, reactors were then placed on the preheated (95 °C) ceramic heater surface and secured using adhesive tape (office tape). The iPhone app was run in continuous mode to capture an images of reactor at one minute intervals. After incubation for a desired time, the convective reactors were removed and the post PCR products were pipetted out for subsequent analysis by agarose gel electrophoresis using the FlashGel system (Lonza; cat # 95015-612). The post PCR samples contained 1µL FlashGel loading dye (Cat. # 50462) and 4 µL of DNA samples with a FlashGel DNA marker (100 bp – 4 kb, Cat # 50473) as a ruler. Samples were run at 280 V for 8 minutes and the separated DNA strands were imaged using standard smartphone camera.

Comparison with other portable PCR based diagnostic tools

It is worthwhile to evaluate how our instrument performs in the context of other efforts to develop portable rapid PCR-based diagnostic tools. A recently reported novel approach to reducing electrical power requirements leverages a solar focusing lens to passively establish the spatially distinct temperature zones needed to perform continuous flow PCR [36]. But electrical power is still required to circulate reagents through the microfluidic network using a syringe pump, post-PCR detection is achieved off-chip using a benchtop microscope, and effective operation is contingent upon availability of sufficient ambient sunlight. The suitcase-sized POCKIT system (GeneReach) is a commercial convective thermo-cycler, but is of limited utility for portable diagnostics due to the lack of an integrated battery and limited endpoint fluorescence detection. Palm PCR (Ahram Biosystems), a competing convection-based instrument, offers battery power but lacks integrated fluorescence detection. Other groups have demonstrated capillary-based convective real time PCR with integrated CCD-based imaging [29, 37], but these instruments are not portable and require a desktop computer for operation and data analysis. Our system is not subject to these limitations, providing a rugged inexpensive platform ideally suited for field deployment. A $20 ($US) hardware cost achieved through the use of readily available parts breaks a significant price barrier, while the simplified imaging approach and device agnostic design makes it possible to leverage the growing used smart-phone marketplace to deliver affordable fluorescence detection. When combined with the use of a 3D printed enclosure it becomes possible for virtually anyone to build their own fully functional fluorescence-based thermo-cycling instruments, introducing exciting new possibilities for democratization of advanced diagnostic technologies.

Conclusion

Our instrument promises to overcome the significant time lag between sample collection, analysis, and implementation of response interventions that currently hinders infectious disease management due to finite availability of static laboratory resources. Convective thermo-cycling enables rapid PCR-based assays to be performed in a robust format using the same reagents employed in conventional protocols. Coupling this approach with smart-phone-based detection introduces extraordinary connectivity, making it possible to leverage existing communication networks to instantly deliver analysis results. Taken together, our technology’s unprecedented ruggedness, low cost, and portability introduces intriguing new possibilities for deployment of gold-standard PCR diagnostic tools. Fleets of consumer-class drones can be readily assembled and programmed to achieve pinpoint delivery and enable strain-specific surveillance of virtually any infectious disease (the \$250 –\$500 retail price point of consumer-class drones is 10 – 20 fold less than the heavy-lift equipment currently envisioned for drone-based cargo delivery). It is therefore conservatively feasible to assemble a “swarm” of 100 drones (including associated batteries and charging equipment) for approximately \$50,000 that can be rapidly deployed via “pop up” field centers to support ~500 tests per day and enable coordinated distribution of testing and therapeutics.

CHAPTER IV

CHAOTIC TARGETING AND ACCELERATION OF SURFACE CHEMISTRY IN PREBIOTIC HYDROTHERMAL MICRO-CAVITIES

Introduction

We have unexpectedly discovered a subset of complex flow trajectories that are highly favorable for PCR due to a synergistic combination of (1) continuous exchange among flow paths that provides an enhanced opportunity for reagents to sample the full range of optimal temperature profiles, and (2) increased time spent within the extension temperature zone—the rate limiting step of PCR. Extremely rapid DNA amplification times (under 10 min) are achievable in reactors designed to generate these flows. This surprising interplay between reaction and flow has led us to consider adaptations beyond the PCR. Specifically, it is well-known that analogous temperature gradients exist naturally in porous hydrothermal vents on the ocean floor, and that chemical reactions within these environments are likely to have played a crucial role in the origin of life by catalyzing prebiotic assembly of simple biomolecules to higher levels of complexity.

RNA world theory

The RNA world theory offers a widely accepted framework to explain spontaneous emergence of biochemical complexity from elementary building blocks likely to have been present under prebiotic conditions. Early studies focused on mechanisms by which lightning and UV radiation in the prebiotic atmosphere could catalyze synthesis of abiogenic precursors[38, 39]. This view has since evolved to embrace the role of hydrothermal vent systems where disequilibrium pathways are naturally established by the inherently strong internal thermal and chemical gradients. Synthesis of simple organic monomers, for example, can be supported in these microenvironments via pH conditions that favor hydrogen-dependent redox processes similar to the CO_2 reducing acetyl-CoA biochemical pathway[40, 41]. But attainment of the high-level structure and function associated with RNA and DNA would have required that these organic precursors experience sufficient enrichment to initiate polymerization[42]. This poses a conundrum because the incredibly dilute concentrations of these compounds in the prebiotic ocean strongly favor hydrolytic decomposition over polymerization[43-45]. Biochemical processes overcome these limitations by following catalyzed pathways so that kinetics are no longer governed solely by proximity among active sites in reacting species, leading to interest in mineral surfaces (e.g., clays) that naturally provide a combination of surface adsorption[46] and catalytic activity[47]. This view is supported by evidence that montmorillonite substrates are able to catalyze synthesis of both polypeptides (chains of amino acids)[48] and RNA oligomers (chains of nucleotides)[49] from organic precursors. Clay surfaces also inhibit competitive hydrolysis of active groups, enable rapid formation of peptide bonds, shield adsorbed species against degradation, and facilitate homochiral selection[50-52]. A variety of minerals such as montmorillonite[53], apatite[54], quartz[55], and zeolites[48] have therefore been examined in connection with prebiotic polymerization.

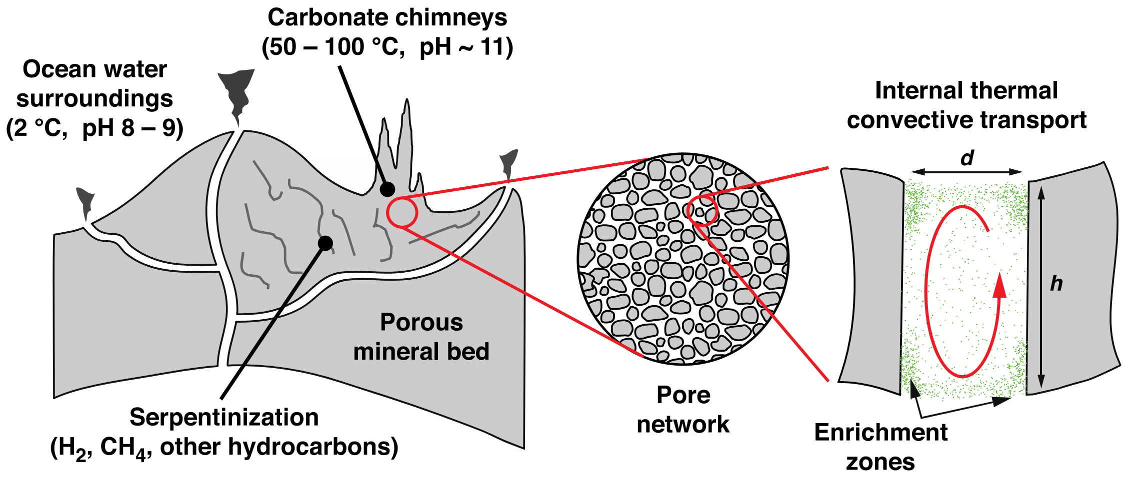

Figure 29: A hydrothermal conveyor based on chaotic thermal convection. Mineral formations near off-ridge hydrothermal vents lining the ocean floor contain embedded pore networks with microenvironments that impose thermal and geometric conditions robustly capable of sustaining internal convective flow fields. These flows display a rich spectrum of 3D chaotic trajectories that continually shuttle chemical species from the bulk fluid to targeted sites on the pore surfaces where they experience accelerated adsorption and enrichment. The highly alkaline surroundings in off-ridge vents also produce strong pH gradients conducive to prebiotic chemical synthesis.

Sub-sea hydrothermal vents

Hydrothermal microenvironments often embed these same catalytically active minerals including montmorillonite (e.g., Middle Valley vent, Juan de Fuca Ridge)[56], kalonite (e.g., submarine vents along the Guaymas Basin on the East Pacific Rise)[57] and apatite (e.g., submarine vents along the Pacific Margin of central Mexico)[58]. This chemical richness becomes further enhanced in the vicinity of volcanic vents (e.g., black smokers) that emit a hot, acidic effluent (400 °C, pH 2 – 3) rich in dissolved transition metals. But highly alkaline hydrothermal environments (pH 9 – 11) can also be established via geochemical serpentinization, yielding hydrogen rich surroundings at relatively moderate temperatures (150 – 200 °C). These unique characteristics, combined with the excess hydrogen's ability to exothermically reduce carbon dioxide into methane, have made alkaline vents (e.g., Lost City vent, mid-Atlantic ridge) particularly intriguing candidates to support chemical processes associated with emergence of life (Figure 29)[40, 59].

Hydrothermal mineral formations also contain intricate embedded pore networks[60, 61] with characteristic length scales ranging from µm to cm at aspect ratios (height (*h*) / diameter (*d*)) of 1 – 1,000 that establish a strong thermal driving force to initiate and sustain internal convective flows. These attributes have motivated previous efforts to explore the possibility that hydrothermal pore networks could function as molecular traps capable of concentrating molecules via the coupled action of laminar (2D) thermal convection and thermophoresis[62]. This trapping mechanism has been exploited experimentally to increase the probability of non-catalytic vesicular assembly[63] and polymerization[64], albeit within a relatively narrow window of hairline pore size scales (*d* ~ 100 µm). Emergence of unexpectedly complex 3D flow fields not captured by this laminar 2D picture has also been reported in microscale pore-like geometries[14]. These thermal instability driven flows, a subset of which exhibit chaotic advection, act over a much broader range of pore size scales extending far beyond the thermophoretic regime[65], raising the intriguing possibility that they could have functioned in a previously unappreciated way as highly efficient conveyors to achieve targeted surface enrichment of organic precursors.

Targeted enrichment

We examined this possibility by quantifying the interplay between thermal convective transport and surface adsorption in a pore-mimicking cylindrical Rayleigh Bénard system across a broad range of size scales representative of hydrothermal microenvironments in off-ridge vent systems. Under these conditions, the accessible states of fluid motion can be mapped in terms of the aspect ratio (h/d) and the dimensionless Rayleigh number ($Ra = [g\,\beta\,(T_2 - T_1)\,h^3] / \nu\,\alpha$, where β is the fluid's thermal expansion coefficient, g is gravitational acceleration, T_1 and T_2 are the temperatures of the top (cold) and bottom (hot) surfaces respectively, h and d are the height and diameter of the cylindrical "pore", α is the thermal diffusivity, and ν is the kinematic viscosity)[14]. Since surface adsorption of species present at dilute concentrations in the surrounding environment is predominantly governed by transport from the bulk fluid to the solid interface[66], we modeled the process via a liquid phase adsorption framework previously applied to describe prebiotic chemical synthesis on mineral adsorbates[43, 67]. Precursor molecules were assumed to be dispersed in water at 10^{-7} M and a vertical temperature gradient was imposed (bottom ~ 95 °C, top ~ 55 °C). An ensemble of 300 randomly distributed Lagrangian passive tracers were simulated in 3D during 5 min of flow, and the location where each trajectory penetrated a 50 μm adsorption boundary layer was recorded to obtain surface enrichment profiles.

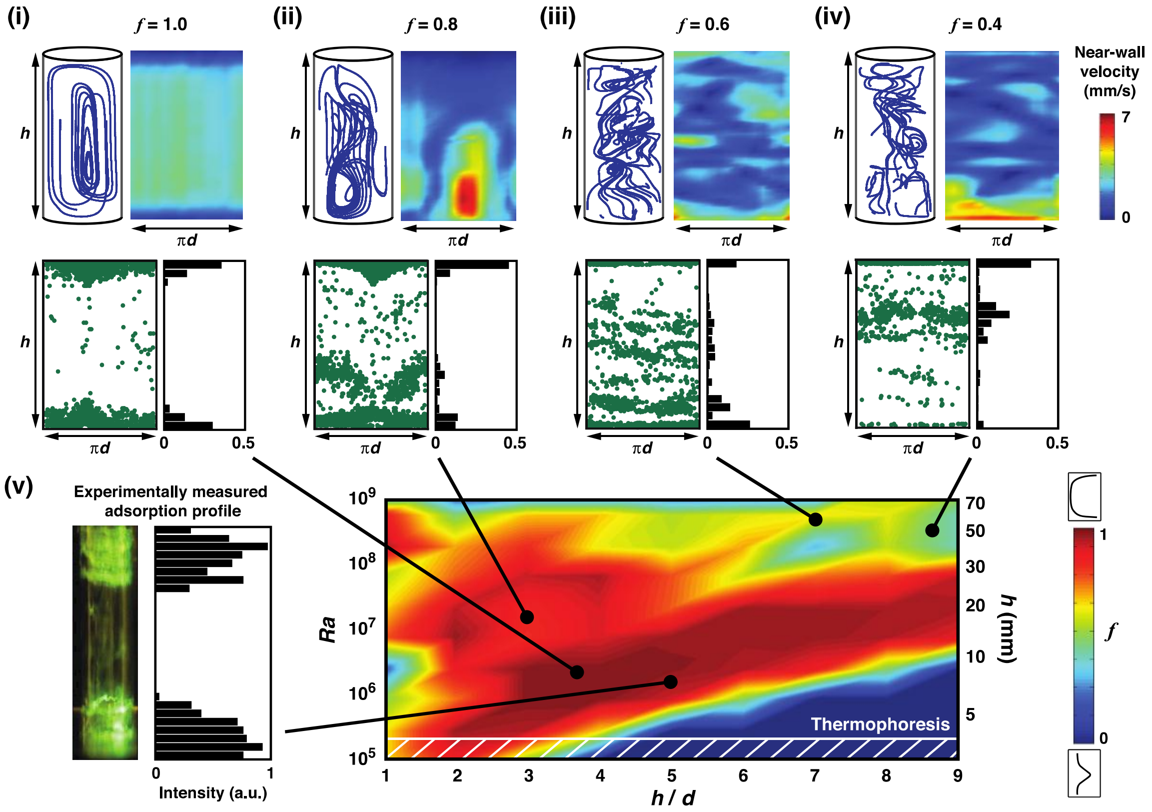

Figure 30: Targeted enrichment is evident by anisotropic surface adsorption profiles. Computational simulations enable the extent of targeted enrichment, quantified in terms of a focusing fraction f, to be parametrically plotted in terms of the Rayleigh number and aspect ratio. The top of the panels in (i) through (iv) depict representative flow trajectories (left) and velocity distributions within a near-wall boundary region (right). The corresponding sidewall adsorption profiles are depicted at the bottom of each panel (individual realizations (left) and vertical distribution histogram (right)). Results are presented for representative values of *f* ranging from 1.0 (anisotropic adsorption localized near the upper and lower surfaces) to 0.4 (uniformly dispersed adsorption over the sidewalls). An experimentally obtained adsorption profile (v) reveals localized accumulation of fluorescent carboxylated microspheres near the upper and lower surfaces of the cell, in agreement with the simulations ($Ra = 10^6$, $h/d = 5$). Conditions relevant to thermophoretic trapping are denoted at the bottom of the parametric plot. Pore geometries associated with the flow trajectories are not depicted to scale in order to facilitate comparison between them.

The anisotropy of each profile was quantified in terms of a focusing fraction *f* expressing the relative amount of surface adsorption localized near the upper and lower boundaries, enabling a parametric map to be constructed depicting the extent of targeted adsorption achievable across a broad range of pore geometries (Figure 30).

Our simulations reveal that highly focused enrichment (i.e., distribution profiles characterized by distinct bands near the upper and lower pore boundaries) is achievable over a wide spectrum of conditions ranging from periodic to chaotic advection (indicated by emergence of complex flow trajectories) [14]. The blue colored region near the bottom right corner of the map indicates conditions where the thermal driving force is not strong enough to initiate convective motion (i.e., molecular diffusion is the dominant transport mechanism). Periodic fluid trajectories are generated upon the onset of convective flow that promote strongly bimodal adsorption profiles (Figure 30, panel (i)). These profiles become distorted at higher *Ra* as the flow trajectories undergo a transition to chaos (Figure 30, panel (ii)), although preferential accumulation near the upper and lower pore boundaries is retained. A further transition to unsteady behavior (i.e., convective turbulence) occurs *Ra* is further increased ($Ra > 10^8$; flows remain inertially laminar with characteristic values of the Reynolds number in the vicinity of 1 ~ 500), leading to uniformly distributed adsorption profiles (Figure 30, panels (iii, iv)).

To confirm the role of the flow in generating targeted surface enrichment, we computed the velocity magnitude within a 750 µm layer adjacent to the sidewall surfaces, representing a characteristic molecular diffusion distance during the time scale of our simulations (upper right images in panels i – iv of Figure 30). The corresponding surface enrichment profiles (lower left images in panels i – iv of Figure 30) would be expected to directly map with regions of zero velocity if adsorption preferentially occurred where the near-wall flow is stagnant. But our simulations show that no consistent connection can be made between the near-wall flow velocity and the location of targeted enrichment, validating the flow's role in governing transport to the sidewalls. We experimentally verified the simulation predictions by coating the inner walls of cylindrical pore-mimicking flow chambers with bovine serum albumin (BSA). The chambers were filled with an aqueous suspension of fluorescently tagged 1-µm dia. carboxylated microspheres, enabling adsorption profiles to be inferred by mapping their surface attachment due to binding with BSA[68]. Not only did we observe nearly complete transport of the dispersed microspheres to the sidewalls upon application of a convective flow, the resulting surface fluorescence profiles display targeted enrichment within discrete bands near the top and bottom of the chamber (Figure 30, panel (v)). Taken together, these results suggest a robust driving force for focused surface adsorption under hydrothermally relevant conditions.

Surface reaction kinetic model

We expanded our 3D flow simulations to incorporate a coupled kinetic model that enabled us to track the time-resolved surface concentration of adsorbed species at the sidewall boundaries. These results closely resemble the response to a step input of first order; $C / C_{max} = (1 - \exp(- t / \tau))$, where C and C_{max} are the instantaneous and final equilibrium (i.e., corresponding to saturation of active sites) surface concentrations respectively, t is time, and τ is a time constant. We also determined time-resolved surface concentrations associated with purely diffusive transport by analytically solving the transient 2D diffusion equation in cylindrical coordinates (Appendix F). Time constants associated with convection (flow; τ_{conv}) and diffusion (no flow; τ_{diff}) could then be extracted from these data. We evaluated our kinetic model across the same ensemble of flow conditions employed in our analysis of steady-state adsorption to generate the parametric map shown in Figure 31. These results reveal that pores displaying the fastest adsorption kinetics are characterized by the most disordered flow fields (Figure 31, panel (i)), and that the process progressively becomes slower as the flow trajectories recover periodicity (Figure 31, panels (ii) and (iii)). Comparison with Fig. 2 therefore suggests an intermediate regime (i.e., $1 < h/d < 4$) spanning a broad parameter space (i.e., multiple orders of magnitude in pore size and thermal gradient) where targeted enrichment and adsorption kinetics can be simultaneously enhanced.

In situ measurement of surface reaction kinetics

Surface reactions are challenging to dynamically probe *in situ* at pore-like size scales, with the majority of experimental approaches focusing on characterization by periodic removal and analysis of reaction products (with limited temporal resolution) or by fluorescence-based methods (with limited and often nonlinear dynamic range). We overcame these limitations by introducing an electrochemically-based technique whereby the upper surfaces of pore-mimicking cylindrical cells were patterned with addressable 100 nm thick microfabricated copper electrodes (Figure 32 a). In this way, surface-mediated reactions within a pore can be represented by electrochemical dissolution of the electrodes, an easily observable process that occurs slowly at neutral pH but becomes rapid in alkaline environments (Figure 32 b).

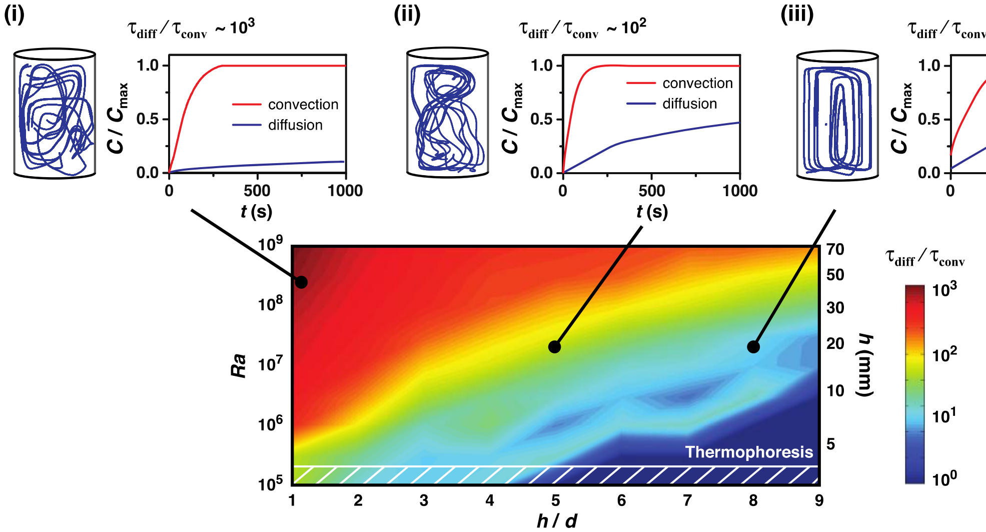

Figure 31: Thermal convective transport greatly accelerates surface adsorption kinetics. Computational simulations incorporating a kinetic surface adsorption model enable the time-resolved surface accumulation of chemical species on the pore sidewalls to be quantified under conditions relevant to the prebiotic environment. A parametric plot reveals that adsorption kinetics are enhanced by up to 1,000 fold in the presence of thermal convection, and this enhancement correlates with the onset of chaotic advection in the corresponding flow trajectories. Conditions relevant to thermophoretic trapping are denoted at the bottom of the parametric plot. Pore geometries associated with the flow trajectories are not depicted to scale in order to facilitate comparison between them.

These conditions mirror those encountered in alkaline off-ridge vent environments[69] within mineral formations embedding surface charge densities capable of generating electrostatic potentials that strongly favor biomolecular adsorption[70].Our electrode dissolution experiments therefore offer a versatile *in situ* platform to explore the role of thermal convection in prebiotic scenarios where surface adsorption and catalysis depends on an interplay among pH, surface charge, and the local ionic environment[71]. The electrode-based format also provides considerable flexibility to impose specific surface chemistries via appropriate surface functionalization.

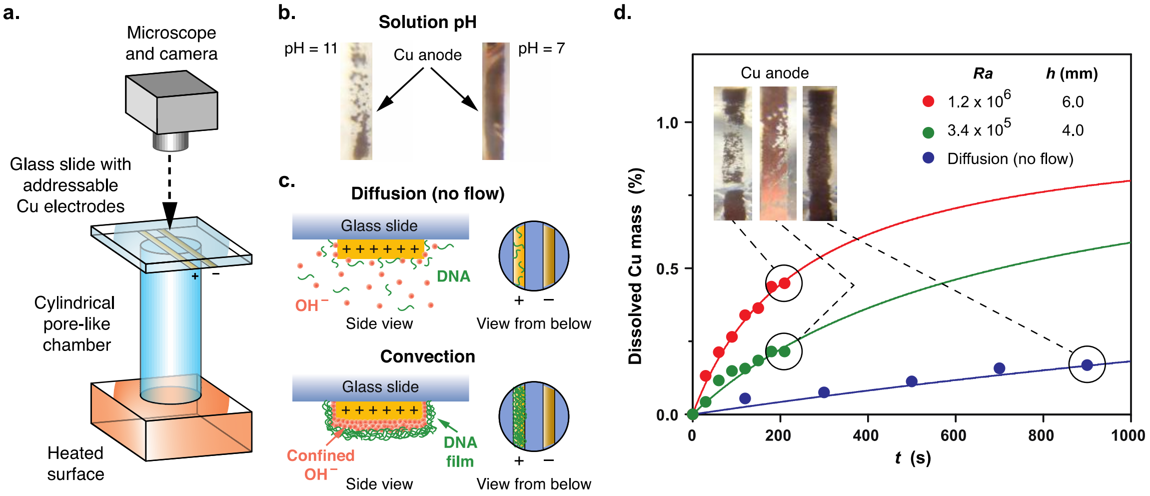

Figure 32: An *in situ* probe reveals dramatically accelerated surface reaction kinetics via chaotic convective transport. (a) Addressable Cu electrodes are patterned on a glass substrate affixed to the top surface of a pore-mimicking cylindrical flow cell enabling electrochemical dissolution to be viewed from above (drawing not to scale). (b) Anodic dissolution occurs slowly at neutral pH, but is accelerated under alkaline conditions (images of the anode taken after a 3 V potential was applied for 1 min, no convective flow imposed). (c) In the absence of convection (above), the anode surface is not visibly changed when a 3 V potential is applied in an aqueous solution containing a 100 base pair double-stranded DNA ladder (1 µg/mL, pH = 7). But dissolution progresses rapidly (below) when a convective flow is imposed that continuously transports negatively charged DNA toward the anode where the electrophoretically compacted film increases the local pH, favoring Cu dissolution. (d) Video recordings of the electrodes were analyzed to quantify anodic dissolution at the upper pore surface as a function of time in different pore geometries (symbols). These data were then used as inputs to a kinetic predictive model (lines). Insets show images of the anode corresponding to each condition. Scale: all electrodes are 500 µm wide

Pore mimicking test cells were loaded with an aqueous solution containing a mixture of double-stranded DNA fragments with lengths in the 100 – 1,000 base pair range, and electrode dimensions (500 µm wide, 1 mm inter-electrode spacing) were selected such that small potentials (3 V) could generate electric fields high enough to electrophoretically trap the negatively charged DNA at the anode[72, 73]. The resulting DNA film imposes a barrier against transport of electrochemically generated OH^- ions into the surroundings, leading to a local increase in pH that acts to accelerate the rate of copper dissolution (Figure 32 c)[74]. The thermal convective flow's ability to mediate surface reaction kinetics can then be monitored *in situ* by analyzing video recordings of the electrodes to quantify the dissolved mass of Cu as a function of time. These experiments reveal that dissolution progresses slowly under quiescent conditions but becomes dramatically accelerated when a convective flow is established (Figure 32 d), owing to transport of DNA from the bulk solution to the anode surface where it accumulates due to electrophoretic confinement. A kinetic rate constant was obtained by fitting data at $Ra = 1.2 \times 10^6$, $h = 6$ mm yielding an order of magnitude enhancement under convective flow (experimental conditions producing much faster Cu dissolution could easily be attained, but the applied potential was quickly disrupted making kinetics difficult to quantify). This rate constant was subsequently applied to generate electrode dissolution predictions under other conditions in Figure 32 d, yielding time-dependent trends that closely mirror the sidewall surface adsorption kinetics in Figure 31 and validate our analysis in terms of a framework chiefly governed by transport from the bulk to the solid interface.

The role of chaotic flows in enhancing molecular transport

Collective insights gained from our experiments and simulations make it possible to elucidate the interplay between the bulk flow field, transport of material to the surface, and subsequent reactions. First, the results in Figure 30 indicate that flow states generating periodic trajectories most effectively achieve focused adsorption profiles, reflecting sustained circulation between the upper and lower boundaries achieved in both the periodic and chaotic regimes (Figure 30, panels (i) and (ii)). Disordered flows also effectively transport material to the surface, however localization is disrupted (Figure 30, panels (iii) and (iv)). The results in Figure 31, however, reveal that accelerated transport to the surface is favored in disordered flow states owing to their strong lateral velocity component (Figure 31, panel (i)), whereas periodic trajectories display slower kinetics (Figure 31, panels (ii) and (iii)). Comparing these results suggests two competing effects: circulatory flow states that display some degree of periodicity produce localized surface adsorption but accumulation occurs slowly, whereas disordered flow states yield the fastest surface accumulation but adsorption is not localized.

To understand the interplay between these effects, we defined a figure of merit consisting of the product $f \cdot (\tau_{diff} / \tau_{conv})$. This parameter, plotted in Figure 33 a, reveals a zone at intermediate Ra and h / d where simultaneous targeted and accelerated adsorption is achievable.

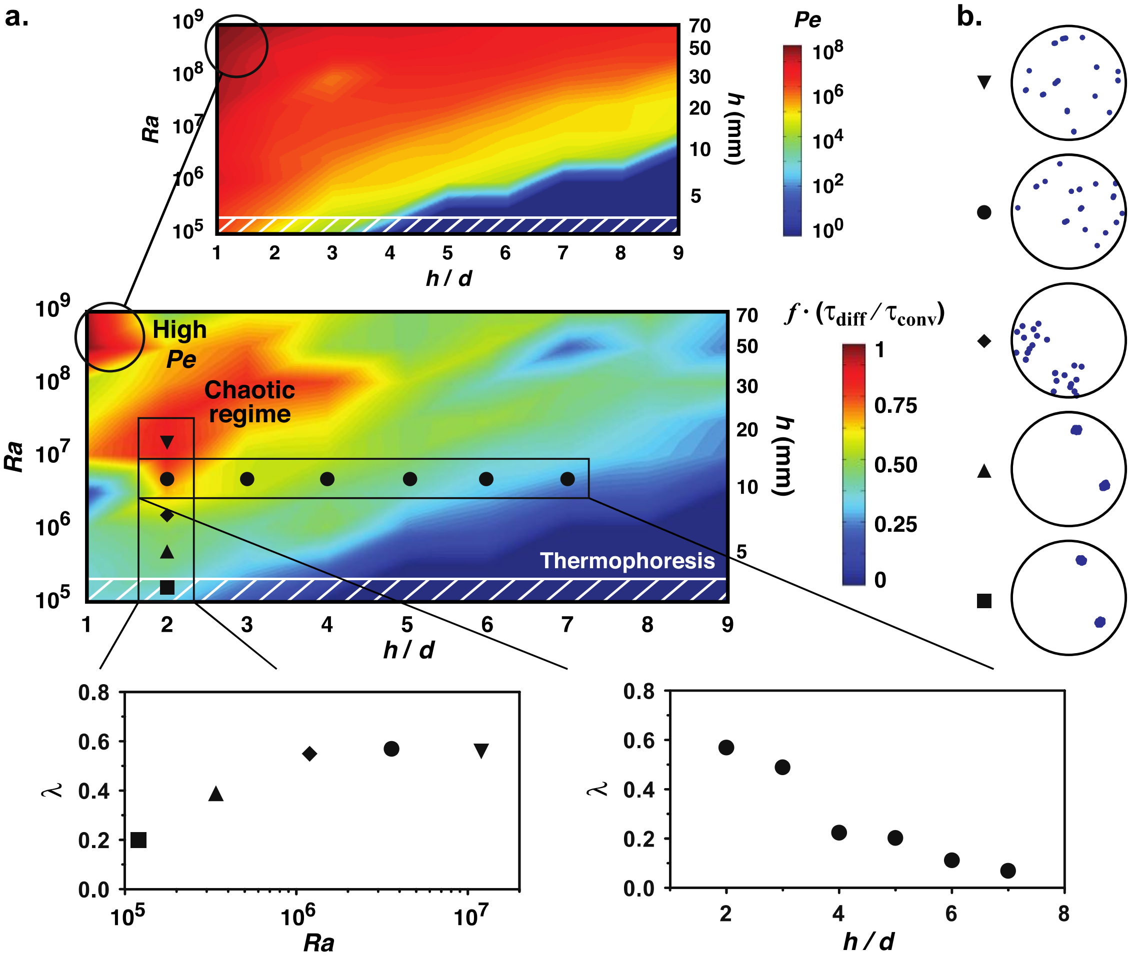

Figure 33: Chaotic thermal convection simultaneously delivers targeted and accelerated surface accumulation under hydrothermally relevant conditions. (a) A parametric plot of the figure of merit *f* (τ_{diff} / τ_{conv}) reveals a regime at intermediate *Ra* and *h* / *d* where simultaneous targeted and accelerated surface enrichment is achievable. This "sweet spot", spanning orders of magnitude in thermal and geometric conditions, is characterized by chaotic flow trajectories. Phenomena in this regime are not solely explained by high values of the Péclet number *Pe*, which monotonically increases with *Ra* (above). The strength of the chaotic component is evident by increased values of the Lyapunov exponent λ, as compared with states at lower *Ra* or higher *h* / *d* where periodic trajectories predominate (below). (b) Mid-plane Poincaré sections at *h* / *d* = 2 confirm a transition away from closed flow trajectories toward disordered states in the chaotic regime (symbols at the left of each image map to the corresponding states in (a)).

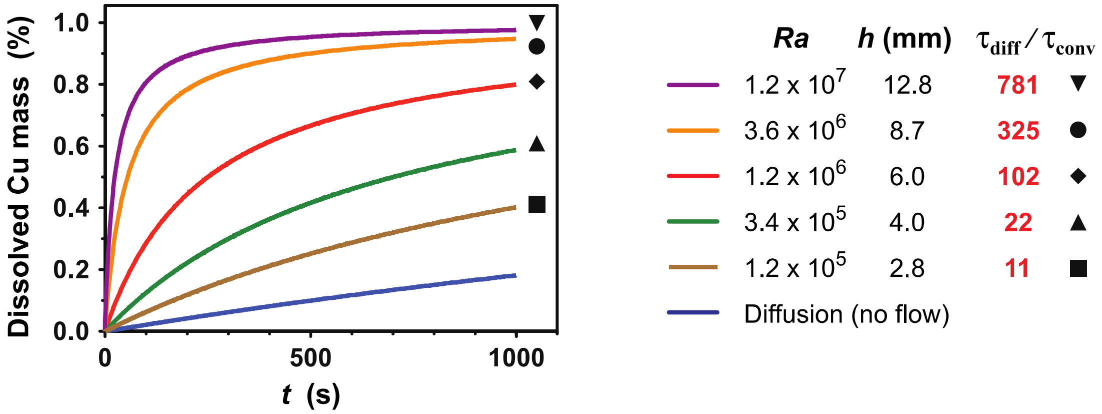

Figure 34: Kinetic model predictions of electrode dissolution confirm that the fastest reaction rates occur in the chaotic regime. Symbols coincide with those in Figure 33 (a). The predicted values of τ_{diff} / τ_{conv} are consistent with the parametric map in Figure 31, validating our analysis in terms of a framework chiefly governed by transport from the bulk to the solid interface.

The desirable features of flow states in this regime can be understood by recalling that targeted accumulation occurs when periodic circulatory flows are established within the pore (Figure 30), and that the process is accelerated in flows displaying a strong laterally-directed component (Figure 31). Chaotic flow states, inherently embedding quasi-periodic trajectories with a lateral (albeit not disordered) component, naturally fulfill both of these criteria. We validated this hypothesis by using our 3D simulations to quantify the chaotic nature of these flow states in terms of their Lyapunov exponent—a parameter representing the rate of divergence experienced by initially neighboring flow trajectories. When superimposed over the parametric plot in Figure 33 a, it becomes evident that the figure of merit “sweet spot” (the red colored zone) directly coincides with the chaotic flow regime. These flow states enable the global periodicity desirable for targeted accumulation to be retained, but because the corresponding flow trajectories are not closed (i.e., following quasi-periodic limit cycles evident by the Poincaré plots in Figure 33 b) they also provide a lateral component that accelerates transport from the bulk to the surface. We used our kinetic model to compute time constants corresponding to the same range of flow states at $h / d = 2$ where Lyapunov exponents were determined (Figure 33 b, symbols are coded to match the conditions in panel (a)). These data reveal that chaotic thermal convection generates nearly a thousand fold enhancement in $\tau_{diff} / \tau_{conv}$. Chaos therefore make simultaneous targeting and accelerated accumulation uniquely possible.

Comparison with thermophoretic trapping

To connect chaotic thermal convection introduced here with previous literature exploring thermophoretic trapping[62, 64], we first note that cavities formed within the cracks of mineral deposits[75-77] and voids encountered between pillow lavas[78] display characteristic size scales (mm to cm) that are closely aligned with the convective regime (thermophoretic effects predominate in hairline pores with $d \sim 100$ µm or less[64], indicated by the narrow hashed region at the bottom of the parametric plots in Figure 30 and Figure 31). Convective transport therefore vastly broadens the range of geometries capable of supporting chemical synthesis to more fully encompass pore size distributions encountered in hydrothermally relevant mineral formations[60, 61]. It is also important to note that previous investigations of bulk reactions under thermophoretic trapping have implicitly assumed an infinite source of chemical precursors (i.e., “open top” pores) that imposes no inherent upper bound on achievable enrichment. We have not invoked this assumption in our analysis because our aim is to consider surface catalyzed processes relevant to the prebiotic scenario (although we could do so and generate comparable enrichment levels).

Another distinguishing feature of our work is that previous studies considered only bulk polymerization where accelerated kinetics are achieved solely by bringing reactive functional groups into close physical proximity (e.g., 100 μm diameter pores of length 5 cm require local monomer concentrations in excess of 10^{-3} moles/m^3 to synthesize oligomers long enough for self-replication (200-mer)[64]). Surface catalyzed processes, on the other hand, eliminate the need to attain these extreme bulk species concentrations because (i) the critical enrichment level is governed by saturation of catalytically active surface sites rather than bulk accumulation, and (ii) catalytic pathways inherently reduce required species concentrations by several orders of magnitude (e.g., surface concentrations of order 10^{-6} moles/m^2 are sufficient to sustain catalytic condensation of 40-50-mer polymer chains in similar sized pores[79]). Additionally, surface catalysis delivers more sophisticated chemical selectivity (e.g., clays such as montmorillonite have been shown to favor homo-chiral selection of nucleotides, a critical step in the formation of selective longer biomolecules[51, 52]). The ability of clay surfaces to simultaneously bring reacting species into close proximity and orient them into favorable positions has also been shown to increase the rate of condensation by a thousand fold[80]. The size scales and boundary conditions associated with thermophoretic trapping may therefore make it best suited to describe phenomena occurring in hairline cracks near the surfaces of hydrothermal formations, whereas chaotic thermal convection may predominate throughout the bulk interior spaces.

Computational modeling of hydrothermal pore system

Geometries for 3D simulation of convective flow fields inside micro-scale cylindrical pores were created and meshed using Gambit (ANSYS). Non uniform hexahedral grids were generated and grid independent solution was verified. The finite volume solver of STAR-CCM+ (CD-adapco) was used to simultaneously evaluate the continuity, 3D Navier-Stokes, and energy conservation equations. The buoyancy driving force was incorporated via the Boussinesq approximation subject to adiabatic sidewalls and isothermal conditions at the upper and lower boundaries. Fluid with properties of water were applied and evaluated at the average of the top and bottom surface temperatures. Computed steady-state velocity and temperature fields were analyzed using Tecplot and Matlab. Bimodality of the sidewall surface adsorption distributions was expressed in terms of a focusing fraction f defined as

$$f = \frac{\int_{0}^{0.1h} Pdl + \int_{0.9h}^{h} Pdl}{\int_{0}^{h} Pdl} \qquad [4.1]$$

where P is an adsorption distribution function and h is the pore height. The fluid elements were tracked as the pierced the pore boundary (Figure 35).

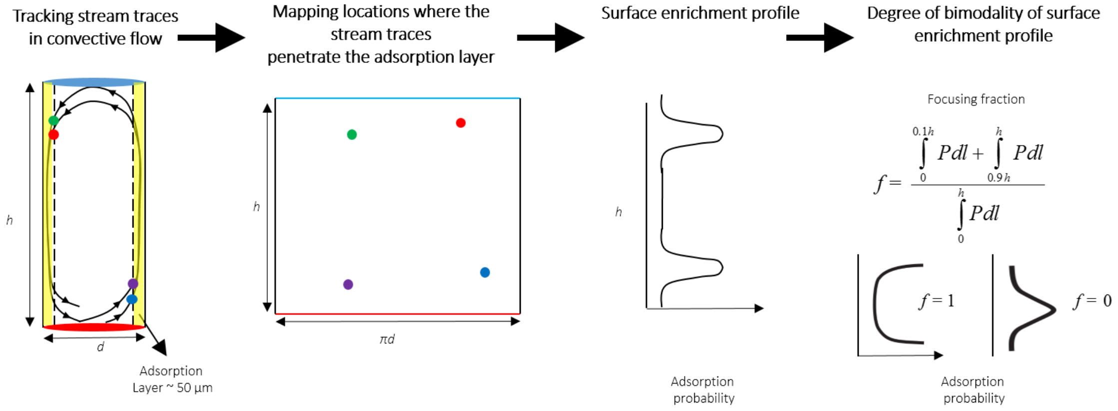

Figure 35: Construction of pore boundary adsorption profile. The fluid elements are tracked as they are converted within the pore and the locations where the stream traces penetrate the boundary layer are mapped. Subsequently an adsorption profile is constructed to quantify the focusing fraction.

A 50 µm mesh size was chosen as representative of the surface roughness (a conservative upper bound estimate). The computational domain of the cylindrical pore was divided into two sections, a central domain and a thin boundary domain (Figure 36 a). The grid in the boundary domain was made finer to accurately resolve the near-wall flow trajectories and adsorption profile, transitioning toward a coarser grid near the pore center. We verified that the adsorption profiles and focusing fractions obtained were unaltered by decreasing the boundary thickness to small as 1 µm (Figure 36 b). These results validate our choice of adsorption layer thickness and ensure that our key results are not sensitively dependent on simulation parameters.

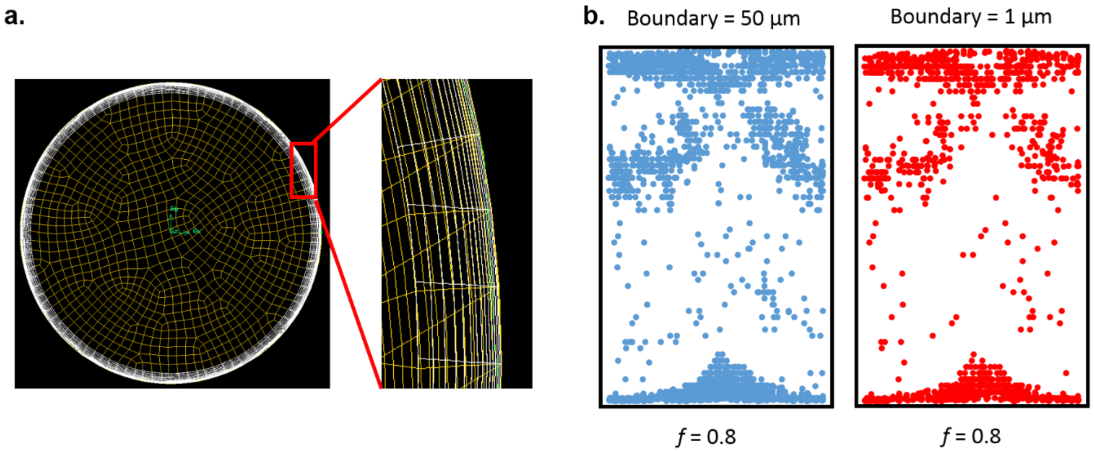

Figure 36: Grid independence on pore tracking profile. (a) Computational domain of the cylindrical pore geometry. (b) Adsorption profiles and focusing fractions obtained at two different boundary thicknesses.

Adsorption rates at the pore sidewalls Ra were represented by coupling the flow equations with a first-order kinetic model.

$$A \underset{k_d}{\overset{k_a}{\leftrightarrow}} B \qquad\qquad R_a = k_a[A]\left(1-\frac{[B]}{[A]_o}\right) \qquad\qquad R_d = k_d(T)[B] \qquad\qquad [4.2]$$

Here $[A]$ represents the concentration of organic monomers in the solution, $[B]$ is the concentration of the organic monomers on the pore surface, k_a is the rate of adsorption and k_d is the rate of desorption (characteristic values of k_a = 100 s^{-1} and k_d = 1 s^{-1} were selected; actual values depend on the specific surface area available for adsorption, which can vary by four orders of magnitude in natural environments from 0.025 m^2/g (quartz) to 750 m^2/g (montmorillonite))[66]. The adsorbing species was assumed to be dispersed in water at 10^{-7} M (typical concentrations of nucleotide and amino acid precursors in the primitive ocean are estimated to be ~ 10^{-6} – 10^{-9} M)[59, 64].

A simplified mass action kinetic model was also developed to capture electrochemical dissolution of the copper anode via the following coupled mechanism[81]

$$\begin{aligned} &2\mathrm{Cu} + \mathrm{H_2O} \overset{k}{\rightarrow} \mathrm{Cu_2O} + \mathrm{H_2} \\ &\mathrm{Cu_2O} + \mathrm{H_2O} \rightarrow \mathrm{Cu^{2+}} + 2\mathrm{OH^-} \end{aligned} \qquad [4.3]$$

where the dissolution rate is given by R = *k*[Cu]2 [H2O]. The role of convective DNA transport from the bulk in increasing the local surface pH via electrophoretic confinement was incorporated by introducing a rate constant proportional to the time-dependent local DNA concentration obtained in the simulation ($k = k_0$[DNA], where k_0 = 10 [M3 s]$^{-1}$ was selected based on fitting data at *Ra* = 1.2 x 10^6, h = 6 mm in Figure 32 d). The copper electrode was modeled as a 100 nm thick rectangular volume (500 µm x 3 mm surface area) positioned on the upper surface of the cylindrical pore-like volume. The bottom surface temperature was maintained at 80 °C and the initial bulk DNA concentration was 1 µg/mL matching experiment conditions. Both convective and diffusive (T = const. = 300 K) transport were simulated.

BSA adsorption experiments

Adsorption studies were performed using pore-mimicking transparent cylindrical acrylic cells (1.5 mm dia.) mounted in an apparatus that permitted the upper and lower surface temperatures to be independently controlled to impose a vertical gradient[65, 82]. The inner walls of each cell were coated with bovine serum albumin (BSA; cat. no. A2153; Sigma-Aldrich) by first sealing the lower surface using thin aluminum tape (cat. no. PCRAS-200; Axygen, Inc.) and rinsing the interior with water. A 10 mg/ml aqueous BSA solution was then loaded, incubated for 5 min, and removed. Coating stability was verified using FITC-BSA (cat. no. A9771, Sigma-Aldrich) which revealed no change in the interior surface fluorescence before and after convective flow. A 10x aqueous dilution of 1 µm dia. carboxylate-modified polystyrene microspheres (cat. no. L4655; Sigma Aldrich) was then pipetted into the cell and the top surface was sealed with aluminum tape. The filled cells were loaded into the convective apparatus after preheating the upper and lower surfaces to desired temperatures (top 55 °C; bottom 95 °C). The heaters were switched off after 15 min of convective flow, after which the cells were removed and allowed to cool under ambient conditions. The sealing tape was removed and the remaining liquid was dried by placing the cells in a 50 °C oven for 10 min. Adsorption profiles were imaged using an Olympus SZX-12 fluorescence microscope with GFP filter set, and the corresponding intensity data were extracted using ImageJ software.

Copper dissolution experiments

Copper film coatings (100 nm thick) were sputter deposited on glass microscope slides (cat. no. 12-550-A3, Fisher). Electrodes (500 µm wide, 1 mm inter-electrode spacing) were patterned on the copper coated slides using dry transfer film (Press-n-Peel Blue, Techniks, Inc.), followed by immersion for ~ 1 min in gold etchant (Transene) after which the remaining dry transfer film was stripped using acetone. Patterned glass slides were affixed to the upper surface of the cylindrical acrylic cells using cyanoacrylate adhesive, and electrical connections were made using conductive tape (xyz-axis Electrically Conductive Tape, 3M). Potentials were applied using a DC power supply

(E3612A, HP/Agilent). Electrode dissolution experiments were carried out in aqueous solutions of NaOH (pH = 11) and a 1 μg/mL 100 bp double-stranded DNA ladder at neutral pH (cat no. 170-8202, Bio-Rad). The bottom surface of the cells were sealed with aluminum tape and the assembly was heated from below using the same apparatus described above. Video recordings of the electrode dissolution process were acquired, converted to image sequences, and analyzed using ImageJ software. Dissolution was quantified within a region of interest overlaying the anode surface by converting the images to 8 bit grayscale and applying a black/white threshold of 160 out of 255. The total white pixel count was then calculated to determine the mass of copper dissolved as a function of time (Figure 37).

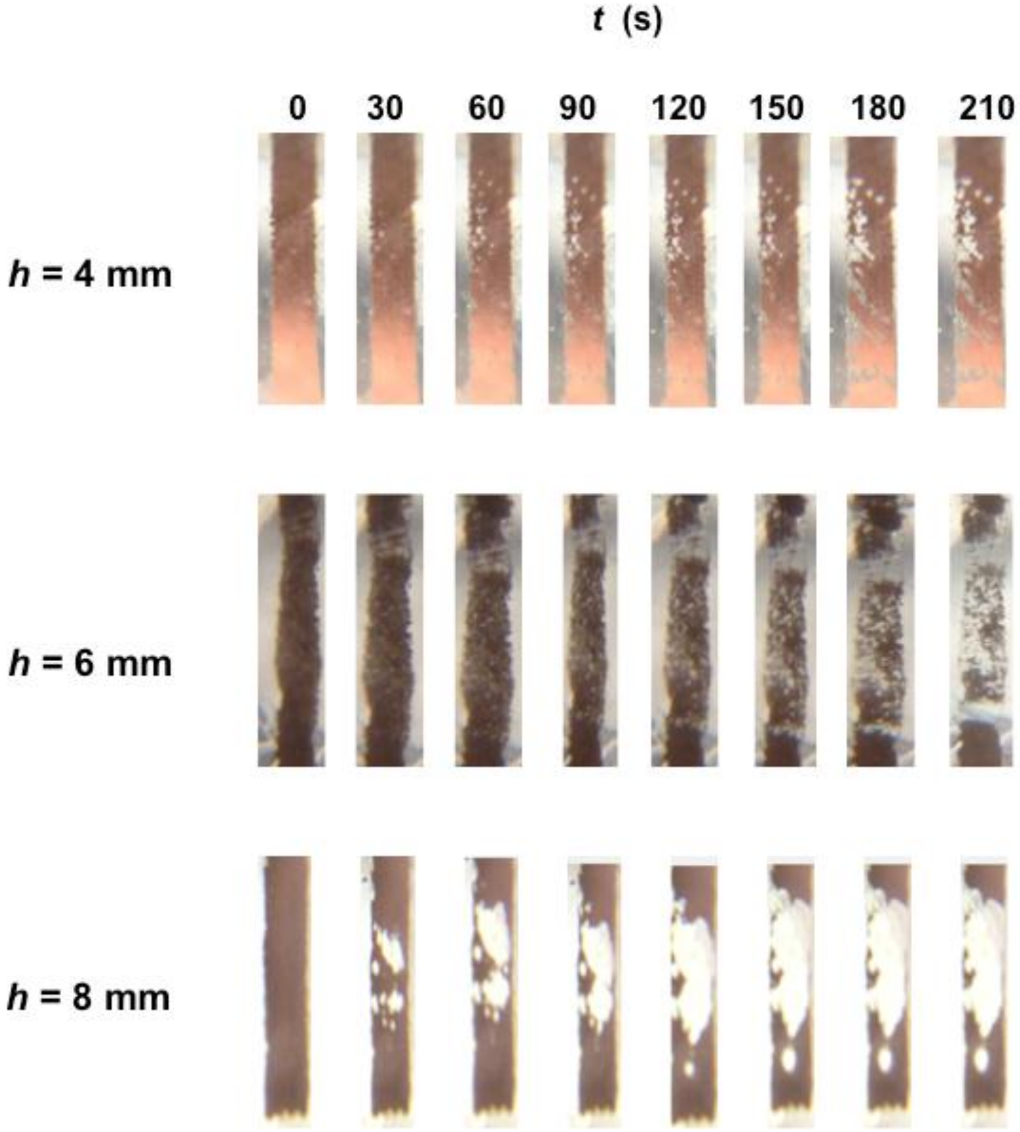

Figure 37: Time sequence of images depicting electrochemical dissolution of 500 µm-wide Cu electrodes under application of a 3 V potential in cylindrical pore-like micro-cavities. An aqueous solution containing 1 µg/mL of a 100 base pair double-stranded DNA ladder is subjected to a convective flow by heating the lower surface of the pore to 80 °C. The chaotic convective flow accelerates anodic dissolution in all cases (data are shown for three different values of cavity height h with aspect ratio held constant at h/d = 2). At h = 8 mm the convective flow accelerates dissolution to such a degree that large sections of the electrode are removed, leaving an open circuit that prematurely arrests further dissolution.

Concentration of precursor molecules

Determining the concentration of autotrophically generated organic monomers within hydrothermal microenvironments is challenging. Based upon knowledge of production and consumption rates and prebiotic concentrations of carbon and other available substrates (CO_2, CO, NO_3, phosphate, methane etc.), it has been estimated that corresponding concentrations of organic monomers could not be more than $O(10^{-3}$ M)[83]. Similar estimates suggest amino acid concentrations of $O(10^{-7}$ M)[84]. More recent studies have suggested that maximum organic monomer concentrations would be in the millimolar range[59, 85]. Taking all these estimates into account, we assumed precursor molecules to be dispersed in water at a concentration of 10^{-7} M.

Characterization of the chaotic flow field

Although the dynamical system representing the thermal convective flow field is at steady state, it is of interest to quantify its chaotic characteristics by analyzing trajectories followed by individual fluid elements. Descriptors of chaotic phenomena generally seek to capture divergence from periodicity, and various methods are available to extract this information (e.g., Lyapunov exponent, correlation dimension, Kolmogorov-Sinia (K-S) entropy, fractal dimension, probability density of stretching, and Poincare sections)[7-9]. We quantified the chaotic nature of the flow fields in our hydrothermal pore mimicking systems by calculating the Lyapunov exponent (λ), a parameter expressing the rate of exponential divergence experienced by nearby trajectories that is frequently used to quantify mixing and chaotic transport in fluids.

The steady-state 3D velocity field solutions we obtained computationally were analyzed to perform Lagrangian tracking of 300 randomly distributed flow trajectories originating from the mid-horizontal plane of the cylindrical pore domains for a period of 5 min. Each fluid element was paired with its initially nearest neighbor, and the coordinates of the paired system were integrated to yield a time series representation of their separation distance. The finite time Lyapunov exponent was then calculated as follows, with the separation distance being normalized after each time step.

$$\lambda = \frac{1}{n\Delta t}\sum_{n=1}^{n=T/\Delta t} ln\left[\frac{d\left(\left(n+1\right)\Delta t\right)}{d\left(n\Delta t\right)}\right] \qquad [4.4]$$

Here Δt is the time step, T is the total time the fluid elements are tracked, and d is the separation distance between the pair of fluid elements.

Initial separation distances and the time steps were independently varied to determine their optimum values. The Lyapunov exponent values should, in principle, only depend on initial and boundary conditions of the system and should remain independent of parameters like time step of integration (Δt) and initial separation distance between neighboring trajectories. We performed a sensitivity analysis and determined that time step values smaller than 0.25 s and initial separation distances smaller than $d/50$ (d is the pore diameter) did not alter the computed λ value. These optimized parameters was then applied toward subsequent analysis of all fluid elements originating from the mid horizontal plane to generate a spectrum of λ values. The maximum value of λ obtained from this spectrum was taken as a metric to quantify chaotic strength flow field. Pores with aspect ratios of $h/d < 5$ display high λ values over a wide pore size range, confirming chaotic phenomena under these conditions. Values of λ decrease at higher aspect ratios where more ordered periodic flows prevail.

Conclusion

Our results point to chaotic thermal convection as a robust mechanism to explain emergence of complex bio-macromolecules from dilute organic precursors in the prebiotic milieu—a key unanswered question in the origin of life. While the ability of these flow phenomena to catalyze bulk homogeneous reactions has been established[3], their potential to tunably mediate chemical activity at the bounding surfaces has not been previously considered. This feature is particularly important in prebiotic scenarios involving coordinated surface adsorption and detachment mechanisms[86, 87]. We also remark that a diverse array of processes beyond prebiotic biochemistry can be catalyzed in hydrothermal microenvironments. Submarine igneous formations such as basalt lavas and ultramafic intrusions of the kind that host hydrothermal convective systems[40] play a key role in geothermal conversion of CO_2 into stable carbonates[88] and partial reduction to formate, carbon monoxide, and methane. These reactions are accelerated within the pores of hydrothermal formations[78], suggesting a compelling role for the thermal convective phenomena described here in governing transport and reaction of CO_2 along pathways not captured in existing climate models.

CHAPTER V

PARTICLE RESUSPENSION MODELING OF IRREGULAR PARTICLES AND SURFACES AT ALL SEPARATIONS[*]

Introduction

The phenomenon of submicron particle attachment and detachment on surfaces holds significance in many fields. Resuspended contaminants such as bioaerosols[89], aeroallergens[90], radionuclides, and carcinogens[91] have been shown to provoke adverse environmental and health effects. Resuspension studies are also important in determining the reliability of the silicon circuits in the fabrication of semiconductor microelectronic device[92] and the aerosolization of pharmaceutical powders in dry powder inhalers[93]. Among many aspects of resuspension modeling, a dominant concern is the accurate description and formulation of the van der Waals (vdW) dispersion interactions between the particle and the substrate. Such interaction between neutral bodies at nano and micro scale holds significance in various scientific fields such as adhesion, wetting, adsorption, colloidal phase equilibrium, collision rates, rheological properties and interfacial phenomena, thus raising the bars on the accurate predictive capabilities of the current description of vdW interactions.

Recent works describing the interaction energy of particles with surfaces for resuspension modeling are based upon the Hamaker's approach, i.e. the summing the pair-

---

[*] Reprinted with permission from "Computations of Lifshitz–van der Waals interaction energies between irregular particles and surfaces at all separations for resuspension modeling" A. Priye and W. H. Marlow, 2013, *Journal of Physics D: Applied Physics*, 425306, Copyright 2013 by IOP Science.

wise fluctuating dipolar interactions in the molecules comprising both bodies. Here we show that this leads to an error in the estimation of the interaction energy and more importantly for resuspension calculation, errors in the interaction force when compared with the results incorporating the Lifshitz many body formulation and retardation effects. We address these issues by (i) developing a novel computational method to approximate the retarded Lifshitz interactions and (ii) applying this formulation to estimate the van der Waals adhesion between macroscopic bodies of arbitrary shapes such as rough surfaces and particles of various shapes.

Hamaker two body interaction

The origin of the atomic vdW interaction is the zero-point and thermal fluctuations in polarization of multipoles in atoms and can be calculated using the time independent perturbation of the wave-function of a single atom due to the presence of the second atom[94, 95]. The original treatment (also known as the Hamaker's formulation) of vdW interaction between macroscopic bodies relies on the pairwise (two body) sum of all such atomic interactions within them[96, 97]. Following Hamaker's approach for calculating these interactions results in separation of the functional form into a dependence on the system's geometric part and a material dependent constant, known as Hamaker's constant[98]. The Hamaker constant is used widely owing to its simple implementation and computational convenience and has been determined for a large number of materials [99]. However, this method suffers from several drawbacks. Firstly, the quasi static approximation which assumes that the polarization of the first molecule instantaneously polarizes the second molecule becomes inaccurate at large distances as a consequence of finite propagation speed of the radiation from the electromagnetic fluctuations[100], also termed the “retardation” of the interaction. Secondly, the internal states of two interacting molecules are modified by the presence of other neighboring molecules making the two-body formulation imprecise for the computation of the total interaction energy for condensed media (Figure 38). A third deficiency in the sum-on-pairs interaction of Hamaker is its neglect of collective electromagnetic modes characteristic of the size and geometries of the interacting bodies, in addition to their compositions.

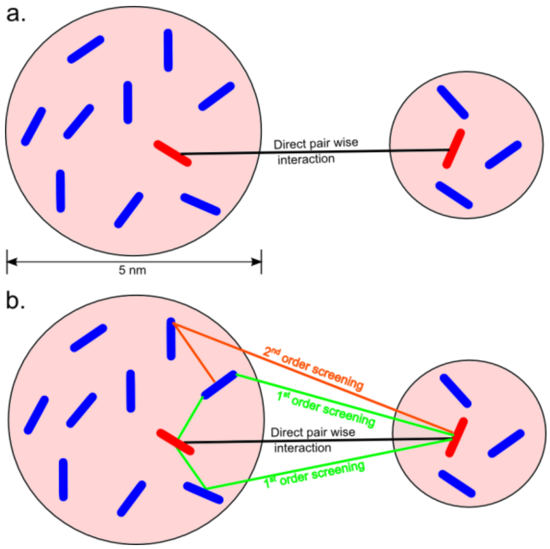

Figure 38: Hamaker two body and Lifshitz continuum interactions. (a) Hamaker's pair wise summation technique where the presence of other molecules does not affect paired interactions. (b) Lifshitz many body interaction takes into account both the direct and indirect (screened) interactions providing a more accurate calculation procedure.

Lifshitz theory of interaction: a continuum formulation

The correct treatment of such interaction lies in the continuum theory of dispersion forces (Lifshitz theory) which uses advanced statistical mechanics and quantum field theory to determine the interaction between two real dielectric half spaces treating the system as a continuum[101, 102]. The first direct measurements of such dispersion interaction between macroscopic bodies were performed by Derjaguin [103] and Kitchener[104]. More elegant experiments[105-114] have further tested and verified the Lifshitz theory to higher accuracy.

The Lifshitz theory of vdW interactions may be derived by use of the fluctuation dissipation theorem[115] which relates the dissipative properties of the material to the resulting electromagnetic fluctuations at equilibrium through the material's dielectric constant. Lifshitz theory was originally solved for interaction between two half spaces. Following the same formulation, analytic solutions for interactions between various simple geometrical setups have been derived[115]. Previous attempts of quantifying vdW interactions between curved surfaces relied on Derjaguin approximation[116] (also known as proximity force approximation) which relates the interaction energy between two curved surfaces to the interaction between planar geometries[117, 118]. However, the proximity force approximation is only accurate in the near contact region and it cannot be used to calculate interaction energies between arbitrary geometries. Other formulations tend to impose the pair wise summation of the Casmir-Polder retarded interactions[119] but like Hamaker's formulation it employs the two body molecular interactions. There have been other recent attempts to compute the many body interaction between arbitrary geometries using various mathematically involved techniques such as multiple scattering methods[120] and path integral formulation[121] which might not be readily amenable to calculation at all separation distances. Our formulation goes well beyond these methods and overcomes these limitations by numerically computing the pairwise sum of the many body Lifshitz interactions between arbitrary geometries to a good approximation at all separation distances.

We are interested in the Lifshitz interaction between two spheres[122-124] for reasons that will be apparent later. The many-body vdW interactions between two spheres (from here on called Lifshitz spheres) was calculated using multipole expansion and spherical Bessel functions which turned out to be computationally intensive and slowly convergent[125]. An approximation to this formulation [126] made calculation of these interactions easier without much compromise on accuracy (KPW approximation). Alternatively, the many-body vdW interactions can also be calculated by implementing the iterated vdW interaction over discrete molecules (Drude molecular oscillators) in the two bodies[127, 128]. In this picture each individual molecule is considered as a point oscillator. The interaction energy between the two bodies is then simply the difference in the energies of interaction of the perturbed (with inter-body interactions) and unperturbed (without inter-body interaction) modes. This method has been used to calculate collision frequencies for gas borne clusters[129].

Interaction between Lifshitz spheres: Formulation

Lifshitz theory as originally formulated is not readily applicable for the interaction between irregular bodies since the asymmetry in the geometries does not facilitate closed-form solutions. Calculations have shown to a high degree of accuracy that the total interaction energy for a single Lifshitz sphere interacting at a distance with a contacting pair of identical Lifshitz spheres in different orientations could be approximated by a simple sum over pairwise interactions between the remote sphere and each member of the contacting pair[130]. In other words, once the many body interactions have been correctly taken into account between two Lifshitz spheres, it is justified to calculate the total interactions by pairwise sum of these many body interactions that neglects the effects of the interaction of the contacting spheres on their interactions with the remote sphere. Therefore, we propose a numerical procedure where the irregular bodies (particles and surfaces) are discretized into numerous Lifshitz spheres and simple pair-wise sum would provide us an accurate many body Lifshitz interaction between them.

We demonstrate and test our method by calculating the interactions between two macro spheres of diameter *D*, comprised of smaller Lifshitz spheres of diameter *d* (figure 1.a). First, the many body Lifshitz non retarded interaction between the Lifshitz spheres is calculated by the following expression.

$$\Delta E(z) = -\frac{kT}{2} g(z,0) - \frac{h}{4\pi^2} \int_{\xi_1}^{\infty} g(i\xi_n, z) d\xi \qquad [5.1]$$

Where ΔE is the Lifshitz interaction energy between two small nanometer sized Lifshitz spheres calculated using Langbein multipole expansion series solution[122], *T* is the temperature, *k* is the Boltzmann's constant, *z* is the center of mass separation between the two spheres and *g*(*z*,iξ) is expressed as a sequence of formulas (Appendix G) incorporating the system's geometric parameters and dielectric constant evaluated on the imaginary frequency using the KPW approximation to accelerate the series convergence[126]. The integral incorporates all thermal wavelengths ($\xi_n=(4\pi^2kT/h)n$, *n*=integer).

It should noted that equation [5.1] is useful for values of $z<<2\pi c/\xi$, i.e. in the non retarded regime. To account for retardation at larger separation, the integral has to take into account the retardation factor $f(\xi,z)$[131], where $p=2z\xi/c$. For homogeneous spheres the point to point retardation integrated over two spheres turns out to be very close to the retardation evaluated when centers of the two spheres are taken into consideration[132].

$$\Delta E(z) = -\frac{kT}{2} g(z,0) - \frac{h}{4\pi^2} \int_{\xi_1}^{\infty} g(\xi_n, z) f(\xi_n, z) d\xi \qquad [5.2]$$

$$f(\xi_n, z) = e^{-p}\left(1 + p + \frac{5}{12} p^2 + \frac{1}{12} p^3 + \frac{1}{48} p^4\right) \qquad [5.3]$$

For resuspension studies it is of prime importance to determine the adhesive forces between the particles and the surface at very close proximity. This force must be calculated as the derivative of the scalar potential due to the vdW interactions which has not been addressed in any resuspension studies, to our knowledge. At very small separation distances where the inter molecular (oscillator) distances are comparable to the separation distance, the point dipole approximation of the continuum theory breaks down and the finite size effects of the molecules have to be taken into account to avoid singular behavior of Lifshitz vdW potential near contact. The task is then to determine the dispersion interactions due to a general spherically symmetric polarizability density tensor for atoms instead of treating them as point dipoles. Here we have applied the formulation devolved in [128, 133], which uses self consistent field calculations (Hartee Fock method) to ensure that the dispersion energies remain finite at short range. From first principle analysis and physical arguments we arrived at the following the form of a spherically symmetric polarizability density tensor:

$$\alpha(\mathbf{r},\omega) = I\,\frac{e^{-\beta r/a_o}}{8\pi(a_o/\beta)^3}\,\alpha(\omega) \qquad [5.4]$$

where $\alpha(r,\omega)$ is the spherically symmetric polarizability density tensor, I is the identity tensor, a_o is the Bohr radius, β is introduced to account for atomic size effects and $\alpha(\omega)$ is frequency dependent polarization. Dispersion energies are small in nature and are completely negligible at short intermolecular separation in comparison with the tremendously large repulsive energies. Following this approach, both short range dispersion interactions along with orbital overlap repulsive interactions were calculated for a system of two interacting spheres[134], yielding analytic and nonsingular interactions at small separation distances which we have incorporated in our formulation to determine Lifshitz interactions at all practical separations for resuspension studies in a computationally feasible way. This phenomenological method can be used to calculate the vdW interactions at small separations but neglects electrostatics and hybridizations effects and any other effects due to chemical bonding[135]. As a practical question, the change is energy is likely to be small because the details of the interaction pertain solely to the interacting surface atoms. As the separation between the spheres increases, molecular size effects become decreasingly important, and the short-range energy converges smoothly to the Lifshitz continuum energy.

Interaction between Lifshitz spheres: Methodology

Even though equation [5.2] requires integrating the function $g(z,\mathrm{i}\xi)$ over the imaginary frequencies which itself is evaluated as sum of a doubly infinite series (Appendix G), the formulation is easily programmable, enabling us to calculate the many body retarded interaction energies between two small Lifshitz spheres at all relevant length scales. We can now populate two microscopic bodies with such nanometer sized Lifshitz spheres and calculate the pair-wise sum of all the interactions among them. To do this in a computationally feasible manner, we discretize the volumes of the two microspheres into computational grids of dimension L (Figure 39 a) and calculate the pair-wise sum of the Lifshitz interaction over all the computational grids in the two bodies by incorporating the volume density of smaller Lifshitz spheres in this packing. Our operational assumption is that we compensate for void fraction by a suitable multiplicative factor (based on the volume density of Lifshitz spheres). This is reasonable in a constant density system where mass and volume are proportional. The implementation of this algorithm automatically takes into account the mass corrections due to the void fractions in this arrangement and yields at least a partially averaged interaction over different filling configurations of the Lifshitz spheres. Furthermore, it was shown earlier that interaction energies between

Lifshitz spheres in different configurations don't vary significantly[130]. In principle, these Lifshitz spheres can populate any arbitrary shape geometry (Figure 39 c).

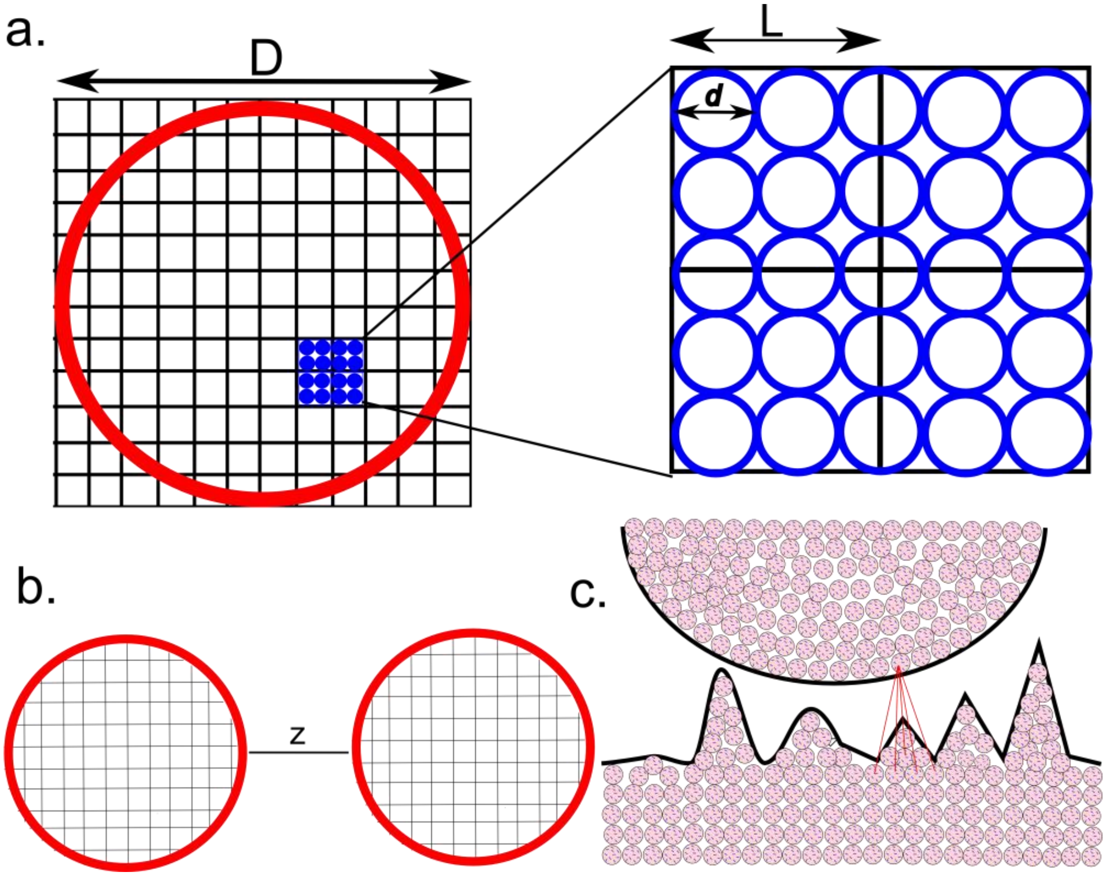

Figure 39: Packing continuous media with nanometer sized Lifshitz spheres. (a) The macroscopic sphere of diameter *D* (~ 1 - 100 microns) discretized into computational grid elements with grid size *L*. Each computational grid consists of Lifshitz spheres of diameter *d* (~1-10 nm). (b) Pair wise sum over the computational grids within the two macro-spheres produces an accurate estimation of the many body Lifshitz interactions between them. (c) The Lifshitz spheres, in principle can fill up any arbitrary geometry to yield the pair-wise many body interaction between them.

Although these interactions between spheres based on Langbein's formulations incorporate the many body, retardation and near contact effects, thus yielding approximate Lifshitz interaction at all separations, the equations do not yield a simple functional form with explicit distance dependence like in the Hamaker's approach

$$\Delta E(z,R) = -\frac{A_{ham}}{6}\left(\frac{2R^2}{z^2-4R^2}+\frac{2R^2}{z^2}+\ln\frac{z^2-4R^2}{z^2}\right) \qquad [5.5]$$

Where, R is the radius of the equal sized spheres and A_{ham} is the material dependent Hamaker constant obtained either from molecular polarizability data or empirically by fitting experimental data. A more precise Hamaker constant can be obtained from the Lifshitz's macroscopic picture for two interacting half spaces[136], which provides a lower bound for the interactions between two spheres[130] (Hamaker-Lifshitz approach).

$$\begin{aligned} A_{L-H} = {} & \frac{3kT}{4}\left[\frac{\varepsilon_1(0)-\varepsilon_3(0)}{\varepsilon_1(0)+\varepsilon_3(0)}\right]\left[\frac{\varepsilon_2(0)-\varepsilon_3(0)}{\varepsilon_2(0)+\varepsilon_3(0)}\right]+ \\ & \frac{3h}{16\pi^2}\int_{\xi_1}^{\infty}\left[\frac{\varepsilon_1(i\xi_n)-\varepsilon_3(i\xi_n)}{\varepsilon_1(i\xi_n)+\varepsilon_3(i\xi_n)}\right]\left[\frac{\varepsilon_2(i\xi_n)-\varepsilon_3(i\xi_n)}{\varepsilon_2(i\xi_n)+\varepsilon_3(i\xi_n)}\right]d\xi \end{aligned} \qquad [5.6]$$

Where ε is the frequency dependent dielectric constant of the material and can be modeled as a real and monotonically decreasing function of the frequency (ξ) on the imaginary axis in a damped harmonic oscillator form[137, 138]. The values of parameters in the eq. [5.7] are listed in Table 11[139].

$$\varepsilon\ (i\xi) = 1+\sum_{j=1}^{4}\frac{f_j}{\omega_j^2+g_j\xi+\xi^2} \qquad [5.7]$$

Table 11: Dielectric properties of polystyrene.

ω (eV)	g (eV)	f (eV)^2
6.35	0.65	14.6
14	5	96.9
11	3.5	44.4
20.1	11.5	136.9

For validation purposes we compare our formulation with the exact Lifshitz interactions, Hamaker-Lifshitz interaction and the Hamaker pair wise interaction between the two polystyrene microspheres (D = 1 micron). These calculations revealed that the solutions converge to the exact Lifshitz interactions as the relative size of the Lifshitz spheres is made larger with respect to microsphere, i.e. for lower values of D/d (Figure 40), where d is the Lifshitz sphere diameter and D is microsphere diameter. At very close distances the collective effects become less important and the interaction is dominated by the short range molecular interactions which are not strongly dependent on the D/d ratio. It should be noted that scaling of these interactions is not linear with the volume of Lifshitz spheres. The exact interaction is obtained by taking all the many body interactions between the two spheres. As the number of Lifshitz spheres increases, fewer many body retarded interactions are taken into account, thus resulting in a deviation from the exact Lifshitz result at larger distances. Grid independence of solution was verified for values of D/d lower than 20. This convergence can be attributed to the consideration of more collective interactions when the sizes of the Lifshitz spheres are made big. Therefore, the largest size of the computational grid elements is only constrained by the smallest feature of the geometry that needs to be resolved in the micro-bodies.

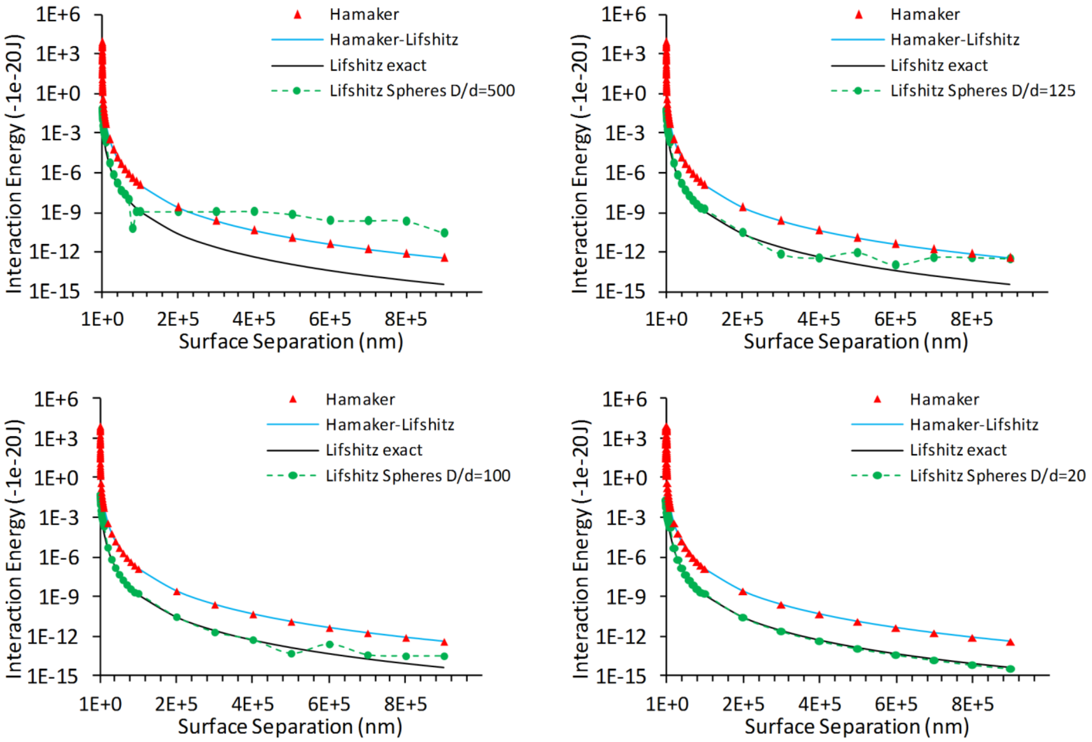

Figure 40: Sensitivity analysis of interacting Lifshitz spheres. Interactions between 2 polystyrene micro-spheres (1 micron in diameter) are calculated by different methods; Hamaker's approach using (i) Hamaker's constant and (ii)Hamaker-Lifshitz constant, (iii) exact many body Lifshitz retarded interactions and (iv) pair-wise retarded interactions between Lifshitz spheres comprising the two micro-spheres. The pair-wise interactions over the Lifshitz spheres converges to the exact many body Lifshitz interactions for sufficiently large Lifshitz spheres.

Limitations of the model

Discussion of the limitations of our formulations is important at this point. By packing the dielectric material with smaller Lifshitz spheres, we are ignoring the effects of surface resonances due to the actual material size[140]. This would appear to be responsible for the improvement in the model as the *D*/*d* ratio decreases in Figure 40.

Furthermore, these calculations are limited to dielectric materials. Conductors are not well described in this formulation which has been discussed earlier[141]. These interactions are based on Langbein's formulation for two spheres which converges to Lifshitz result at small separation distances. For large separation distances, retardation becomes significant and has been introduced here in a phenomenological way in the form of a retardation factor. In recent years, several new treatments of Lifshitz theory for compact objects have been given [120, 121, 142-144]. While they are more general in formulation than Langbein's earlier development based upon Drude oscillators and the Clausius-Mossotti equation, they share a similar basis in their development of the multipolar interactions that are the basis for Lifshitz interactions. In the scope of this study we have limited our focus to rigid particulate materials and surfaces. However the methods developed here are general and in future studies they can be extended to treat adhesion in the case of deformable bodies. We are treating the interacting bodies as electrically neutral, neglecting any electrostatic interactions between them. We are also only considering separation distances over which chemical bonding interactions are negligible. Condensate effects are not taken into account and the interacting material and the medium considered here are composed of homogenous dielectric material.

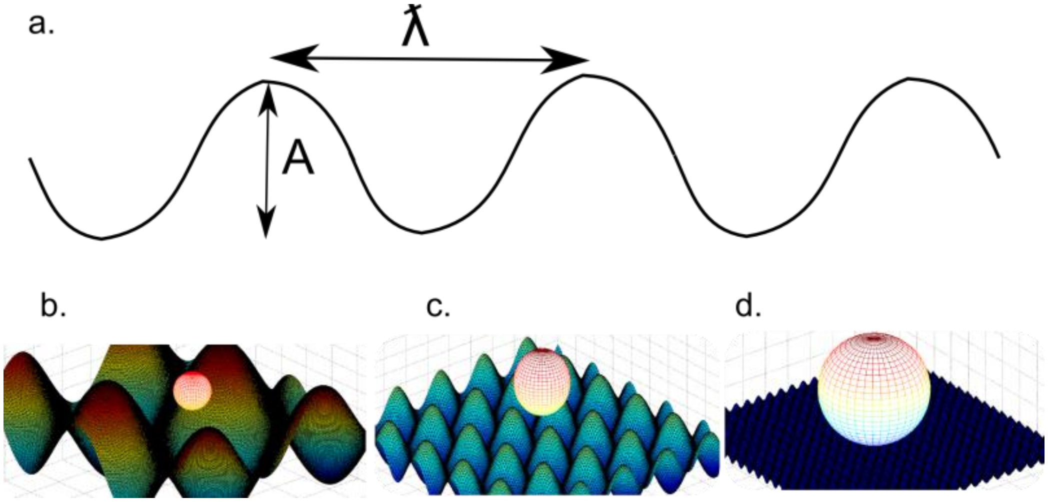

Figure 41: Modeling surface roughness with a sinusoidally varying roughness profile of a given amplitude and wavelength**.** The amplitude can be changed with respect to particle diameter to achieve different levels of surface roughness i.e. (b) high roughness, (c) moderate roughness and (d) low roughness.

Interaction between a spherical particle and rough surfaces

In resuspension studies, an important factor in the calculation of the adhesion force between the substrate and the particle is the surface roughness. Surface roughness can be determined by interferometric methods using an optical profilometer. Rough surfaces tend to decrease the adhesion forces by decreasing the effective area of contact and increasing the distance between particle and the surface[145, 146]. Unfortunately, the magnitude of these effects is not understood well. There have been previous attempts to quantify such effects by modeling surface roughness as semi hemispherical asperities[147] where the total vdW interaction was split into the sum of interaction of the particle with the flat surface and the hemispherical asperity. This model was later modified, incorporating more parameters to better represent the surface roughness[148, 149]. Other models tend to impose the Hamaker's integral formulation to other simple geometries (cones and hemispheres)[150, 151] and even more complicated geometries[152]. Fewer attempts have been made to formulate interactions between rough surfaces using the continuum approach. One such method treats roughness as a diffuse layer whose dielectric properties vary continuously between those of the surface and the medium[153]. The vdW interactions are then calculated using Lifshitz formulation for multi-layered system.

We are now in a position to extend our formulation to calculate Lifshitz interactions in systems with irregular and rough surfaces. Although one can choose any profile to represent the surface roughness, for illustration purposes we select a sinusoidally varying rough surface with two parameters to tune the roughness (Figure 41 a), namely the roughness amplitude (A) and the roughness wavelength (λ). For modeling convenience we can relate the roughness wavelength to the roughness amplitude ($\lambda = 4A$). Both the particle and the surface are made of polystyrene separated by air. The rough surface is discretized into computational grids composed of smaller Lifshitz spheres of diameter 1/10 the roughness amplitude (based on our previous grid independence study and sensitivity analysis), enabling us to capture the finest features of the sinusoidally rough surfaces. The roughness was taken in an area of 25 μm^2 on the surface centered directly below the particle. The many body interactions were summed up between the computational grids comprising the surface and the spherical particle. Interaction energies were computed over a series of separation distances ranging from the equilibrium contact distance to 100 times the particle diameter. Points near the surface were taken to be more dense. These interactions were compared with the exact Lifshitz interactions and the

Hamaker-Lifshitz interactions between a spherical particle and a smooth surface. In the near contact region (0 - 20 nm) where retardation effects are less prominent, the Lifshitz interaction curve between a smooth surface and a spherical particle yields a constant slope (Figure 42 log-log scale). At separation distances farther from the surface, the slope of the interaction curve decreases due to retardation of interaction at these length scales (figure 4). The Lifshitz-Hamaker interactions which do not take retardation into account has a constant slope at all separations. Interaction energies for systems with varying particle diameter (*D* = 1, 5 and 20 microns) and rough surfaces with sinusoidally varying roughness profile (*A* = 3, 10, 25, 50, 100, 500 nm) were analyzed (Figure 42). For surfaces with small roughness amplitude (*A* = 3 nm), the interaction energy deviates from that of smooth surface interaction in the near contact region. This deviation increases upon increasing the surface roughness amplitude. All rough surface interactions asymptotically converge to flat surface interactions at larger separation distances as the roughness features of the surface is not significant at these length scales and the surface can be treated as smooth. The distance at which this happens depends on the roughness amplitude and the size of the particle (Figure 42 a).

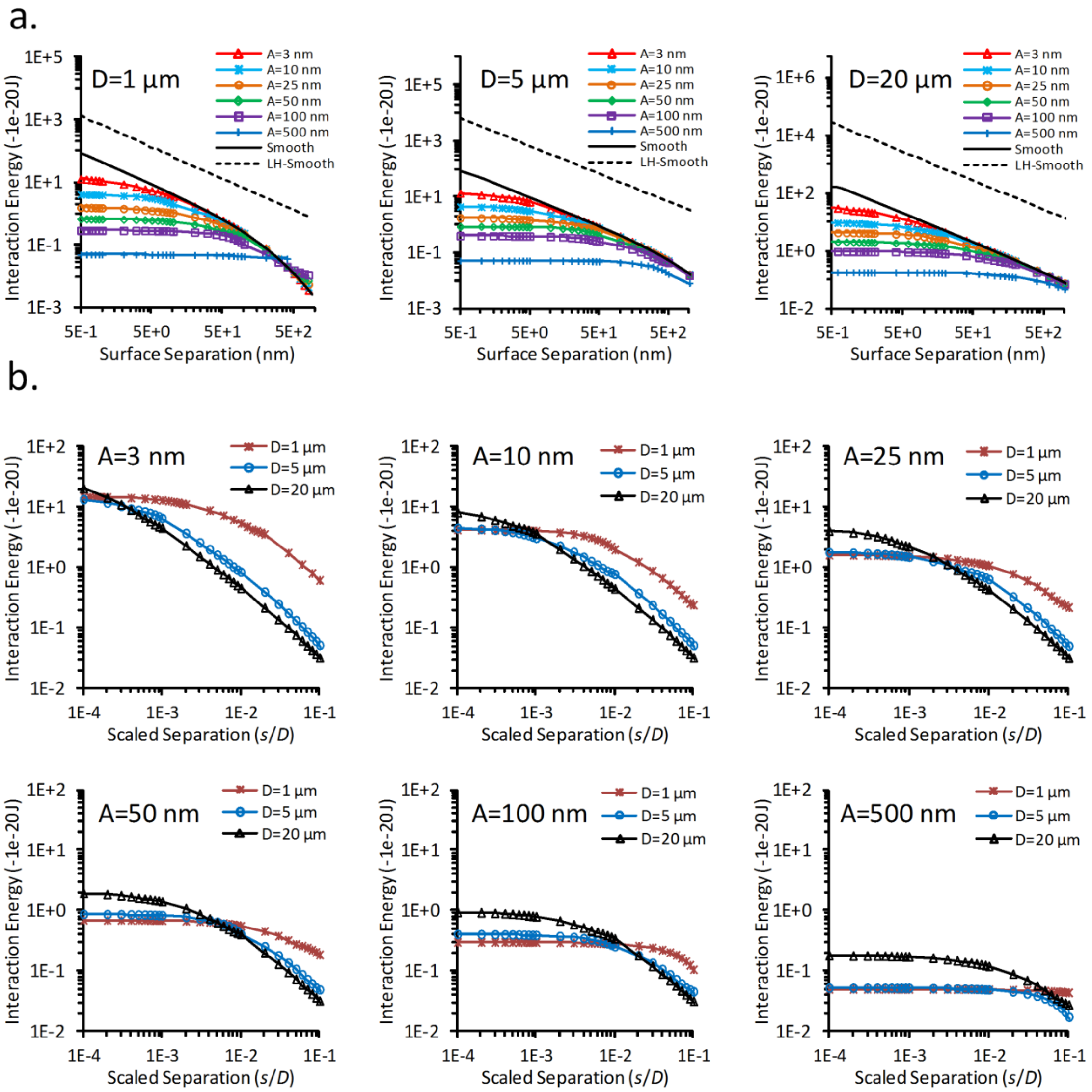

Figure 42: Variation of vdW interaction energies for different combinations of particle diameter and surface roughness profile. The roughness wavelength is taken to be proportional to the roughness amplitude ($\lambda = 4A$). (a) The Interaction energy between a spherical particle and rough surface with various roughness amplitudes (A = 3, 10, 25, 50, 100 and 500 nm) on log-log scale. The 'LH-smooth' indicates the Interaction between two half spaces and 'smooth' indicates the Lifshitz interaction between a smooth surface with a spherical particle (b) Variation of the interaction energy between a surface of a given roughness amplitude and particles of different diameter (D = 1, 5 and 20 microns) as a function of the separation distance scaled by the particle diameter on a log-log scale.

Figure 42 b shows the analysis of these interactions as a function of the separation distance scaled by the individual particle diameter for each of the six roughness profiles. For the smallest roughness amplitude, the highest interaction energy is obtained for the 20 micron dia. particle followed by 5 and 1 micron dia. particles. As the roughness amplitude is increased, the interaction energies decreases for the 20 micron particle in comparison to the smaller particles and the individual interaction energy curves cross over at a certain scaled separation which increases with the surface roughness amplitude.

Particles with different shapes

Our formulation can also be applied to study interactions of non-spherical particles with surfaces. In addition to random aggregates formed by collisional processes, many particles in nature are often formed by fracturing larger chunks of material into smaller pieces and differ quite significantly from their spherical counterparts (spheroid, cube, rod, disk, tetrahedron etc). Such shape factors can have significant impact on the interactions of particles with surfaces and to our knowledge these effects have not been quantified in any particle resuspension study. The objective of the following study is to analyze the effect of dissimilar particle shapes and their orientation on their Lifshitz interactions with a flat surface.

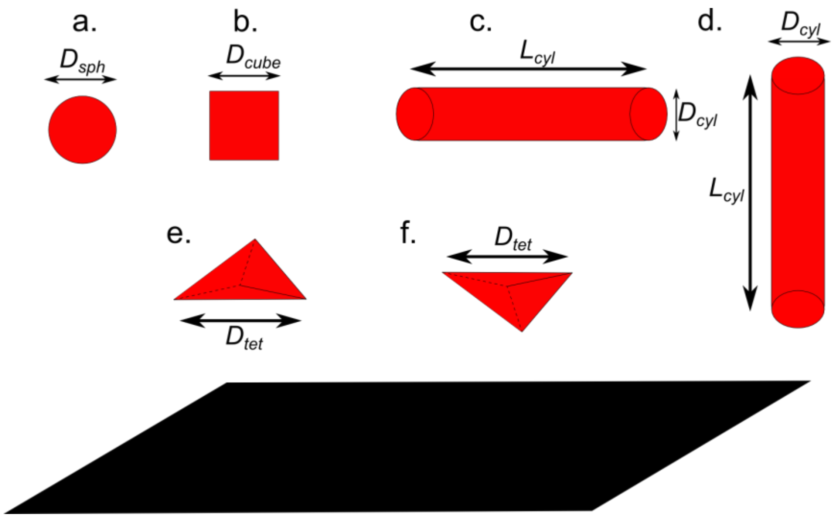

Figure 43: Geometrical configurations of particles of different shapes interacting with a flat surface. (a) Spherical particle, (b) Cubical particle, cylindrical particle with major axis (c) parallel and (d) perpendicular to the surface, tetrahedron particle with base (e) near and (f) away from the surface.

Geometrical shapes of particles considered are spherical, cubical, cylindrical (major axis aligned parallel and perpendicular to the surface) and a regular tetrahedron (with base facing towards and away from the surface) with varying characteristic lengths (Figure 43). The height of the cylindrical particle was taken to be 10 times its base diameter. The characteristic dimensions of all the particles were determined by making the volumes of different particles equal to the volumes of corresponding spheres of diameter 1, 5 and 20 microns. Particles and surfaces were composed of Lifshitz polystyrene spheres separated in air. The pair-wise sum of the retarded Lifshitz interactions was calculated for each of particle-surface system, from equilibrium contact distance to 1000 times the sphere diameter. The regular tetrahedron with its base facing the surface is orientated in such a way that most its mass (dielectric material) is near the surface; therefore in the near contact region this configuration has the lowest energy (highest on the negative energy scale in Figure 44 a) whereas the interaction energy for the tetrahedron with its base facing away from the surface lies on the opposite end of the spectrum as most of its mass is distributed away from the surface. The interaction energies for other shapes (sphere, cube and cylinders) lie between these two extremes in the near contact region (Figure 44 a). The adhesive force of these particles with the surface can be determined by the gradient of their respective interaction energy curve i.e. the slope of the interaction curves in non log scales. These plots reveal that in the near contact region, the tetrahedron shaped particle with its base facing towards and away from the surface has the largest and the smallest slopes in magnitude respectively. The regular tetrahedron with base facing towards the surface, the cylindrical particle with its major axis perpendicular to the surface and the cubical particle experience the maximum adhesive force (maximum slope). Thus, it can be inferred that particles with flatter sides near the surface experience stronger adhesive force in the near contact region. Away from the surface where the distinguishable geometric feature of the particle is not significant, the interaction energy is found to depend only on the particle's aspect ratio. Particle shapes with aspect ratio ~ 1 i.e. sphere, cube and tetrahedron, converge to identical interaction energies away from the surface whereas the cylindrical geometries with an aspect ratio of 10 seems to converge to a different interaction energy for the three characteristic dimensions. Such interactions involving high aspect ratio particles/fibers are quite significant, for example, the millions of high aspect ratio cylindrical setae (adhesive foot hair) on the toes of geckos enhance the vdW interactions[154] between the foot and the walls enabling it to climb vertical and even inverted surfaces.

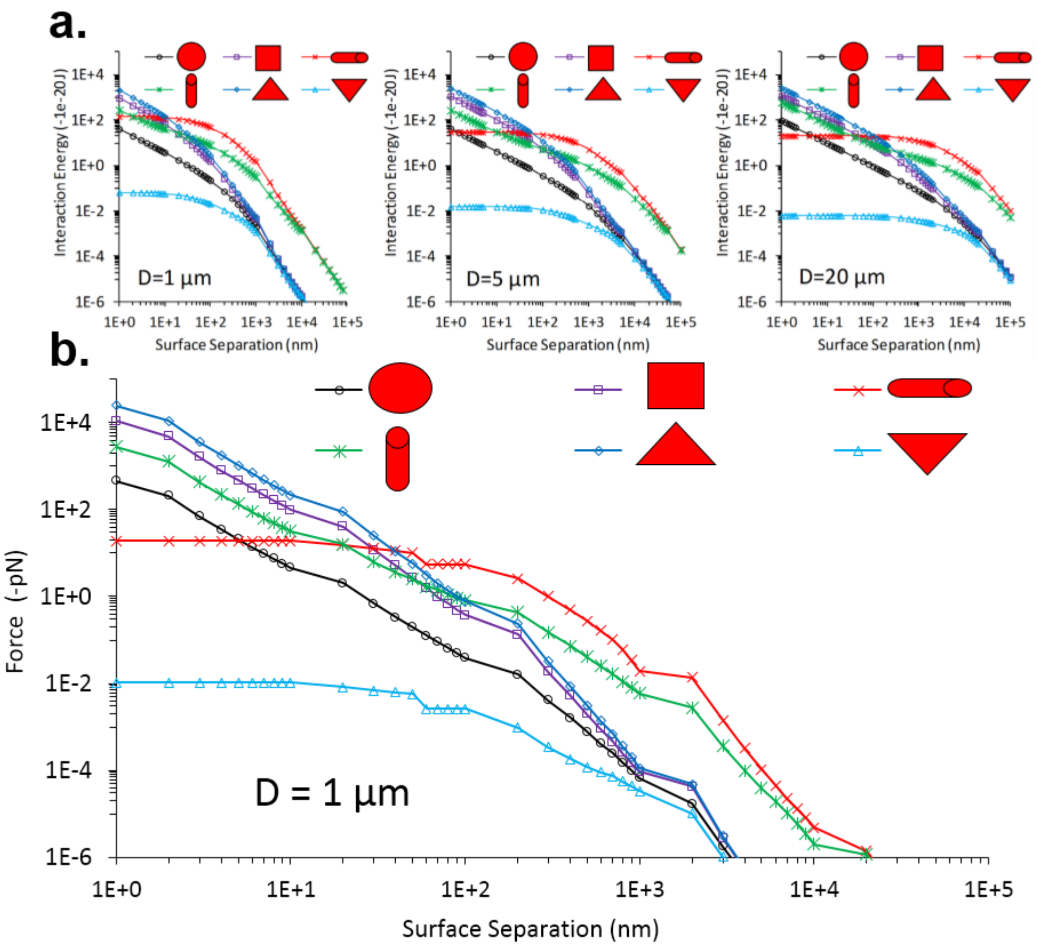

Figure 44: Interactions of particles of different shapes, size and configuration (sphere, cube, cylinder and regular tetrahedron) with a flat surface. (a) The volume of the particles of the six different shaped particles were made equal to the volumes of corresponding spheres of diameter =1, 5, and 20 microns. The height of the cylinder is 10 times it base diameter. The interaction in the near contact and far field region depends on the particle's shape and aspect ratio respectively for all three volumes. (b) Gradient of the interaction energy yields the adhesion force experienced by the particles.

Conclusion

Having laid this foundation, we envision our future work to incorporate the results from this study to particle resuspension modeling. Current resuspension models either take the force/moment balance approach on the particle (Dynamic models) or treat the adhesion resuspension from a statistical approach (Energy accumulation models). In the dynamic models, all the forces and moments on the particles are calculated and resuspension is characterized when the detachment forces (fluid drag) exceeds the adhesive forces. Even though the flow near the surface is quite intricate due to turbulence and is itself a subject of greater study, Computational fluid dynamics (CFD) incorporating various turbulence models such as Large eddy simulations (LES) or Reynolds averaged Navier-Stokes equation (RANS) can be used to resolve the near wall turbulence effects, enabling us to determine the hydrodynamic forces acting of the particles residing in the viscous sub layer. The rigorous treatment of the many body vdW interactions at all separations can then be integrated as distance dependent parameterized field functions to complement the CFD models in determining the strength of adhesion in the near contact region (Figure 44 b). We would also be able to probe various systems with rough surfaces and nonspherical particles more accurately, a feature not captured by previous resuspension models. The inputs to the model are the frequency dependent dielectric data of the materials composting the surface, particles and the medium. The model can be extended to incorporate more general scenarios such as multilayer deposits with heterogeneous dielectric properties within the material and even to deformable bodies. We anticipate that incorporation of this formulation to determine adhesive interactions in complex systems would improve the predictive capabilities of particle resuspension dynamics.

CHAPTER VI

FLUID PARTICLE INTERACTIONS AND SIZE BASED PARTICLE SEPARATION IN A MEMBRANE LESS MICROCHANNEL

Introduction

There is a critical need for advanced filtration methods adaptable for separation of cells and cell-sized components from blood, specifically offering the capability to rapidly process large volumes (> mL/min flow rates) [155, 156]. Microfluidic technologies provide a natural platform to address these challenges, but these methods generally take too long, making them impractical for routine use. Another key area where high-throughput blood separation is important is the analysis of rare cell biomarkers relevant to cancer (e.g., circulating tumor cells (CTCs)). Microfluidic methods based on micromachined filtration structures that act either alone (to provide size-selective isolation)[157, 158], or in tandem with functionalized antibodies (to provide affinity capture) show considerable promise[159, 160], but also suffer from limitations inherent to the filtration-based design. Most notably, achievable flow rates are typically very small due to the large pressures that must be applied to inject a cell laden suspension through the tiny internal pore-like networks. Consequently, highly diluted cell suspensions must often be used (making it necessary to process even greater volumes due to the rare nature of CTCs), and large internal shear stresses make recovery of viable cells challenging unless extremely low flow rates are applied (further increasing the analysis time).

Passive separation in microfluidic systems without external equipment which purely relies on flow phenomena and channel geometry has been widely studied and applied to separate blood components[161-165], microorganisms[166, 167] and even rare cells[158, 168-171]. These soft lithography based microfluidic devices lacks rigidity owing to the soft mechanical property of PDMS (polydimethylsiloxane) elastomer, often limiting the filtration performance due to the deformation of the channel structures[172]. The difficulty to fabricate complex microstructure geometries constrains further development of these systems.

We have engineered a novel membrane-less microfluidic filtration device embedding complex microscale features fabricated by harnessing enzymatic activity of proteinase K on rigid biodegradable substrate Poly(lactic acid)[173]. The microfluidic architecture incorporates an embedded weir-like barrier separating two lanes with different depths, oriented parallel to the flow direction and extending along the entire centerline length of the microchannel (Figure 45). The channel was designed to employ the inertial effects in the curved section of the microchannel to separate particles by centrifugally transporting smaller sized particles across the barrier.

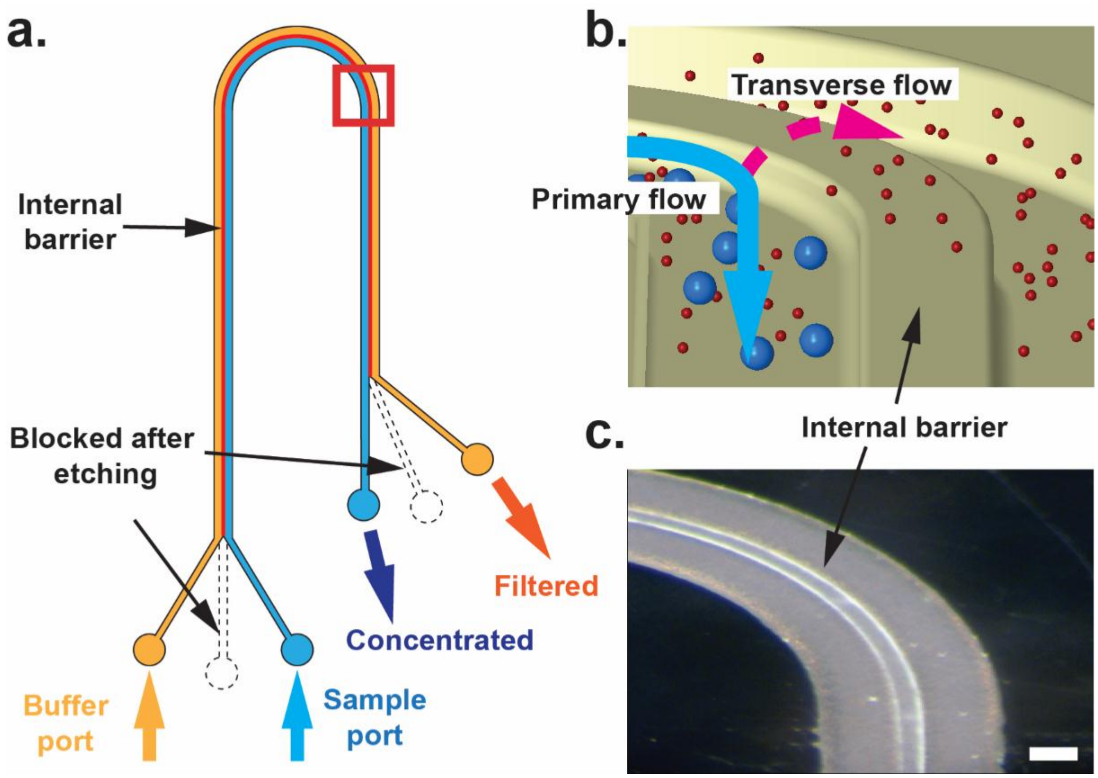

Figure 45: Mechanism of size based micro separator. (a) Schematic of enzymatically machined micro separator with desired internal barrier enables the concentration and filtration of mixture size of sample. (b) Size-selective filtration depends on the gap of internal barrier. The sample stream mainly flows to inner loop of channel. Due to the curved microchannel segment and difference of channel depth, the transverse flow can carry small particles cross barrier into the outer loop. (c) Side view of a U-shaped microchannel fabricated using enzymatic etching. Scale bar = 100 µm.

We unexpectedly found that the difference in depths of the two parallel lanes provides a much stronger pressure gradient driving force to transport the smaller sized components in the flow across the barrier from the shallow lane to the deeper lane while constraining the larger components in the shallow lane. This arrangement when combined with the transverse centrifugal flow generated in the curved section of the microchannel further enhances the separation[174]. When the interplay between these effects is considered, we found that performance can be enhanced beyond what is possible if either mechanism is applied alone. The mechanism of particle separation and quantification of separation efficiency were analyzed by tracking motion of fluorescent particles in three scenarios: (1) curved channel with equal depth, (2) straight channel with unequal depth, and (3) curved channel with unequal depth. A 3-D computational fluid dynamics model was developed to study the detailed features of the secondary flow and analyze the trajectories of particles under the influence of all relevant hydrodynamic forces in order to gain insights on the important design parameters to maximize separation efficiency. The CFD simulations also enabled us to determine impartant dimensionless parameters for which governs the separation efficiency in straigh channels.

Secondary flow and hydrodynamic forces

Flow of micron sized particles in microfluidic channels has been studied and described in terms of various hydrodynamic forces acting on it such as the drag force, shear induced lift force[175] (Saffman force), particle spin induced lift force (magnus force) [176], Dean vortex induced drag force, and other surface and body forces[177-179]. Centrifugally driven flow instabilities in the curved channel section results in the onset of counter rotating vortices in the plane perpendicular to primary flow direction. These secondary flow features, called Dean flow can be characterized in terms of a dimensionless number “Dean number”, κ (κ = (Dh/2R)0.5Re, where Dh is the channel hydraulic diameter for the entire channel cross section, R is the flow path radius of curvature of the barrier lane (Figure 47 a), and Re is the Reynolds number with the hydraulic diameter as the length scale) which quantifies the relative magnitudes of inertial and centrifugal forces to viscous forces[174]. While there have been a number of particle separation studies which harness Dean coupled inertial migration of particles based on their size, only few of them employ a cross flow barrier pressure driven filtering mechanism demonstrating high throughput and separation efficiency[173, 180, 181].

The trajectory of a particle can be described in a lagrangian sense by integrating all relevant hydrodynamic forces acting on it over time[182]. However, a complete description is not possible analytically as some forces act in a more intricate fashion requiring a two way coupling approach to resolve the motion of the particle. Computational fluid dynamics can provide a much higher resolved solution to particle fluid interactions by solving the problem numerically. Here we incorporate all the relevant surface forces (Table 12) and torques (Table 13) experienced by the particle. This enabled us to resolve intricate fluid particle interaction phenomena such as inertial migration, inter particle collision and spin induced drag. The net force experienced by each particle is then given by eq [6.1].

$$m_{particle}\frac{dv_{particle}}{dt} = F_{drag} + F_p + F_{vm} + F_g + F_{lr} + F_{ls} \qquad [6.1]$$

Table 12: Translational surface forces on the particles.

Primary translational forces (Lagrangian particle tracking)		
Force	**Expression**	**Comments**
Drag force	$F_{drag} = \frac{1}{2} C_D \rho A_p \left\| v_s \right\| v_s$	The drag force model was invoked to calculate the viscosity induced fluid resistance resulting in a translational motion of the particle. (C_d = drag coefficient; ρ = density of fluid (980 kg/m^3); A_p = projected area of the particle; v_s = particle slip velocity). Schiller-Naumann drag correlation which is suitable for spherical particles was incorporated for drag coefficient calculations [183].
Pressure gradient force	$F_P = -V_p \nabla P_{static}$	This arises due to local static pressure gradient in the fluid around the particle (V_p = particle volume; ∇P_{static} = gradient of the static pressure in the fluid phase).
Virtual mass force	$F_{vm} = C_{vm} \rho V_p \left(\frac{Dv}{Dt} - \frac{dv_p}{dt} \right)$	This is an inertia driven force due to particle acceleration around the fluid (C_{vm} = virtual mass coefficient (0.5 for spherical particles [184]); D/Dt = material derivative operator, v = fluid velocity; v_p = particle velocity).

Table 13: Rotational surface forces on the particles.

Secondary rotational forces (discrete element modeling)		
Force	**Expression**	**Comments**
Rotational torque	$\Gamma = \frac{1}{2}\rho R_p^5 C_R \lvert\Omega\rvert \Omega$ $\Omega = \frac{1}{2}\nabla \times v - \omega_p$ $C_R = f(Re_R)$ $Re_R = \frac{4\rho R_p^2 \lvert\Omega\rvert}{\mu}$	The local fluid velocity field around the surface of the particle additionally imposes a rotational torque. The resulting change in angular momentum of the particle induces other forces which manifest in the form of lift and shear forces, causing the particle to migrate laterally in the plane perpendicular to the primary flow direction. Discrete element model (DEM) was invoked to calculate drag torque (Γ) on the particle. where (ρ = fluid density; R_p = particle radius; μ = viscosity; C_R = rotational drag coefficient and is a function of rotational Reynolds number (Re_R) [185]; v = fluid velocity; ω_p = particle angular velocity and **Ω** = relative angular velocity of the particle with respect to the fluid (slip rotation)).
Spin induced lift force	$F_{lr} = \frac{1}{2}\rho\pi R_p^2 C_L \frac{\Omega \times v_s}{\lvert\Omega\rvert}$	Spin induced lift force is caused due the particle spinning relative to the fluid [185] (C_L = coefficient of rotational lift; **Ω** = relative angular velocity; v_s = particle slip velocity).
Shear induced lift force	$F_{ls} = \rho\pi R_p^3 C_{LS} \left(v_s \times \omega\right)$	Shear induced lift force (Saffman force) on a particle arises when there is a local velocity gradient in the direction perpendicular to the relative motion of the particle [175] (C_{LS} = shear lift coefficient; v_s = particle slip velocity; ω = curl of fluid velocity (∇ x v)).

Discrete element modeling

A 3-D computational fluid dynamics (CFD) model was formulated to analyze the intricate primary and secondary flow features and fluid-particle interactions in both curved and straight microchannels. The microfluidic channels were designed and meshed in gambit (ANSYS) with a mix of cartesian and curvilinear grid systems to account for both the straight and curved sections. A much finer grid was generated in the barrier region to resolve the strong cross flow and particle migration, resulting in ~ 5 x 10^4 computational cells. The length of the straight section was chosen such that the flow is fully developed before the curvature starts. Other geometric parameters was chosen to closely resemble the channels used in experiments (Figure 46).

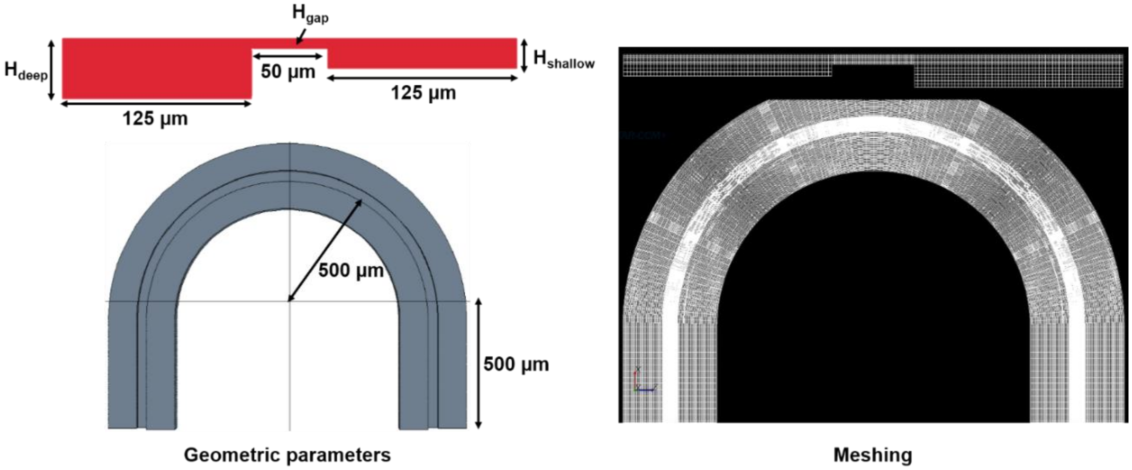

Figure 46: Geometric parameters and meshing of microchannel. Mixed grid system comprising of both cartesian and curvilinear coordinates were used for the respective sections of the channel. A much finer grid density was used in the barrier section.

Finite volume method (STAR-CCM+, CD-adapco) was used to solve complete 3D Navier-Stokes equations in a coupled flow solver. The domain fluid was water at constant density and all its properties were evaluated at room temperature. Fluid was injected at a constant flow rate at both the shallow and deep lanes of the channel which was assigned a “velocity inlet” boundary condition. The sidewalls were made non permeable with “no slip” velocity boundary condition.

Lagrangian multiphase model was employed to introduce micron sized rigid particles with a density of 1 g/mL to match typical cell densities [186] at a flow rate of 1.68 x 10^6 particles/mL in the computational domain. Gravity was invoked as the only body force acting on both the fluid and particle phases. The lagrangian framework allowed us to invoke the relevant translational hydrodynamic forces such as the drag force, pressure gradient force and virtual mass force in the form of sub-models. The discrete element modeling (DEM) capabilities of STARCCM+ allowed us to additionally resolve the rotational drag torques which enabled us to invoke spin and shear induced lift forces on the particles due to surrounding fluid [177], a feature not captured by traditional lagrangian particle formulations. DEM also enabled both the particle and fluid phases to be solved simultaneously by invoking two way coupling, yielding a more detailed resolution of the fluid-particle interactions. The inbuilt Hertz Mindlin contact model was invoked to further take into account friction, rolling and collisions between other particles and wall surfaces. Particles were injected randomly at the inlet of the shallow lane with an initial zero angular velocity (ω_p) and linear velocity (v_p). An implicit unsteady scheme was used to march the solution forward in time. Particles were removed from the simulation domain once they reached the outlet and data files containing information about the particle position, residence time and velocities were extracted and further analyzed in MATLAB.

Particle separation experiments

To determine separation efficiency, separated particles were collected from two outlet streams and analyzed by Coulter counter and hemocytometer. Separation efficiency is quantitatively defined as the fraction of particles that cross the barrier N_b / (N_s+N_b) = (C_b x V_b) / (C_s x V_s+ C_b x V_b), where N_b and N_s are total number of particles collected in buffer stream and sample stream, respectively. C_b and C_s are particle concentration of buffer and sample stream measured by Coulter counter. V_b and V_s are total volume of buffer and sample collected at the same time. Key features of the underlying flow phenomena governing such filtration can be inferred from 3D computational fluid dynamics simulations. Particle fluid interactions were resolved using discrete element modeling (DEM) which enabled us to determine the 3D trajectories of particles under the influence of all relevant hydrodynamic forces and torques. Simulated separation efficiencies were then calculated, defined in the same manner as before.

Separation in curved channel with equal heights

First we analyze the particle separation efficiencies in a curved channel with equal depths on both sides of the barrier (inner and outer lanes: 40 µm deep, centerline barrier gap: 5 µm deep, radius of curvature: 500 µm). At low flow rates ($\kappa = 2.3$, Q = 0.1 mL/min), centrifugal effects are not strong enough to disrupt the laminar flow along the channel. At higher flow rates (κ = 46.2, flow rate = 2 mL/min), two counter-rotating vortices are generated separately in both inner and outer lanes in the curved region (Figure 47 b) and the for most part, the fluids in the inner and outer lanes don't mix significantly except after the curved section where curvature induced flow transports some fluid from the inner to the outer lane as revealed by injecting two different colored dyes into these streams (Figure 48 a). Simulated 2 micron particles injected in the inner lane (flow rate = 2 mL/min) tend to circulate under the influence of secondary Dean flow with a very small fraction of particles crossing over the barrier, a result which was mirrored when monitoring the motion of fluorescent 2 micron particles under the same operating conditions (Figure 48 b). When analyzing the separation efficiencies channel (cross section: 40-5-40 μm (inner-gap-outer)) it was found that none of the particles migrate across the barrier at low flow rates. Even at higher flow rates, the separation efficiency is very low (5%), suggesting that the Dean flow in curved region cannot act alone as the major driving force to separate particles (Figure 48 c).

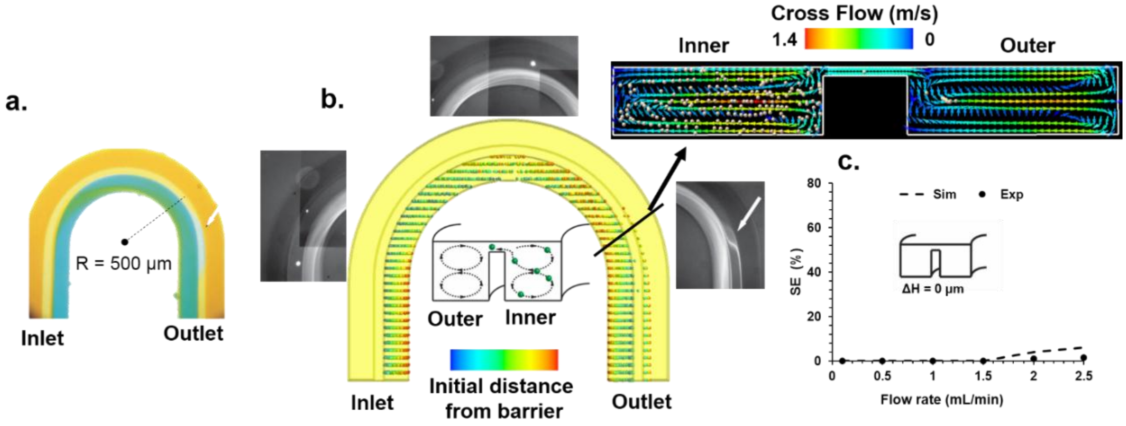

Figure 47: Even height curved channel. Curvature induced migration of particles in an even height curved channel with central barrier (inner and outer lanes: 40 μm deep, centerline barrier gap: 5 μm deep, radius of curvature: 500 μm) (a) Top view image illustrates that two streams labeled with blue (inner) and yellow (outer) dye don't mix significantly and remain separated in their respective lanes except just after the curvature ends where the blue dye crosses over the barriers into the outer lane (flow rate = 2 mL/min). (b) Simulation of particle trajectories reveals the evolution of lateral particle position under the influence of curvature induced Dean vortices as they are transported through the straight and curved sections of the channel (flow rate = 2 mL/min; particles color coded to represent initial distance from the barrier). Inset images of experiments performed at same operating conditions reveals similar migration pattern of 2 μm fluorescent particles. (c) Separation efficiency (particles in the outer lane/ total particles; at outlet) of particles remains very low even at higher flow rates suggesting that Dean vortices are not sufficient to efficiently separate particles (Particle dia. = 2 μm for all cases).

Separation in straight channel with unequal heights

In addition to the transverse secondary Dean flow, the viscosity difference between the two injected streams has been studied and applied to analyze diffusion coefficient of small molecules or biological samples[187]. However, parallel flows with a transverse pressure difference has not been widely studied. For the same flow rate at both inner and outer lane inlet with different depths, an initial pressure difference exists between shallow and deep lanes in the entry region and can be described by $\Delta P_{barrier} = \frac{12\mu QL}{w}\left[\frac{1}{h_s^3} - \frac{1}{h_d^3}\right]$ where Q is flow rate, w is the width of barrier, L is the length of the channel, μ is the viscosity, h_s and h_d are the heights of shallow and deep lanes respectively. The multi-level lane design generates high enough pressure difference across the barrier ($\Delta P_{\text{barrier}}$) to deliver a strong cross flow from the shallow to the deep lane. This was confirmed by examining the flow pattern of two dye labeled parallel streams in a straight channel with uneven lane depths (shallow lane: 20 µm, deep lane: 40 µm, centerline barrier gap: 7 µm deep, flow rate = 2mL/min), where the blue dye is transported across the barrier to the deeper end near the channel inlet (Figure 48 a). Simulated particle tracks reveals that the strong cross flow in the barrier region transports the particles near the barrier at the shallow lane (blue and green particles) while particles further away (red particles) from the barrier are transported downstream to the outlet under the influence of the channel pressure drop ($\Delta P_{\text{channel}}$) without being separated. Similar migration trends are observed when paths of 2 micron fluorescent particles were analyzed experimentally (Figure 48 a). For channels with unequal depths across the barrier (cross section: 20-7-40 and 30-7-40 µm (inner-gap-outer)), it was found that the particle separation efficiencies dramatically increased when compared to even height channel with separation efficiencies going as high ~70% at low flow rates (0.1 mL/min) and dropping by 10-20% at higher flow rates (2.5 mL/min) (Figure 48 b).

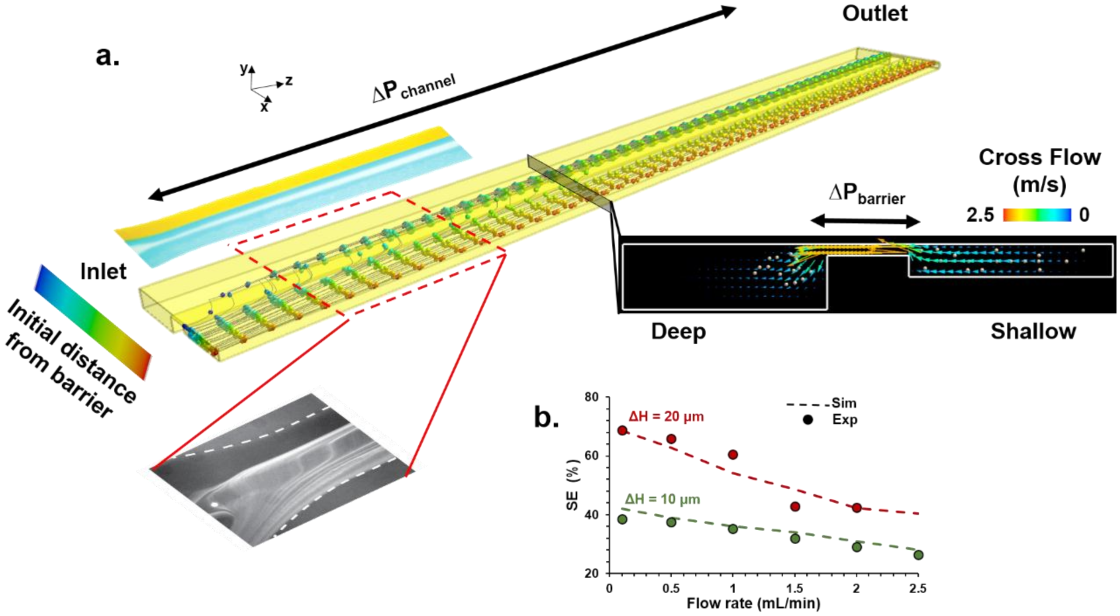

Figure 48: Straight channel with uneven height. Barrier embedded in straight channels with height difference (shallow lane: 20 µm, deep lane: 40 µm, centerline barrier gap: 7 µm deep, radius of curvature: 500 µm) (a) Two parallel dye streams co-injected into the deep (yellow) and shallow (blue) channel reveals an immediate transfer of the blue dye from the shallow lane to the deep lane at the inlet suggesting a strong barrier cross flow (flow rate = 2 mL/min). The positions of the simulated particles evolve under the action of the barrier pressure drop ($\Delta P_{barrier}$,*x* direction) and the channel pressure drop ($\Delta P_{channel}$,*z* direction) and depending of their relative magnitudes, the particle may either cross the barrier or remain in the shallow lane. Fluorescent particle streak-lines confirm maximum particle migration form the shallow to the deep lane near the inlet in accordance with simulated particle trajectories (flow rate = 2 mL/min). (b) The separation efficiency (particles in the outer lane/ total particles; at outlet) of particles decreases as the flow rate increases for both channels with unequal depths (cross section: 20-7-40 and 30-7-40 µm (inner-gap-outer).

At first, this seems to be in odds with the finding that $\Delta P_{\text{barrier}}$ increases with flow rate which in turn should increase the separation efficiency. However, simulations also reveals that the pressure drop across the channel length ($\Delta P_{\text{channel}}$) which drives the particles downstream, increases at a much faster rate with increasing flow rate (Figure 49 a). One can thus construct a dimensionless pressure drop ($[\Delta P_{\text{barrier}}/\Delta P_{\text{channel}}] * [L/w]$) to represent the tendency of a particle cross over the barrier to the deeper side as opposed to exiting the channel without being separated. This dimensionless pressure is larger for channels with a larger height difference between the shallow and deeper lanes (ΔH) and decreases on increasing the flow rate (Figure 49 b). It was found that data points obtained for geometries with three different ΔH at five different flow rates tend to collapse in a linear fashion when viewed on the dimensionless pressure – separation efficiency plot (Figure 49 c). Thus the dimensionless pressure which embodies information about both the geometric parameters of the channel (ΔH, L, w) and the flow rate (Q) can ultimately provide important insights about design guidelines and operating conditions for manufacturing better separation devices.

Separation in a channel featuring both a curved sections and unequal heights

After separation these particles are focused near the barrier region in the deeper lane and therefore have a tendency to migrate back to the shallow lane once the barrier pressure equalizes near the channel outlet (Figure 50). Also, the particles in the shallow lane which are further away from the barrier don't get separated as there is no mechanism to transport them towards the barrier. We therefore explored the addition of a curved region into this "free" movement zone to generate secondary flow that reinforces particle migration to enhance separation efficiency (shallow lane: 20 µm, deep lane: 40 µm, centerline barrier gap: 7 µm deep, radius of curvature: 500 µm, Q = 2 mL/min, κ = 44.25).

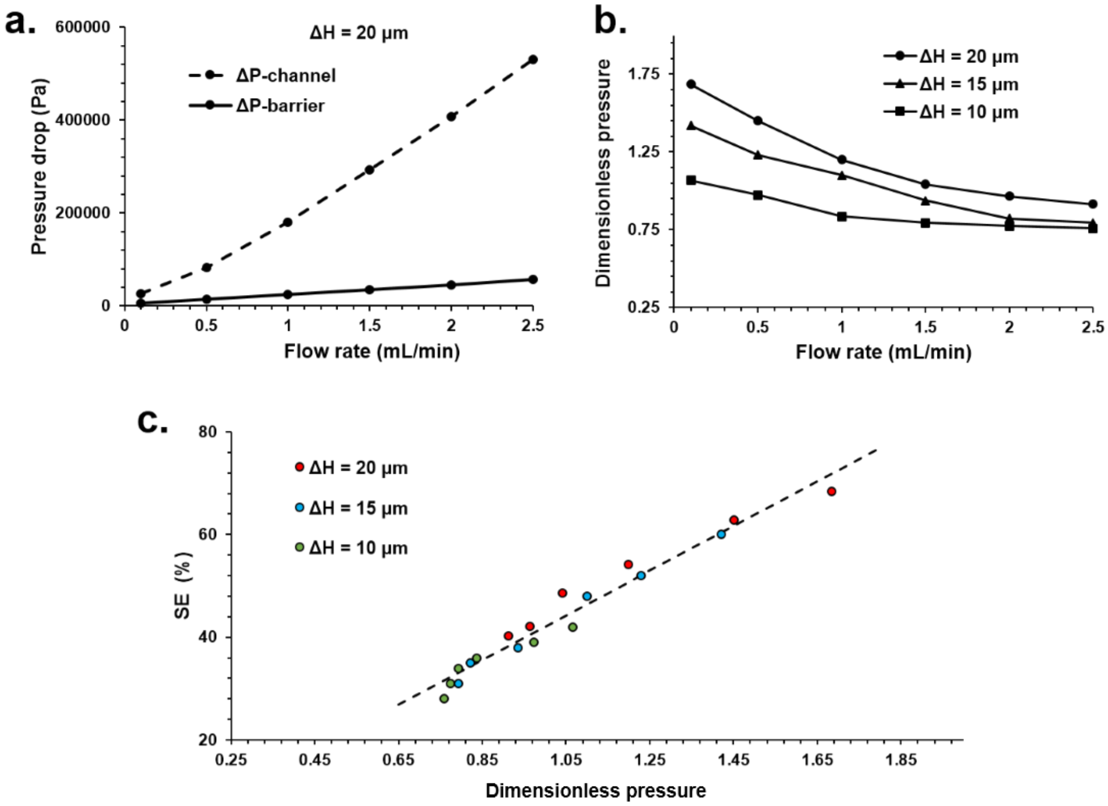

Figure 49: Separation efficiency as a function of dimensionless pressure in the channel. (a) The rate of increase of the $\Delta P_{channel}$ is much faster than the rate of increase of $\Delta P_{barrier}$ with increasing flow rate. (b) A dimensionless pressure ($[\Delta P_{barrier}/\Delta P_{channel}]*[L/w]$; L and w represent the length and width of the channel respectively) can then be defined to assess the ability of an uneven height channel to separate particles. (c) Data points for flow in three different geometries at different flow rates tend to collapse linearly suggesting important channel design rules to obtain better separation efficiency.

The added curved section redistributes the blue dye from the inner to the outer end of the deeper lane due to secondary Dean vortices which is also mirrored in the motion of fluorescent particles (Figure 51 a). The simulated velocity field gave us an overlook that the secondary flow was directed from inner lane towards the outer lane and the symmetrical counter rotating vortices were present in both lanes (Figure 51 b). Thus, particles experience a centrifugal driving force which directs them towards the outer half of the curved flow path—an effect that is enhanced by the unequal depths on each side of the central barrier (Figure 51 c).

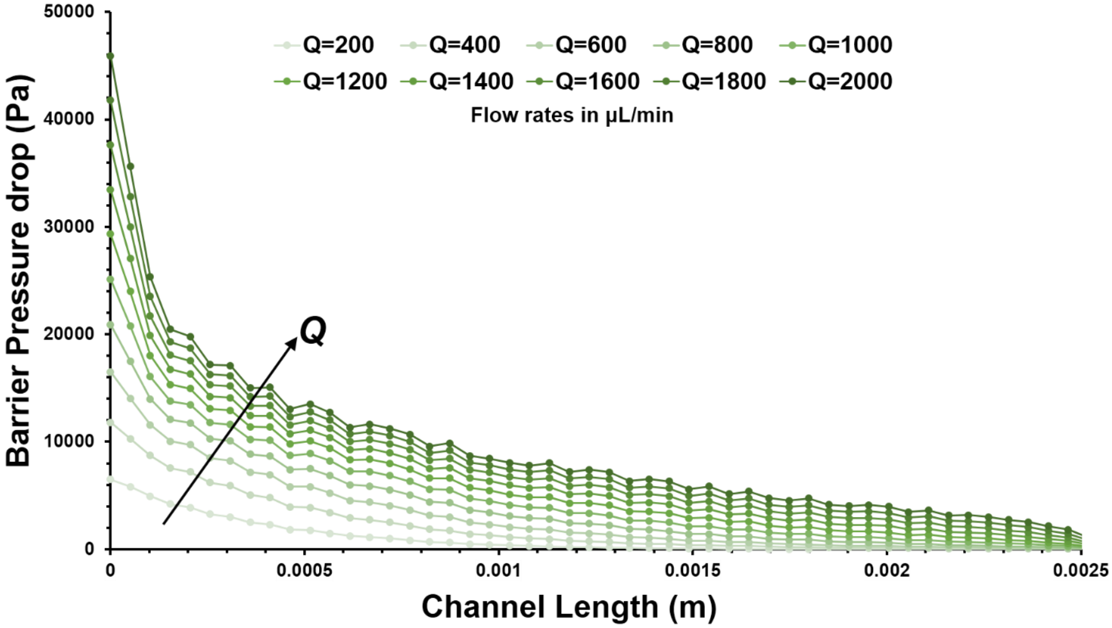

Figure 50: Pressure drop across the barrier near the inlet of a channel with uneven heights increases with increasing flow rate and falls sharply down the channel length at a given flow rate. This supports the view that a large fraction of the particles are separated near the inlet where there is high barrier pressure drop.

Along with the particles near the barrier (blue particles), particles away from the barrier (red particles) are also successfully separated as suggested by the simulated particle tracks (Figure 51 b**)**. This is because the Dean vortices in the curved section transports these particles from the outer edge of the inner lane towards the barrier where now under the influence of the barrier pressure they are able to cross over to the deeper end. The Dean vortices are also responsible for redistributing the separated particles focused near the barrier in the deep lane making it difficult for them to re-enter the shallow lane. The corresponding fluorescent particle tracks verify the particle migration from the shallow to the deep lane just after the curved section (Figure 51 b). Unlike other passive hydrodynamics in microchannels (i.e. diffusion dominated cross-flow filtration), the transverse barrier pressure driven by uneven height lanes provides a new separation mechanism simply affected by channel geometry and by introducing curvature induced secondary Dean vortices, lateral particle migration and separation efficiency can be enhanced up to 80 %, even at higher from rates (Q = 0.1 – 2.0 mL/min, κ = 2.2 – 44.25) making it ideally suited for high-throughput processing of large sample volumes (Figure 51 d). For the range of operating flow rates and channel dimensions the resulting Dean numbers (κ) are suitable to generate and sustain two symmetric counter rotating vortices to enhance separation efficiency (Figure 52).

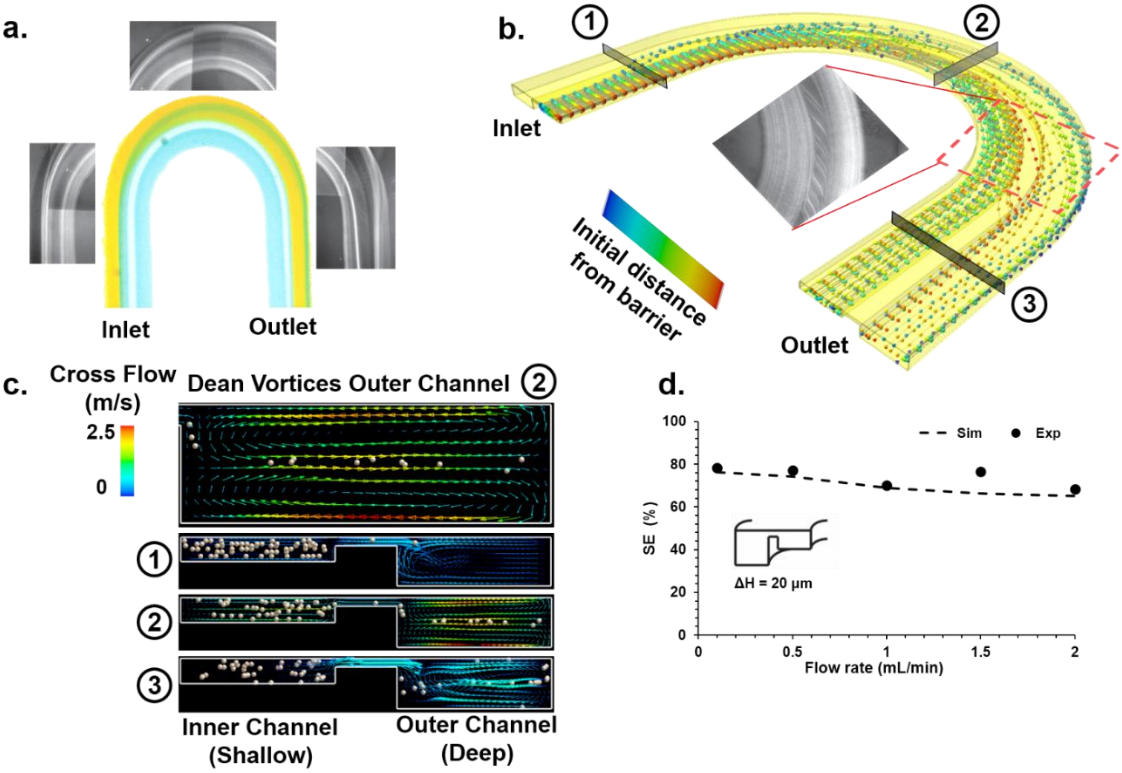

Figure 51: Curved channel with uneven height. Barrier embedded in a curved channel with height difference (shallow lane: 20 μm, deep lane: 40 μm, centerline barrier gap: 7 μm deep, radius of curvature: 500 μm, flow rate = 2mL/min). Blue dye injected into the shallow stream migrates to the deep lane and recirculates towards the outer edge as mirrored by the migration of fluorescent particles. (b) Simulated particle tracks suggest that even the particles away from the barrier (red) are separated as they are transported towards the barrier under the influence of (c) Dean vortices in the curved section. These secondary flow also defocuses the separated particles from the barrier vicinity in the deeper lane thus further increases separation efficiency. (d) The combined effect of uneven height across the barrier and curvature enhances the separation efficiency even at higher flow rates.

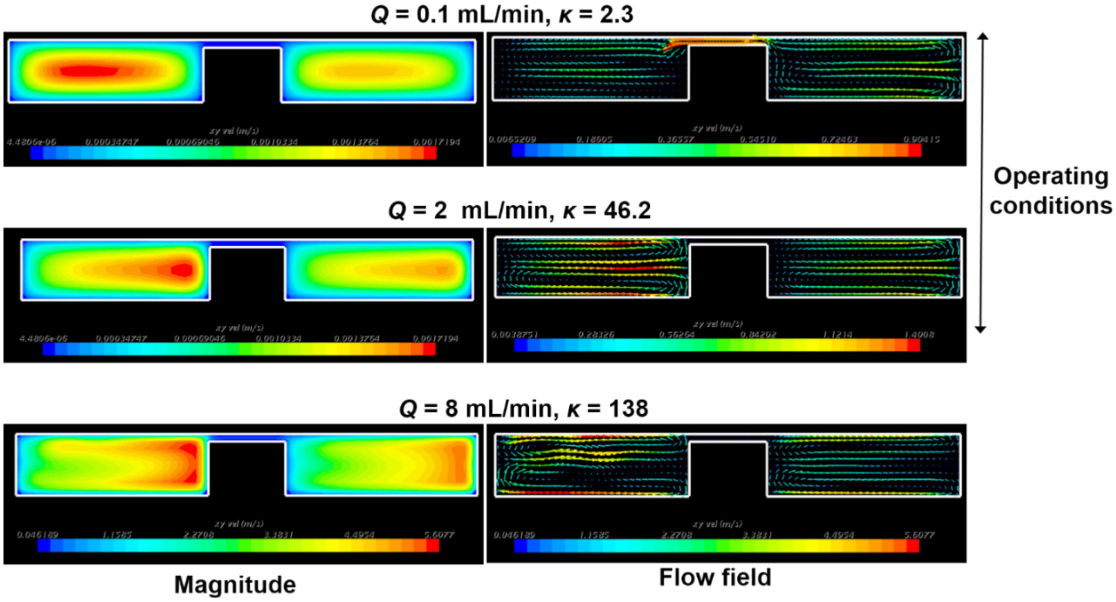

Figure 52: Secondary Dean flow in a curved microchannel. (inner and outer lanes: 40 µm deep, centerline barrier gap: 5 µm deep, radius of curvature: 500 µm). Secondary flow starts to appear in the curved section at low flow rates (Q = 0.1 mL/min, κ = 2.3) in the form of two symmetric counter rotating Dean vortices. These curvature induced symmetric rolls are stable under the operating flow rates of our interest and start to disrupt at higher flow rates (Q = 8 mL/min, κ = 138). ($\kappa = (D_h/2R)^{0.5}Re$, where D_h is the channel hydraulic diameter, R is the flow path radius of curvature, and Re is the Reynolds number with the hydraulic diameter as the length scale)

Conclusion

We have demonstrated high throughput separation of distinct sized particles in curved and straight channels with a central barrier filter. This separation mechanism is distinct from conventional cross-flow filtration methods where devices are specifically designed to suppress inertial effects [158, 188-191]. The membrane less arrangement does not impose an excessive pressure drop and is less susceptible to clogging because the barrier is oriented parallel to the flow direction rather than perpendicular to it so that the primary flow continually sweeps material downstream. This approach is most effective at high flow rates where the curvature-induced forces are maximized, making it ideally suited for high-throughput processing of large sample volumes.

CHAPTER VII

EDUCATION: DNA REPLICATION USING MICROSCALE NATURAL CONVECTION[*]

Introduction

Microfluidics is an incredibly versatile field encompassing a host of disciplines including engineering, biotechnology, physics, chemistry, and microelectronics. As discussed in chapters I-III, one area where miniaturization has proven to be particularly impactful involves analysis of minute quantities of DNA. Here, a major challenge lies in the design of instrumentation used to perform a key step in the analysis. This step, the polymerase chain reaction (PCR), consists of a sequence of thermally activated biochemical processes that selectively replicate well-defined sub regions within a longer DNA strand.[192] The PCR is incredibly efficient (the number of DNA copies increases exponentially with each cycle; 2^N after N cycles) and is straightforward to perform. Typically, a reagent mixture containing template DNA, primers, dNTPs, thermostable *Taq* polymerase enzyme, and buffering agents is dispensed into plastic reaction tubes or multiwell plates that are then inserted into a programmable thermocycling machine. This instrument has a single function: to repeatedly heat and cool the reagent mixture through 30 – 40 cycles between temperatures corresponding to *denaturation* of the double-stranded target DNA, *annealing* of primers to complimentary locations on the denatured

---

[*] Reprinted with permission from “Education: DNA replication using microscale natural convection”, A. Priye, Y. A. Hassan and V. Ugaz, 2012, *Lab on a Chip*, 4946-4954, Copyright 2012 by RCS publishing.

single-stranded fragments, and enzyme catalyzed extension to synthesize the complimentary strands.

Microfluidic approaches have been widely explored to enable the PCR to be performed faster, less expensively, and with greater portability. One innovative methodology involves harnessing convective flows such as those initiated by the buoyancy driven instability that arises when a microfluidic enclosure is heated from below (Rayleigh-Bénard flow)[3, 13, 31, 193-197]. By applying a static temperature gradient across an appropriately designed reactor geometry, a continuous circulatory flow can be established that will repeatedly transport PCR reagents through temperature zones associated with each stage of the reaction (Figure 53). Thermocycling can therefore be actuated in a pseudo-isothermal manner by simply holding two opposing surfaces at fixed temperatures, eliminating the need to repeatedly heat and cool the instrument. The interplay between the destabilizing buoyancy force and the opposing action of thermal and viscous diffusion is expressed in terms of the dimensionless Rayleigh number ($Ra = [g\beta(T_2 - T_1)h^3]/\nu\alpha$; where β is the fluid's thermal expansion coefficient, g is gravitational acceleration, T_1 and T_2 are the temperatures of the top (cool) and bottom (hot) surfaces respectively, h is the height of the fluid layer, α is the thermal diffusivity, and ν is the kinematic viscosity).

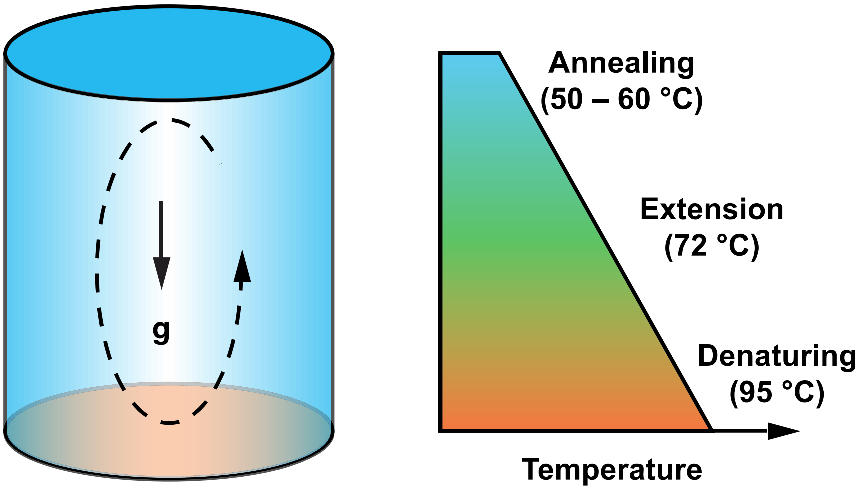

Figure 53: Thermal convection in a cylindrical chamber whose top and bottom surfaces are maintained at different fixed temperatures. If the temperature at the bottom surface is higher than at the top, a vertical density gradient is established within the enclosed fluid that is capable of generating a circulatory flow pattern. With the right choice of geometric parameters (height *h* and diameter *d*), the convective flow field can be harnessed to actuate PCR thermocycling when the top and bottom surfaces are maintained near annealing and denaturing temperatures, respectively (gravity acts vertically downward).

Optimal design of convective thermocyclers involves selecting reactor geometries that generate circulatory flows capable of transporting reagents through the temperature field in a manner that maximizes the DNA replication rate. The geometric parameters that can be varied to accomplish this are the height (*h*) and diameter (*d*), or equivalently the aspect ratio (*h*/*d*). We have explored 3-D flow fields inside microliter convective PCR reactors over a range of different aspect ratios using computational fluid dynamics (CFD), and found that unexpectedly complex patterns can emerge. More importantly, our analysis has uncovered a subset of these complex flow fields that significantly accelerate the reaction. Extremely rapid DNA replication timescales (under 10 min) are achievable in reactors designed to generate these flows.[14]

Inspired by the conceptual simplicity of the convective thermocycler design and its ability to uniquely merge fundamental concepts in transport phenomena and biochemistry, we have formulated laboratory exercises that guide students through the process of designing, building, and operating microfluidic convective PCR thermocyclers. Here we describe our efforts to implement this educational experience in two different ways during the Spring 2012 semester.

Hands-on convective PCR lab

The molecular biology component was highlighted in a hands-on microfluidic convective PCR laboratory experience presented to students enrolled in a professional science master's program in biotechnology (Texas A&M Professional Program in Biotechnology; ppib.tamu.edu). For this audience, we devised an experientially oriented assignment tailored toward a scenario of evaluating new technology (as might occur in a biotech company). Prior to beginning the lab experiment, the concept of convective PCR was presented in a lecture and reinforced by a video demonstration we produced.[198] DNA replication experiments were performed using dedicated convective PCR stations (Lynntech, Inc.) that incorporate a simple design for loading and mounting plastic cylindrical PCR reactors between independently controlled thermal plates (Figure 54 a, b). Each station interfaces with a Windows-based PC via a USB connection, and is operated by a custom designed software package that enables temperature profiles to be easily input and monitored (Figure 54 c). All components are sufficiently portable to enable easy setup in virtually any lab or classroom environment.

Reactions were performed in both convective and conventional thermocyclers to enable comparison of reaction time and replication efficiency. Each student was provided with a set of reagents to make a 50 µL PCR master mix, and students practiced loading and sealing the cylindrical cells with water before proceeding with the reagents (Figure 54 d). Appropriate volumes were aliquoted into the convective cell, with the remainder retained for use as the conventional thermocycler control. Each student was given a different reactor geometry to evaluate. After starting reactions in a conventional thermocycler (T-Gradient; Biometra), students loaded the cylindrical cells with reagents and mounted them in the convective PCR instrument (Figure 54 e). Temperatures of the upper and lower surfaces (55 and 95 °C, respectively) were set and maintained via the instrument software. After a sufficient reaction time elapsed (~ 10 – 20 min), the cells were removed and the products were stored until completion of the conventional thermocycler reaction (1 – 2 h). Products were analyzed using agarose gel electrophoresis (Figure 54 f).

A Keyence VW-6000 motion analysis microscope enabled flow patterns inside the convective PCR reactors to be directly visualized and recorded (Figure 54 g, h). Visualization was accomplished by loading an aqueous dispersion of 10 µm florescent polystyrene beads (Fluoresbrite YG; Polysciences) into the convective reactors to serve as tracers. Blue laser pointers (available for under $20 US each at amazon.com) mounted on portable camera tripods provided an inexpensive and highly effective illumination. The video images from the Keyence motion analysis microscope were projected onto a screen using an LCD projector so that the internal convective flow field could be easily visualized. If flow visualization is to be performed for a long period of time, it is recommended to density match the fluid to the microspheres (e.g., using sucrose) to reduce sedimentation.

Since the students were experienced with PCR through prior coursework, they were therefore asked to critically evaluate both technical performance (in terms of raw speed, sensitivity, specificity, etc.) and practicality from a product and end-user standpoint (in terms of operator input, sample and instrument preparation, turn-around time between runs, cost of components and consumables, etc.) in comparison with traditional instruments. They were also asked to make recommendations about what improvements could be made to make this device competitive with existing technology. Questions from the assessment assignment included the following.

Initial impression: Describe your initial impression of this technology based on hearing about it in the lecture (*before* attempting it in the lab). What advantages and disadvantages did you foresee? What questions did you have in your mind about the technology?

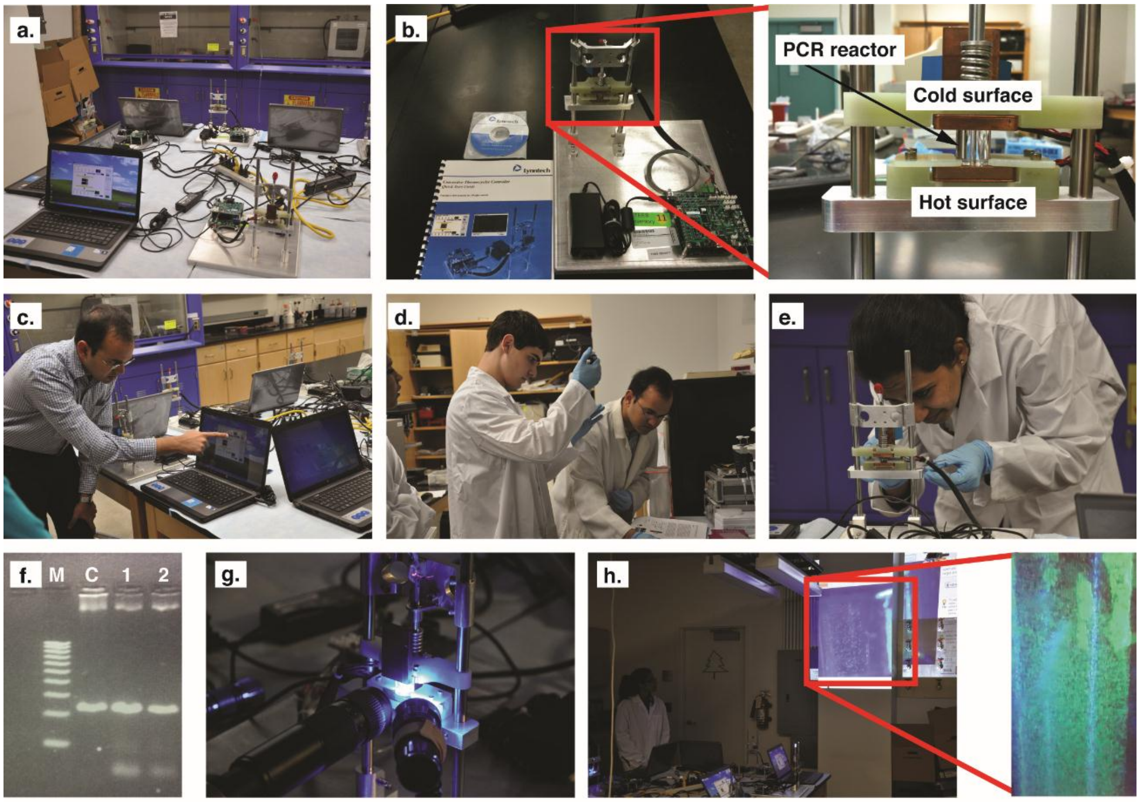

Figure 54: Design of the convective PCR laboratory experience presented to students enrolled in a professional science master's program in biotechnology. (a) Individual convective PCR stations used in the hands-on lab activity. (b) Cylindrical transparent reactors with various geometries ($d \sim 1 – 2$ mm, $h \sim 1 – 2$ cm) are clamped between upper and lower heating plates. (c) Reaction temperatures are controlled and monitored using a software interface in a USB connected PC. (d) PCR reagents are prepared and sealed inside the cylindrical reactors, after which (e) they are loaded into the heating device. (f) After the convective and control reactions are complete, the products are analyzed using gel electrophoresis (lane M: 100 bp ladder, lane C: control reaction run in conventional thermocycler; lanes 1,2: two independent reactions run in the convective thermocycler at $h/d = 6$. (g) Flow visualization is performed using a portable motion analysis microscope by loading a cylindrical reactor with an aqueous suspension of fluorescent bead tracers. (h) The microscope's video image can be projected to reveal the internal flow patterns.

Using the instrument: Briefly discuss your experience in operating the instrument (sample loading, software operation, etc.). In your opinion, would an average lab technician be able to operate a system like this? Why or why not?

Performance: Compare the performance of the instrument with conventional PCR thermocyclers. Would you characterize it as better or worse than the conventional instrument (and by how much)? Briefly explain your answer.

Final impression: Having completed the lab, describe how your impressions of convective PCR technology have changed. Describe how using the device was similar or different than you expected. What areas are the most promising? What aspects could be improved?

Future applications: In what markets or application areas (if any) could you envision this instrument being used? Briefly explain. What barriers could you foresee to entry into these markets?

Initial impressions conveyed skepticism because the concept was in a research stage, as opposed to a commercial product. Some comments included “I was skeptical about the convective PCR technology when I first heard about it. If it was so advantageous, why was it not already in the market?”; “It did not occur to me that convection currents could be used for PCR. The major question in my mind is why has this technology not been commercialized yet?”; and “It was tough to imagine that PCR can be done in such less time.”

After completing the lab, however, the students’ impressions changed to focus on the simplicity of operating the device. It should be noted, however, that these perspectives were shaped by the student's prior hands-on knowledge of performing PCR in a molecular biology lab setting. Comments along these lines included "This is a great lab to take, but you have to know and understand to take away this lab's implications. If you have never mixed together a PCR reaction and waited on a thermocycler, then you won't understand how significant this technology is." and "I see the entire practical lab experience in front of me. The concept and the steps are clear to me which is a testament to the simplicity of the instrument." It was also evident that being able to actually see the internal flow field within the reaction chamber using fluorescent bead tracers effectively conveyed the operating principles of the device, as expressed in comments like "It was simply amazing to actually see the movement of the sample based on different aspect ratios." and "One specific thing that comes to my mind when I think about the experience is the circulation of the fluid within the cell shown with the help of fluorescent beads."

These responses helped catalyze a discussion about issues involved in successful commercialization of basic research. This is a process that involves multiple steps on a myriad of levels, each with its own considerations. Often research that appears promising in the lab is not ultimately successful as a commercial product for reasons that may have little to do with the scientific or technical merits of the innovation. The students (and instructor) came away with an increased awareness of these issues, and a greater focus on this aspect is planned in future labs targeted at this audience.

Some challenges were encountered in tailoring the content to the appropriate audience, and adjusting the scope of the hands-on activities to fit the time constraints of the allotted class period. We dealt with this by performing some rinsing and preparation steps prior to beginning the lab. This needs to be considered, however, when evaluating student comments about the device operation. Some timing issues also arise when students simultaneously run reactions using different geometries in which the reaction needs to be performed for different lengths of time. We found that it was desirable to have all students begin their reactions simultaneously to ensure synchronized timing, especially with a larger class size. The video introduction to convective PCR was helpful because students can watch it additional times outside of class to help familiarize them with the fundamental concepts. The lab protocol incorporates downtime during the gel electrophoresis analysis that can be used to demonstrate the flow patterns inside the reactors using fluorescent beads. Alternatively if time is short, the gel separations can be performed by the instructor and results returned to the students at the next class period.

Computational simulation of microscale thermal convection

The undergraduate implementation focused on computational simulation of microscale convective flow fields as part of a three class-period module in the undergraduate core fluid mechanics class in the Department of Chemical Engineering at Texas A&M (incoming Junior-level students), part of a three course transport sequence covering momentum, heat, and mass transport. The first class period consisted of a two-part lecture aimed at presenting the fundamental concepts underlying buoyancy driven convective flows. First, students were introduced to PCR biochemistry and its application in molecular biology. Reference to DNA analysis in the context of forensics and infectious disease surveillance was incorporated to help students connect the concepts with real world applications and identify how this set of tools can be applied in a variety of important and relevant ways. We also emphasized the timely tie-in with broader ongoing research throughout the microfluidics community (including our own research group) and pointed out how this represents a “non traditional” application of fluid mechanics. The second part of the lecture then presented fundamental aspects of buoyancy driven convective flows, using the design of lava lamps as a relatable illustrative example. This content was designed to integrate with other coursework in the transport sequence. Some key learning outcomes included:

- Apply the conservation of momentum in the case of a buoyancy driving force, and compare the resulting governing equations with the case of pressure driven flows previously studied in the course.
- Define and explain the Boussinesq approximation, whereby thermal variations in density are only considered in the buoyancy source term where a linear temperature dependence is assumed ($\rho = \rho_0[1 - \beta(T - T_0)]$; ρ is the fluid density and the subscript 0 refers to a reference state).
- Demonstrate ability to non-dimensionalize the momentum balance to obtain the Rayleigh number, analogously to how the origin of the Reynolds number was presented earlier in the course.
- Demonstrate ability to apply the conservation of energy and show how it is coupled with the momentum balance through temperature.
- Explain how the fluid properties and temperatures associated with PCR constrain the problem, leaving geometry (h and d) as the key adjustable parameter.

- Identify appropriate boundary and initial conditions to fully specify the mathematical problem.
- Appreciate that the complexity of the resulting system of nonlinear partial differential equations requires computational tools to solve.

The second and third class periods were held in the computer lab (Figure 55). During the first half of the second class period, students were introduced to CFD and the considerations involved in creating computational models. Some of the concepts emphasized included application of numerical differentiation within discretized domains and a comparison between finite element and finite difference schemes, connecting with related coursework in numerical methods; and an overview of computational modeling, focusing on the importance of grid/mesh generation and highlighting tradeoffs between accuracy and computation time. The heat conduction equation was presented as an archetypical problem to illustrate application of the finite difference scheme in a 2D domain. Common solution algorithms were also discussed. We then showed how this basic framework can be applied to the more complex set of coupled PDEs associated with the convection problem. A key point we repeatedly emphasized was that the underlying physics and governing equations remain identical to those previously presented in class. Although not a comprehensive treatment, this basic knowledge equipped the students to appreciate the CFD "toolbox" and its usefulness to solve complex 3D problems. Ideally, these facets of the problem would dovetail with a dedicated numerical methods course in the curriculum, with microfluidic thermal convection offering a convenient archetypical problem to help establish this connection.

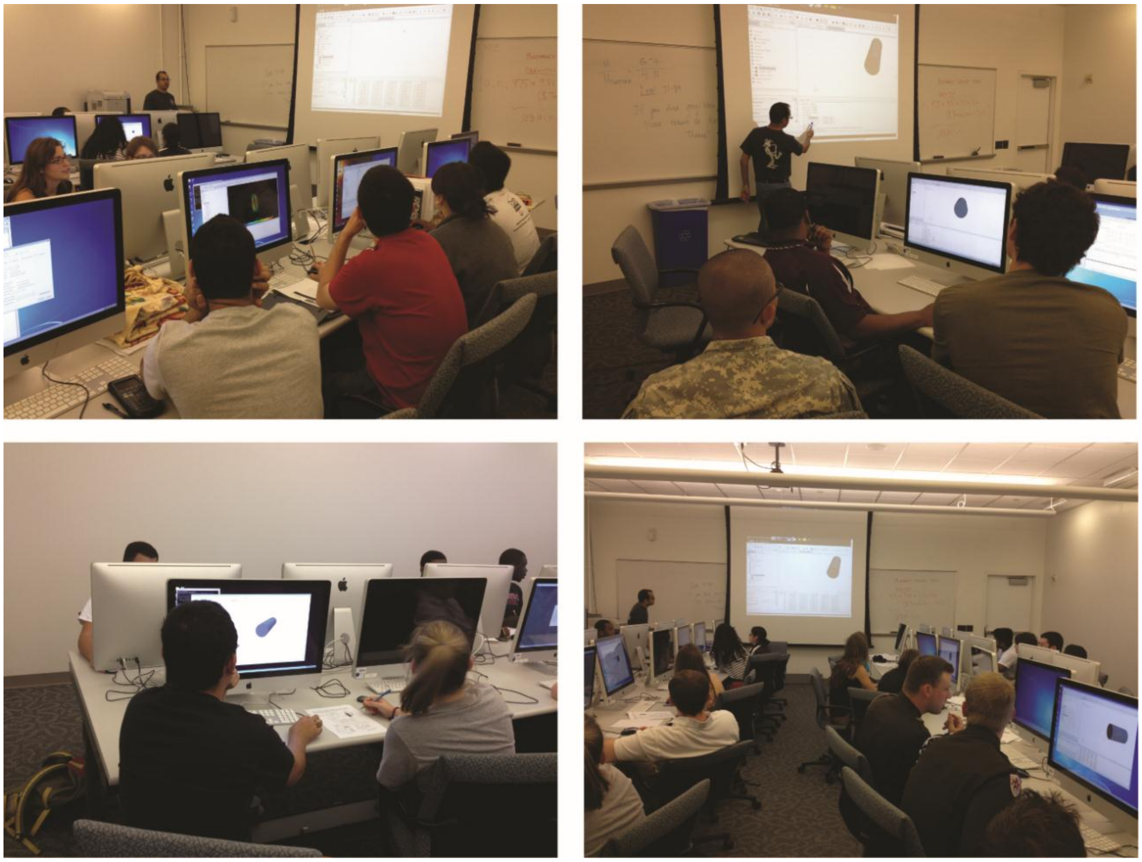

Figure 55: Design of a Computational fluid dynamics laboratory for undergraduate students. Hands-on CFD modeling exercise delivered to an undergraduate fluid mechanics class. Students worked in teams of two to simulate the velocity and temperature fields inside various convective reactor designs and evaluate which ones may be best suited for PCR.

With this background, the students proceeded to set up their own computational models of microscale natural convection in a cylindrical geometry heated from below during the second half of the class. 3D models were created using STAR-CCM+ software (CD-adapco), following a step-by-step procedure outlined in a lab manual we distributed to the students. We selected STAR-CCM+ owing to its enhanced flexibility to handle biochemical reaction kinetics relevant to PCR, and because a 3D model is necessary to fully capture the flow phenomena (2D models can also be constructed using COMSOL multiphysics [17, 199]). The partial differential equations governing conservation of mass, momentum, and energy are cast in terms of dimensionless variables (v^*, p^*, θ, t^*, *Re*, *Ra*, and *Pr*; representing velocity, pressure, temperature, time, Reynolds number, Rayleigh number, and Prandtl number respectively).

$$\begin{aligned} &\nabla^* \cdot v^* = 0 \\ &\frac{\partial v^*}{\partial t^*} + v^* \cdot \nabla^* v^* = -\frac{1}{\mathrm{Re}} \nabla^* P^* + \frac{\mathrm{Ra}}{\mathrm{Pr}} \theta \hat{e}_z + \frac{1}{\mathrm{Re}} \nabla^{*2} v^* \\ &\frac{\partial \theta}{\partial t^*} + v^* \cdot \nabla^* \theta = \frac{1}{\mathrm{Re.Pr}} \nabla^{*2} \theta \end{aligned} \qquad [7.1]$$

We found that providing students with a basic model as a starting point, with a pre-generated mesh geometry and pre-entered solver parameters not relevant to the physics, allowed class time to be used more efficiently. Students were responsible for correctly specifying the buoyancy driving force term, boundary conditions, and reactor dimensions. Finally, an assignment was distributed during the remaining class period that asked students to simulate the steady-state velocity and temperature fields associated with microscale thermal convection, and evaluate the effect of employing different cylindrical geometries by scaling the reactor dimensions to match given aspect ratios. A unique set of geometric conditions was assigned to each team, but algfl were chosen to include flows associated with regimes near the onset of convective motion, uniform circulatory flow, and chaotic advection. This enabled students to practically judge the significance of geometric parameters in the model in determining the steady state flow field. Finally, a subset of the assigned convective flow fields were experimentally demonstrated in class using the aforementioned portable motion analysis system to validate the results of the computational simulations.

We would like to emphasize that our goal in the context of this exercise was not to provide CFD training in one or two lectures. Our objectives were more focused: (1) to show how the governing differential equations and boundary conditions are implemented in a computational package, (2) to demonstrate how a driving force different from pressure driven flow can be applied, and (3) to use the simulation as a visualization tool to see the results of a problem that cannot be treated analytically. While it is not realistic to expect that the students will possess significant expertise in CFD simulations after completing this exercise, the micro-scale Rayleigh Bénard problem offers several uniquely attractive features that make it well-suited as a vehicle to introduce these concepts. First, it provides an unusually rich complexity of flow phenomena extending beyond conventional pressure driven laminar flow through a microchannel of rectangular cross-section (this is not always the case, but speaking in general). Second, since only the Rayleigh number and aspect ratio need to be varied to access these diverse flow regimes, construction of the CFD geometry is greatly simplified. In fact, this feature allowed us to assign multiple cases to each group of students using the same computational geometry (i.e., the same height to diameter ratio), albeit with different physical dimensions (i.e., different combinations of h and d yielding the same h/d). In other words, the same aspect ratio can yield different flow regimes depending on the value of h because this parameter also determines the Rayleigh number. This unique feature allows the focus of the assignment to be directed away from geometry construction/meshing, so that the physics can be better emphasized.

Cognitive assessment

Although a variety of assessment methodologies can be applied to evaluate student perceptions associated with this kind of coursework (e.g., see the review by Marsh [200]) we found that evaluation strategies specifically pertinent to virtual laboratories (i.e., computational labs) were not as widely documented. Some relevant examples we considered include those of Wolf [201] (evaluated student perceptions of a computer lab by comparing pre-lecture, post-lecture, and post-lab assessments) and Dalgarno, et. al. [202] (combined personal interviews with written responses to survey questions on a seven point Likert scale). Recently, Koretsky et. al. [203] described a methodology involving a set of free response questions presented after completion of the exercise. These survey questions were crafted to assess cognitive skills, content knowledge, critical thinking, simulation design, and situated nature. We selected this approach because the questions were simply designed yet framed in a way that evoked reflective responses (as opposed to ranking on a fixed point scale). This provided flexibility for us to group the responses into categories based on what we intended to be the most important aspects of the experience. We therefore felt that the reflective nature of this assessment instrument provided the most straightforward path to evaluate the cognitive impact of this exercise [204].

Cognitive impact was assessed by asking students to communicate their perceptions in a post assignment reflection consisting of the following free response questions.

1. What do you think the instructor intended for you to learn by doing the computational modeling exercise?
2. How would you explain this computational experience to an undergraduate student?
3. When you close your eyes and picture this computational exercise, what do you see?
4. Did the exercise influence your interest in fluid mechanics? If so, how (did it make it more interesting or less interesting) and why? Would you like to see more or less of these kinds of activities?

Responses were categorized based on the focus and learning outcomes of the computational assignment (each response could be assigned to multiple categories). A binary coding was then used to obtain a numerical score representing the responses in each category (1 if the response satisfied the category's criteria, 0 otherwise). Cognition was quantified based on the number of different categories addressed.

Question #1: "What do you think the instructor intended for you to learn by doing the computational modeling exercise?" Representative responses to this question included.

- *They intended for us to learn how changing the height and diameter changes the flow*
- *For students exposure to course material in practice*
- *Highlight how useful software can be for complex engineering problems*
- *How to implement what we learned in the course*

- *They wanted us to see the connection between courses such as fluids and numerical methods*
- *To see real world applications of the use of fluid dynamics*
- *That these computations are complex and can only be solved using CFD*
- *That we must rely on numerical methods to solve complex differential equations*
- *The instructor wanted us to see an example of fluid dynamics in real world applications*

Overall, the responses recognized that the instructor’s intent was to relate the modeling exercise to real world applications and future professional environments (situated nature), and to connect with material presented in class (specific content) (Figure 56 a). Approximately 40% of the responses demonstrated high cognition, based on the criterion of simultaneously addressing both of these categories. An example of a high cognition response was “The instructor wanted us to learn how to use the concepts taught in class for real world applications. Computational modeling is necessary to solve difficult problem that can’t be solved analytically.” Whereas an example of a low cognition response was “They intended for us to learn how to input specifications for a fluid and run its corresponding model.”

Question #2: “How would you explain this computational exercise to an undergraduate student?” Representative responses to this question included.

- *Exercise is very advanced but enjoyable*
- *Changing the height and diameter of the cylinder changes the flow*
- *After spending a semester learning the principles of fluid mechanics as well as applying it to pipe flow problems, this exercise allows you to compute and visualize flow fields through a simulator*

- *I will explain it with a lava lamp example*
- *The exercise uses supercomputers to calculate fluid flow due to temperature differences*
- *Confusing but easier to understand when looking at the visuals to see the overall concept*
- *I would describe the math behind the calculations*

Here, the majority of responses focused on connecting the exercise with current and future coursework in chemical engineering (specific content), with lower but approximately equal mention of ambiguity, lab skills and simulation design (Figure 56 b). In contrast to Question #1, only one response emphasized the real word application of the exercise. Again, approximately 40% of the responses demonstrated high cognition, based on the criterion of simultaneously addressing 3 out of the 4 categories (excluding situated nature). An example of a high cognition response was "Conceptually a first year college student should be familiar with convection. I would explain this exercise by describing the fundamental fluid flow equations: conservation of mass, momentum and energy and the temperature dependence of the density. I would describe the numerical procedure involved in the assignment and explain why computers are necessary to solve the problem." Whereas an example of a low cognition response was "I would explain it the same way it was explained to me in class."

a.

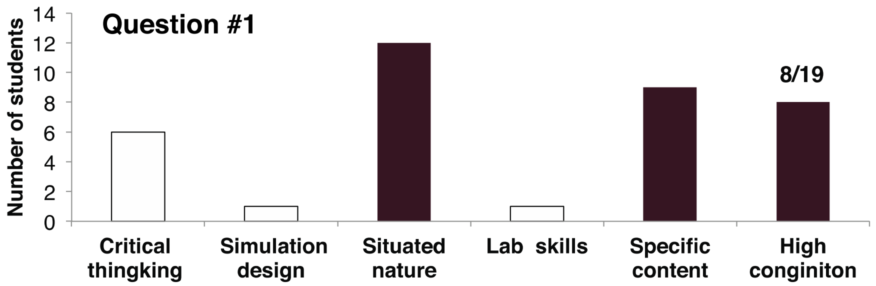

Category	Central theme: The instructor's intent was for the student to...
Critical thinking	Develop higher level of critical and creative thinking such as identification of the important simulation parameters.
Simulation design	Learn the nature of designing simulations including the process of indentifying problem statement and analyzing the results.
Situated nature	Place the modeling experience in the context of their future professional environments and real world applications.
Lab skills	Develop specific techniques and skills of hands on simulations assignment.
Specific content	Learn the specific topics or content within the simulation assignment or reinforce understanding of content learned in lecture classes.

b.

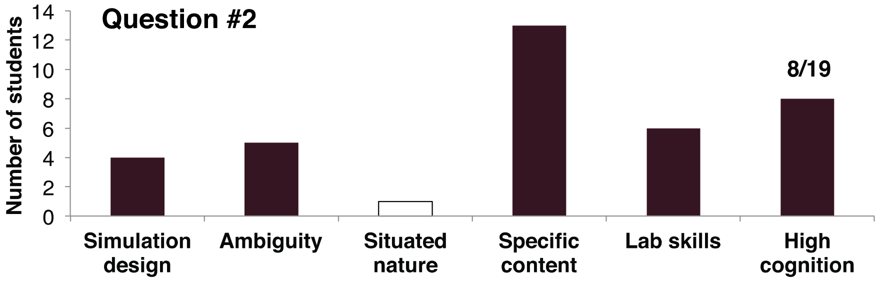

Category	Central theme: The computational exercise was described by...
Simulation design	Learning the nature of designing simulations including the process of identifying problem statement and analyzing the results.
Ambiguity	The ambiguous and open ended nature of the experience or how they need to adaptively learn.
Situated nature	Placing the laboratory experience in the context of their future professional environments and real world applications.
Specific content	Learning the specific topics or content within the simulation assignment or reinforcing the understanding of content learned in lecture classes.
Lab skills	Developing specific techniques and skills of hands on simulations assignment.

Figure 56: Student cognition was assessed through a series of three free response questions (*n* = 19). (a) Question #1: "What do you think the instructor intended for you to learn by doing the computational modeling exercise?" High cognition responses simultaneously addressed themes in the situated nature and specific content categories. (b) Question #2: "How would you explain this computational exercise to an undergraduate student?" High cognition responses simultaneously addressed themes in three of the following four categories: specific content, lab skills, ambiguity, and simulation design.

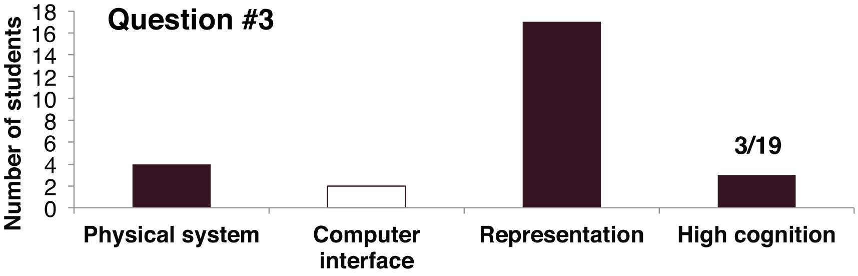

Category	Central theme: The student described seeing...
Physical system	Actual physical systems in real world/nature with convection driven flows.
Computer interface	The computer interface or supercomputers.
Representation	The analysis aspect of the exercise such as the flow patterns and temperature profiles.

Figure 57: Student cognition was assessed through a series of three free response questions (*n* = 19) continued. Question #3: "When you close your eyes and picture this computational exercise, what do you see?" High cognition responses simultaneously addressed themes in the representation and physical system categories.

Question #3: "When you close your eyes and picture this computational exercise, what do you see?" Representative responses to this question included.

- *I see rectangular box with arrows representing flow field*
- *The colors in the flow field and some cases would produce an 8 like flow field*
- *Velocity profile of the fluid*
- *Lava lamp, blobs falling and rising*
- *A plot with slowly converging lines*

Responses to this question overwhelmingly centered on visualization of the internal convective velocity and temperature profiles obtained in the computational simulations (representation) (Figure 57). Three responses related these patterns to other scenarios (e.g., the flow pattern in a lava lamp) and two of them described the computer interface. A high cognition response was therefore defined as simultaneously addressing the representation and physical system categories, a criterion satisfied by only 3 out of 19 responses. An example of a high cognition response was "I see the flow patterns generated by the computer program and how it matches with the lava lamp and the DNA synthesis example presented in class." Whereas an example of a low cognition response was "An interesting flow diagram."

Question #4: "Did the exercise influence your interest in fluid mechanics? If so, how (did it make it more interesting or less interesting) and why? Would you like to see more or less of these kinds of activities?" Representative responses to this question included.

- *All of sudden fluid mechanics seems very interesting to me, I would like to have more class periods dedicated to this*
- *It helps to put our class work into live action and see where our knowledge is leading us*
- *It's nice to see actual videos and moving things, as opposed to just equations*
- *It was interesting to see how changing a few parameters could greatly change the flow field*
- *I learned that fluid mechanics is more than just pipe flow problems with pressure difference as the driving force*
- *Yes, It made it more interesting. I never thought fluid mechanics application outside the class until this exercise. I would like to see more.*
- *I wish I could have set the entire problem myself in the program but due to lack of time I know this was not possible*

This question was not intended assess cognition, but instead captured overall student satisfaction with the computational exercise. Responses to this question were overwhelmingly positive, revealing that the CFD simulations seem to particularly excite student interest because it allowed them to actually “see” what they have been learning in the lecture. These impressions are consistent with broader student feedback we have received from recent graduating senior exit interviews where a desire for increased hands-on exposure to simulation tools was expressed.

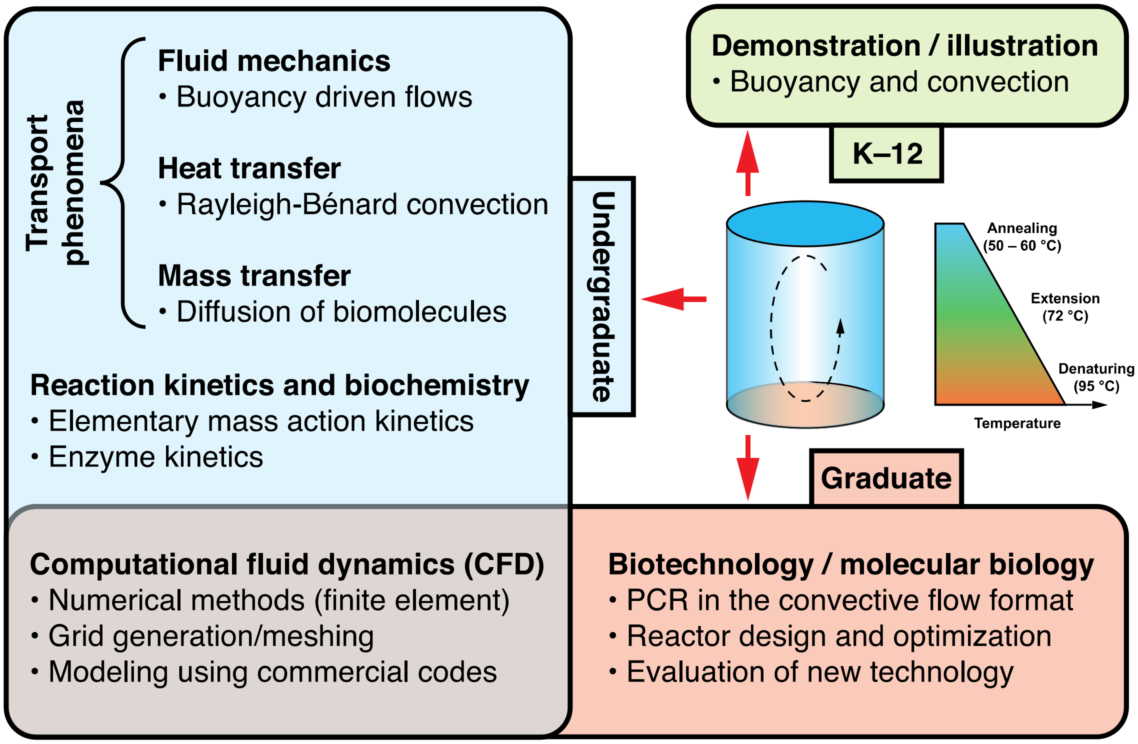

Figure 58: Microfluidic convective PCR bridges the physical, chemical, and life sciences in a uniquely relatable way. This incredible versatility enables educational experiences to be tailored toward a broad spectrum of audiences ranging from elementary school, to undergraduate, to graduate levels. Its portability and simplicity make it feasible to embed in a classroom setting.

A key conclusion from our cognitive assessment is that the hands-on computational exercise effectively reinforced course content, highlight connections with other courses in the curriculum, and demonstrate practical applications of the fundamental material presented in class. Interestingly, however, there appeared to be conflicting perceptions of practical application. This aspect was the most highly recognized in students' perception of the instructor's learning objectives (Question #1), but was the least recognized in students' perception of how they would explain the exercise to peers (Question #2). We also conclude that cognition could be improved by incorporating companion design or hands-on experiment components (Question #3). An additional challenge is that limited class time is available for students to become proficient using the computational software. For this reason, and due to introductory transport focus of the course, we did not include thermally actuated biochemical reactions in this simulation exercise. But this component can be readily incorporated, and we plan to do so in future courses with lesson plans focusing on the reaction kinetics of PCR and mass transfer of the biochemical reagents. This will ultimately enable students to evaluate a series of reactor designs to estimate thermal residence times and quantify reaction product yields.

Conclusions

There is currently a drive to incorporate more experiential and cross-disciplinary activities into science and engineering education.[205, 206] These active discovery-oriented experiences excite students and bolster understanding of fundamental concepts. Microfluidics offers an ideal platform on which to base these activities owing to its inherently low cost and portability, overcoming barriers that have previously hindered the ability to embed sustainable high impact learning activities in the classroom, particularly in large classes.[207, 208] But it is also important to assess cognitive impact in order to justify the effort and expense involved in crating these experiences.

The problem of microscale convective PCR provides a particularly effective vehicle to connect concepts bridging the physical, chemical, and life sciences. Part of this appeal stems from the rich complexity of flow phenomena that can be accessed in relatively simple geometries. Looking ahead, we envision that this foundation can be readily integrated throughout our undergraduate chemical engineering transport sequence and beyond because its strong multidisciplinary focus provides considerable flexibility to tailor instructional content across a range of target audiences (Figure 58). For example, we leveraged the portable flow visualization system to demonstrate micro-scale convective flows (micro-scale lava lamps) to students at a local elementary school during a recent science-themed event. This relatable activity, uniquely enabled by microfluidics, helped make the students aware of buoyancy and convection phenomena in nature. These research-connected experiences also create new opportunities for graduate students and postdocs to become deeper partners in the educational process (i.e., beyond traditional assignment-focused grading roles) by communicating their own scientific discoveries to a broader audience.

CHAPTER VIII

CONCLUSIONS AND FUTURE WORK

Conclusion

In this dissertation, both computational and experimental tools have been used to investigate the intricate features of the micoscale flows. Most of the content (Chapter I-IV, VII) focusses on harnessing microscale Rayleigh-Bénard convective flows to perform biochemical reactions and enhance surface chemistry.

Recently, Ebola has become a major worldwide health concern. With the outbreak in Africa, and isolated cases on other continents, the need for an affordable, rapid and portable diagnostic solution has been repeatedly stressed and is one of the most critical issues confronting global health. Unfortunately, the current conventional PCR instrumentation needed to perform “gold standard” DNA-based diagnostic tests is bulky, slow, and expensive, making it unsuitable for resource limited settings in developing countries where dedicated laboratory facilities are not available.

We have tried to address this need by coupling an innovative thermal convention based PCR system with a versatile smart-phone based detection unit enabling speedy diagnostics (10-20 minutes). PCR, a very important tool in molecular biology, requires repeated heating (~ 95 ºC, denaturing) and cooling (~ 55 ºC, annealing) of the reagents. Rayleigh-Bénard convective flows are able to execute these thermally actuated biochemical reactions in a pseudo isothermal fashion by driving the reagents from the hot to the cold regions repeatedly in a microscale cylindrical enclosure under a vertical temperature gradient. By altering the geometry of the enclosure (aspect ratio) and thermal boundary conditions (Rayleigh number), one can select convective flow states that exhibit periodic, quasi-periodic or chaotic trajectories. Computational fluid dynamics (CFD) studies reveal that reactors with smaller aspect ratios generate disordered flow fields (reflected by chaotic trajectories) that display a greater capacity to actuate PCR in convective format. Furthermore, coupling a PCR kinetic model with the CFD model reveals a wide range of cylindrical geometries exhibiting chaotic advection capable of enabling robust convective PCR.

With these new optimal design rules, we introduce an inexpensive, rapid, ultra-portable bio-analysis platform for nucleic acid-based diagnostics and surveillance of infectious disease. Our approach exploits the unique ability to isothermally execute PCR via a single miniature heater, dramatically reducing electrical consumption to a level provided by ordinary 5 V USB sources that power consumer mobile devices (even using solar or hand crank action). Time resolved fluorescence detection is achieved via a smart-phone camera and integrated image analysis app. These advancements make it possible to build a complete DNA analysis system for under $20 ($US) that can deliver results in 10 – 15 min. Our instrument is incredibly robust and lightweight, enabling pinpoint deployment of gold standard nucleic acid-based diagnostics to remote field sites using commercially available quad-copter drones. We also demonstrate in-flight analysis, suggesting potential to obtain an unprecedented dynamic picture of outbreaks that can inform improved resource deployment strategies.

Microscale Rayleigh-Bénard convective flows can also be found naturally within the pores of sub-sea hydrothermal vent systems. These porous mineral formations embed richly complex microenvironments capable of catalytically polymerizing monomers and orchestrating fundamental electrochemistry central to prebiotic evolution of metabolic processes. But a unified framework explaining how surface-mediated synthesis can be orchestrated by the interplay among physical, chemical, and thermal processes within these catalytically active networks remains elusive. We explored the emerging convective flows in hydrothermally relevant pore sizes and discovered that they have the capacity to act as highly efficient conveyors to continually shuttle molecular precursors from the bulk fluid to targeted locations on the solid boundaries where they assemble into membrane-like films capable of electrochemically generating pH gradients. We quantitatively mapped the enrichment of biomolecular species achievable via this process, and introduced an in situ approach to directly probe its influence on surface reaction kinetics. Our results suggest that chaotic thermal convection may supply a previously unappreciated driving force to support emergence of early bioenergetic pathways—a key unanswered question in the origin of life.

Our simple convective flow PCR system was also leveraged to create an innovative educational experiences that excite and empower students by helping them recognize how interdisciplinary knowledge can be applied to develop new products and technologies that benefit society. We created novel hands-on activities that introduce chemical engineering students to molecular biology by challenging them to harness microscale natural convection phenomena to perform DNA replication via the PCR. Experimentally, we constructed convective PCR stations incorporating a simple design for loading and mounting cylindrical microfluidic reactors between independently controlled thermal plates. A portable motion analysis microscope enabled flow patterns inside the convective reactors to be directly visualized using fluorescent bead tracers. We also developed a hands-on CFD exercise based on modeling microscale thermal convection to identify optimal geometries for DNA replication. A cognitive assessment revealed that these activities strongly impact student learning in a positive way.

Apart from the investigation of microscale convective flows, the dissertation also works towards development of a new adhesion model for particle resuspension modeling. The phenomenon of particle resuspension plays a vital role in numerous fields. Among many aspects of particle resuspension dynamics, a dominant concern is the accurate description and formulation of the van der Waals (vdW) interactions between the particle and substrate. Current models treat adhesion by incorporating a material dependent Hamaker's constant which relies on the heuristic Hamaker's two body interactions. However, this assumption of pair wise summation of interaction energies can lead to significant errors in condensed matter as it does not take into account the many body interaction and retardation effects. To address these issues, an approach based on Lifshitz continuum theory of vdW interactions was developed to calculate the principal many body interactions between arbitrary geometries at all separation distances to a high degree of accuracy through Lifshitz's theory. We applied this numerical implementation to calculate the many body vdW interactions between spherical particles and surfaces with sinusoidally varying roughness profile and also to non spherical particles (cubes, cylinders, tetrahedron etc.) orientated differently with respect to the surface. Our calculations revealed that increasing the surface roughness amplitude decreases the adhesion force and non spherical particles adhere to the surfaces more strongly when their flatter sides are oriented towards the surface. Such practical shapes and structures of particle-surface systems has not been previously considered in resuspension models and this rigorous treatment of vdW interactions provide more realistic adhesion forces between the particle and the surface which can then be coupled with CFD models to improve the predictive capabilities of particle resuspension dynamics.

Finally, we employ discrete element modeling to analyze trajectories of micro sized particles subject to all relevant hydrodynamic forces and torques. The results provide us with important design rules to construct membraneless microfluidic filtration channels where pressure driven transverse flows and curvature induced Dean flows can be simultaneously harnessed to assist size based particle separation with high throughput.

Future work

Quantification of chaos in convective flows

In Chapter I, we visualized the onset of chaotic advection via Poincaré sections and quantifed the convective flow's chaotic strength by calculating the Lyapunov exponents. However, study of chaos in such microscale flow systems is fairly new, and further investigation can provide additional insights about the flow characteristics. There are other parameters available to quantify chaos in such time series dynamical variable systems, including the correlation dimension and the box dimension. The correlation dimension has been used extensively in literature to characterize chaotic attractors[209]. The advantage of using this method is that one can quantify the chaotic nature of the flow field from a one-dimensional time series data representing the flow field. Thus, nonlinear time-series and chaos analysis techniques can be used to gain insight about the the dynamical nature of the flow field in these systems. The box counting method is another metric uset to quantify the extent of mixing in flows[210]. Tracer particles are initially positioned within a small segment of the flow domain which is divided into numerous small boxes. As the flow evolves and the tracer particles spread, they occupy an increasing number of boxes. The rate of increase of box occupancy (box entropy) provides an estimate of the rate of mixing and stretching statistics in the system. In future work, we would like incorporate these two techniques in our study of Rayleigh-Bénard convective flows to not only quantify the chaotic streingth of the system but also the rate at which chaotic advection emerges. This would provide us with information about time required for such systems to evolve into a chaotic strength.

Refinement and enhancement of the convective PCR device

While our convective PCR device has a simple design and is fairly easy to operate, we want to pursue additional modifications to to improve its performance and reliabiltiy. Firstly, sample loading can be simplified. Currently, the user needs to use thin pipette tips to inject the PCR mixture into the cylindrical reactor followed by carefully sealing the reactor top with an adhesive film. We want to make this step easier to perform by users who may not have specialized training. One way to achieve this would be to use a novel capillary-based approach that is self-sealing and requires minimal manual sample handling. The operator need only place a drop of the PCR reagents on the outer surface of a disposable reactor cartridge pre-filled with oil after which the fluid is passively drawn into the reactor with the aid of a capillary “sipper” that also seals the reagents inside the chamber by leaving a thin layer of transparent oil on top. In preliminary work, we have tested a promising oleophilic porous sipper that is capable of driving the oil out of the reactor while simultaneously drawing in the aqueous PCR reagents (Figure 59).

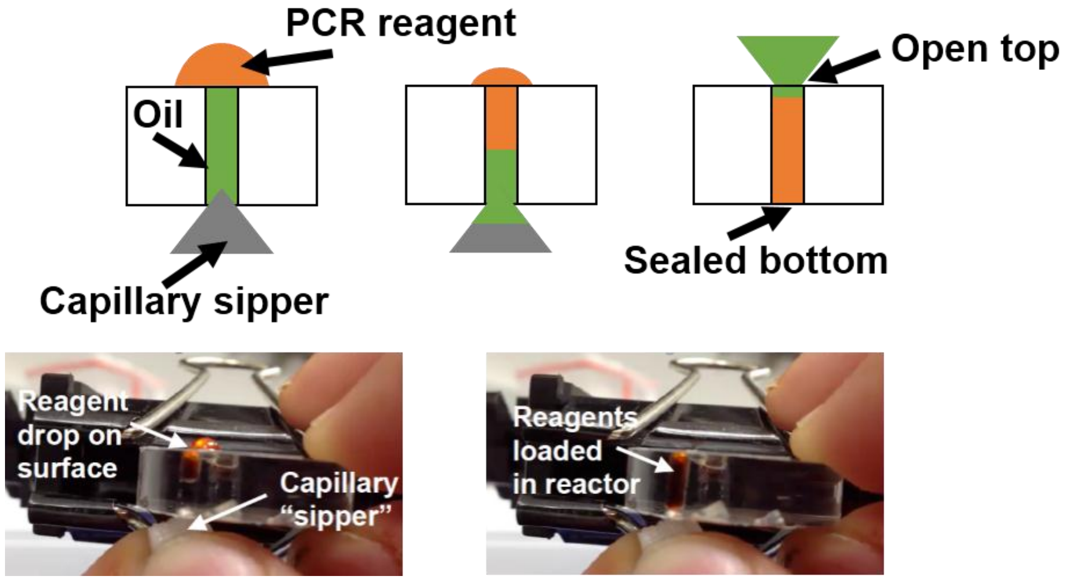

Figure 59: A capillary sipper passively draws the reagents into the convective PCR reactor with minimum fluid handling. The cylindrical reactor is pre-filled with oil (lighter than water) and a drop of aqueous PCR mixture is placed on top. An oleophilic porous polymer scaffold then selectively draws the oil out of the reactor while simultaneously driving the PCR mixture in. Subsequently, the top of the reactor is sealed with tape and the reactor is inverted leaving a thin layer of oil on top to prevent evaporation of PCR mixture during the reaction.

Another area for improvement is reduction/elimination of air bubble formation during the course of convective PCR runs. These bubbles tend to nucleate at sharp corners and other micro features within the reactor and mostly migrate to the reactor top making it difficult to perform fluorescence based smart-phone detection of amplified products because they can obscure the acquired images. Additionally, if the air bubbles become too large, they can disrupt the convective flow pattern resulting in PCR failure. There are several possible avenues to address these issues. First, sealing the reactors under pressure may help to suppress any initial bubble formation. Secondly, a bonding interface cladding [211] can be applied which adopts an ‘inking and place’ operation to transfer the cladding material onto the acrylic surface of the reactor. This would ensure that all surface defects are covered with the cladding material. Third, and perhaps most promising, is construction of reactors using injection molding, as opposed to the current machining process. Molding processes are envisioned to be used for mass production, and are likely to significantly reduce sidewall roughness that generates bubble nucleation sites. These modifications suggest strong potential to significantly reduce bubble formation while convective PCR and thus improve operational reliability.

Particle resuspension modeling

We developed new adhesion model which allows the vdW interactions between particles and surfaces of arbitrary shapes to be calculated for all separation distances. In future studies we would like to incorporate this formulation into CFD codes to provide a comprehensive physics-based description of particle resuspension and deposition phenomenon. The deposited particles reside in the viscous sub-layer where they are subjected to turbulent bursts. The dynamical relationships between the inner region of intense turbulence production and the large scale, less active outer layers needs considerable understanding and there are many modeling approaches such as multi equation turbulence models, large eddy simulation (LES) and direct numerical simulation (DNS) to capture the transient near wall flow. Futrue studies aimed at employing different near wall turbulence models with LES technique will be able to completely resolve the large scale motion while characterizing the small scale flow with a physics based model. A local averaging scheme can also be implemented to ensure that these models can be applied to complex geometries. The adhesion force determined using the approach developed here would then be an input to this CFD model to accurately capture the dynamics of the particle near the surface.

For deformable bodies, the problem of adhesion on surfaces is descirbed by JKR and DMT models in contact mechanics. JKR model is valid for large, soft bodies with high surface energies while the DMT model is more appropriate for small, hard solid particles with low surface energies. However both models are limited to smooth spherical surfaces and these theories use the mean adhesion force (statistical approach) for deformation calculations. Futrue studies can improve upon the implementation of these existing contact mechanics-based deformation models by calculating the cluster interactions and thus allowing the clusters to change their relative positions and deform. Taken together, these additions should provide major improvements to current particle resuspension modeling formulations.

REFERENCES

1. Rayleigh, L., *LIX. On convection currents in a horizontal layer of fluid, when the higher temperature is on the under side.* The London, Edinburgh, and Dublin Philosophical Magazine and Journal of Science, 1916. **32**(192): p. 529-546.

2. Boussinesq, J., *Theorie analytic de la chaleur, Vol. 2*. 1903, Gauthier-Villars, Paris.

3. Krishnan, M., V.M. Ugaz, and M.A. Burns, *PCR in a Rayleigh-Bénard convection cell.* Science, 2002. **298**: p. 793.

4. Müller, G., G. Neumann, and W. Weber, *Natural convection in vertical Bridgman configurations.* Journal of Crystal Growth, 1984. **70**(1): p. 78-93.

5. Aref, H. and M. El Naschie, *Chaos applied to fluid mixing*. 1995, Pergamon, New York.

6. Stroock, A.D., et al., *Chaotic mixer for microchannels.* Science, 2002. **295**(5555): p. 647-651.

7. Muddu, R., Y.A. Hassan, and V.M. Ugaz, *Chaotically accelerated polymerase chain reaction by microscale Rayleigh-Benard convection.* Angew Chem Int Ed Engl, 2011. **50**(13): p. 3048-52.

8. Hilborn, R.C., *Chaos and nonlinear dynamics: an introduction for scientists and engineers*. 2000, Oxford University Press, New York.

9. Kim, H.J. and A. Beskok, *Quantification of chaotic strength and mixing in a micro fluidic system.* Journal of Micromechanics and Microengineering, 2007. **17**(11): p. 2197-2210.

10. Wolf, A., et al., *Determining Lyapunov exponents from a time series.* Physica D: Nonlinear Phenomena, 1985. **16**(3): p. 285-317.

11. Priye, A., Y.A. Hassan, and V.M. Ugaz, *Microscale chaotic advection enables robust convective DNA replication.* Anal Chem, 2013. **85**(21): p. 10536-41.

12. Krishnan, M., V.M. Ugaz, and M.A. Burns, *PCR in a Rayleigh-Benard convection cell.* Science, 2002. **298**(5594): p. 793-793.

13. Krishnan, M., et al., *Reactions and fluidics in miniaturized natural convection systems.* Analytical Chemistry, 2004. **76**(21): p. 6254-6265.

14. Muddu, R., Y.A. Hassan, and V.M. Ugaz, *Chaotically accelerated PCR by microscale Rayleigh-Bénard convection.* Angewandte Chemie International Edition, 2011. **50**: p. 3048-3052.

15. Priye, A., Y.A. Hassan, and V.M. Ugaz, *Education: DNA Replication Using Microscale Natural Convection.* Lab on a Chip, 2012. **12**: p. 4946-4954.

16. Muddu, R., Y.A. Hassan, and V.M. Ugaz, *Rapid PCR Thermocycling using Microscale Thermal Convection.* Journal of Visualized Experiments: JoVE, 2011(49).

17. Yariv, E., G. Ben-Dov, and K.D. Dorfman, *Polymerase chain reaction in natural convection systems: A convection-diffusion-reaction model.* Europhysics Letters, 2005. **71**: p. 1008-1014.

18. Allen, J.W., M. Kenward, and K.D. Dorfman, *Coupled flow and reaction during natural convection PCR.* Microfluidics and Nanofluidics, 2009. **6**(1): p. 121-130.

19. Mehra, S. and W.S. Hu, *A kinetic model of quantitative real-time polymerase chain reaction.* Biotechnology and bioengineering, 2005. **91**(7): p. 848-860.

20. Robertson, R.M., S. Laib, and D.E. Smith, *Diffusion of isolated DNA molecules: Dependence on length and topology.* Proceedings of the National Academy of Sciences of the USA, 2006. **103**: p. 7310-7314.

21. Teraoka, I., *Polymer Solutions: An Introduction to Physical Properties*. 2002, New York: Wiley-Interscience.

22. Doi, M., *Introduction to Polymer Physics*. 1995, Oxford: Oxford University Press.

23. Yamakawa, H. and M. Fujii, *Translational friction coefficient of wormlike chains.* Macromolecules, 1973. **6**(3): p. 407-415.

24. Stellwagen, E., Y. Lu, and N.C. Stellwagen, *Unified description of electrophoresis and diffusion for DNA and other polyions.* Biochemistry, 2003. **42**(40): p. 11745-11750.

25. Dorfman, K.D., et al., *Beyond gel electrophoresis: Microfluidic separations, fluorescence burst analysis, and DNA stretching.* Chemical reviews, 2012. **113**(4): p. 2584-2667.

26. Kirby, B.J., *Micro- and Nanoscale Fluid Mechanics: Transport in Microfluidic Devices*. 2010, Cambridge: Cambridge University Press. 512.

27. Priye, A., Y.A. Hassan, and V.M. Ugaz, *Microscale chaotic advection enables robust convective DNA replication.* Analytical chemistry, 2013. **85**(21): p. 10536-10541.

28. Yao, D.-J., J.-R. Chen, and W.-T. Ju, *Micro–Rayleigh-Bénard convection polymerase chain reaction system.* Journal of Micro/Nanolithography, MEMS, and MOEMS, 2007. **6**(4): p. 043007-043007-9.

29. Chou, W.P., et al., *Rapid DNA amplification in a capillary tube by natural convection with a single isothermal heater.* Biotechniques, 2011. **50**(1): p. 52.

30. Chang, H.F.G., et al., *A thermally baffled device for highly stabilized convective PCR.* Biotechnology Journal, 2012. **7**(5): p. 662-666.

31. Ugaz, V.M. and M. Krishnan, *Novel convective flow based approaches for high-throughput PCR thermocycling.* Journal of the Association for Laboratory Automation (JALA), 2004. **9**: p. 318-323.

32. Priye, A., Y.A. Hassan, and V.M. Ugaz, *Education: DNA replication using microscale natural convection.* Lab on a chip, 2012.

33. Shen, L., J.A. Hagen, and I. Papautsky, *Point-of-care colorimetric detection with a smartphone.* Lab on a Chip, 2012. **12**(21): p. 4240-4243.

34. Oncescu, V., D. O'Dell, and D. Erickson, *Smartphone based health accessory for colorimetric detection of biomarkers in sweat and saliva.* Lab on a Chip, 2013. **13**(16): p. 3232-3238.

35. García, A., et al., *Mobile phone platform as portable chemical analyzer.* Sensors and Actuators B: Chemical, 2011. **156**(1): p. 350-359.

36. Jiang, L., et al., *Solar thermal polymerase chain reaction for smartphone-assisted molecular diagnostics.* Scientific reports, 2014. **4**.

37. Hsieh, Y.-F., et al., *A real-time convective PCR machine in a capillary tube instrumented with a CCD-based fluorometer.* Sensors and Actuators B: Chemical, 2013. **183**: p. 434-440.

38. Miller, S.L., *A production of amino acids under possible primitive earth conditions.* Science, 1953. **117**(3046): p. 528-529.

39. Joyce, G.F., *The antiquity of RNA-based evolution.* Nature, 2002. **418**(6894): p. 214-221.

40. Martin, W., et al., *Hydrothermal vents and the origin of life.* Nature Reviews Microbiology, 2008. **6**(11): p. 805-814.

41. Lane, N., J.F. Allen, and W. Martin, *How did LUCA make a living? Chemiosmosis in the origin of life.* BioEssays, 2010. **32**(4): p. 271-280.

42. Budin, I. and J.W. Szostak, *Expanding roles for diverse physical phenomena during the origin of life.* Annual Review of Biophysics, 2010. **39**: p. 245-263.

43. Lahav, N. and S. Chang, *The possible role of solid surface area in condensation reactions during chemical evolution: reevaluation.* Journal of Molecular Evolution, 1976. **8**: p. 357-380.

44. Pace, N.R., *Origin of life-facing up to the physical setting.* Cell, 1991. **65**(4): p. 531-533.

45. Wächtershäuser, G., *Before enzymes and templates: theory of surface metabolism.* Microbiological reviews, 1988. **52**(4): p. 452.

46. Bernal, J.D., *The physical basis of life.* Science, 1949. **149**(3687): p. 931-6.

47. Ferris, J.P., et al., *Catalysis in prebiotic chemistry: application to the synthesis of RNA oligomers.* Advances in Space Research, 2004. **33**(1): p. 100-105.

48. Paecht-Horowitz, M., J. Berger, and A. Katchalsky, *Prebiotic synthesis of polypeptides by heterogeneous polycondensation of amino-acid adenylates.* Nature, 1970. **228**: p. 636-639.

49. Joshi, P.C., et al., *Mechanism of Montmorillonite Catalysis in the Formation of RNA Oligomers.* Journal of the American Chemical Society, 2009. **131**(37): p. 13369-13374.

50. Vettori, C., et al., *Amplification of bacterial DNA bound on clay minerals by the random amplified polymorphic DNA (RAPD) technique.* FEMS Microbiology Ecology, 1996. **20**(4): p. 251-260.

51. Joshi, P.C., M.F. Aldersley, and J.P. Ferris, *Progress in demonstrating homochiral selection in prebiotic RNA synthesis.* Advances in Space Research, 2013. **51**: p. 772-779.

52. Joshi, P.C., M.F. Aldersley, and J.P. Ferris, *Homochiral selectivity in RNA synthesis: Montmorillonite-catalyzed quaternary reactions of D, L-purine with D, L- pyrimidine nucleotides.* Origins of Life and Evolution of the Biosphere, 2011. **41**: p. 213-236.

53. Ertem, G. and J.P. Ferris, *Formation of RNA oligomers on montmorillonite: Site of catalysis.* Origins of Life and Evolution of the Biosphere, 1998. **28**(4-6): p. 485-499.

54. Neuman, M., W. Neuman, and F. Burton, *On the possible role of crystals in the origins of life, II. The adsorption of Amino Acids by apatite crystals.* Biosystems, 1969. **3**(1): p. 69-73.

55. Jackson, T.A., *Evidence for Selective Adsorption and Polymerization of L-Optical Isomers of Amino Acids Relative to D-Optical Isomers on Edge Faces of Kaolinite.* Experientia, 1971. **27**(3): p. 242-&.

56. Dekov, V.M., et al., *Deposition of talc—kerolite–smectite—smectite at seafloor hydrothermal vent fields: Evidence from mineralogical, geochemical and oxygen isotope studies.* Chemical Geology, 2008. **247**(1): p. 171-194.

57. Dekov, V., et al., *Occurrence of kaolinite and mixed-layer kaolinite/smectite in hydrothermal sediments of Grimsey Graben, Tjörnes Fracture Zone (north of Iceland).* Marine geology, 2005. **215**(3): p. 159-170.

58. Prol-Ledesma, R., et al., *Cinnabar deposition in submarine coastal hydrothermal vents, Pacific Margin of central Mexico.* Economic Geology, 2002. **97**(6): p. 1331-1340.

59. Russell, M.J., et al., *The drive to life on wet and icy worlds.* Astrobiology, 2014. **14**(4): p. 308-343.

60. Brace, W., *Permeability of crystalline and argillaceous rocks.* International Journal of Rock Mechanics and Mining Sciences & Geomechanics Abstracts, 1980. **17**(5): p. 241-251.

61. Russell, M.J., et al., *On hydrothermal convection systems and the emergence of life.* Economic Geology, 2005. **100**(3): p. 419-438.

62. Baaske, P., et al., *Extreme accumulation of nucleotides in simulated hydrothermal pore systems.* Proceedings of the National Academy of Sciences of the United States of America, 2007. **104**(22): p. 9346-9351.

63. Budin, I., R.J. Bruckner, and J.W. Szostak, *Formation of protocell-like vesicles in a thermal diffusion column.* Journal of the American Chemical Society, 2009. **131**: p. 9628-9629.

64. Mast, C.B., et al., *Escalation of polymerization in a thermal gradient.* Proceedings of the National Academy of Sciences of the United States of America, 2013. **110**: p. 8030-8035.

65. Priye, A., Y.A. Hassan, and V.M. Ugaz, *Microscale chaotic advection enables robust convective DNA replication.* Analytical Chemistry, 2013. **85**: p. 10536–10541.

66. Squires, T.M., R.J. Messinger, and S.R. Manalis, *Making it stick: convection, reaction and diffusion in surface-based biosensors.* Nature Biotechnology, 2008. **26**(4): p. 417-426.

67. Wu, Z., H. Joo, and K. Lee, *Kinetics and thermodynamics of the organic dye adsorption on the mesoporous hybrid xerogel.* Chemical Engineering Journal, 2005. **112**(1-3): p. 227-236.

68. Xu, L.C. and B.E. Logan, *Adhesion forces between functionalized latex microspheres and protein-coated surfaces evaluated using colloid probe atomic force microscopy.* Colloids and Surfaces B-Biointerfaces, 2006. **48**(1): p. 84-94.

69. Brookins, D.G., *Eh-pH diagrams for geochemistry*. 1988, New York: Springer-Verlag.

70. Churchill, H., H. Teng, and R.M. Hazen, *Correlation of pH-dependent surface interaction forces to amino acid adsorption: Implications for the origin of life.* American Mineralogist, 2004. **89**: p. 1048-1055.

71. Delgado, A., F. Gonzalez-Caballero, and J. Bruque, *On the zeta potential and surface charge density of montmorillonite in aqueous electrolyte solutions.* Journal of colloid and interface science, 1986. **113**(1): p. 203-211.

72. Huang, Y.-W., F. Shaikh, and V.M. Ugaz, *Tunable synthesis of encapsulated microbubbles by coupled electrophoretic stabilization and electrochemical inflation.* Angewandte Chemie International Edition, 2011. **50**: p. 3739-3743.

73. Shaikh, F. and V.M. Ugaz, *Collection, focusing, and metering of DNA in microchannels using addressable electrode arrays for portable low-power bioanalysis.* Proceedings of the National Academy of Sciences of the United States of America, 2006. **103**: p. 4825-4830.

74. Huang, Y.-W. and V.M. Ugaz, *Smartphone-based detection of unlabeled DNA via electrochemical dissolution.* Analyst, 2013. **138**: p. 2522-2526.

75. Fisher, A.T., *Permeability within basaltic oceanic crust.* Reviews of Geophysics, 1998. **36**(2): p. 143-182.

76. Bear, J., *Dynamics of fluids in porous media*. 1972: Courier Dover Publications.

77. Ergun, S. and J. Owen, *Determination of Size Distribution of Macropores in Porous Materials.* Analytical chemistry, 1953. **25**(8): p. 1222-1226.

78. Goldberg, D.S., T. Takahashi, and A.L. Slagle, *Carbon dioxide sequestration in deep-sea basalt.* Proceedings of the National Academy of Sciences, 2008. **105**(29): p. 9920-9925.

79. Ferris, J.P. and G. Ertem, *Montmorillonite catalysis of RNA oligomer formation in aqueous solution. A model for the prebiotic formation of RNA.* Journal of the American Chemical Society, 1993. **115**(26): p. 12270-12275.

80. Kawamura, K. and J.P. Ferris, *Kinetic and mechanistic analysis of dinucleotide and oligonucleotide formation from the 5'-phosphorimidazolide of adenosine on* Na^+*-montmorillonite.* Journal of the American Chemical Society, 1994. **116**: p. 7564-7572.

81. Chen, J. and L. Lim, *Recovery of precious metals by an electrochemical deposition method.* Chemosphere, 2005. **60**(10): p. 1384-1392.

82. Priye, A., Y.A. Hassan, and V.M. Ugaz, *Education: DNA replication using microscale natural convection.* Lab on a Chip, 2012. **12**: p. 4946-4954.

83. Miller, S.L. and L.E. Orgel, *The origins of life on the earth.* 1974.

84. Dose, K. *Chemical and catalytical properties of thermal polymers of amino acids (proteinoids).* in *Cosmochemical Evolution and the Origins of Life. Proceedings of the Fourth International Conference on the Origin of Life and the First Meeting of the International Society for the Study of the Origin of Life*. 1974. Barcelona: Springer.

85. Mast, C.B., et al., *Escalation of polymerization in a thermal gradient.* Proceedings of the National Academy of Sciences, 2013. **110**(20): p. 8030-8035.

86. Hanczyc, M.M., S.M. Fujikawa, and J.W. Szostak, *Experimental models of primitive cellular compartments: encapsulation, growth, and division.* Science, 2003. **302**(5645): p. 618-622.

87. Briones, C., M. Stich, and S.C. Manrubia, *The dawn of the RNA World: toward functional complexity through ligation of random RNA oligomers.* RNA, 2009. **15**(5): p. 743-749.

88. Matter, J.M. and P.B. Kelemen, *Permanent storage of carbon dioxide in geological reservoirs by mineral carbonation.* Nature Geoscience, 2009. **2**(12): p. 837-841.

89. Chen, Q. and L.M. Hildemann, *The effects of human activities on exposure to particulate matter and bioaerosols in residential homes.* Environmental science & technology, 2009. **43**(13): p. 4641-4646.

90. Gomes, C., J. Freihaut, and W. Bahnfleth, *Resuspension of allergen-containing particles under mechanical and aerodynamic disturbances from human walking—*

introduction to an experimental controlled methodology. Proceedings of Indoor Air, 2005: p. 1445-1449.

91. Ould-Dada, Z. and N.M. Baghini, *Resuspension of small particles from tree surfaces.* Atmospheric Environment, 2001. **35**(22): p. 3799-3809.

92. Kern, W., *Handbook of semiconductor wafer cleaning technology*. Vol. 623. 1993: Noyes Park Ridge.

93. Gradon, L., T. Sosnowski, and A. Moskal, *Resuspension of powders and deposition of aerosol particles in the upper human airways.* Optimization of aerosol drug delivery. Kluwer, Dordrecht, 2003: p. 123-137.

94. London, F., *The general theory of molecular forces.* Transactions of the Faraday Society, 1937. **33**: p. 8b-26.

95. Mahanty, J. and B.W. Ninham, *Dispersion forces*. Vol. 5. 1976: IMA.

96. Hamaker, H., *The London—van der Waals attraction between spherical particles.* Physica, 1937. **4**(10): p. 1058-1072.

97. Bradley, R., *LXXIX. The cohesive force between solid surfaces and the surface energy of solids.* The London, Edinburgh, and Dublin Philosophical Magazine and Journal of Science, 1932. **13**(86): p. 853-862.

98. Israelachvili, J.N., *Intermolecular and surface forces: revised third edition*. 2011: Academic press.

99. Bergström, L., *Hamaker constants of inorganic materials.* Advances in Colloid and Interface Science, 1997. **70**: p. 125-169.

100. Casimir, H. and D. Polder, *The influence of retardation on the London-van der Waals forces.* Physical Review, 1948. **73**(4): p. 360.

101. Dzyaloshinskii, I., E. Lifshitz, and L.P. Pitaevskii, *GENERAL THEORY OF VAN DER WAALS'FORCES.* Physics-Uspekhi, 1961. **4**(2): p. 153-176.

102. Lifshitz, E., *The theory of molecular attractive forces between solids.* Sov. Phys. JETP, 1956. **2**(1): p. 73-83.

103. Derjaguin, B., *Abrikosova, 1.1. 1954 Disc.* Faraday Soc. **18**: p. 33.

104. Kitchener, J. and A. Prosser, *Direct measurement of the long-range van der Waals forces.* Proceedings of the Royal Society of London. Series A. Mathematical and Physical Sciences, 1957. **242**(1230): p. 403-409.

105. Tabor, D. and R. Winterton, *Surface forces: Direct measurement of normal and retarded van der Waals forces.* Nature, 1968. **219**: p. 1120-1121.

106. Parsegian, V. and B. Ninham, *Application of the Lifshitz theory to the calculation of Van der Waals forces across thin lipid films.* Nature, 1969. **224**: p. 1197-1198.

107. DA HAYDON, J.L.T., *Contact angles for thin lipid films and the determination of London-van der Waals forces.* 1968.

108. Richmond, P. and B. Ninham, *Calculation of van der Waals forces across mica plates using Lifshitz theory.* Journal of Colloid and Interface Science, 1972. **40**(3): p. 406-408.

109. Sabisky, E. and C. Anderson, *Verification of the Lifshitz theory of the van der Waals potential using liquid-helium films.* Physical Review A, 1973. **7**(2): p. 790-806.

110. Israelachvili, J. and D. Tabor, *The measurement of van der Waals dispersion forces in the range 1.5 to 130 nm.* Proceedings of the Royal Society of London. A. Mathematical and Physical Sciences, 1972. **331**(1584): p. 19-38.

111. van Blokland, P.H.G.M. and J.T.G. Overbeek, *Van der Waals forces between objects covered with a chromium layer.* J. Chem. Soc., Faraday Trans. 1, 1978. **74**: p. 2637-2651.

112. Hunklinger, S., H. Geisselmann, and W. Arnold, *A dynamic method for measuring the van der Waals forces between macroscopic bodies.* Review of Scientific Instruments, 1972. **43**(4): p. 584-587.

113. Lamoreaux, S.K., *Demonstration of the Casimir force in the 0.6 to 6 μm range.* Physical Review Letters, 1997. **78**(1): p. 5-8.

114. Coakley, C. and D. Tabor, *Direct measurement of van der Waals forces between solids in air.* Journal of Physics D: Applied Physics, 2001. **11**(5): p. L77.

115. Parsegian, V.A., *Van der Waals forces: a handbook for biologists, chemists, engineers, and physicists*. 2005: Cambridge University Press.

116. Derjaguin, B., *Friction and adhesion. IV. The theory of adhesion of small particles.* Kolloid Zeits, 1934. **69**: p. 155-164.

117. Rempel, A., J. Wettlaufer, and M. Worster, *Interfacial premelting and the thermomolecular force: Thermodynamic buoyancy.* Physical Review Letters, 2001. **87**(8): p. 88501.

118. Rajter, R.F., et al., *van der Waals–London dispersion interactions for optically anisotropic cylinders: Metallic and semiconducting single-wall carbon nanotubes.* Physical Review B, 2007. **76**(4): p. 045417.

119. Sedmik, R., I. Vasiljevich, and M. Tajmar, *Detailed parametric study of Casimir forces in the Casimir Polder approximation for nontrivial 3D geometries.* Journal of computer-aided materials design, 2007. **14**(1): p. 119-132.

120. Yannopapas, V. and N.V. Vitanov, *First-Principles Theory of van der Waals Forces between Macroscopic Bodies.* Physical review letters, 2007. **99**(12): p. 120406.

121. Golestanian, R., *Lifshitz interaction between dielectric bodies of arbitrary geometry.* Physical review letters, 2005. **95**(23): p. 230601.

122. Langbein, D., *Non-retarded dispersion energy between macroscopic spheres.* Journal of Physics and Chemistry of Solids, 1971. **32**(7): p. 1657-1667.

123. Love, J.D., *On the van der Waals force between two spheres or a sphere and a wall.* J. Chem. Soc., Faraday Trans. 2, 1977. **73**(5): p. 669-688.

124. Mitchell, D. and B. Ninham, *Van der Waals forces between two spheres.* The Journal of Chemical Physics, 1972. **56**: p. 1117.

125. Langbein, D., *Retarded dispersion energy between macroscopic bodies.* Physical Review B, 1970. **2**(8): p. 3371.

126. Kiefer, J., V. Parsegian, and G. Weiss, *Some convenient bounds and approximations for the many body Van der Waals attraction between two spheres.* Journal of Colloid and Interface Science, 1978. **67**(1): p. 140-153.

127. Renne, M. and B. Nijboer, *Microscopic derivation of macroscopic Van der Waals forces.* Chemical Physics Letters, 1967. **1**(8): p. 317-320.

128. Amadon, A. and W. Marlow, *Cluster-collision frequency. I. The long-range intercluster potential.* Physical Review A, 1991. **43**(10): p. 5483.

129. Amadon, A. and W. Marlow, *Cluster-collision frequency. II. Estimation of the collision rate.* Physical Review A, 1991. **43**(10): p. 5493.

130. Arunachalam, V., W. Marlow, and J. Lu, *Development of a picture of the van der Waals interaction energy between clusters of nanometer-range particles.* Physical Review E, 1998. **58**(3): p. 3451.

131. Marlow, W.H., *Lifshitz–van der Waals forces in aerosol particle collisions. I. Introduction: Water droplets.* The Journal of Chemical Physics, 1980. **73**: p. 6288.

132. Arunachalam, V., *Ultrafine aerosol particles: Long range interaction, aggregation kinetics and structure*, in *Nuclear Engineering*1996, Texas A&M University. p. 147, For homogeneous spheres the point to point retardation integrated over two spheres turns out to be very close to the retardation evaluated when centers of the two spheres are taken into consideration.

133. Lu, J. and W. Marlow, *Nonsingular van der Waals potentials.* Physical Review A, 1995. **52**(3): p. 2141.

134. Lu, J., W. Marlow, and V. Arunachalam, *Nonsingular van der Waals potentials for nonconducting condensed bodies.* Journal of Colloid and Interface Science, 1996. **181**(2): p. 429-442.

135. DiStasio, R.A., O.A. von Lilienfeld, and A. Tkatchenko, *Collective many-body van der Waals interactions in molecular systems.* Proceedings of the National Academy of Sciences, 2012. **109**(37): p. 14791-14795.

136. Krupp, H., *Particle adhesion, theory and experiment*. 1967: Advan. Colloid Interface Sci. 1 (1967), 111-239.

137. Ninham, B. and V. Parsegian, *van der Waals Forces across Triple-Layer Films.* The Journal of Chemical Physics, 1970. **52**: p. 4578.

138. Nir, S., R. Rein, and L. Weiss, *On the applicability of certain approximations of the Lifshitz theory to thin films.* Journal of theoretical biology, 1972. **34**(1): p. 135-153.

139. Parsegian, V., *Long range van der Waals forces.* Physical chemistry: enriching topics from colloid and surface science, 1975: p. 27-72.

140. Bohren, C.F. and D.R. Huffman, *Absorption and scattering of light by small particles*. 2008: Wiley. com.

141. Marlow, W.H., *Size effects in aerosol particle interactions: the van der Waals potential and collision rates.* Surface Science, 1981. **106**(1): p. 529-537.

142. French, R.H., et al., *Long range interactions in nanoscale science.* Reviews of Modern Physics, 2010. **82**(2): p. 1887.

143. Kenneth, O. and I. Klich, *Opposites attract: A theorem about the Casimir force.* Physical Review Letters, 2006. **97**(16): p. 160401.

144. Emig, T., et al., *Casimir forces between arbitrary compact objects.* Physical Review Letters, 2007. **99**(17): p. 170403.

145. Tabor, D., *Surface forces and surface interactions.* Journal of Colloid and Interface Science, 1977. **58**(1): p. 2-13.

146. Johnson, K., K. Kendall, and A. Roberts, *Surface energy and the contact of elastic solids.* Proceedings of the Royal Society of London. A. Mathematical and Physical Sciences, 1971. **324**(1558): p. 301-313.

147. Rumpf, H. and F. Bull, *Particle technology*. Vol. 116. 1990: chapman and hall London, UK.

148. Rabinovich, Y.I., et al., *Adhesion between nanoscale rough surfaces: II. Measurement and comparison with theory*. Journal of Colloid and Interface Science, 2000. **232**(1): p. 17-24.

149. Beach, E., et al., *Pull-off force measurements between rough surfaces by atomic force microscopy.* Journal of Colloid and Interface Science, 2002. **247**(1): p. 84-99.

150. Herman, M.C. and K.D. Papadopoulos, *Effects of asperities on the van der Waals and electric double-layer interactions of two parallel flat plates.* Journal of colloid and interface science, 1990. **136**(2): p. 385-392.

151. Herman, M.C. and K.D. Papadopoulos, *A method for modeling the interactions of parallel flat plate systems with surface features.* Journal of colloid and interface science, 1991. **142**(2): p. 331-342.

152. Sun, N. and J.Y. Walz, *A model for calculating electrostatic interactions between colloidal particles of arbitrary surface topology.* Journal of colloid and interface science, 2001. **234**(1): p. 90-105.

153. Dagastine, R.R., et al., *Calculation of van der Waals forces with diffuse coatings: applications to roughness and adsorbed polymers.* The Journal of Adhesion, 2004. **80**(5): p. 365-394.

154. Autumn, K., et al., *Evidence for van der Waals adhesion in gecko setae.* Proceedings of the National Academy of Sciences, 2002. **99**(19): p. 12252-12256.

155. Cristofanilli, M., et al., *Circulating tumor cells, disease progression, and survival in metastatic breast cancer.* New England Journal of Medicine, 2004. **351**(8): p. 781-791.

156. Mantovani, A., et al., *Neutrophils in the activation and regulation of innate and adaptive immunity.* Nature Reviews Immunology, 2011. **11**(8): p. 519-531.

157. Zheng, S., et al., *Membrane microfilter device for selective capture, electrolysis and genomic analysis of human circulating tumor cells.* Journal of Chromatography A, 2007. **1162**(2): p. 154-161.

158. Chen, Z.Z., et al., *Pool-dam structure based microfluidic devices for filtering tumor cells from blood mixtures.* Surface and Interface Analysis, 2006. **38**(6): p. 996-1003.

159. Nagrath, S., et al., *Isolation of rare circulating tumour cells in cancer patients by microchip technology.* Nature, 2007. **450**(7173): p. 1235-1239.

160. Stott, S.L., et al., *Isolation of circulating tumor cells using a microvortex-generating herringbone-chip.* Proceedings of the National Academy of Sciences of the United States of America, 2010. **107**(43): p. 18392-18397.

161. Sethu, P., A. Sin, and M. Toner, *Microfluidic diffusive filter for apheresis (leukapheresis).* Lab on a Chip, 2006. **6**(1): p. 83-89.

162. VanDelinder, V. and A. Groisman, *Perfusion in microfluidic cross-flow: Separation of white blood cells from whole blood and exchange of medium in a continuous flow.* Analytical Chemistry, 2007. **79**(5): p. 2023-2030.

163. Zheng, S.Y., J.Q. Liu, and Y.C. Tai, *Streamline-based microfluidic devices for erythrocytes and leukocytes separation.* Journal of Microelectromechanical Systems, 2008. **17**(4): p. 1029-1038.

164. Choi, S., et al., *Continuous blood cell separation by hydrophoretic filtration.* Lab on a Chip, 2007. **7**(11): p. 1532-1538.

165. Inglis, D.W., M. Lord, and R.E. Nordon, *Scaling deterministic lateral displacement arrays for high throughput and dilution-free enrichment of leukocytes.* Journal of Micromechanics and Microengineering, 2011. **21**(5): p. 054024.

166. Wu, Z.G., et al., *Soft inertial microfluidics for high throughput separation of bacteria from human blood cells.* Lab on a Chip, 2009. **9**(9): p. 1193-1199.

167. Mach, A.J. and D. Di Carlo, *Continuous Scalable Blood Filtration Device Using Inertial Microfluidics.* Biotechnology and Bioengineering, 2010. **107**(2): p. 302-311.

168. Tan, S.J., et al., *Microdevice for the isolation and enumeration of cancer cells from blood.* Biomedical Microdevices, 2009. **11**(4): p. 883-892.

169. Jain, A. and L.L. Munn, *Biomimetic postcapillary expansions for enhancing rare blood cell separation on a microfluidic chip.* Lab on a Chip, 2011. **11**(17): p. 2941-2947.

170. Bhagat, A.A.S., et al., *Pinched flow coupled shear-modulated inertial microfluidics for high-throughput rare blood cell separation.* Lab on a Chip, 2011. **11**(11): p. 1870-1878.

171. Hur, S.C., A.J. Mach, and D. Di Carlo, *High-throughput size-based rare cell enrichment using microscale vortices.* Biomicrofluidics, 2011. **5**(2).

172. Chung, J., et al., *Microfluidic Cell Sorter (μFCS) for On-chip Capture and Analysis of Single Cells.* Advanced Healthcare Materials, 2012. **1**(4): p. 432-436.

173. Huang, J.H., A. Jayaraman, and V.M. Ugaz, *Enzymatic sculpting of nanoscale and microscale surface topographies.* Angew Chem Int Ed Engl, 2012. **51**(38): p. 9619-23.

174. Sudarsan, A.P. and V.M. Ugaz, *Multivortex micromixing.* Proceedings of the National Academy of Sciences of the United States of America, 2006. **103**(19): p. 7228-7233.

175. Saffman, P., *The lift on a small sphere in a slow shear flow.* Journal of Fluid Mechanics, 1965. **22**(02): p. 385-400.

176. Di Carlo, D., et al., *Particle segregation and dynamics in confined flows.* Physical Review Letters, 2009. **102**(9): p. 094503.

177. Zhu, H., et al., *Discrete particle simulation of particulate systems: theoretical developments.* Chemical Engineering Science, 2007. **62**(13): p. 3378-3396.

178. Ookawara, S., et al., *Quasi-direct numerical simulation of lift force-induced particle separation in a curved microchannel by use of a macroscopic particle model.* Chemical Engineering Science, 2007. **62**(9): p. 2454-2465.

179. Seo, J., M.H. Lean, and A. Kole, *Membrane-free microfiltration by asymmetric inertial migration.* Applied Physics Letters, 2007. **91**(3): p. 033901.

180. Geng, Z., et al., *Multi-component continuous separation chip composed with micropillar arrays in splitlevel spiral channel.* RSC Adv., 2013.

181. Geng, Z., et al., *Continuous blood separation utilizing spiral filtration microchannel with gradually varied width and micro-pillar array.* Sensors and Actuators B: Chemical, 2012.

182. Maxey, M.R. and J.J. Riley, *Equation of motion for a small rigid sphere in a nonuniform flow.* Physics of Fluids (1958-1988), 1983. **26**(4): p. 883-889.

183. Schiller, L. and Z. Naumann, *A drag coefficient correlation.* Vdi Zeitung, 1935. **77**(318): p. 51.

184. Milne-Thomson, L. and N. Rott, *Theoretical hydrodynamics.* Journal of Applied Mechanics, 1968. **35**: p. 846.

185. Sommerfeld, M., *Theoretical and Experimental Modelling of Particulate Flows.* von Karman Institute for Fluid Dynamics 2000. **2000-06**: p. 20-23.

186. Grover, W.H., et al., *Measuring single-cell density.* Proceedings of the National Academy of Sciences, 2011. **108**(27): p. 10992-10996.

187. Hatch, A., et al., *A rapid diffusion immunoassay in a T-sensor.* Nature Biotechnology, 2001. **19**(5): p. 461-465.

188. Chen, X., et al., *Microfluidic chip for blood cell separation and collection based on crossflow filtration.* Sensors and Actuators B-Chemical, 2008. **130**(1): p. 216-221.

189. Ji, H.M., et al., *Silicon-based microfilters for whole blood cell separation.* Biomedical Microdevices, 2008. **10**(2): p. 251-257.

190. Kuo, J.S., et al., *Microfabricating high-aspect-ratio structures in polyurethane-methacrylate (PUMA) disposable microfluidic devices.* Lab on a Chip, 2009. **9**(13): p. 1951-1956.

191. Mohamed, H., et al., *Isolation of tumor cells using size and deformation.* Journal of Chromatography A, 2009. **1216**(47): p. 8289-8295.

192. Spitzack, K.D. and V.M. Ugaz, *Polymerase chain reaction in miniaturized systems: big progress in little devices*, in *Microfluidic Techniques: Reviews and Protocols*, S.D. Minteer, Editor. 2005, Humana Press: Totowa, New Jersey, USA. p. Chapter 10.

193. Agrawal, N., Y.A. Hassan, and V.M. Ugaz, *A Pocket-sized convective PCR thermocycler.* Angewandte Chemie International Edition, 2007. **46**: p. 4316-4319.

194. Braun, D., N.L. Goddard, and A. Libchaber, *Exponential DNA replication by laminar convection.* Physical Review Letters, 2003. **91**(15): p. 158103.

195. Chen, Z., et al., *Thermosiphon-based PCR reactor: experiment and modeling.* Analytical Chemistry, 2004. **76**: p. 3707-3715.

196. Wheeler, E.K., et al., *Convectively driven polymerase chain reaction thermal cycler.* Analytical Chemistry, 2004. **76**: p. 4011-4016.

197. Yao, D.J., J.R. Chen, and W.T. Ju, *Micro-Rayleigh-Benard convection polymerase chain reaction system.* Journal of Micro-Nanolithography MEMS and MOEMS, 2007. **6**: p. 043007.

198. Muddu, R., Y.A. Hassan, and V.M. Ugaz, *Rapid PCR thermocycling using microscale thermal convection.* Journal of Visualized Experiments (JoVE), 2011. **49**: p. DOI: 10.3791/2366 (http://www.jove.com/details.stp?id=2366).

199. Allen, J.W., M. Kenward, and K.D. Dorfman, *Coupled flow and reaction during natural convection PCR.* Microfluidics and Nanofluidics, 2009. **6**: p. 121-130.

200. Marsh, H.W., *Students' evaluations of university teaching: Research findings, methodological issues, and directions for future research.* International Journal of Educational Research, 1987. **11**(3): p. 253-388.

201. Wolf, T., *Assessing student learning in a virtual laboratory environment.* IEEE Transactions on Education, 2010. **53**(2): p. 216-222.

202. Dalgarno, B., et al., *Effectiveness of a virtual laboratory as a preparatory resource for distance education chemistry students.* Computers & Education, 2009. **53**(3): p. 853-865.

203. Koretsky, M., C. Kelly, and E. Gummer, *Student perceptions of learning in the laboratory: comparison of industrially situated virtual laboratories to capstone physical laboratories.* Journal of Engineering Education, 2011: p. 540-573.

204. Silverman, D., *Analyzing talk and text*, in *Handbook of Qualitative Research, 2nd Edition*, N.K. Denzin and Y.S. Lincoln, Editors. 2000, Sage Publications, Inc.: Thousand Oaks. p. 821-834.

205. Jamieson, L.H. and J.R. Lohmann, *Innovation with Impact: Creating a Culture for Scholarly and Systematic Innovation in Engineering Education*. 2012, Washington: American Society for Engineering Education.

206. Singer, S.R., N.R. Nielsen, and H.A. Schweingruber, *Discipline-Based Education Research: Understanding and Improving Learning in Undergraduate Science and Engineering*. 2012, Washington: The National Academies Press.

207. Greener, J., et al., *Education: a microfluidic platform for university-level analytical chemistry laboratories.* Lab on a Chip, 2012. **12**: p. 696-701.

208. Fintschenko, Y., *Education: A modular approach to microfluidics in the teaching laboratory.* Lab on a Chip, 2011. **11**: p. 3394-3400.

209. Grassberger, P. and I. Procaccia, *Characterization of strange attractors.* Physical review letters, 1983. **50**(5): p. 346.

210. Liu, M., F. Muzzio, and R. Peskin, *Quantification of mixing in aperiodic chaotic flows.* Chaos, Solitons & Fractals, 1994. **4**(6): p. 869-893.

211. Liu, H.-B., et al., *Micro air bubble formation and its control during polymerase chain reaction (PCR) in polydimethylsiloxane (PDMS) microreactors.* Journal of Micromechanics and Microengineering, 2007. **17**(10): p. 2055.

APPENDIX A

LINEAR STABILITY ANALYSIS OF RAYLEIGH-BÉNARD CONVECTION

Rayleigh Bérnard instability develops when a fluid in a gravitational field has a temperature gradient in the direction of gravity. The buoyancy forces on the less dense hotter fluid at the bottom works against the viscous and thermal dissipation leading to an unstable top heavy arrangement. The governing equations describing the motion of the fluid are given by:

Continuity equation

$$\frac{\partial\rho}{\partial t}+\vec{\nabla}\bullet(\rho\vec{u})=0 \qquad [8.1]$$

Momentum equation

$$\begin{gathered}\rho\left(\frac{\partial\vec{u}}{\partial t}+\vec{u}\bullet(\vec{\nabla}\vec{u})\right)=-\vec{\nabla}p+\vec{f}+\vec{\nabla}\bullet\overline{\overline{\prod}}\\ \overline{\overline{\prod}}_{ij}=\left(\mu\left(\frac{\partial u_i}{\partial x_j}+\frac{\partial u_j}{\partial x_i}\right)-\frac{2}{3}\mu\vec{\nabla}\bullet\vec{u}\delta_{ij}\right)\hat{e}_i\hat{e}_j \qquad [8.2]\\ \vec{f}=\rho\vec{g}\end{gathered}$$

Energy equation

$$\begin{gathered}\left(\frac{\partial E}{\partial t}+\vec{u}\bullet(\vec{\nabla}E)\right)=-\vec{\nabla}\vec{Q}_{cond}-p\vec{\nabla}\bullet\vec{u}+\phi\\ E=\rho c_vT \qquad [8.3]\\ \vec{Q}_{cond}=-k\vec{\nabla}T\\ \phi=\text{viscous heating}\end{gathered}$$

The Boussinesq approximation states that fluid properties such as viscosity, thermal conductivity and thermal expansion coefficient don't change significantly on changing the temperature of the fluid. Furthermore, the density of the fluid is also assumed constant everywhere except in the buoyancy force term where it is assumed to vary linearly with temperature.

$$\rho = \rho_o(1-\alpha(T-T_o)) \qquad [8.4]$$

On substituting eq. [8.4] into the continuity equation (eq. [8.1])

$$\begin{aligned}
&\frac{\partial\rho}{\partial t}+\vec{\nabla}\bullet(\rho\vec{u})=0\\
&\frac{\partial\rho_o(1-\alpha(T-T_o))}{\partial t}+\vec{\nabla}\bullet(\rho_o(1-\alpha(T-T_o))\vec{u})=0\\
&\frac{\partial(1-\alpha(T-T_o))}{\partial t}+\vec{\nabla}\bullet\vec{u}-\alpha\nabla\bullet(\vec{u}(T-T_o))=0\\
&\alpha\frac{\partial T}{\partial t}+\vec{\nabla}\bullet\vec{u}-\alpha\nabla\bullet(\vec{u}(T-T_o))=0\\
&\alpha<<1
\end{aligned}$$

$$\vec{\nabla}\bullet\vec{u}\simeq 0 \qquad [8.5]$$

On substituting eq. [8.4] into the momentum equation (eq.[8.2])

$$\begin{aligned}
&\rho\left(\frac{\partial\vec{u}}{\partial t}+\vec{u}\bullet(\vec{\nabla}\vec{u})\right)=-\vec{\nabla}p+\rho\vec{g}+\mu\nabla^2\vec{u}\\
&\vec{g}=g\hat{e}_z\\
&\rho_o(1-\alpha(T-T_o))\left(\frac{\partial\vec{u}}{\partial t}+\vec{u}\bullet(\vec{\nabla}\vec{u})\right)=-\vec{\nabla}p+\rho_o(1-\alpha(T-T_o))g\hat{e}_z+\mu\nabla^2\vec{u}\\
&\rho_o\left(\frac{\partial\vec{u}}{\partial t}+\vec{u}\bullet(\vec{\nabla}\vec{u})\right)-\underbrace{\rho_o\left(\frac{\partial\vec{u}}{\partial t}+\vec{u}\bullet(\vec{\nabla}\vec{u})\right)\alpha(T-T_o)}_{\text{Neglect because }\alpha.u\text{ is small compared to }\alpha.g}=-\vec{\nabla}p+\rho_o g\hat{e}_z-\rho_o g\hat{e}_z\alpha(T-T_o)+\mu\nabla^2\vec{u}
\end{aligned}$$

$$\left(\frac{\partial\vec{u}}{\partial t}+\vec{u}\bullet(\vec{\nabla}\vec{u})\right)=-\frac{\vec{\nabla}p}{\rho_o}+g\hat{e}_z-g\hat{e}_z\alpha(T-T_o)+\nu\nabla^2\vec{u} \qquad [8.6]$$

On substituting eq. [8.4] into the momentum equation (eq. [8.3])

$$\left(\frac{\partial \rho c_v T}{\partial t}+\vec{u}\bullet(\vec{\nabla}\rho c_v T)\right)=\vec{\nabla}k\vec{\nabla}T$$

$$\rho_o c_v\left(\frac{\partial(T-\alpha T(T-T_o))}{\partial t}+\vec{u}\bullet(\vec{\nabla}(T-\alpha T(T-T_o)))\right)=k\nabla^2 T$$

$$\frac{\partial T}{\partial t}+\vec{u}\bullet\vec{\nabla}T\underbrace{+\alpha\frac{\partial T(T-T_o)}{\partial t}-\alpha\vec{u}\bullet\vec{\nabla}\left(T(T-T_o)\right)}_{\text{Neglect because }\alpha<<1}=\frac{k}{\rho_o c_v}\nabla^2 T$$

$$\frac{\partial T}{\partial t}+\vec{u}\bullet\vec{\nabla}T=\kappa\nabla^2 T \qquad [8.7]$$

Therefore the Boussinesq equations reduce to

$$\vec{\nabla}\bullet\vec{u}=0$$

$$\left(\frac{\partial\vec{u}}{\partial t}+\vec{u}\bullet(\vec{\nabla}\vec{u})\right)=-\frac{\vec{\nabla}p}{\rho_o}+g\hat{e}_z-g\hat{e}_z\alpha(T-T_o)+\nu\nabla^2\vec{u}$$

$$\frac{\partial T}{\partial t}+\vec{u}\bullet\vec{\nabla}T=\kappa\nabla^2 T$$

We can now use linear stability analysis to analyze the solutions to these equations for small perturbations to the base flow state of no fluid motion at the onset of convective motion. Then the base flow condition are:

$$\begin{aligned}\vec{u}_b&=\left[0,0,0\right]\\ T_{z=l}&=T_{top}\\ T_{z=0}&=T_{bottom}\end{aligned}$$

The base flow satisfies the continuity equation. Analyzing the energy (eq. [8.7]) and momentum equations (eq. [8.6])

$$\underset{0\ \text{steady state}}{\frac{\partial T}{\partial t}}+\vec{u_b}\bullet\vec{\nabla}T=\kappa\nabla^2 T$$

$$\nabla^2 T = 0$$

$$\underbrace{\frac{\partial^2 T}{\partial x^2} + \frac{\partial^2 T}{\partial y^2}}_{=0 \text{ No horizontal temperature gradient}} + \frac{\partial^2 T}{\partial z^2} = 0$$

$$\frac{\partial^2 T}{\partial z^2} = 0 \qquad [8.8]$$

$$\begin{aligned} T &= C_1 z + C_2 \\ T_{z=l} &= T_{top} \\ T_{z=0} &= T_{bottom} \\ T_{bottom} &> T_{top} \\ T_{top} &= C_1 l + T_{bottom} \end{aligned}$$

$$C_1 = \frac{T_{top} - T_{bottom}}{l} = -\frac{T_{bottom} - T_{top}}{l} = -\beta$$

$$\beta = -\frac{dT}{dz} \qquad [8.9]$$

$$T_b = T_{bottom} - \beta z = T_o - \beta z \qquad [8.10]$$

$$\left(\frac{\partial \overrightarrow{u_b}}{\partial t} + \overrightarrow{u_b} \bullet (\overrightarrow{\nabla} \overrightarrow{u_b}) \right) = -\frac{\overrightarrow{\nabla} p}{\rho_o} + g\hat{e}_z - g\hat{e}_z \alpha (T - T_o) + \nu \nabla^2 \overrightarrow{u_b}$$

$$\overrightarrow{\nabla} p = \rho_o \left(1 - \alpha (T - T_o)\right) g\hat{e}_z$$

$$\left(\frac{\partial p}{\partial x}\hat{e}_x + \frac{\partial p}{\partial y}\hat{e}_y + \frac{\partial p}{\partial z}\hat{e}_z \right) = \rho_o \left(1 - \alpha (T - T_o)\right) g\hat{e}_z$$

$$\begin{aligned} \frac{\partial p}{\partial x}\hat{e}_x &= 0 \\ \frac{\partial p}{\partial y}\hat{e}_y &= 0 \end{aligned}$$

$$\frac{\partial p}{\partial z}\hat{e}_z = \rho_o\left(1-\alpha(T-T_o)\right)g\hat{e}_z$$

$$T_b = T_o - \beta z$$

$$\frac{\partial p}{\partial z} = \rho_o\left(1+\alpha\beta z\right)g$$

$$\int_{p_o}^{p_b} dp = \int_0^z \rho_o\left(1+\alpha\beta z\right)gdz$$

$$p_b = p_o + \rho_o g\left(z+\frac{\alpha\beta z^2}{2}\right) \qquad [8.11]$$

Eq. [8.11] provides the vertical pressure distribution at the base flow state. Now we introduce a small perturbation to the base flow state equations.

$$\begin{aligned}
&\vec{u} = \vec{u}_b + \tilde{\vec{u}} = \tilde{\vec{u}}\\
&T = T_b + T = T_o - \beta z + T\\
&p = p_b + p = p_o - \rho_o g\left(z+\frac{\alpha\beta z^2}{2}\right) + p
\end{aligned}$$

Substituting these in the continuity (eq. [8.5]), momentum (eq. [8.6]) and energy equations (eq. [8.7])

$$\vec{\nabla}\bullet\tilde{\vec{u}} = 0 \qquad [8.12]$$

$$\left(\frac{\partial\tilde{\vec{u}}}{\partial t} + \tilde{\vec{u}}\bullet(\vec{\nabla}\tilde{\vec{u}})\right) = -\frac{\vec{\nabla}\left(p_b+p\right)}{\rho_o} + g\hat{e}_z - g\hat{e}_z\alpha(T_o-\beta z+T-T_o) + \nu\nabla^2\tilde{\vec{u}}$$

$$\left(\frac{\partial\tilde{\vec{u}}}{\partial t} + \underbrace{\tilde{\vec{u}}\bullet(\vec{\nabla}\tilde{\vec{u}})}_{\substack{\text{product}\\ \text{of 2 perturbed}\\ \text{quatities}}}\right) = -\frac{\vec{\nabla}\left(p_o+\rho_o g\left(z+\frac{\alpha\beta z^2}{2}\right)+p\right)}{\rho_o} + g\hat{e}_z - g\hat{e}_z\alpha(-\beta z+T) + \nu\nabla^2\tilde{\vec{u}}$$

$$\frac{\partial \tilde{\vec{u}}}{\partial t} = -\frac{\left(\vec{\nabla} p_o + \rho_o g\left(\vec{\nabla} z + \frac{\alpha\beta\vec{\nabla} z^2}{2}\right) + \vec{\nabla} p\right)}{\rho_o} + g\hat{e}_z - g\hat{e}_z\alpha(-\beta z + T) + \nu\nabla^2\tilde{\vec{u}}$$

$$\frac{\partial \tilde{\vec{u}}}{\partial t} = g\left(-\hat{e}_z - \alpha\beta z\hat{e}_z\right) - \frac{\vec{\nabla} p}{\rho_o} + g\hat{e}_z - g\hat{e}_z\alpha(-\beta z + T) + \nu\nabla^2\tilde{\vec{u}}$$

$$\frac{\partial \tilde{\vec{u}}}{\partial t} = -\frac{\vec{\nabla} p}{\rho_o} - g\hat{e}_z\alpha T + \nu\nabla^2\tilde{\vec{u}} \qquad [8.13]$$

$$\frac{\partial\left(T_o - \beta z + T\right)}{\partial t} + \tilde{\vec{u}}\bullet\vec{\nabla}\left(T_o - \beta z + T\right) = \kappa\nabla^2\left(T_o - \beta z + T\right)$$

$$\frac{\partial T}{\partial t} - \beta\tilde{\vec{u}}\bullet\hat{e}_z + \underbrace{\tilde{\vec{u}}\bullet\vec{\nabla} T}_{\substack{\text{product of 2}\\ \text{perturbations}}} = \kappa\nabla^2 T$$

$$\frac{\partial T}{\partial t} - \beta\tilde{u}_z = \kappa\nabla^2 T$$

Thus the equations of motion for the perturbed quantities become

$$\vec{\nabla}\bullet\tilde{\vec{u}} = 0 \qquad [8.14]$$

$$\frac{\partial \tilde{\vec{u}}}{\partial t} = -\frac{\vec{\nabla} p}{\rho_o} - g\hat{e}_z\alpha T + \nu\nabla^2\tilde{\vec{u}} \qquad [8.15]$$

$$\frac{\partial T}{\partial t} - \beta\tilde{u}_z = \kappa\nabla^2 T \qquad [8.16]$$

Equations [8.14], [8.15] and [8.16] determine the evolution of perturbed quantities. These equations can be solved by some vector algebra manipulation followed by normal mode analysis. Some useful vector identities

$\vec{\nabla}\times\vec{\nabla}S = 0$ for any scalar field S

$\vec{\nabla}\times\left(S\vec{V}\right) = S\vec{\nabla}\times\left(\vec{V}\right) - \vec{V}\times\vec{\nabla}S$ for any scalar field S and vector field V

$$\vec{\nabla}(\vec{V}\bullet\vec{W}) = \left(\vec{V}\bullet\vec{\nabla}\right)\vec{W} + \left(\vec{W}\bullet\vec{\nabla}\right)\vec{V} + \vec{V}\times\left(\vec{\nabla}\times\vec{W}\right) + \vec{W}\times\left(\vec{\nabla}\times\vec{V}\right)$$

$$\vec{\nabla}(\vec{\nabla}\bullet\vec{\nabla}) = \left(\vec{\nabla}\bullet\vec{\nabla}\right)\vec{\nabla} + \left(\vec{\nabla}\bullet\vec{\nabla}\right)\vec{\nabla} + \vec{\nabla}\times\left(\vec{\nabla}\times\vec{\nabla}\right) + \vec{\nabla}\times\left(\vec{\nabla}\times\vec{\nabla}\right) = 2\left(\vec{\nabla}\bullet\vec{\nabla}\right)\vec{\nabla}$$

$$\vec{\nabla}(\vec{\nabla}\bullet\vec{\nabla}) = 0$$

$$\vec{\nabla}\times\left(\nabla^2\vec{V}\right) = \nabla^2\left(\vec{\nabla}\times\vec{V}\right) - \vec{V}\times\vec{\nabla}(\vec{\nabla}\bullet\vec{\nabla})$$

$$\vec{\nabla}\times\left(\nabla^2\vec{V}\right) = \nabla^2\left(\vec{\nabla}\times\vec{V}\right) - 0 = \nabla^2\left(\vec{\nabla}\times\vec{V}\right)$$

Taking curl of eq. [8.15]

$$\vec{\nabla}\times\frac{\partial\tilde{\vec{u}}}{\partial t} = \vec{\nabla}\times\left(-\frac{\vec{\nabla}p}{\rho_o} - g\hat{e}_z\alpha T + \nu\nabla^2\tilde{\vec{u}}\right)$$

$$\frac{\partial\vec{\nabla}\times\tilde{\vec{u}}}{\partial t} = -\frac{\vec{\nabla}\times\vec{\nabla}p}{\rho_o} - g\alpha\vec{\nabla}\times\left(\hat{e}_z T\right) + \nu\vec{\nabla}\times\nabla^2\tilde{\vec{u}}$$

$$\frac{\partial\vec{\nabla}\times\tilde{\vec{u}}}{\partial t} = -g\alpha\left\{T\left(\vec{\nabla}\times\hat{e}_z\right) - \hat{e}_z\times\vec{\nabla}T\right\} + \nu\nabla^2\left(\vec{\nabla}\times\tilde{\vec{u}}\right)$$

$$\vec{\nabla}\times\hat{e}_z = 0$$

$$\frac{\partial\vec{\nabla}\times\tilde{\vec{u}}}{\partial t} = -g\alpha\left\{-\hat{e}_z\times\vec{\nabla}T\right\} + \nu\nabla^2\left(\vec{\nabla}\times\tilde{\vec{u}}\right) \qquad [8.17]$$

Taking curl of eq. [8.17]

$$\vec{\nabla}\times\frac{\partial\vec{\nabla}\times\tilde{\vec{u}}}{\partial t} = \vec{\nabla}\times\left[g\alpha\left\{\hat{e}_z\times\vec{\nabla}T\right\} + \nu\nabla^2\left(\vec{\nabla}\times\tilde{\vec{u}}\right)\right]$$

$$\frac{\partial\vec{\nabla}\times\vec{\nabla}\times\tilde{\vec{u}}}{\partial t} = \left[g\alpha\left\{\vec{\nabla}\times\left(\hat{e}_z\times\vec{\nabla}T\right)\right\} + \nu\vec{\nabla}\times\nabla^2\left(\vec{\nabla}\times\tilde{\vec{u}}\right)\right]$$

$$\vec{\nabla}\times\vec{\nabla}\times\tilde{\vec{u}} = \vec{\nabla}\left(\vec{\nabla}\bullet\tilde{\vec{u}}\right) - \nabla^2\tilde{\vec{u}} = -\nabla^2\tilde{\vec{u}}$$

$$\vec{\nabla}\times\left(\vec{W}\times\vec{V}\right)=\vec{W}\left(\vec{\nabla}\bullet\vec{V}\right)-\vec{V}\left(\vec{\nabla}\bullet\vec{W}\right)+\left(\vec{V}\bullet\vec{\nabla}\right)\vec{W}-\left(\vec{W}\bullet\vec{\nabla}\right)\vec{V}$$

$$\vec{\nabla}\times\left(\hat{e}_z\times\vec{\nabla}T\right)=\hat{e}_z\left(\vec{\nabla}\bullet\vec{\nabla}T\right)-\vec{\nabla}T\left(\vec{\nabla}\bullet\hat{e}_z\right)+\left(\vec{\nabla}T\bullet\vec{\nabla}\right)\hat{e}_z-\left(\hat{e}_z\bullet\vec{\nabla}\right)\vec{\nabla}T$$

$$\vec{\nabla}\times\left(\hat{e}_z\times\vec{\nabla}T\right)=\hat{e}_z\left(\nabla^2T\right)-\vec{\nabla}T\left(0\right)+\left(\frac{\partial T}{\partial x}\frac{\partial}{\partial x}+\frac{\partial T}{\partial y}\frac{\partial}{\partial y}+\frac{\partial T}{\partial z}\frac{\partial}{\partial z}\right)\times\left(1\right)\hat{e}_z-\left(\frac{\partial}{\partial z}\right)\vec{\nabla}T$$

$$\vec{\nabla}\times\left(\hat{e}_z\times\vec{\nabla}T\right)=\hat{e}_z\left(\nabla^2T\right)-\left(\frac{\partial}{\partial z}\right)\vec{\nabla}T=\hat{e}_z\left(\nabla^2T\right)-\vec{\nabla}\left(\frac{\partial T}{\partial z}\right)$$

$$\vec{\nabla}\times\nabla^2\left(\vec{\nabla}\times\tilde{\vec{u}}\right)=\left(\nabla^2\vec{\nabla}\times\left(\vec{\nabla}\times\tilde{\vec{u}}\right)\right)-\left(\vec{\nabla}\times\tilde{\vec{u}}\right)\times\vec{\nabla}\left(\vec{\nabla}\bullet\vec{\nabla}\right)=\left(\nabla^2\vec{\nabla}\times\left(\vec{\nabla}\times\tilde{\vec{u}}\right)\right)$$

$$=-\left(\nabla^2\left(\nabla^2\tilde{\vec{u}}\right)\right)$$

$$\frac{\partial\vec{\nabla}\times\vec{\nabla}\times\tilde{\vec{u}}}{\partial t}=\left[g\alpha\left\{\vec{\nabla}\times\left(\hat{e}_z\times\vec{\nabla}T\right)\right\}+\nu\vec{\nabla}\times\nabla^2\left(\vec{\nabla}\times\tilde{\vec{u}}\right)\right]$$

$$-\frac{\partial\nabla^2\tilde{\vec{u}}}{\partial t}=\left[g\alpha\left\{\hat{e}_z\left(\nabla^2T\right)-\vec{\nabla}\left(\frac{\partial T}{\partial z}\right)\right\}-\nu\left(\nabla^2\left(\nabla^2\tilde{\vec{u}}\right)\right)\right]$$

$$\frac{\partial\nabla^2\tilde{\vec{u}}}{\partial t}=g\alpha\left\{\vec{\nabla}\left(\frac{\partial T}{\partial z}\right)-\hat{e}_z\left(\nabla^2T\right)\right\}+\nu\left(\nabla^2\left(\nabla^2\tilde{\vec{u}}\right)\right)\qquad[8.18]$$

The z component of eq. [8.18] becomes

$$\frac{\partial\nabla^2\tilde{\vec{u}}_z}{\partial t}=g\alpha\left\{\left(\frac{\partial^2T}{\partial z^2}\right)-\nabla^2T\right\}+\nu\left(\nabla^2\left(\nabla^2\tilde{\vec{u}}_z\right)\right)$$

$$\frac{\partial\nabla^2\tilde{\vec{u}}_z}{\partial t}=-g\alpha\left\{\nabla^2_{xy}T\right\}+\nu\left(\nabla^2\left(\nabla^2\tilde{\vec{u}}_z\right)\right)\qquad[8.19]$$

$$\nabla^2_{xy}=\frac{\partial^2}{\partial x^2}+\frac{\partial^2}{\partial y^2}$$

The z component of perturbed energy equation becomes

$$\frac{\partial T}{\partial t} - \beta \tilde{u}_z = \kappa \nabla^2 T \qquad [8.20]$$

$$\frac{\partial T}{\partial t} - \kappa \nabla^2 T = \beta \tilde{u}_z$$

$$\left(\frac{\partial}{\partial t} - \kappa \nabla^2 \right) T = \beta \tilde{u}_z \qquad [8.21]$$

Eliminating Temperature from eq. [8.19] and eq. [8.21]. First take the time derivate of eq. [8.19]

$$\frac{\partial}{\partial t}\left[\frac{\partial \nabla^2 \tilde{\vec{u}}_z}{\partial t} - \nu \left(\nabla^2 \left(\nabla^2 \tilde{\vec{u}}_z \right) \right) \right] = -g\alpha \frac{\partial}{\partial t}\left\{ \nabla^2_{xy} T \right\} \qquad [8.22]$$

$$\kappa \nabla^2 \left[\frac{\partial \nabla^2 \tilde{\vec{u}}_z}{\partial t} - \nu \left(\nabla^2 \left(\nabla^2 \tilde{\vec{u}}_z \right) \right) \right] = -g\alpha\kappa \nabla^2 \left\{ \nabla^2_{xy} T \right\} \qquad [8.23]$$

[8.22] - [8.23]

$$\left(\frac{\partial}{\partial t} - \kappa \nabla^2 \right) \left[\frac{\partial \nabla^2 \tilde{\vec{u}}_z}{\partial t} - \nu \left(\nabla^2 \left(\nabla^2 \tilde{\vec{u}}_z \right) \right) \right] = -g\alpha \left(\frac{\partial}{\partial t} - \kappa \nabla^2 \right) \left\{ \nabla^2_{xy} T \right\}$$

$$\left(\frac{\partial}{\partial t} - \kappa \nabla^2 \right) \left(\frac{\partial}{\partial t} - \nu \nabla^2 \right) \nabla^2 \tilde{\vec{u}}_z = -g\alpha \nabla^2_{xy} \left(\frac{\partial}{\partial t} - \kappa \nabla^2 \right) T$$

From eq. [8.16]

$$\left(\frac{\partial}{\partial t} - \kappa \nabla^2 \right) \left(\frac{\partial}{\partial t} - \nu \nabla^2 \right) \nabla^2 \tilde{\vec{u}}_z = -g\alpha \nabla^2_{xy} \beta \tilde{u}_z \qquad [8.24]$$

Non-dimensionalizing the eq. [8.24]

$$\left(\frac{\partial}{\partial t} - \kappa \nabla^2 \right) \left(\frac{\partial}{\partial t} - \nu \nabla^2 \right) \nabla^2 \tilde{\vec{u}}_z = -g\alpha\beta \nabla^2_{xy} \tilde{u}_z$$

$$\nabla^* = \frac{\nabla}{(1/d)} \Rightarrow \nabla = \frac{\nabla^*}{d}$$

$$t^* = \frac{t}{(d^2/\nu)} \Rightarrow t = \frac{t^* d^2}{\nu}$$

$$U^* = \frac{\tilde{\vec{u}}_z}{(\nu/d)} \Rightarrow \tilde{\vec{u}}_z = \frac{U^* \nu}{d}$$

$$\nabla^* = \frac{\nabla}{(1/d)} \Rightarrow \nabla = \frac{\nabla^*}{d}$$

$$t^* = \frac{t}{(d^2/\nu)} \Rightarrow t = \frac{t^* d^2}{\nu}$$

$$U^* = \frac{\tilde{\vec{u}}_z}{(\nu/d)} \Rightarrow \tilde{\vec{u}}_z = \frac{U^* \nu}{d}$$

$$\left(\frac{\nu}{d^2}\frac{\partial}{\partial t^*} - \kappa\frac{\nabla^{*2}}{d^2}\right)\left(\frac{\nu}{d^2}\frac{\partial}{\partial t^*} - \nu\frac{\nabla^{*2}}{d^2}\right)\frac{\nabla^{*2}}{d^2}\frac{U^*\nu}{d} = -g\alpha\beta\frac{\nabla^{*2}_{xy}}{d^2}\frac{U^*\nu}{d}$$

$$\kappa\nu\left(\frac{\nu}{\kappa}\frac{\partial}{\partial t^*} - \nabla^{*2}\right)\left(\frac{\partial}{\partial t^*} - \nabla^{*2}\right)\nabla^{*2}U^* = -g\alpha\beta d^4\nabla^{*2}_{xy}U^*$$

$$\left(Pr\frac{\partial}{\partial t^*} - \nabla^{*2}\right)\left(\frac{\partial}{\partial t^*} - \nabla^{*2}\right)\nabla^{*2}U^* = -Ra\nabla^{*2}_{xy}U^* \qquad [8.25]$$

$$Pr = \frac{\nu}{\kappa} \qquad [8.26]$$

$$Ra = \frac{g\alpha\beta d^4}{\kappa\nu} \qquad [8.27]$$

Solution to eq. [8.25] can be obtained by separation of variables. Since these equation are linear (constant coefficients), they can be cast as normal modes.

$$U^* = X(x)Y(y)Z(z)T(t)$$

$$U^* = Ae^{-ik_x x}e^{-ik_y y}Z(z)e^{\omega t}$$

$$\frac{\partial}{\partial t^*}U^* = \omega U^*$$

$$\nabla^{*2}U^* = \frac{\partial}{\partial x^{*2}}U^* + \frac{\partial}{\partial y^{*2}}U^* + \frac{\partial}{\partial z^{*2}}U^* = -k_x^2 U^* + -k_y^2 U^* + \frac{\partial}{\partial z^{*2}}U^*$$

$$\nabla^{*2}U^* = -\left(k_x^2 + k_y^2\right)U^* + \frac{\partial}{\partial z^{*2}}U^* = -k^2 U^* + \frac{\partial}{\partial z^{*2}}U^*$$

$$\nabla_{xy}^{*2}U^* = -k^2 U^*$$

$$k^2 = k_x^2 + k_y^2$$

$$\left(Pr\frac{\partial}{\partial t^*} - \nabla^{*2}\right)\left(\frac{\partial}{\partial t^*} - \nabla^{*2}\right)\nabla^{*2}U^* = -Ra\nabla_{xy}^{*2}U^*$$

$$\left(\frac{\partial}{\partial z^{*2}} - \omega Pr - k^2\right)\left(\frac{\partial}{\partial z^{*2}} - \omega - k^2\right)\left(\frac{\partial}{\partial z^{*2}} - k^2\right)U^* = Rak^2U^*$$

$$D^2 = \frac{\partial}{\partial z^{*2}}$$

$$\left(D^2 - \omega Pr - k^2\right)\left(D^2 - \omega - k^2\right)\left(D^2 - k^2\right)U^* = Rak^2U^* \qquad [8.28]$$

Eq. [8.28] is an eigenvalue problem and can be solved to yield the stability characteristics as a function of *Ra*.

APPENDIX B

VARIATION IN PROPERTIES OF WATER WITH TEMPERATURE

Table 14: Properties of water as a function of temperature.

Temp. (˚C)	**Kinematic viscosity (m^2/s)**	**Thermal expnasion coefficient (1/K)**	**Prandtl Number**	**Density (kg/m^3)**	**Specific heat (KJ/(Kg.K))**	**Thermal diffusivity (m^2/s)**
30	8.01E-07	0.000303	5.43	995.7	4179	1.394E-07
35	7.3E-07	0.000345	4.885	994.1	4178	1.396E-07
40	6.58E-07	0.000385	4.34	992.3	4179	1.399E-07
45	6.06E-07	0.00042	3.95	990.2	4181	1.401E-07
50	5.53E-07	0.000457	3.56	988	4182	1.404E-07
55	5.14E-07	0.000486	3.275	986	4183	1.406E-07
60	4.74E-07	0.000523	2.99	983	4185	1.41E-07
65	4.44E-07	0.000544	2.775	980	4188	1.413E-07
70	4.13E-07	0.000585	2.56	978	4191	1.415E-07
75	3.89E-07	0.000596	2.395	975	4194	1.418E-07
80	3.65E-07	0.000643	2.23	972	4198	1.421E-07
85	3.46E-07	0.000644	2.095	968	4203	1.426E-07
90	3.26E-07	0.000665	1.96	965	4208	1.428E-07
95	3.11E-07	0.000687	1.855	962	4213	1.431E-07
100	2.95E-07	0.000752	1.75	958	4219	1.435E-07

APPENDIX C

CFD MODELING OF RAYLEIGH-BÉNARD CONVECTIVE FLOWS

A 3-D computational flow model was formulated to examine and analyze the Rayleigh Bénard convective flow induced in microfluidic cylindrical cells. The geometries were created and meshed in Gambit (non uniform hexahedral grids) and grid independence of solutions was verified. A finite volume solver (STAR-CCM+, CD-adapco) was used to simultaneously solve the continuity equation, 3D Navier-Stokes equations and the energy equation with the Boussinesq approximation in consideration of the buoyancy driven forces to obtain the flow field for the prescribed boundary conditions (bottom = 97 °C and top = 53 °C). The sidewalls of the reactor were made insulating with no slip and no penetration (u = 0) boundary conditions. Water was used as fluid with its properties evaluated at an average temperature of the top and bottom surfaces. Both steady state and transient velocity and temperature fields were obtained and further analyzed in Tecplot and Matlab. For the reaction kinetic model, the species transport equation was solved with the coupled transient flow equations to obtain a time resolved evolution of individual reagent concentration. A step by step meshing and simulation instructions are provided below.

Mesh Generation

Gambit (ANSYS) was used for creating and meshing the cylindrical geometries. Journal files (.jou) were written with the instructions that create and mesh the PCR reactor of a given height and diameter (Figure 60). The mesh density is specified on the edges. Quadrilateral elements are used to mesh the complete volume. The volume inside is made a fluid continuum and the faces are identified as boundaries. All the parameters can be changed in this journal file and then it can be read by Gambit compiler to create and mesh the any desired geometry.

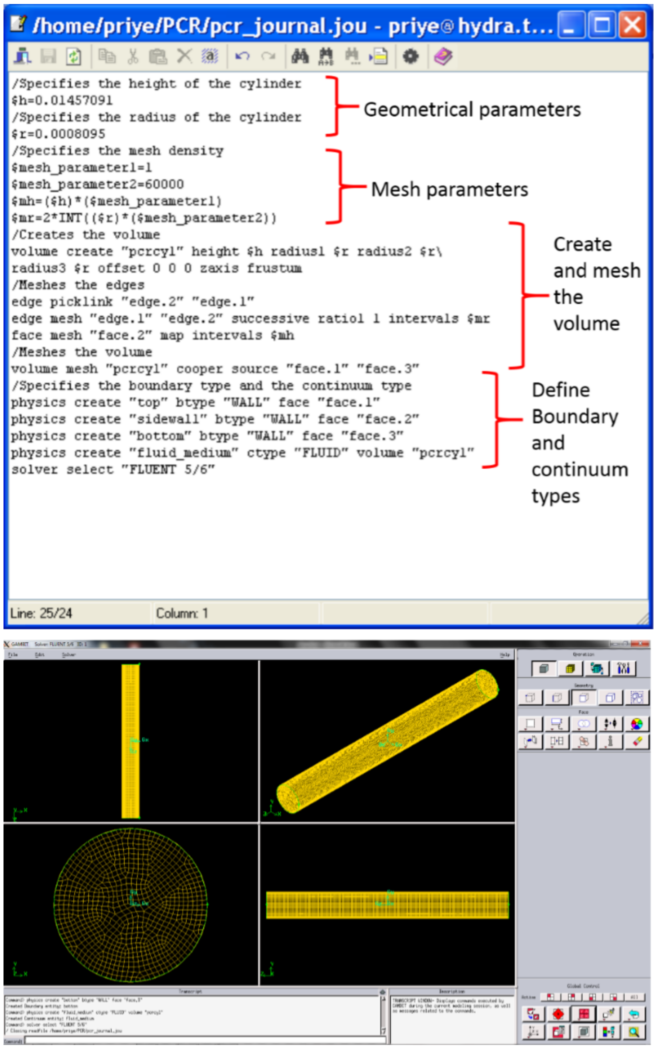

```
/Specifies the height of the cylinder
$h=0.01457091
/Specifies the radius of the cylinder
$r=0.0008095
/Specifies the mesh density
$mesh_parameter1=1
$mesh_parameter2=60000
$mh=($h)*($mesh_parameter1)
$mr=2*INT(($r)*($mesh_parameter2))
/Creates the volume
volume create ”pcrcyl” height $h radius1 $r radius2 $r\
radius3 $r offset 0 0 0 zaxis frustum
/Meshes the edges
edge picklink ”edge.2” ”edge.1”
edge mesh ”edge.1” ”edge.2” successive ratio1 1 intervals $mr
face mesh ”face.2” map intervals $mh
/Meshes the volume
volume mesh ”pcrcyl” cooper source ”face.1” ”face.3”
/Specifies the boundary type and the continuum type
physics create ”top” btype ”WALL” face ”face.1”
physics create ”sidewall” btype ”WALL” face ”face.2”
physics create ”bottom” btype ”WALL” face ”face.3”
physics create ”fluid_medium” ctype ”FLUID” volume ”pcrcyl”
solver select ”FLUENT 5/6”
```

Figure 60: PCR reactor meshing instructionsAll cylindrical reactors were created and meshed in Gambit.

Finite volume solver

Once the geometry is made, meshed and exported, it will then was imported into CFD Solver (STARCCM+). The objective of the solver is to obtain a solution to the following equations for PCR relevant boundary and initial conditions.

Continuity equation

$$\frac{\partial u}{\partial x}+\frac{\partial v}{\partial y}+\frac{\partial w}{\partial z}=0 \qquad [9.1]$$

Navier-Stokes Equations

$$\begin{aligned}
&\frac{\partial u}{\partial t}+u\frac{\partial u}{\partial x}+v\frac{\partial u}{\partial y}+w\frac{\partial u}{\partial z}=-\frac{1}{\rho}\frac{\partial p}{\partial x}+f_x+\nu\left(\frac{\partial^2 u}{\partial x^2}+\frac{\partial^2 u}{\partial y^2}+\frac{\partial^2 u}{\partial z^2}\right)\\
&\frac{\partial v}{\partial t}+u\frac{\partial v}{\partial x}+v\frac{\partial v}{\partial y}+w\frac{\partial v}{\partial z}=-\frac{1}{\rho}\frac{\partial p}{\partial y}+f_y+\nu\left(\frac{\partial^2 v}{\partial x^2}+\frac{\partial^2 v}{\partial y^2}+\frac{\partial^2 v}{\partial z^2}\right) \qquad [9.2]\\
&\frac{\partial w}{\partial t}+u\frac{\partial w}{\partial x}+v\frac{\partial w}{\partial y}+w\frac{\partial w}{\partial z}=-\frac{1}{\rho}\frac{\partial p}{\partial z}+f_z+\nu\left(\frac{\partial^2 w}{\partial x^2}+\frac{\partial^2 w}{\partial y^2}+\frac{\partial^2 w}{\partial z^2}\right)
\end{aligned}$$

Energy equation

$$\rho C_p\left(\frac{\partial T}{\partial t}+u\frac{\partial T}{\partial x}+v\frac{\partial T}{\partial y}+w\frac{\partial T}{\partial z}\right)=-k\left(\frac{\partial^2 T}{\partial x^2}+\frac{\partial^2 T}{\partial y^2}+\frac{\partial^2 T}{\partial z^2}\right) \qquad [9.3]$$

In the above equations f_x , f_y are 0, but due to the buoyancy driven forces, we can invoke the Boussinesq approximation and therefore

$$f_z = g\beta\rho(T-T_o) \qquad [9.4]$$

where g, β, ρ are the acceleration due to gravity, thermal expansion coefficient of water and density of water respectively and T and T_o are the fluid and reference temperature respectively. This buoyancy term was added by incorporating it as a momentum source term in the field function in the Navier-Stokes equations.

Once the solver converged, the flow fields were extracted as data files and post-processed using Tecplot and MATLAB.

APPENDIX D

CONVECTIVE THERMAL-CYCLING PROTOCOL

The following convective PCR protocol is based on amplification of a short target sequence (237 bp) of lambda phage DNA. KOD polymerase enzyme kit was used to amplify the target sequence. A step by step instruction is presented in the following section.

Procedure

Conventional thermo-cycler:

1. After the reagents have been thawed from their frozen state, pipette appropriate amounts of each reagent in that sequence into a micro-tube. Add the polymerase enzyme at the very end.
2. Place the micro tubes with the reagent mixture in the thermo-cycler wells and follow the following thermo-cycling protocol:

Steps	Temperature °C	Hold time (s)
1	96	10
2	95	10
3	60	30
4	72	30
5	72	300
6	4	Pause

X 30

3. After the thermo-cycling, remove the micro-tubes from the thermo-cycler and pipette the products out for analysis using gel electrophoresis.

Convective flow thermo-cycler:

1. Before loading the reagent mixture, seal the bottom of the convective cells with thin aluminum sheets. Rinse the cell walls with a 10 mg/ml aqueous solution of bovine serum albumin followed by Rain-X Anti-Fog. This is done minimize adhesion of reagents on the cell walls.
2. After the reagents have been thawed from their frozen state, pipette appropriate amounts of each reagent in that sequence into a micro-tube. Add the polymerase enzyme at the very end.
3. Transfer the reagents with the help of a micro pipette into the convective cells. Seal the top of the cell with aluminum sheet and ensure that no air bubbles show up.
4. Clamp the convective cells between the top and the bottom heating plates (Figure 61) of the convective device tightly and run the lynntech software through the computer interface (Figure 62) to maintain the temperature of the top and bottom plate as 55 °C and 95 °C respectively.
5. After running the reaction for desired time (15 -30 minutes), remove the top aluminum sheet and pipette the products out of the convective cells into another micro tube for analysis using gel electrophoresis.

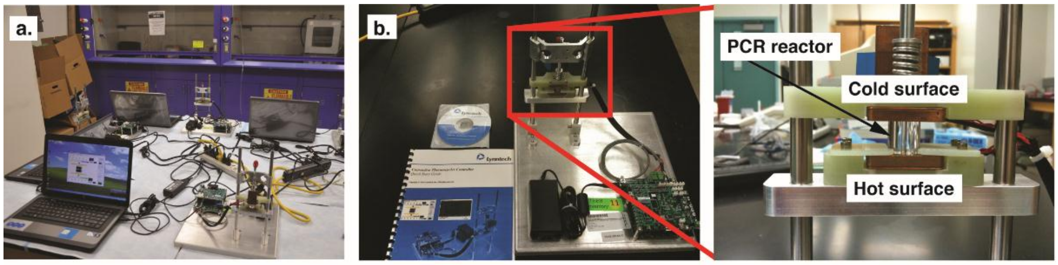

Figure 61: Convective PCR apparatus. (a) Individual convective PCR stations used in the hands-on lab activity. (b) Cylindrical transparent reactors with various geometries (d ~ 1 – 2 mm, h ~ 1 – 2 cm) are clamped between upper and lower heating plates.

Software operation:

1. Set Operation Mode Selector to “Man” (7). In manual mode the user can set each heater temperature individually.
2. Input temperature (˚C) for single or both heaters in the heater input boxes (2, 12). Press “Board” (9) to update temperature for selected test unit. Heaters will heat to the input values and remain at that temperature until values are changed.
3. Logging temperature data can be performed by the user pressing “Log Data”, the box will turn red, and temperature data will now be logged. To stop the data logging press “Log Data” again.
4. The temperature variation of the two heaters can be viewed under the “Plots” tab.
5. When the operation is completed, set the Operation Mode Selector to “Off”. This will disable the heaters.

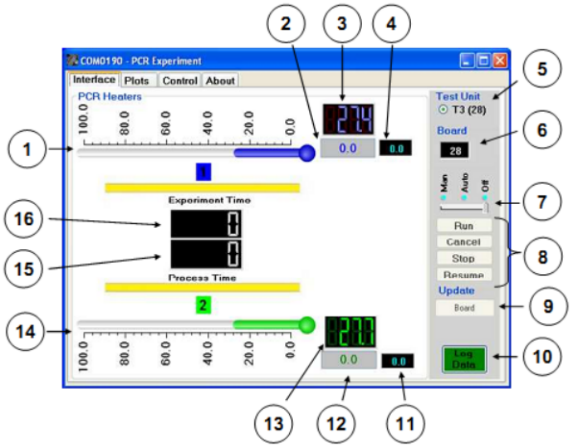

1. Graphical representation of top heater temperature (˚C).
2. User input box for setting top heater temperature (˚C).
3. Actual temperature (˚C) of top heater as measured by the system.
4. Temperature value (˚C) for top heater that the controller board has been programmed to achieve.
5. Test unit numbur with corresponding controller board ID number selected for data display and control. by the software application.
6. Controller board ID number feedback from the controller board.
7. Operation Mode Selector.
8. Operation controls for running unit in Auto mode.
9. Operation controls for running unit in Manual mode.
10. Controls for logging temperature data.
11. Temperature value (˚C) for bottom heater that the controller board has been programmed to achieve.
12. User input box for setting bottom heater temperature (˚C).
13. Actual temperature (˚C) of bottom heater as measured by the system.
14. Graphical representation of bottom heater temperature (˚C).
15. Displays time of current process the instrument is performing.
16. Displays total time experiment has been running in seconds.

Figure 62: Lynntech isothermal heater software. Operation of the COM0190 software in manual mode

Gel electrophoresis analysis:

1. Prepare a 2 wt % agarose gel by heating 10 g of agarose with 500 ml of 1x buffer on a stirring hot plate until the solution becomes clear.
2. Load the agarose gel into the casting tray and insert the comb and let the gel set for 30 minutes.
3. Remove the comb and add 1x TAE buffer until the gel is submerged.
4. Prepare fluorescently stained DNA samples by mixing 2 μL 100x SYBR Green I solution, 2 μL PCR product from convective cells/thermo-cycler, 2 μL 6x orange loading dye and 4 μL TAE buffer.

5. Add DNA samples into the wells and run the separation at 60 V for 1 h with a 100 bp DNA ladder sizing marker.
6. Remove the gel and photograph it under UV light to view results.

APPENDIX E

ARDUINO CODE FOR SINGLE HEATER DESIGN

The following arduino code was developed to maintain the temperature of the ceramic heaters at 95 °C in the circuit described in chapter III.

```
void Lcd Character(char character)

{LcdWrite(LCD_D, 0x00);
for (int index = 0; index < 5; index++)
{LcdWrite(LCD_D, ASCII[character - 0x20][index]);}
LcdWrite(LCD_D, 0x00);}

void LcdClear(void)

{for (int index = 0; index < LCD_X * LCD_Y / 8; index++)
{LcdWrite(LCD_D, 0x00);}

void LcdInitialise(void)

{pinMode(PIN_SCE,   OUTPUT);
pinMode(PIN_RESET, OUTPUT);
pinMode(PIN_DC,    OUTPUT);
pinMode(PIN_SDIN,  OUTPUT);
pinMode(PIN_SCLK,  OUTPUT);
digitalWrite(PIN_RESET, LOW);
digitalWrite(PIN_RESET, HIGH);
LcdWrite(LCD_CMD, 0x21);  // LCD Extended Commands.
LcdWrite(LCD_CMD, 0xBf);  // Set LCD Vop (Contrast). //B1
LcdWrite(LCD_CMD, 0x04);  // Set Temp coefficent. //0x04
LcdWrite(LCD_CMD, 0x14);  // LCD bias mode 1:48. //0x13
LcdWrite(LCD_CMD, 0x0C);  // LCD in normal mode. 0x0d for inverse
LcdWrite(LCD_C, 0x20);
LcdWrite(LCD_C, 0x0C);}

void LcdString(char *characters)

{while (*characters)
{LcdCharacter(*characters++);}

void LcdWrite(byte dc, byte data)
```

```
{digitalWrite(PIN_DC, dc);
digitalWrite(PIN_SCE, LOW);
shiftOut(PIN_SDIN, PIN_SCLK, MSBFIRST, data);
digitalWrite(PIN_SCE, HIGH);}
void gotoXY(int x, int y)
{LcdWrite( 0, 0x80 | x);  // Column.
LcdWrite( 0, 0x40 | y);  // Row.
}

void setup(void)

{Serial.begin(9600);
LcdInitialise();
LcdClear();
pinMode(3, OUTPUT);//Pin to MOSFET is output
pinMode(5, OUTPUT);//Pin to LED is output
pinMode(4,OUTPUT);//Pin to Relay laser control
digitalWrite(3, LOW);//MOSFET OFF
digitalWrite(5,LOW);//LED OFF
digitalWrite(4,LOW);//Nothing to the relay
}
long previousMillis = 0;
int H=1;

void loop(void)

{gotoXY(25,0);
LcdString("PCR2GO");  // LCD display
Serial.print("Uptime (s): ");
Serial.println(millis() / 1000);
float voltage, temperature;
voltage = analogRead(PIN_TMP); //read in analog value
temperature =((voltage*(5.0/1024))/0.01)+15; //calibration for temperature sensor
itoa(temperature,strBuffer,10);
gotoXY(0,1);
LcdString("Temp = ");  // LCD display
gotoXY(45,1);
LcdString(strBuffer); // Calibrating temperature changing voltage to temp and display it.
gotoXY(70,1);
LcdString("C");  // LCD display
unsigned long currentMillis = millis();
gotoXY(0,2);
LcdString("Time = ");  // LCD display
gotoXY(45,2);
```

```
itoa(((currentMillis)/1000),strBuffer,10);
LcdString(strBuffer);
gotoXY(70,2);
LcdString("s");  // LCD display
if (H==1)
{gotoXY(0,5);
LcdString("LED t= ");  // LCD display
gotoXY(45,5);
itoa(((currentMillis-previousMillis)/1000),strBuffer,10);
LcdString(strBuffer);
gotoXY(70,5);
LcdString("s");  // LCD display
}

// LASER OPERATION
/////////////////////////////////////////////////////

if (H==1)
{if(((currentMillis - previousMillis)/1000) > (7-1))
{previousMillis = currentMillis; // save the last laser Pulse
Serial.println("Toggled Laser Pulse");
Serial.println(millis() / 1000);
digitalWrite(3, LOW);//MOSFET OFF
gotoXY(0,3);
LcdString("HEAT OFF        ");
gotoXY(0,4);
LcdString("LED ON          ");
digitalWrite(4,HIGH);//RELAY ON
delay(5*1000); //5 seconds wait
gotoXY(0,4);
digitalWrite(4,LOW);//RELAY OFF
LcdString("LED OFF          ");}}
Serial.println(analogRead(4));

//HEATER OPERATION
 //////////////////////////////////////////////////

int Heat;//Pulse width of output
if(temperature < 90 )//If temp is less than 97
{gotoXY(0,3);
LcdString("HEAT ON < 90");
Heat=255; //100%
}
```

```
else if(temperature <= 97 && temperature >= 90       {
H=1;
gotoXY(0,3);
LcdString("HEAT ON 93 97");
Heat=225; //88%
}

else//If temp is greater than 97
{gotoXY(0,3);
LcdString("HEAT ON > 97");
Heat=0; }
delay(1000);//1000ms delay until next temperature sensing}
```

APPENDIX F

SERIES SOLUTION OF TWO DIMENSIONAL DIFFUSION EQUATION IN CYLINDRICAL COORDINATES

The time resolved species concentration dynamics without convective flow can be obtained by solving the diffusive transport equation in cylindrical coordinates.

$$\begin{aligned} &\frac{\partial C}{\partial t} = D\frac{1}{r}\frac{\partial}{\partial r}\left(r\frac{\partial C}{\partial r} \right) = D\left(\frac{\partial^2 C}{\partial r^2} + \frac{1}{r}\frac{\partial C}{\partial r} \right) \\ &C(r,0) = C_i \\ &C(R,t) = 0 \end{aligned} \qquad [10.1]$$

where C is the species molar concentration and D is the diffusivity of the species. Our initial condition is that the concentration is uniform throughout the cylindrical pore (at $t = 0$) and our boundary condition assumes that the concentration is 0 at curved surface (for $t > 0$). Analytical solution to the above partial differential equation can be obtained appby separation of variables i.e. assuming $C = R(r) \times T(t)$ thus converting the partial differential equations into two ordinary differential equations.

$$\frac{\partial T}{\partial t} + \lambda^2 DT = 0 \qquad [10.2]$$

$$r^2\frac{\partial^2 R}{\partial r^2} + r\frac{\partial R}{\partial r} + r^2\lambda^2 R = 0 \qquad [10.3]$$

where λ is an arbitrary constant. The first order differential equation gives an exponential solution and the second order differential equation is the Bessel's equation of order zero and can be solved using power series. The constants in the series solution can be determined from the initial and boundary conditions. Combing the two solutions provides an analytic form for the transient concentration profiles of the organic molecules within the cylindrical pore transported purely by diffusion.

$$C(r,t) = 2C_i \sum_{n=0}^{\infty} e^{\frac{-\beta_n^2 Dt}{R^2}} \frac{J_0(\beta_n r / R)}{\beta_n J_1(\beta_n)} \qquad [10.4]$$

The surface concentration (kg/m^2) is then the species mass diffused to the surface per unit curved surface area.

$$C_s(t) = \frac{MW}{1000}\left[\frac{C_i \pi R^2 h - \int_0^R 2\pi h C(r,t) r dr}{2\pi R h}\right] \qquad [10.5]$$

where *MW* is the molecular weight of the species.

APPENDIX G

MANY BODY INTERACTION BETWEEN TWO LIFSHITZ SPHERES

Let R_1 and R_2 denote the radii of the two interacting spheres, z denotes the centre of mass separation between the two spheres and $\varepsilon_s(i\xi_n)$ is the real, monotonically decreasing dielectric function evaluated at imaginary frequencies ξ_n for material s.

Let, $$E_{22} = \frac{R_1 R_2}{2}\left[\frac{1}{z^2-\left(R_1+R_2\right)^2}+\frac{1}{z^2-\left(R_1-R_2\right)^2}-\frac{2}{z^2-R_1^2}-\frac{2}{z^2-R_2^2}+\frac{2}{z^2}\right] \qquad [11.1]$$

Then

$$T = E_{22}+\sum_{p=1}^{\infty}\sum_{q=1}^{\infty}{}^{2p+2q}C_{2p}\left(\frac{p}{p+\left(\frac{\varepsilon_1(i\xi_n)}{\varepsilon_m(i\xi_n)}+1\right)^{-1}}\frac{q}{q+\left(\frac{\varepsilon_1(i\xi_n)}{\varepsilon_m(i\xi_n)}+1\right)^{-1}}-1\right)\left(\frac{R_1}{z}\right)^{2p+1}\left(\frac{R_2}{z}\right)^{2q+1} \qquad [11.2]$$

and

$$Q=\sqrt{\left(\frac{T}{E_{22}}\right)\left(\frac{\varepsilon_1(i\xi_n)-\varepsilon_m(i\xi_n)}{\varepsilon_1(i\xi_n)+\varepsilon_m(i\xi_n)}\right)\left(\frac{\varepsilon_2(i\xi_n)-\varepsilon_m(i\xi_n)}{\varepsilon_2(i\xi_n)+\varepsilon_m(i\xi_n)}\right)} \qquad [11.3]$$

with $\cosh(2\theta)=\dfrac{z^2-R_1^{\,2}-R_2^{\,2}}{2R_1R_2}$

For odd values of m

$$a(1,m)=b(1,m)=\left[\frac{z}{\sqrt{R_1R_2}}\,\frac{\sinh\left((m+1)\theta\right)}{\sinh\left(2\theta\right)}\right]^{-1} \qquad [11.4]$$

For even values of m

$$a(1,m)=\left[\frac{\sinh\left((m+2)\theta\right)}{\sinh\left(2\theta\right)}+\frac{R_2}{R_1}\frac{\sinh\left(m\theta\right)}{\sinh\left(2\theta\right)}\right]^{-1}$$

$$b(1,m)=\left[\frac{\sinh\left((m+2)\theta\right)}{\sinh\left(2\theta\right)}+\frac{R_1}{R_2}\frac{\sinh\left(m\theta\right)}{\sinh\left(2\theta\right)}\right]^{-1}$$

For $1< k \le m$

For even values of m

$$a(k,m)=\sum_{j=1}^{m+1-k} a(1,j)a(k-1,m-j),$$

$$b(k,m)=\sum_{j=1}^{m+1-k} b(1,j)b(k-1,m-j)$$

For odd values of m

$$a(k,m)=\sum_{j=1}^{m+1-k} a(1,j)b(k-1,m-j),$$

$$b(k,m)=\sum_{j=1}^{m+1-k} b(1,j)a(k-1,m-j)$$

with

$$P_\nu=\sum_{k=1}^{2\nu}\left(\frac{-1^k}{k}\right)\left[a(k,2\nu)+b(k,2\nu)\right] \qquad [11.5]$$

$$g(z,i\xi_n)=\sum_{\nu=1}^{\infty}\left\{\left[\frac{1}{8\nu}\left(\frac{1}{\sinh^2(\nu\theta)}+\frac{1}{\cosh^2(\nu\theta)}\right)\right]+P_\nu\right\}Q^{2\nu} \qquad [11.6]$$

Finally, the interaction energy between the two spheres is given by:

$$\Delta E(z)=-\frac{kT}{2}g(z,0)-\frac{h}{4\pi^2}\int_{\xi_1}^{\infty} g(i\xi_n,z)d\xi \qquad [11.7]$$